



저작자표시-비영리-변경금지 2.0 대한민국

이용자는 아래의 조건을 따르는 경우에 한하여 자유롭게

- 이 저작물을 복제, 배포, 전송, 전시, 공연 및 방송할 수 있습니다.

다음과 같은 조건을 따라야 합니다:



저작자표시. 귀하는 원저작자를 표시하여야 합니다.



비영리. 귀하는 이 저작물을 영리 목적으로 이용할 수 없습니다.



변경금지. 귀하는 이 저작물을 개작, 변형 또는 가공할 수 없습니다.

- 귀하는, 이 저작물의 재이용이나 배포의 경우, 이 저작물에 적용된 이용허락조건을 명확하게 나타내어야 합니다.
- 저작권자로부터 별도의 허가를 받으면 이러한 조건들은 적용되지 않습니다.

저작권법에 따른 이용자의 권리는 위의 내용에 의하여 영향을 받지 않습니다.

이것은 [이용허락규약\(Legal Code\)](#)을 이해하기 쉽게 요약한 것입니다.

[Disclaimer](#)

농학박사학위논문

토양 및 수계 환경에서 비산염과 인산염  
거동 예측을 위한 철(수)산화물 표면 결합구조의  
DFT, ATR-FTIR 및 XAFS 분광학적 해석

**Environmental Fate and Behavior of Arsenate and  
Phosphate in Soil and Water based on the Surface  
Complexation at Iron (Hydr)oxides by DFT  
Calculation and ATR-FTIR and XAFS Spectroscopy**

2018년 8월

서울대학교 대학원

농생명공학부 응용생명화학전공

한 준 호

(This page intentionally left blank)

**A Dissertation for the Degree of Doctor of Philosophy**

**Environmental Fate and Behavior of Arsenate and  
Phosphate in Soil and Water based on the Surface  
Complexation at Iron (Hydr)oxides by DFT  
Calculation and ATR-FTIR and XAFS Spectroscopy**

**August 2018**

**Junho Han**

**Applied Life Chemistry Major**

**Department of Agricultural Biotechnology**

**Seoul National University**

(This page intentionally left blank)

**Environmental Fate and Behavior of Arsenate and Phosphate in Soil and Water based on the Surface Complexation at Iron (Hydr)oxides by DFT Calculation and ATR-FTIR and XAFS Spectroscopy**

토양 및 수계 환경에서 비산염과 인산염 거동 예측을 위한 철(수)산화물 표면 결합구조의 DFT, ATR-FTIR 및 XAFS 분광학적 해석

지도교수 노 희 명

이 논문을 농학박사학위논문으로 제출함  
2018년 7월

서울대학교 대학원  
농생명공학부 응용생명화학전공  
한 준 호

한준호의 박사학위논문을 인준함

2018년 7월

위원장 김 정 한 (인)

부위원장 노 희 명 (인)

위원 배 의 안 (인)

위원 김 민 희 (인)

위원 高橋 嘉夫 (인)

(This page intentionally left blank)

**Environmental Fate and Behavior of Arsenate and Phosphate in Soil and Water based on the Surface Complexation at Iron (Hydr)oxides by DFT Calculation and ATR-FTIR and XAFS Spectroscopy**

Advisor: Hee-Myong Ro

A Dissertation Submitted in Partial Fulfillment  
of the Requirement for the Degree of

DOCTOR OF PHILOSOPHY

to the Faculty of  
Applied Life Chemistry Major,  
Department of Agricultural Biotechnology

at

SEOUL NATIONAL UNIVERSITY

by

Junho Han

Date Approved

20. July, 2018

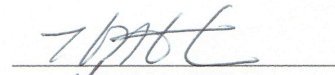
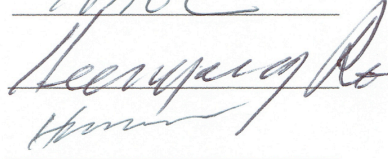
JEONG HAN KIM

HEE MYONG RO

EUIYOUNG BAE

YOSHIO TAKAHASHI

MINHEE KIM


(This page intentionally left blank)

(This page intentionally left blank)

## ABSTRACT

Oxyanions are key components of organism, and mutual interaction among oxyanions, organic acids, and metal (hydr)oxides determines the bioavailability and leachability of the oxyanion in the soil environment. The structural configuration, competition, and preferential sorption control the behaviors of oxyanions but it has not fully understood under various environmental fluctuations yet. In this study, previous studies were reviewed on the iron (hydr)oxides transformation and structural configuration, competitive sorption, and preferential sorption of oxyanions. The structural configuration of oxyanions by changing the pH and surface loading condition was studied, and the competitive and preferential sorption were examined by employing bi-sorbate system or bi-sorbent system. As a result, the EXAFS study identified tridentate complex of arsenate on a goethite surface at low pH and surface loading condition, and a bidentate and monodentate complex were observed at high pH and surface loading condition. Langmuir isotherm with batch experiment examined that the arsenate is more preferentially adsorbed at low pH on four synthetic iron (hydr)oxides but *vice versa* in the phosphate (bi-sorbate system). The sequential development of promotive effect and competition was observed by increasing the surface loading in the bi-sorbate system. In the bi-sorbent experiment, the preferential adsorption of phosphate on the maghemite over the goethite was firstly identified using ATR-FTIR and FE-SEM-EDS. Based on our observation, it was concluded that the environmental conditions such as pH, surface loading, sample phase, competitor concentration and type of available surface determines not only the structural configuration, competitive and preferential sorption of oxyanions, but also the transformation of iron (hydr)oxides, and the complexly inter-connected mechanism determines the behavior of

oxyanions in the soil environment. I believe that the bottom-up approach from simplest system to the more complex system would eventually explain the adsorption characteristics of all types of soils, and the environmental problems would be diminished by controlling the bioavailability and leachability.

**Key words:** EXAFS, ATR-FTIR, Competitive Sorption, Preferential Sorption, Oxyanion, Iron (hydr)oxide

***Student Number: 2014-31235***

# LIST OF CONTENTS

<b>ABSTRACT</b> .....	<b>i</b>
<b>LIST OF CONTENTS</b> .....	<b>iii</b>
<b>LIST OF TABLES AND FIGURES</b> .....	<b>v</b>
<b>LIST OF ABBREVIATIONS</b> .....	<b>x</b>

<b>CHAPTER 1. GENERAL INTRODUCTION</b> .....	<b>1-1</b>
1.1. Oxyanion in the soil environment .....	1-1
1.2. Iron (hydr)oxide as a key sorbent .....	1-6
1.3. Bioavailability in the rhizosphere .....	1-9
1.4. Importance of a structural configuration .....	1-10
1.5. Analytical technique for interfacial measurement .....	1-13
1.6. Aims of dissertation .....	1-14
References .....	1-16
<b>CHAPTER 2. LITERATURE REVIEW</b> .....	<b>2-1</b>
List of contents .....	2-1
Abstract .....	2-2
2.1. Introduction .....	2-4
2.2. Abundance and transformation of iron (hydr)oxides .....	2-7
2.3. Structural configuration .....	2-20
2.4. Competitive sorption .....	2-45
2.5. Conclusions .....	2-64
References .....	2-70
<b>CHAPTER 3. EXPERIMENTAL PROCEDURE</b> .....	<b>3-1</b>
List of contents .....	3-1
Abstract .....	3-2
3.1. Introduction .....	3-3
3.2. Theoretical calculation using computational chemistry .....	3-5
3.3. Experimental measurement using ATR-FTIR .....	3-8
3.4. Spectral interpretation of ATR-FTIR .....	3-23
3.5. Experimental measurement using XAS .....	3-35
3.6. Spectral interpretation of XAS .....	3-40
3.7. Sorbent characterization .....	3-44
References .....	3-48

<b>CHAPTER 4. IDENTIFICATION OF BERNALITE TRANSFORMATION AND TRIDENTATE ARSENATE COMPLEX AT NANO-GOETHITE UNDER DRYING, PH AND SURFACE LOADING .....</b>	<b>4-1</b>
List of contents .....	4-1
Abstract .....	4-2
4.1. Introduction .....	4-3
4.2. Material and methods .....	4-5
4.3. Result and discussion .....	4-17
4.4. Environmental implication .....	4-49
References .....	4-53
<b>CHAPTER 5. INTERPRETING COMPETITIVE ADSORPTION OF ARSENATE AND PHOSPHATE ON SYNTHETIC NANO-IRON (HYDR)OXIDES: EFFECT OF PH AND SURFACE LOADING .....</b>	<b>5-1</b>
List of contents .....	5-1
Abstract .....	5-2
5.1. Introduction .....	5-4
5.2. Material and methods .....	5-6
5.3. Result and discussion .....	5-14
5.4. Conclusion .....	5-41
References .....	5-43
<b>CHAPTER 6. CHARACTERIZING PREFERENTIAL ADSORPTION OF PHOSPHATE ON BINARY SORBENTS OF GOETHITE AND MAGHEMITE SURFACE USING <i>in situ</i> ATR-FTIR AND FE-SEM/EDS. ....</b>	<b>6-1</b>
List of contents .....	6-1
Abstract .....	6-2
6.1. Introduction .....	6-3
6.2. Material and methods .....	6-5
6.3. Result and discussion .....	6-19
6.4. Conclusion .....	6-41
References .....	6-47
<b>CHAPTER 7. SUMMARY AND CONCLUSION .....</b>	<b>7-1</b>
7.1. Summary .....	7-2
7.2. Conclusion .....	7-5
<b>ABSTRACT IN KOREAN .....</b>	<b>xi</b>
<b>LIST OF PUBLICATION .....</b>	<b>xii</b>
<b>ACKNOWLEDGEMENT .....</b>	<b>xiii</b>

# LIST OF TABLE AND FIGURES

## CHAPTER 1. GENERAL INTRODUCTION

<b>Table 1-1</b> Fundamental properties, toxicity, and uptake mechanism of oxyanions. ....	1-5
<b>Fig. 1-1</b> pH-Eh diagrams of arsenic (a) and phosphorus (b), re-illustrated works from Vancen (1995) and Pasek (2007). ....	1-3
<b>Fig. 1-2</b> Schematic illustration for soil heterogeneity and oxyanion dynamics in gas, aqueous and solid phases. ....	1-7
<b>Fig. 1-3</b> Schematic illustration of competitive sorption between root-derived organic acids and oxyanions in the soil. ....	1-11

## CHAPTER 2. LITERATURE REVIEW

<b>Table 2-1</b> The dominant structural configuration as a function of the pH of oxyanions and organic acids on six iron (hydr)oxides. ....	2-23
<b>Table 2-2</b> Summary of the atomic distance among oxyanion element, oxygen shell and iron shell using EXAFS studies. ....	2-33
<b>Table 2-3</b> Summary of vibrational band position in each structural configuration from the previous literature ....	2-38
<b>Table 2-4</b> The dominant oxyanion species of competitive sorption among the various oxyanions and organic acids on each iron (hydr)oxide surface. ....	2-47
<b>Table 2-5</b> The average values of reduced sorption percent ( <i>RSP</i> , %) among the oxyanions and organic acids by pH ranges. ....	2-53
<b>Fig. 2-1</b> Abundance of iron (hydr)oxide in the climate zone and the common pathway of formation and transformation in the environment. ....	2-11
<b>Fig. 2-2</b> Schematic diagram to describe iron (hydr)oxide transformation in the soil environment based on the land-use regime for crop cultivation. ....	2-17
<b>Fig. 2-3</b> Scatter plot between $\Gamma_{As}$ ( $\mu\text{mol m}^{-2}$ ) and SL ( $\mu\text{mol m}^{-2}$ ) for arsenate sorption on six iron (hydr)oxides using extended X-ray absorption fine structure spectroscopy results from previous papers ( $N=15$ ) (a), and scatter plot between competition effect and SL in the competition of arsenate with arsenite ( $N=45$ ) (b). ....	2-29
<b>Fig. 2-4</b> Scatter plot of arsenate on iron (hydr)oxides between pH and As-Fe distance measured by EXAFS studies. ....	2-31
<b>Fig. 2-5</b> Box plot of the reduced sorption percentage ( <i>RSP</i> , %) of each oxyanion with all other oxyanions. ....	2-61
<b>Fig. 2-6</b> Scatter plot between surface loading (molecule $\text{nm}^{-2}$ ) and surface site density (site $\text{nm}^{-2}$ ) from the single batch experiment. ....	2-65

### CHAPTER 3. EXPERIMENTAL PROCEDURE

<b>Table 3-1</b> Penetration depth between crystal material and metal oxide ( $T=25\text{ }^{\circ}\text{C}$ , pressure=1 atm, $n_w=1.33$ , $\lambda=10\text{ }\mu\text{m}$ , $\theta_i=45^{\circ}$ ). .....	3-17
<b>Fig. 3-1</b> Fundamental schematic diagram of analysis technique using Fourier transform infrared spectroscopy. ....	3-11
<b>Fig. 3-2</b> Schematic diagram showing optical pathway during internal reflection at solid-liquid interface measurement using <i>in situ</i> ATR-FTIR. ....	3-15
<b>Fig. 3-3</b> Theoretically calculated depth of penetration ( $d_p$ ) as function of wavenumber (a) and refractive index (b). ....	3-21
<b>Fig. 3-4</b> Example of peak identification in aqueous phosphate speciation measured by <i>in situ</i> ATR-FTIR using derivative spectroscopy under pH 5.5 and 8.0 (a) and synchronous (b) and asynchronous correlation spectrum (c) from pH 5.5 to pH 8.0 using two dimensions correlation spectroscopy. ....	3-27
<b>Fig. 3-5</b> Contour map of aqueous phosphate speciation measured by pH change using <i>in situ</i> ATR-FTIR (a), two identified spectrum and its experimental peak position calculated using DFT (b), pH versus concentration graph fitted by MCR-ALS (c). ....	3-33
<b>Fig. 3-6</b> Peak deconvolution spectrum at pH 5.5 (a) and 8.0 (b), and the assigned vibrational mode for each deconvoluted peak, and deconvoluted peak area change as function of pH (c). ....	3-36
<b>Fig. 3-7</b> Data reduction process of XAFS spectra using $\text{Na}_2\text{HAsO}_4$ powder as an example. Raw data of XAFS spectra (a), background, pre-edge and post-edge identification using Athena software (b), normalized spectra with background (c), 2 <sup>nd</sup> derivative of spectra for $E_0$ identification, conversion to $k^3$ -space (e), and Fourier transform to $R$ -space (d). ....	3-42

### CHAPTER 4. IDENTIFICATION OF BERNALITE TRANSFORMATION AND TRIDENTATE ARSENATE COMPLEX AT NANO-GOETHITE UNDER DRYING, PH AND SURFACE LOADING

<b>Table 4-1</b> Physiochemical characteristics of nano-goethite. ....	4-9
<b>Table 4-2</b> Results from batch experiment and linear combination fitting of EXAFS spectra acquired in sedimented and dried samples. ....	4-38
<b>Fig. 4-1</b> X-ray diffraction spectrum of goethite sample (black dot) and reference of goethite (blue bar, AMCSD-0003165) and bernalite (red bar, AMCSD-0001607) from the American mineralogist crystal structure database. ....	4-7
<b>Fig. 4-2</b> Schematic illustration for the batch experiment, DFT calculation, ICP-OES, TEM and EXAFS measurement and the output from the interpretation. ....	4-11
<b>Fig. 4-3</b> Optimized geometry by DFT calculation of B3LYP with 6-311+G* basis set. ....	4-15

<b>Fig. 4-4</b> Langmuir sorption isotherm of arsenate (0, 0.1, 1, 5 and 10 mM initial concentration) on nano-goethite plotted with surface density at pH 4 (red), 7 (black) and 10 (blue) (a). .....	4-19
<b>Fig. 4-5</b> HRTEM image of rod-shaped goethite (a) and spherical bernalite by transformation from goethite (c), their distribution at pH 10 with 10 mM arsenate concentration (b), and selected area electron diffraction pattern of spherical bernalite at $Z = [001]$ (d). .....	4-23
<b>Fig. 4-6</b> Fourier transform magnitude of As K-edge $k^3$ -weighted EXAFS spectra in sedimented samples at various pH values (4, 7, 10) and concentrations (1, 10 mM) (a), experimental spectra of arsenate solution and $\text{Na}_2\text{HAsO}_4 \cdot 7\text{H}_2\text{O}$ powder as the references, and theoretical spectra of five configurations by DFT calculation (b). .....	4-27
<b>Fig. 4-7</b> Fourier transform magnitude from As K-edge $k^3$ -weighted EXAFS spectra of dried samples under various pH (4, 7 and 10) and surface loading. ....	4-29
<b>Fig. 4-8</b> As K-edge $k^3$ -weighted EXAFS spectra (a) and the corresponding Fourier transform magnitude (b) of 10 mM aqueous arsenate at pH 4 (red), 7 (black) and 10 (blue). .....	4-31
<b>Fig. 4-9</b> Experimental As K-edge $k^3$ -weighted EXAFS spectra of 1 mM (dotted line) and 10 mM arsenate (solid line) on the goethite at pH 4 (red), 7 (black) and 10 (blue) under different sample phase (sedimented (top) and dried (middle)), and theoretical As K-edge $k^3$ -weighted EXAFS spectra of five clusters of the complex from DFT calculation (bottom). .....	4-33
<b>Fig. 4-10</b> As K-edge XANES spectra of 1 mM (dashed line) and 10 mM arsenate (solid line) on the goethite at pH 4 (red), 7 (black) and 10 (blue) under different sample phase (sedimented (a) and dried (b)), and the aqueous arsenate (dotted line) and precipitate (dotted line). .....	4-35
<b>Fig. 4-11</b> Fourier transform magnitude from As K-edge $k^3$ -weighted EXAFS spectra of sedimented and dried samples at pH 4 (red), 7 (black) and 10 (blue) at 1 and 10 mM arsenate surface loading. ....	4-41
<b>Fig. 4-12</b> Distribution of five configurations of the complex by pH and arsenate concentration. ....	4-43
<b>Fig. 4-13</b> Distribution of five configurations of the complex and precipitated arsenate (using $\text{NaH}_2\text{AsO}_4 \cdot 7\text{H}_2\text{O}$ ) at pH 4, 7 and 10 and arsenate concentration (1 and 10 mM) after drying. ....	4-45
<b>Fig. 4-14</b> Schematic illustration for the transition of structural configuration by the change of pH and surface loading conditions. ....	4-51

**CHAPTER 5. INTERPRETING COMPETITIVE ADSORPTION OF ARSENATE AND PHOSPHATE ON SYNTHETIC NANO-IRON (HYDR)OXIDES: EFFECT OF PH AND SURFACE LOADING**

**Table 5-1** Physicochemical characteristics of Iron oxides. .... 5-10

**Table 5-2** Langmuir fitting results with different oxyanion inputs, pH values and iron oxides. .... 5-21

**Fig. 5-1** Scatter plot of pH and competitive sorption ratio ( $CSR_{As(V)/P(V)}$ ) of arsenate and phosphate from the previous studies. .... 5-7

**Fig. 5-2** Measured XRD spectrum (black line) and reference position (red bar) of nano-sized goethite (0004538), hematite (0017806), maghemite (0020585) and magnetite (0020645). .... 5-11

**Fig. 5-3** HRTEM image of nano-sized goethite (a), hematite (b), maghemite (c) and magnetite (d). .... 5-17

**Fig. 5-4** Stacked bar graph of the adsorbed oxyanion per unit mass in the arsenate, phosphate and mixture treatments under 10 mM of total oxyanion input on the goethite, hematite, maghemite and magnetite at pH values of 4, 7 and 10. ... 5-19

**Fig. 5-5** Line and scatter plot of the pH and competitive sorption ratio ( $CSR$ ) (a) and the pH and competitive effect ( $CE$ ) (b) calculated for interpreting the competitive sorption between arsenate and phosphate. .... 5-23

**Fig. 5-6** Line and scatter plot of surface loading and competitive sorption ratio ( $CSR$ ) on goethite, hematite, maghemite and magnetite. A value greater than 1 in  $CSR_{As(V)/P}$  indicates that As(V) is predominant *versus* phosphate and *vice versa*. .... 5-27

**Fig. 5-7** Line and scatter plot of surface density (molecule  $nm^{-2}$ ) and competitive effect ( $CE$ ) of arsenate and phosphate on goethite, hematite, maghemite and magnetite at pH values of 4 (a), 7 (b) and 10 (c). .... 5-29

**Fig. 5-8** Schematic illustration for the isotherm adsorption, competitive sorption ratio ( $CSR$ ) and competitive effect ( $CE$ ) on two chemicals, A and B, with increasing surface loading. .... 5-33

**Fig. 5-9** The average of iron dissolution rates ( $nmol\ m^{-2}\ h^{-1}$ ) at 10 mM of the arsenate (red), phosphate (blue) and mixture (black) treatments as a function of pH on goethite (a), hematite (b), maghemite (c) and magnetite (d). .... 5-39

**CHAPTER 6. CHARACTERIZING PREFERENTIAL ADSORPTION OF PHOSPHATE ON BINARY SORBENTS OF GOETHITE AND MAGHEMITE SURFACE USING *in situ* ATR-FTIR AND FE-SEM/EDS**

**Table 6-1** Physicochemical characteristics of goethite and maghemite. .... 6-6

**Fig. 6-1** X-ray diffraction pattern of goethite and maghemite. .... 6-7

**Fig. 6-2** HR-TEM image of nanosized goethite (a) and maghemite (b). .... 6-9

<b>Fig. 6-3</b> Schematic diagram of experimental setup, spectral measurement and data processing for characterizing the preferential adsorption using <i>in situ</i> ATR-FTIR in the binary adsorbents. ....	6-13
<b>Fig. 6-4</b> Langmuir adsorption isotherm of phosphate (0, 0.11, 1.1, 5.5 and 11 mM initial concentration) on the goethite (square) and maghemite (circle) plotted with adsorbed phosphate (mmol g <sup>-1</sup> ) at pH 4 (red) and 7 (black) after 48 h of incubation. ....	6-21
<b>Fig. 6-5</b> Scatter plot between the surface loading (molecule nm <sup>-2</sup> ) and surface density (molecule nm <sup>-2</sup> ) on the goethite from the previous literature (triangle, diamond, hexagon and circle) and this study (rectangle) at pH 4 (black) and 7 (white). The axis was log-scaled for better understanding. ....	6-23
<b>Fig. 6-6</b> Sedimentation photographs of nanosized goethite (Gt) and maghemite (Mh) at different phosphate concentrations (0, 0.5 and 5 mM) after standing for 1, 15, 30 and 120 min. DW is the abbreviation of distilled water. ....	6-25
<b>Fig. 6-7</b> Micro-scale image of the goethite surface (a) and maghemite surface (b) on the ZnSe crystal, 20-degree tilted image of goethite layer (c) and maghemite surface (d) on ZnSe crystal by SE2 mode under 25 kV using FE-SEM, and nanoscale image of the goethite (e) and maghemite film (f) by InLens mode under 2 kV. ....	6-29
<b>Fig. 6-8</b> Stitched image of FE-SEM at 100 x magnification using SE2 mode (a), mapping image of FE-SEM-EDS at 30,000 x magnification at dark spot (b) and crystal structure (c). The right side is the marginal part of the maghemite layer, and the left side is the direction to the center part of layer. ....	6-31
<b>Fig. 6-9</b> Evolution of time series ATR-FTIR spectra of 1 mM phosphate on the single goethite (a), single maghemite (b) and binary mixture (c) at different times up to 3 h after phosphate addition. ....	6-33
<b>Fig. 6-10</b> Absorbance over time at 1012 cm <sup>-1</sup> in the single goethite (black circle), 1012 cm <sup>-1</sup> in the binary sorbents (white circle), 1079 cm <sup>-1</sup> in the single maghemite (black rectangle) and 1079 cm <sup>-1</sup> in the binary sorbents (white rectangle). ....	6-37
<b>Fig. 6-11</b> The ATR-FTIR spectra of kinetic study (a) and dried samples (b). The spectra used in multiple linear regressions (MLR) to calculate the fraction of individual components. ....	6-43
<b>Fig. 6-12</b> Measured spectra of background, phosphate precipitate, dried single sorbent and binary sorbents (a), phosphate adsorbed and dried single goethite, single maghemite and binary sorbents (b), and kinetic studies from the initial and final single goethite, single maghemite and binary sorbents (c). The small graphs in (c) are the enlargement of single sorbent (d) and binary sorbent experiment (e) from the kinetic studies for better illustration. ....	6-45

## LIST OF ABBREVIATIONS

- 2D-COS:** Two-dimensional correlation spectroscopy  
**AMCSD:** American mineralogist crystal structure database  
**ATR-FTIR:** Attenuated total reflection-Fourier transform infrared spectroscopy  
**BB:** Bidentate binuclear complex  
**BET:** Brunauer-Emmett-Teller  
**BM:** Bidentate mononuclear complex  
**CE:** Competition effect  
**CSR:** Competitive sorption ratio  
**DFT:** Density functional theory  
**DR<sub>Fe</sub>:** Dissolution rate of iron  
**EC:** Electrical conductivity ( $\mu\text{S cm}^{-1}$ )  
**EDS:** Energy dispersive X-ray spectroscopy  
**EXAFS:** Extended X-ray absorption fine structure  
**FE-SEM:** Field emission-scanning electron microscopy  
**HF:** Hartree Fock molecular orbital theory  
**HR-TEM:** High resolution-transmission electron microscopy  
 **$K_L$ :** Langmuir constant  
**LCF:** Linear combination fitting  
**LIBS:** Laser induced breakdown spectroscopy  
**ICP-OES:** Inductively coupled plasma-optical emission spectroscopy  
**IS:** Inner-sphere complex  
**OS:** Outer-sphere complex  
 **$Q_{max}$ :** Maximum adsorption capacity ( $\mu\text{mol kg}^{-1}$ )  
**RSP:** reduced sorption percentage  
**SA:** Surface area ( $\text{m}^2 \text{g}^{-1}$ )  
**SAED:** Selected area electron diffraction  
**SR:** Specular reflection  
**PNZC:** Point of net zero charge  
**MCR-ALS:** Multivariate curve resolution-alternating least square  
**MB:** Monodentate binuclear complex  
**MM:** Monodentate mononuclear complex  
**TB:** Tridentate binuclear complex  
**XANES:** X-ray absorption near edge structure  
**XAS:** X-ray absorption spectroscopy  
**XRD:** X-ray diffraction spectroscopy  
**XRF:** X-ray fluorescent spectroscopy  
 **$\Gamma_{max}$ :** Maximum adsorption capacity ( $\text{molecule nm}^{-2}$ )

# CHAPTER 1. GENERAL INTRODUCTION

## 1.1. Oxyanions in the soil environment

An oxyanion is a negatively charged molecule with the generic formula  $A_xO_y^{z-}$ . Carbonate ( $CO_3^{2-}$ ), nitrate ( $NO_3^-$ ), phosphate ( $PO_4^{3-}$ ), silicate ( $SiO_4^{2-}$ ) and sulfate ( $SO_4^{2-}$ ) are the major oxyanions in the soil environment, whereas arsenate ( $AsO_4^{3-}$ ), antimonate ( $SbO_4^{3-}$ ), borate ( $BO_3^{3-}$ ), selenate ( $SeO_4^{2-}$ ), and tellurate ( $TeO_4^{2-}$ ) are generally found at trace levels (Johnson, 1971; Sparks, 2000) (Table 1-1). Oxyanions are ubiquitous on Earth and are fundamental constituents of organisms and the environment. Based on their chemical structures, oxyanions can easily undergo reactions that change them into other chemical species, a process called species transformation (Templeton and Fujishiro, 2017). The species transformation of oxyanions in the soil is caused by environmental fluctuations, such as changes in the pH, redox potential and concentrations of ligands (Georgiadis et al., 2006; Masscheleyn et al., 1991) (Fig. 1-1). The species transformation not only changes the oxyanion species but also affects its affinity to the adsorbent; thus, it determines the behavior of oxyanions in the soil environment (Mir et al., 2007; Panssar-Kallio and Manninen, 1997).

Arsenic is one of the most notorious elements in the earth because of its abundance, toxicity and usage worldwide (Jain and Ali, 2000; Leermakers et al., 2006). Over 20 countries have suffered from groundwater contamination by arsenic originating from the natural and anthropogenic sources, such as mining, agricultural chemicals and wood preservatives (Smedley and Kinniburgh, 2002; Zhang and Selim, 2006), which have accelerated arsenic contamination in the soil environment (Hyun et al., 2012; Singh et al., 2015; Zhang and Selim, 2006). Arsenic accumulation poses a serious threat to human and ecosystems health (Han et al.,

2014; Hughes, 2002; Jain and Ali, 2000; Leermakers et al., 2006), since arsenate (major oxyanion form of arsenic) resembles phosphate and can block phosphate metabolism, causing various problems to humans (Hughes, 2002; Li et al., 2007; Ratnaike, 2003). However, it is extremely difficult to diminish such problems due to its distinctive dynamics in the soil environment such as species transformation, methylation, transport, precipitation and adsorption (Diaz-Bone et al., 2011; Leermakers et al., 2006; Rosen and Liu, 2009).

Phosphorus is one of the essential elements in the soil environment and is a key element for the growth of terrestrial organisms in most environments. In the past, phosphorus acted as a limiting factor for cultivation; however, recent developments in fertilization have caused over-fertilization in most agricultural regions to maximize agricultural productivity (Elser et al., 2007). As a consequence, the excess phosphorus has leached out into the water system, leading to eutrophication, creating serious health and environmental problems worldwide (Barberis et al., 1995; Elser et al., 2007). Therefore, it is essential to understand how the phosphorus interacts with soil components and what critical factor governs the structural configuration of phosphorus to retain the phosphorus in the soil environment (Kubicki et al., 2007).

Both arsenic and phosphorus are located in group VII in the periodic table, and their electrochemical properties are similar, while their environmental impacts are extremely different (Luengo et al., 2007; Woolson et al., 1971). Recent anthropogenic activities, natural abundance and development in fertilization have accelerated arsenic contamination in over 20 countries, and the eutrophication of water system is caused by over-fertilization of phosphorus worldwide (Barberis et al., 1995; Elser et al., 2007; Jain and Ali, 2000; Leermakers et al., 2006). They are known as the most notorious elements used to control the dynamics in the soil

**Fig. 1-1** pH-Eh diagrams of arsenic (a) and phosphorus (b), re-illustrated works from Lu and Zhu (2010) and Pasek (2008).

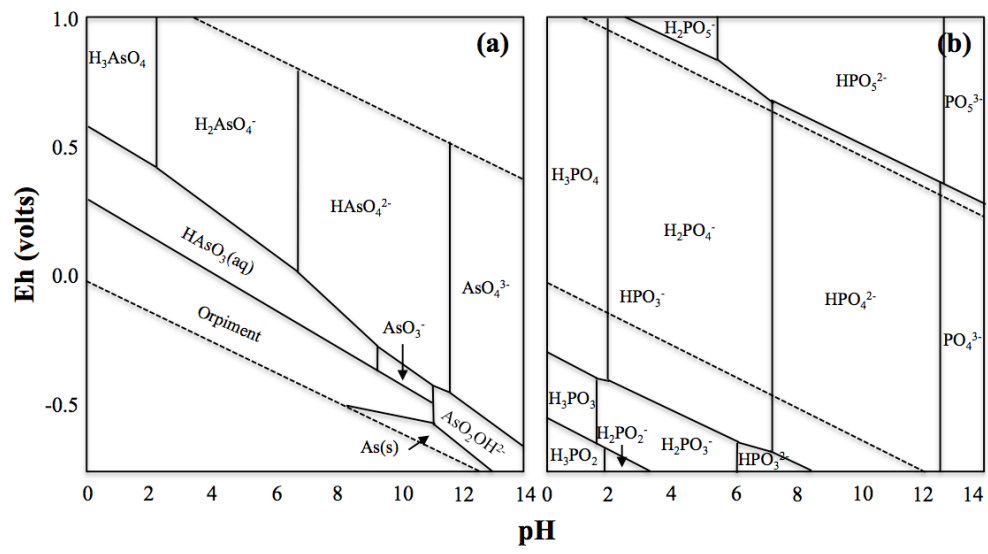


**Table 1-1** Fundamental properties, toxicity, and uptake mechanism of oxyanions

Element	Symbol	Number	Atomic weight	Oxidation states	Electro-negativity	Atomic radius	Covalent radius	Van der Waals radius	Isotope	Toxicity	Uptake mechanism in plant
Arsenic	As	33	74.92	5,3,-1,-3	2.18	119	119	185	73-75	Tox.	As(III) Si transporter (Zhao et al., 2009) As(V) P transporter (Smith et al., 2008; Zhao et al., 2009) DMA/MMA unknown (Zhao et al., 2009)
Selenium	Se	34	78.96	6,4,2,1,-2	2.55	120	120	190	72/74-80/82	Ess., Tox.	Se(IV) inhibited by Phosphate (Li et al., 2008) Se(VI) Sulfate transporter (Li et al., 2008)
Carbon	C	6	12.01	-4-4	2.55	-	77	170	11-14	Ess., Tox.	-
Sulfur	S	16	32.06	6-1, -1, -2	2.58	-	105	180	32-36	Ess.	Sulfate transporter (Takahashi, 2010)
Phosphorus	P	15	30.97	5-1, -1,-2,-3	2.19	-	107	180	31/32/33	Ess.	Phosphate transporter (Bucher, 2007)
Nitrogen	N	7	14.01	5-1,-1,-2,-3	3.04	-	71	155	13-15	Ess.	Ammonium transporter (Von Wirén et al., 2000) Nitrate transporter (Parker and Newstead, 2014)
Tellurium	Te	52	127.6	6,5,4,2,-2	2.1	140	138	206	120-130	unknown	unknown
Antimony	Sb	51	121.8	5,3,-3	2.05	140	139	206	121/123/125	Tox.	unknown

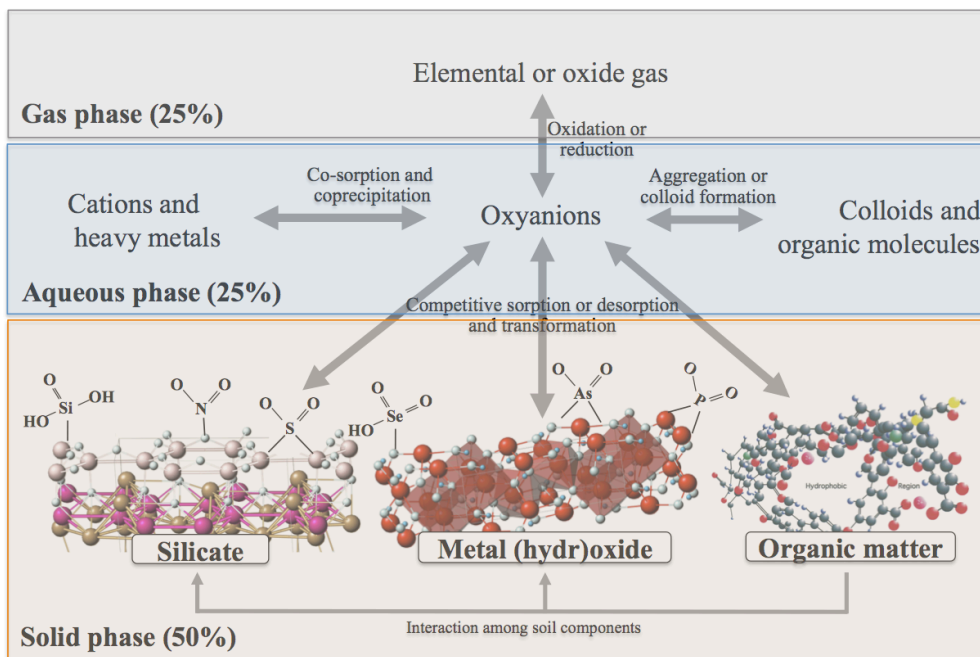
environment because a majority of soil problems occur due to cationic heavy metals, but oxyanion has the opposite characteristics; the oxyanion exists as various species depending upon the environmental conditions (Han et al., 2016; Kwon et al., 2010).

## 1.2. Iron (hydr)oxides as a key sorbent

The solid component of soil is a complex of various materials, such as phyllosilicates, metal (hydr)oxides, and organic matter (Fig. 1-2). Iron (hydr)oxide is one of the key sorbents in retaining both nutrients and pollutants because of its reactivity, surface area and surface charge (Adegoke et al., 2013; Lefevre, 2004; Panias et al., 1996). Environmental fluctuation causes oxyanions to undergo species transformation, and the transformation of iron (hydr)oxide, which changes its crystal structure and morphology, ultimately affects the sorption characteristics of oxyanions in the soil environment (Kubicki et al., 2012; Michael Bolanz et al., 2013).

Iron is the fourth most abundant element in the crust of the Earth, at 5.1 % by mass (Cox, 1989). Biotite, pyroxene, olivine, magnetite and pyrite are the main iron-containing minerals (Cornell and Schwertmann, 2003), and weathering by hydrolysis and oxidation forms iron (hydr)oxide in the soil (Cornell and Schwertmann, 2003; Udo and Rochelle, 2008). During the weathering process, once the primary rock containing iron is exposed to oxic conditions,  $\text{Fe}^{2+}$  is readily oxidized to  $\text{Fe}^{3+}$  by providing an electron to oxygen at soil pH, and then soluble  $\text{Fe}^{3+}$  oxides are easily formed by hydrolysis. Based on the parent materials, climate, redox conditions and organisms involved, various iron (hydr)oxides can be formed, such as amorphous iron (hydr)oxide (AIO), goethite ( $\alpha$ -FeOOH), lepidocrocite ( $\gamma$ -FeOOH), ferrihydrite ( $\text{Fe}_2\text{O}_3 \cdot 0.5\text{H}_2\text{O}$ ), hematite ( $\alpha$ - $\text{Fe}_2\text{O}_3$ ) and maghemite ( $\gamma$ - $\text{Fe}_2\text{O}_3$ ) (Cornell and Schwertmann, 2003; Udo and Rochelle, 2008).

**Fig. 1-2** Schematic illustration for soil heterogeneity and oxyanion dynamics in gas, aqueous and solid phases.



### 1.3. Bioavailability in the rhizosphere

Plant uptakes aqueous or weakly bound oxyanions from soil rhizosphere *via* specific transporter at cell membrane, and the abundance of bioavailable fraction of the adsorbed complex controls the growth of organisms in the terrestrial environment (Fig. 1-3). The plant developed several mechanisms to optimize nutrient uptake, for instance, dual pathways of uptake as ammonium and nitrate ions, and nitrogen fixation by leguminous bacteria. Unlike the nitrogen, the phosphorus only exists as trivalent phosphate in soil pore water through phosphorous cycle (Fig. 1.1), and the aqueous phosphate also easily precipitates as minerals with multivalent cations such as apatite with calcium and vivianite with iron; thus, the bioavailability of phosphorous controls the plant growth in the most terrestrial system.

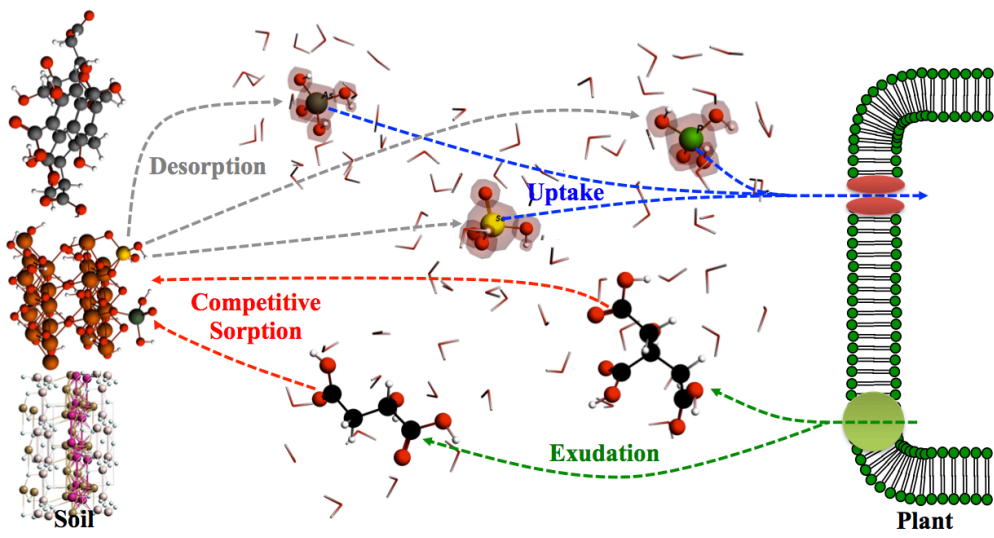
However, recent development and production of chemical fertilizer caused that no longer consider such oxyanions as the limiting factors in cultivation. The over-fertilization was conducted to maximize the agricultural productivity; less attention was paid to optimize bioavailability through study and management of soil. In consequence, excessive nutrients have leached out from the pedosphere to the hydrosphere, and it raises severe environmental problems worldwide. In case of nitrogen, it has several pathways to circulate nitrogen cycle, such as atmospheric discharge *via* volatilization of  $\text{NH}_3$  by ammonification, and emission of  $\text{N}_2$ ,  $\text{N}_2\text{O}$  and  $\text{NO}_x$  by denitrification, and nitrification into nitrate and nitrite under oxidizing condition with high pH, or ammonification as  $\text{NH}_4^+$  under reducing condition with low pH. On the other hand, the phosphorus only existed as phosphate in aqueous and mineral phase, most of it transports to water system by water movement and causing severe eutrophication. To diminish such problem, maintaining optimum bioavailability of nutrient is crucial, but the heterogeneity and complexity of soil makes it hard to estimates optimum bioavailability.

#### 1.4. Importance of structural configuration

Not only the sorbent characteristics but also the interactions of the oxyanions with iron (hydr)oxide are important. There are two main types of interactions: the inner-sphere (IS) complex is formed by adsorption through covalent bonds, while the outer-sphere (OS) complex is formed by adsorption through electrostatic attraction and dispersion interactions (Sparks, 2003; Stumm and Morgan, 1981). The IS complex can be monodentate, bidentate or tridentate, and its structural configuration is essential to understanding the behavior of oxyanions in the soil environment because it determines their leachability and bioavailability (Fendorf et al., 1997; Liu et al., 2015; Zhu et al., 2013).

Numerous studies have attempted to reveal the structural configuration of oxyanions on the iron oxides, but it is still controversial. A bidentate binuclear (BB) complex has been confirmed as the major structural configuration of arsenate and phosphate on the iron oxides (Antelo et al., 2005; Farquhar et al., 2002; Fendorf et al., 1997; Gao et al., 2013; Morin et al., 2008; Neupane et al., 2014; Randall et al., 2001; Waychunas et al., 1993), but few studies also identified bidentate mononuclear (BM) (Fendorf et al., 1997; Neupane et al., 2014) and monodentate mononuclear (MM) complexes (Fendorf et al., 1997; Loring et al., 2009; Waychunas et al., 1993). Previous studies confirmed the transition of structural configuration by the environmental condition, Elzinga and Sparks (Elzinga and Sparks, 2007), Waychunas et al. (Waychunas et al., 1993), He et al. (He et al., 2009) and Abdala et al. (Abdala et al., 2015) reported the pH and surface loading effect on the transition, while Gu et al. (Gu et al., 2016) reported the drying effect. From the literature, it is clear that the transition of structural configuration is highly dependent on the environmental condition, but the inter-connection among the environmental conditions was not fully addressed yet.

**Fig. 1-3** Schematic illustration of competitive sorption between root-derived organic acids and oxyanions in the soil.



Recent study revealed that plant secretes root exudate, and possibility of increase in bioavailability by competitive sorption between root-derived organic acids and sorbed oxyanions or reductive dissolution of oxyanion-containing mineral, but concrete evidence has not been provided yet. Three reasons would be inferred; in first, previous soil analysis is based on completely dry sample instead of practical wet sample. Bioavailable oxyanion only existed as low level in the soil by aqueous ion, outer-sphere complex, and monodentate inner-sphere complex. During the drying process, the weakly bound oxyanion easily precipitates with multivalent cation from soil component or mainly sorbs onto metal oxides. The structural configuration of sorbed oxyanion controls the bioavailability of nutrients (López-Arredondo et al., 2014). In the most environments, we do not concern the concentration of silica and sulfur, which are known as essential element because of the abundance while we concern the oxyanions in the trace level or high consumption, such as nitrogen, phosphorus and selenium (Andrew et al., 2000; Zamparas and Zacharias, 2014).

#### 1.5. Analytical technique for interfacial measurement

Several studies have attempted to reveal the structural configuration of oxyanions and organic acids on an iron (hydr)oxide surface. There are few experimental and theoretical methods for identifying this structural configuration. The surface complexation model is the most versatile method and is based on theoretical approximation combined with sorption data from batch experiments (Goldberg, 2013; Sharif et al., 2011). Theoretical calculation based on computational chemistry is a promising way to reveal the structural configuration (Acelas et al., 2013; Johnston and Chrysochoou, 2012; Kubicki et al., 2007), but it is still unsuitable for simulating a multicomponent system because it requires

excessive computational resources, and the structure must be confirmed by comparison with experimental data (Luengo et al., 2015; Yang et al., 2016). Spectroscopy is an applicable technique, and X-ray and infrared are common light sources for the experiments (Ferrari et al., 2004; Lefevre, 2004; Liu et al., 2015; Mudunkotuwa et al., 2014; Ona-Nguema et al., 2005). X-ray absorption spectroscopy (XAS) includes extended X-ray absorption fine structure (EXAFS) and X-ray absorption near edge structure (XANES), both techniques that enable us to see the local structure and oxidation number of the target element (Scott et al., 1992; Waychunas et al., 1993). Fourier-transform infrared spectroscopy (FTIR) equipped with attenuated total reflection (ATR) or diffuse reflectance (DRIFT) is frequently used to reveal the structural configuration of adsorption (Madejová, 2003; Mudunkotuwa et al., 2014).

#### 1.6. Aims of dissertation

Recent development and production of chemical fertilizer led that the minor elements are no longer considered as limiting factors in the cultivation (López-Arredondo et al., 2014; Riley et al., 2001). Over-fertilization was encouraged to maximize the agricultural productivity, so less attention was paid to optimize bioavailability through the research and management of the soil (Andrew et al., 2000; López-Arredondo et al., 2014; Riley et al., 2001; Timmons and Dylla, 1981). The industrialization demands unexposed rare elements from the crust, such as arsenic, antimony and tellurium (Babula et al., 2008; Gleyzes and Tellier, 2001; Rosen and Liu, 2009). As a consequence, excessive nutrients and toxicants leached out from the pedosphere to hydrosphere, and it raises severe environmental problems such as eutrophication and metal poisoning worldwide (Jain and Ali, 2000; Meharg et al., 2002; Smith et al., 2006; Smith and Schindler, 2009). To diminish

such problem, maintaining optimum bioavailability of nutrient and reducing lechability of toxicant are essential, but the heterogeneity and complexity of soil makes it hard to understand the bioavailability.

Therefore, It is essential to understand not only the individual characteristics of oxyanion, organic acid and iron oxide, but also the mutual interactions among oxyanion, organic acid and iron oxide in the rhizosphere for better comprehension and insight of the bioavailability. Previous studies already dealt with the individual characteristics; thus, here the literatures were summarized regarding the transformation of iron oxides, structural configuration of oxyanions and organic acids and competitive sorption among the oxyanions and organic acids. The experimental procedures for identifying the structural configuration, competitive and preferential sorption were explained. Beside, the environmental effects on the structural configuration, competitive and preferential sorption were discussed.

## References

- Abdala, D.B., Northrup, P.A., Arai, Y., Sparks, D.L., 2015. Surface loading effects on orthophosphate surface complexation at the goethite/water interface as examined by extended X-ray Absorption Fine Structure (EXAFS) spectroscopy. *J. Colloid Interface Sci.* 437, 297–303. doi:10.1016/j.jcis.2014.09.057
- Acelas, N.Y., Mejia, S.M., Mondragón, F., Flórez, E., 2013. Density functional theory characterization of phosphate and sulfate adsorption on Fe-(hydr)oxide: Reactivity, pH effect, estimation of Gibbs free energies, and topological analysis of hydrogen bonds. *Comput. Theor. Chem.* 1005, 16–24. doi:10.1016/j.comptc.2012.11.002
- Adegoke, H.I., Adekola, F.A., Fatoki, O.S., Ximba, B.J., 2013. Sorptive Interaction of Oxyanions with Iron Oxides : A Review. *Pol. J. Environ. Stud.* 22, 7–24.
- Andrew, S., Bob, F., Paul, W., 2000. Practical and innovative measures for the control of agricultural phosphorus losses to water. *J. Environ. Qual.* 29, 1–9.
- Antelo, J., Avena, M., Fiol, S., López, R., Arce, F., 2005. Effects of pH and ionic strength on the adsorption of phosphate and arsenate at the goethite-water interface. *J. Colloid Interface Sci.* 285, 476–486. doi:10.1016/j.jcis.2004.12.032
- Babula, P., Adam, V., Opatrilova, R., Zehnalek, J., Havel, L., Kizek, R., 2008. Uncommon heavy metals, metalloids and their plant toxicity: A review. *Environ. Chem. Lett.* 6, 189–213. doi:10.1007/s10311-008-0159-9
- Barberis, E., Ajmone Marsan, F., Scalenghe, R., Lammers, A., Schwertmann, U., Edwards, A.C., Maguire, R., Wilson, M.J., Delgado, A., Torrent, J., 1995. European soils overfertilized with phosphorus: Part 1. Basic properties. *Fertil. Res.* 45, 199–207. doi:10.1007/BF00748590
- Bucher, M., 2007. Functional biology of plant phosphate uptake at root and mycorrhiza interfaces. *New Phytol.* 173, 11–26.
- Cornell, R.M., Schwertmann, U., 2003. *The iron oxides : structure, properties, reactions, occurrences, and uses.* Wiley-VCH.
- Cox, P.A., 1989. *The elements : their origin, abundance and distribution,* Oxford science publications. Oxford University Press.
- Diaz-Bone, R. a., Raabe, M., Awibus, S., Keuter, B., Menzel, B., Küppers, K., Widmann, R., Hirner, A. V., 2011. Investigation of biomethylation of arsenic and tellurium during composting. *J. Hazard. Mater.* 189, 653–659. doi:10.1016/j.jhazmat.2010.12.011
- Elser, J.J., Bracken, M.E.S., Cleland, E.E., Gruner, D.S., Harpole, W.S., Hillebrand, H., Ngai, J.T., Seabloom, E.W., Shurin, J.B., Smith, J.E., 2007. Global analysis of nitrogen and phosphorus limitation of primary producers in freshwater, marine and terrestrial ecosystems. *Ecol. Lett.* 10, 1135–1142. doi:10.1111/j.1461-0248.2007.01113.x
- Elzinga, E.J., Sparks, D.L., 2007. Phosphate adsorption onto hematite: An in situ ATR-FTIR investigation of the effects of pH and loading level on the mode of phosphate surface complexation. *J. Colloid Interface Sci.* 308, 53–70. doi:10.1016/j.jcis.2006.12.061
- Farquhar, M.L., Charnock, J.M., Livens, F.R., Vaughan, D.J., 2002. Mechanisms of arsenic uptake from aqueous solution by interaction with goethite, lepidocrocite, mackinawite, and pyrite: An X-ray absorption spectroscopy study. *Environ. Sci. Technol.* 36, 1757–1762. doi:10.1021/es010216g
- Fendorf, S., Eick, M.J., Grossl, P., Sparks, D.L., 1997. Arsenate and chromate retention mechanisms on goethite. 1. Surface structure. *Environ. Sci. Technol.* 31, 315–320. doi:10.1021/es950653t
- Ferrari, M., Mottola, L., Quaresima, V., 2004. Principles, techniques, and limitations of near

- infrared spectroscopy. *Can. J. Appl. Physiol.* 29, 463–487. doi:10.1139/h04-031
- Gao, X., Root, R.A., Farrell, J., Ela, W., Chorover, J., 2013. Effect of silicic acid on arsenate and arsenite retention mechanisms on 6-L ferrihydrite: A spectroscopic and batch adsorption approach. *Appl. Geochemistry* 38, 110–120. doi:10.1016/j.apgeochem.2013.09.005
- Georgiadis, M., Cai, Y., Solo-Gabriele, H.M., 2006. Extraction of arsenate and arsenite species from soils and sediments. *Environ. Pollut.* 141, 22–29. doi:10.1016/j.envpol.2005.08.028
- Gleyzes, C., Tellier, S., 2001. Arsenic characterisation in industrial soils by chemical extractions. *Environ. ...* 22, 27–38. doi:10.1080/09593332208618313
- Goldberg, S., 2013. Modeling Selenite Adsorption Envelopes on Oxides, Clay Minerals, and Soils using the Triple Layer Model. *Soil Sci. Soc. Am. J.* 77, 64–71. doi:10.2136/sssaj2012.0205
- Gu, C., Wang, Z., Kubicki, J.D., Wang, X., Zhu, M., 2016. X-ray Absorption Spectroscopic Quantification and Speciation Modeling of Sulfate Adsorption on Ferrihydrite Surfaces. *Environ. Sci. Technol.* 50, 8067–8076. doi:10.1021/acs.est.6b00753
- Han, J., Kim, J., Kim, M., Moon, D.H., Sung, J.-S., Hyun, S., 2014. Chemical extractability of As and Pb from soils across long-term abandoned metallic mine sites in Korea and their phytoavailability assessed by *Brassica juncea*. *Environ. Sci. Pollut. Res. Int.* 22, 1270–8. doi:10.1007/s11356-014-3441-3
- Han, J., Ro, H.-M., Cho, K.H., Kim, K.-W., 2016. Fluxes of nutrients and trace metals across the sediment-water interface controlled by sediment-capping agents: bentonite and sand. *Environ. Monit. Assess.* 188, 566. doi:10.1007/s10661-016-5583-x
- He, G., Zhang, M., Pan, G., 2009. Influence of pH on initial concentration effect of arsenate adsorption on TiO<sub>2</sub> surfaces: Thermodynamic, DFT, and EXAFS interpretations. *J. Phys. Chem. C* 113, 21679–21686. doi:10.1021/jp906019e
- Hughes, M.F., 2002. Arsenic toxicity and potential mechanisms of action. *Toxicol. Lett.* 133, 1–16. doi:10.1016/S0378-4274(02)00084-X
- Hyun, S., Kim, J., Kim, D.-Y., Moon, D.H., 2012. Effect of seepage conditions on chemical attenuation of arsenic by soils across an abandoned mine site. *Chemosphere* 87, 602–7. doi:10.1016/j.chemosphere.2012.01.013
- Jain, C., Ali, I., 2000. Arsenic: occurrence, toxicity and speciation techniques. *Water Res.* 34, 4304–4312.
- Johnson, D.L., 1971. Simultaneous Determination of Arsenate and Phosphate in Natural Waters. *Environ. Sci. Technol.* 5, 411–414. doi:10.1016/j.apmr.2010.12.011
- Johnston, C.P., Chrysochoou, M., 2012. Investigation of chromate coordination on ferrihydrite by in situ ATR-FTIR spectroscopy and theoretical frequency calculations. *Environ. Sci. Technol.* 46, 5851–5858. doi:10.1021/es300660r
- Kubicki, J., Paul, K., Kaban, L., Zhu, Q., 2012. ATR-FTIR and Density Functional Theory Study of the Structures, Energetics, and Vibrational Spectra of Phosphate Adsorbed onto Goethite. *Langmuir* 28, 14573–14587.
- Kubicki, J.D.J., Kwon, K.D., Paul, K.W., Sparks, D.L., 2007. Surface complex structures modelled with quantum chemical calculations: Carbonate, phosphate, sulphate, arsenate and arsenite. *Eur. J. Soil Sci.* 58, 932–944. doi:10.1111/j.1365-2389.2007.00931.x
- Kwon, J.S., Yun, S.T., Lee, J.H., Kim, S.O., Jo, H.Y., 2010. Removal of divalent heavy metals (Cd, Cu, Pb, and Zn) and arsenic(III) from aqueous solutions using scoria: Kinetics and equilibria of sorption. *J. Hazard. Mater.* 174, 307–313. doi:10.1016/j.jhazmat.2009.09.052

- Leermakers, M., Baeyens, W., De Gieter, M., Smedts, B., Meert, C., De Bisschop, H.C., Morabito, R., Quevauviller, P., 2006. Toxic arsenic compounds in environmental samples: Speciation and validation. *TrAC - Trends Anal. Chem.* 25, 1–10. doi:10.1016/j.trac.2005.06.004
- Lefevre, G., 2004. In situ Fourier-transform infrared spectroscopy studies of inorganic ions adsorption on metal oxides and hydroxides. *Adv. Colloid Interface Sci.* 107, 109–123. doi:10.1016/j.cis.2003.11.002
- Li, C.X., Feng, S.L., Shao, Y., Jiang, L.N., Lu, X.Y., Hou, X.L., 2007. Effects of arsenic on seed germination and physiological activities of wheat seedlings. *J. Environ. Sci.* 19, 725–732.
- Li, H., McGrath, S., Zhao, F., 2008. Selenium uptake, translocation and speciation in wheat supplied with selenate or selenite. *New Phytol.* 92–102.
- Liu, C.H., Chuang, Y.H., Chen, T.Y., Tian, Y., Li, H., Wang, M.K., Zhang, W., 2015. Mechanism of Arsenic Adsorption on Magnetite Nanoparticles from Water: Thermodynamic and Spectroscopic Studies. *Environ. Sci. Technol.* 49, 7726–7734. doi:10.1021/acs.est.5b00381
- López-Arredondo, D.L., Leyva-González, M.A., González-Morales, S.I., López-Bucio, J., Herrera-Estrella, L., 2014. Phosphate nutrition: improving low-phosphate tolerance in crops. *Annu. Rev. Plant Biol.* 65, 95–123. doi:10.1146/annurev-arplant-050213-035949
- Loring, J.S., Sandström, M.H., Norén, K., Persson, P., 2009. Rethinking arsenate coordination at the surface of goethite. *Chem. - A Eur. J.* 15, 5063–5072. doi:10.1002/chem.200900284
- Lu, P., Zhu, C., 2010. Arsenic Eh–pH diagrams at 25°C and 1 bar. *Environ. Earth Sci.* 62, 1673–1683. doi:10.1007/s12665-010-0652-x
- Luengo, C., Brigante, M., Avena, M., 2007. Adsorption kinetics of phosphate and arsenate on goethite. A comparative study. *J. Colloid Interface Sci.* 311, 354–360. doi:10.1016/j.jcis.2007.03.027
- Luengo, C. V., Castellani, N.J., Ferullo, R.M., 2015. Quantum chemical study on surface complex structures of phosphate on gibbsite. *Spectrochim. Acta Part A Mol. Biomol. Spectrosc.* doi:10.1016/j.saa.2015.03.013
- Madejová, J., 2003. FTIR techniques in clay mineral studies. *Vib. Spectrosc.* 31, 1–10.
- Masscheleyn, P.P.H., Delaune, R.D., Patrick, W.H., 1991. Effect of redox potential and pH on arsenic speciation and solubility in a contaminated soil. *Environ. Sci. Technol.* 25, 1414–1419. doi:10.1021/es00020a008
- Meharg, A. a. A., Hartley-Whitaker, J., Hartley-Whitaker, J., 2002. Arsenic uptake and metabolism in arsenic resistant and nonresistant plant species. *New Phytol.* 154, 29–43.
- Michael Bolanz, R., Blöss, U., Ackermann, S., Ciobotaru, V., Röscher, P., Tarcea, N., Popp, J., Majzlan, J., 2013. The effect of antimonate, arsenate, and phosphate on the transformation of ferrihydrite to goethite, hematite, ferrioxhyte, and tripuyite. *Clays Clay Miner.* 61, 11–25. doi:10.1346/CCMN.2013.0610102
- Mir, K. a., Rutter, A., Koch, I., Smith, P., Reimer, K.J., Poland, J.S., 2007. Extraction and speciation of arsenic in plants grown on arsenic contaminated soils. *Talanta* 72, 1507–1518. doi:10.1016/j.talanta.2007.01.068
- Morin, G., Ona-Nguema, G., Wang, Y., Menguy, N., Juillot, F., Proux, O., Guyot, F., Calas, G., Brown, G.E., 2008. Extended X-ray absorption fine structure analysis of arsenite and arsenate adsorption on maghemite. *Environ. Sci. Technol.* 42, 2361–2366. doi:10.1021/es072057s
- Mudunkotuwa, I. a, Minshid, A. Al, Grassian, V.H., 2014. ATR-FTIR spectroscopy as a tool

- to probe surface adsorption on nanoparticles at the liquid-solid interface in environmentally and biologically relevant media. *Analyst* 139, 870–81. doi:10.1039/c3an01684f
- Neupane, G., Donahoe, R.J., Arai, Y., 2014. Kinetics of competitive adsorption/desorption of arsenate and phosphate at the ferrihydrite-water interface. *Chem. Geol.* 368, 31–38. doi:10.1016/j.chemgeo.2013.12.020
- Ona-Nguema, G., Morin, G., Juillot, F., Calas, G., Brown, G.E., 2005. EXAFS analysis of arsenite adsorption onto two-line ferrihydrite, hematite, goethite, and lepidocrocite. *Environ. Sci. Technol.* 39, 9147–9155. doi:10.1021/es050889p
- Panias, D., Taxiarchou, M., Paspaliaris, I., Kontopoulos, a., 1996. Mechanisms of dissolution of iron oxides in aqueous oxalic acid solutions. *Hydrometallurgy* 42, 257–265. doi:10.1016/0304-386X(95)00104-O
- Pantsar-Kallio, M., Manninen, P.K.G., 1997. Speciation of mobile arsenic in soil samples as a function of pH. *Sci. Total Environ.* 204, 193–200.
- Parker, J.L., Newstead, S., 2014. Molecular basis of nitrate uptake by the plant nitrate transporter NRT1.1. *Nature* 507, 68–72. doi:10.1038/nature13116
- Pasek, M.A., 2008. Rethinking early Earth phosphorus geochemistry. *Proc. Natl. Acad. Sci.* 105, 853–858. doi:10.1073/pnas.0708205105
- Randall, S.R., Sheerman, D.M., Ragnarsdottir, K.V., 2001. Sorption of As(V) on green rust (Fe<sub>4</sub>(II)Fe<sub>2</sub>(III)(OH)<sub>12</sub>SO<sub>4</sub>·3H<sub>2</sub>O) and lepidocrocite?(-FeOOH): Surface complexes from EXAFS spectroscopy. *Geochim. Cosmochim. Acta* 65, 1015–1023.
- Ratnaike, R.N., 2003. Acute and chronic arsenic toxicity. *Postgrad. Med. J.* 79, 391–396. doi:10.1136/pmj.79.933.391
- Riley, W., Ortiz-Monasterio, I., Matson, P., 2001. Nitrogen leaching and soil nitrate, nitrite, and ammonium levels under irrigated wheat in Northern Mexico. *Nutr. Cycl. ...* 61, 223–236.
- Rosen, B.P., Liu, Z., 2009. Transport pathways for arsenic and selenium: A minireview. *Environ. Int.* 35, 512–515. doi:10.1016/j.envint.2008.07.023
- Scott, R. a., Yamashita, S., Taniguchi, K., Nomoto, S., Yamaguchi, T., Wakita, H., 1992. X-ray Absorption Spectroscopy. *X??Ray Spectrom.* 21, 91–97. doi:10.1002/xrs.1300210209
- Sharif, M.S.U., Davis, R.K., Steele, K.F., Kim, B., Hays, P.D., Kresse, T.M., Fazio, J.A., 2011. Surface complexation modeling for predicting solid phase arsenic concentrations in the sediments of the Mississippi River Valley alluvial aquifer, Arkansas, USA. *Appl. Geochemistry* 26, 496–504. doi:10.1016/j.apgeochem.2011.01.008
- Singh, R., Singh, S., Parihar, P., Singh, V.P., Prasad, S.M., 2015. Arsenic contamination, consequences and remediation techniques: A review. *Ecotoxicol. Environ. Saf.* 112, 247–270. doi:10.1016/j.ecoenv.2014.10.009
- Smedley, P.L., Kinniburgh, D.G., 2002. A review of the source, behaviour and distribution of arsenic in natural waters. *Appl. Geochemistry* 17, 517–568. doi:10.1016/S0883-2927(02)00018-5
- Smith, P.G., Koch, I., Reimer, K.J., 2008. Uptake, transport and transformation of arsenate in radishes (*Raphanus sativus*). *Sci. Total Environ.* 390, 188–197. doi:10.1016/j.scitotenv.2007.09.037
- Smith, V.H., Joye, S.B., Howarth, R.W., 2006. Eutrophication of freshwater and marine ecosystems. *Limnol. Oceanogr.* 51, 351–355. doi:10.4319/lo.2006.51.1\_part\_2.0351
- Smith, V.H., Schindler, D.W., 2009. Eutrophication science: where do we go from here? *Trends Ecol. Evol.* 24, 201–7. doi:10.1016/j.tree.2008.11.009

- Sparks, D.L., 2003. Environmental soil chemistry. Academic Press.
- Sparks, D.L., 2000. New frontiers in elucidating the kinetics and mechanisms of metal and oxyanion sorption at the soil mineral/water interface. *J. Plant Nutr. Soil Sci.* 163, 563–570. doi:10.1002/1522-2624(200012)163:6<563::aid-jpln563>3.0.co;2-0
- Stumm, W., Morgan, J.J., 1981. Aquatic chemistry: an introduction emphasizing chemical equilibria in natural waters. Wiley.
- Takahashi, H., 2010. Regulation of sulfate transport and assimilation in plants, 1st ed, International Review of Cell and Molecular Biology. Elsevier Inc. doi:10.1016/S1937-6448(10)81004-4
- Templeton, D.M., Fujishiro, H., 2017. Terminology of elemental speciation – An IUPAC perspective. *Coord. Chem. Rev.* 352, 424–431. doi:10.1016/j.ccr.2017.02.002
- Timmons, D.R., Dylla, A.S., 1981. Nitrogen Leaching as Influenced by Nitrogen Management and Supplemental Irrigation Level. *J. Environ. Qual.* 10, 421–426.
- Udo, S., Rochelle, M.C., 2008. Iron Oxides in the Laboratory. Preparation and Characterization, Wiley-vch.
- Von Wirén, N., Gazzarrini, S., Gojon, A., Frommer, W.B., 2000. The molecular physiology of ammonium uptake and retrieval. *Curr. Opin. Plant Biol.* 3, 254–261. doi:10.1016/S1369-5266(00)00073-X
- Waychunas, G. A., Rea, B. A., Fuller, C. C., Davis, J. A., 1993. Surface chemistry of ferrihydrite: Part 1. EXAFS studies on geometry of coprecipitated and adsorbed arsenate. *Geochim. Cosmochim. Acta* 57, 2251–2269. doi:10.1016/0016-7037(93)90567-G
- Woolson, E. a, Axley, J.H., Kearney, P.C., 1971. The chemistry and phytotoxicity of arsenic in soils: 1. Contaminated field soils. *Soil Sci. Soc. Am. Proc.* 35, 938–944.
- Yang, Y., Wang, S., Xu, Y., Zheng, B., Liu, J., 2016. Molecular-Scale Study of Aspartate Adsorption on Goethite and Competition with Phosphate. *Environ. Sci. Technol.* 50, acs.est.5b05450. doi:10.1021/acs.est.5b05450
- Zamparas, M., Zacharias, I., 2014. Restoration of eutrophic freshwater by managing internal nutrient loads. A review. *Sci. Total Environ.* 496, 551–62. doi:10.1016/j.scitotenv.2014.07.076
- Zhang, H., Selim, H.M., 2006. Modeling the Transport and Retention of Arsenic (V) in Soils. *Soil Sci. Soc. Am. J.* 70, 1677. doi:10.2136/sssaj2006.0035
- Zhao, F., Ma, J., Meharg, A., McGrath, S., 2009. Arsenic uptake and metabolism in plants. *New Phytol.* 777–794.
- Zhu, M., Northrup, P., Shi, C., Billinge, S.J.L., Sparks, D.L., Waychunas, G.A., 2013. Structure of Sulfate Adsorption Complexes on Ferrihydrite. *Environ. Sci. Technol. Lett.* 1, 97–101. doi:10.1021/ez400052r

## CHAPTER 2. LITERATURE REVIEW

### List of contents

<b>CHAPTER 2. LITERATURAL REVIEW</b> .....	<b>2-1</b>
List of contents .....	2-1
Abstract .....	2-2
2.1. Introduction .....	2-4
2.2. Abundance and transformation of iron (hydr)oxides .....	2-7
2.2.1. Formation and Abundance of iron (hydr)oxides .....	2-7
2.2.2. Transformation of iron (hydr)oxides .....	2-9
2.2.3. Biological effect on iron (hydr)oxides .....	2-14
2.2.4. Iron (hydr)oxide profile in upland vs. paddy .....	2-16
2.3. Structural configuration .....	2-20
2.3.1. Structural configuration of oxyanions .....	2-21
2.3.2. Structural configuration of organic acids .....	2-42
2.4. Competitive sorption .....	2-45
2.4.1. Competitive sorption among oxyanions .....	2-49
2.4.2. Competitive sorption between oxyanions and organic acids .....	2-58
2.4.3. Selectivity sequence using reduced sorption percentage .....	2-60
2.4.4. Surface site density by crystal structures .....	2-63
2.5. Conclusions .....	2-64
References .....	2-70

## Abstract

Understanding mutual interactions among oxyanions, organic acids and iron (hydr)oxides is essential for controlling the bioavailability of oxyanions in the rhizosphere. In this review, the literature regarding the transformation of iron (hydr)oxides, structural configuration and competitive sorption of organic acids and oxyanions on the iron (hydr)oxides were analyzed. As a result, the oxyanions, pH and time controls the transformation of iron (hydr)oxides during the adsorption experiment, and the exudates also affect the transformation indirectly. The inner-sphere bidentate complex was predominant for arsenate, arsenite, phosphate and silicate, the monodentate and bidentate complexes were abundant in carbonate, chromate, selenite, and selenate whereas only a monodentate complex was observed in sulfate. The competing ions, pH and surface loading (SL) significantly affected the structural configuration, and a higher SL with a lower sorption site decreased the dentation in arsenate. For competitive sorption, reduced sorption percentage ( $RSP = q_{dual,A}/q_{single,A} \times 100$ ) was used to draw a numerical selectivity sequence, and competition effect ( $CE = 0.5 - q_{dual,sum}/q_{single,sum}$ ) was used for a quantitative comparison ( $CE=0$ : no competition,  $CE>0$ : competition,  $CE<0$ : promotive effect). A similar pattern between the selectivity sequence using RSP and previous literature was found, and the CE between arsenate and arsenite was increased by the SL increment. The organic acid competed with the oxyanions at low pH, and it also affected the iron (hydr)oxides. The pH and SL were the most significant factors for controlling competitive sorption. Based on these observations, I concluded that the complex with higher dentation would dominate the sorption sites during competitive sorption but the increase of competition or decrease of sorption site reduces the dentation of complex. For that reason, environmental fluctuation yields an extensive effect on the dynamics of oxyanions by transforming the sorption site

and structural configuration, and the inter-connected and complex interaction should be comprehensively revealed to understand the dynamics of oxyanions.

Keywords

iron (hydr)oxide, oxyanion, organic acid, transformation, structural configuration, competitive sorption

## 2.1. INTRODUCTION

An oxyanion is a negatively charged molecule with the generic formula  $A_xO_y^{z-}$ . Carbonate ( $CO_3^{2-}$ ), nitrate ( $NO_3^-$ ), phosphate ( $PO_4^{3-}$ ), silicate ( $SiO_4^{2-}$ ) and sulfate ( $SO_4^{2-}$ ) are the major oxyanions in the soil environment, whereas arsenate ( $AsO_4^{3-}$ ), antimonate ( $SbO_4^{3-}$ ), borate ( $BO_3^{3-}$ ), selenate ( $SeO_4^{2-}$ ), and tellurate ( $TeO_4^{2-}$ ) are generally found at trace levels (Johnson, 1971; Sparks, 2000). Oxyanions are ubiquitous on Earth and are fundamental constituents of organisms and the environment. Based on their chemical structures, oxyanions can easily undergo reactions that change them into other chemical species, a process called species transformation (Templeton and Fujishiro, 2017). The species transformation of oxyanions in the soil is caused by environmental fluctuations, such as changes in the pH, redox potential and concentrations of ligands (Georgiadis et al., 2006; Masscheleyn et al., 1991). Species transformation not only changes the oxyanion species but also affects its affinity to the adsorbent; thus, it determines the behavior of oxyanions in the soil environment (Mir et al., 2007; Pansar-Kallio and Manninen, 1997).

Within the rhizosphere, the plant influences the soil through various mechanisms, most significantly by releasing compounds into the soil (Bais et al., 2006; Huang et al., 2014). This process is referred to as rhizodeposition (Bais et al., 2006; Hütsch et al., 2002), and the major types of rhizodeposition include exudate, mucilage, border cells, and gas (Haichar et al., 2014). An exudate is a soluble, low-weight molecule that undergoes passive diffusion (Bertin et al., 2003), and recent

studies have revealed that exudates such as root-derived organic acids increase bioavailability by competing with sorbed oxyanions, by dissolving oxyanion-sorbed minerals or by causing secondary exudation from microbes (Dakora and Phillips, 2002; Eick et al., 1999; Jones et al., 2009). Citric, glutaric, oxalic and malonic acids are the most common exudates found in the rhizosphere (Baetz and Martinoia, 2014; Shi et al., 2010; Y. Wang et al., 2008) and are known as nutrient sources for the microbial community and as stimulators for the uptake of ions, such as those of Al, Cu, Fe, N and P (Dakora and Phillips, 2002; Tu et al., 2004). The effects and pathway of the competition have not been fully addressed, because of the heterogeneity and complexity of the soil environment (Dakora and Phillips, 2002). However, the organic acids not only affect the sorption of oxyanions directly but also clearly cause changes in the soil indirectly.

The solid component of soil is a complex of various materials, such as phyllosilicates, metal (hydr)oxides, and organic matter. Iron (hydr)oxide is one of the key sorbents in retaining both nutrients and pollutants because of its reactivity, surface area and surface charge (Adegoke et al., 2013; Lefevre, 2004; Panias et al., 1996). Environmental fluctuation causes oxyanions to undergo species transformation, and the transformation of iron (hydr)oxide, which changes its crystal structure and morphology, ultimately affects the sorption characteristics of oxyanions in the soil environment. Not only the sorbent characteristics but also the interactions of the oxyanions with iron (hydr)oxide are important. There are two main types of interactions: the inner-sphere (IS) complex is formed by adsorption through covalent bonds, while the outer-sphere (OS) complex is formed by

adsorption through electrostatic attraction and dispersion interactions (Sparks, 2003; Stumm and Morgan, 1981). The IS complex can be monodentate, bidentate or tridentate, and its structural configuration is essential to understanding the behavior of oxyanions in the soil environment because it determines their leachability and bioavailability (Fendorf et al., 1997; Liu et al., 2015; Zhu et al., 2013).

With the recent development and production of chemical fertilizers, minor elements are no longer considered limiting factors in cultivation (López-Arredondo et al., 2014; Riley et al., 2001). With the use of overfertilization to maximize agricultural productivity, the attention paid to optimizing bioavailability through soil research and management decreased (Andrew et al., 2000; López-Arredondo et al., 2014; Riley et al., 2001; Timmons and Dylla, 1981). Furthermore, the demands of industrialization exposed rare elements in the crust, such as arsenic, antimony and tellurium (Babula et al., 2008; Gleyzes and Tellier, 2001; Rosen and Liu, 2009). As a consequence, excessive nutrients and toxicants leached from the pedosphere to the hydrosphere, causing severe environmental problems worldwide such as eutrophication and metal poisoning (Jain and Ali, 2000; Meharg et al., 2002; Smith et al., 2006; Smith and Schindler, 2009). Essential methods to diminish such problems include maintaining the optimum bioavailability of nutrients by the uptake ability of plants themselves, minimizing the bioaccessibility of toxicants by controlling environmental conditions, and reducing the leachability of nutrients and toxicants by regulating both plants and the environment, but the heterogeneity and complexity of soil makes bioavailability difficult to understand.

Therefore, it is important to understand not only the individual

characteristics of oxyanions, organic acids and iron (hydr)oxides but also their complexly interconnected interactions in the rhizosphere to obtain better comprehension of and insight into bioavailability; thus, here, we have summarized the literature regarding the transformation of iron (hydr)oxides, the structural configuration of oxyanions and organic acids and competitive sorption among oxyanions and organic acids, and I have examined the effects of the environment on transformation, structural configuration and competitive sorption.

## **2.2. ABUNDANCE AND TRANSFORMATION OF IRON (HYDR)OXIDES**

### **2.2.1. Formation and Abundance of Iron (hydr)oxides**

Iron is the fourth most abundant element in the crust of the Earth, at 5.1 % by mass (Cox, 1989). Biotite [ $K(Fe^{2+})_3Si_3(AlO_{10}(OH)_2]$ , pyroxene [ $(Fe^{2+})_2(Si,Al)_2O_6$ ], olivine [ $Fe^{2+}_2SiO_4$ ], magnetite ( $Fe_3O_4$ ) and pyrite ( $FeS_2$ ) are the main iron-containing minerals (Cornell and Schwertmann, 2003), and weathering by hydrolysis and oxidation forms iron (hydr)oxide in the soil (Cornell and Schwertmann, 2003; Udo and Rochelle, 2008). During the weathering process, once the primary rock containing iron is exposed to oxic conditions,  $Fe^{2+}$  is readily oxidized to  $Fe^{3+}$  by providing an electron to oxygen at soil pH, and then soluble  $Fe^{3+}$  oxides are easily formed by hydrolysis. Based on the parent materials, climate, redox conditions and organisms involved, various iron (hydr)oxides can be formed, such as amorphous iron (hydr)oxide (AIO), goethite ( $\alpha$ - $FeOOH$ ), lepidocrocite ( $\gamma$ - $FeOOH$ ), ferrihydrite ( $Fe_2O_3 \cdot 0.5H_2O$ ), hematite ( $\alpha$ - $Fe_2O_3$ ) and maghemite ( $\gamma$ - $Fe_2O_3$ )

(Cornell and Schwertmann, 2003; Udo and Rochelle, 2008).

AIO is the term for an iron and oxygen complex without crystallization, and recent studies have reported that AIO has a large surface area, superior catalytic activity and superparamagnetic behavior (Machala et al., 2007; Yusuf et al., 2010). Its abundance in the soil environment has not yet been fully investigated but is likely to be low because of its high reactivity and low stability (Srivastava et al., 2002). Goethite is a common iron (hydr)oxide because of its thermodynamic stability and is yellow-brown in color (Schwertmann, 1993). It is found in all regions with oxic and anoxic soils, often in the low part of a toposequence (Fig. 2-1) (Schwertmann, 1985). Like goethite, hematite also has high thermodynamic stability, but it is mostly found in warm and oxic climates (Schwertmann, 1985). The red color in topsoil at low latitudes is mainly caused by the presence of hematite (Schwertmann, 1993). Goethite and hematite sometimes occur together, and the color indirectly indicates their ratio (Shaw et al., 2005). Lepidocrocite is less common in soil than goethite and hematite but is generally found in redoxomorphic conditions in cool and temperate climates (Vodyanitskii, 2010). In the presence of a high level of carbonate or bacterial activity, the formation of goethite is preferred, while no lepidocrocite is formed; however, lepidocrocite is frequently associated with goethite in noncalcareous soils (Cornell and Schwertmann, 2003). Ferrihydrite is structurally unstable and is found only in less weathered soil in cool and temperate zones under anoxic conditions (Schwertmann, 1993). A high oxidation rate of  $\text{Fe}^{2+}$  with organic matter or silicate yields ferrihydrite instead of goethite or hematite in the soil environment (Cornell and

Schwertmann, 2003; Johnson and McBride, 1989). Magnetite is a common lithogenic mineral in the heavy mineral fraction of soils with high magnetic properties (Cornell and Schwertmann, 2003; Schwertmann, 1985). Pedogenic magnetite was also discovered by recent studies, but the pedogenic process is still debatable (Fine et al., 1995; Geiss and Zanner, 2006). Maghemite is widespread in the topsoil in tropical regions (Cornell and Schwertmann, 2003), and its known formation pathways are the aerial oxidation of lithogenic magnetite and the heating of lepidocrocite, goethite and ferrihydrite.

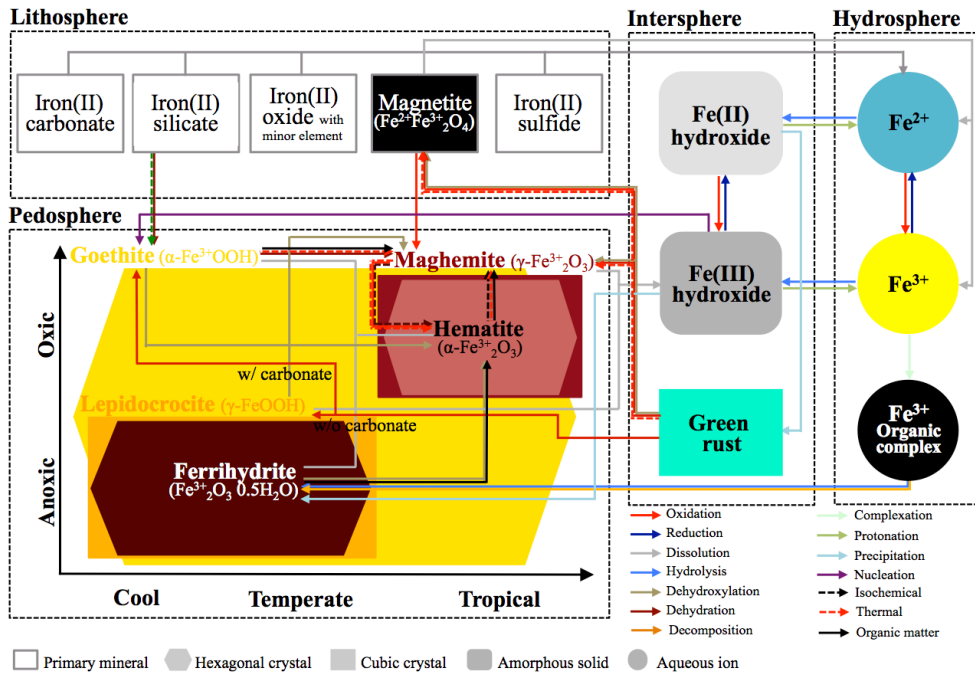
### **2.2.2. Transformation of iron (hydr)oxides**

The transformation of iron (hydr)oxides can be categorized by two factors, changes in chemical composition and in crystal structure (Cornell and Schwertmann, 2003). Dehydration, dehydroxylation and oxidation/reduction are examples of chemical transformation resulting in changes in composition and structure, while topotactic and reconstructive transformation are direct and indirect changes in the structure alone (Adegoke et al., 2013; Cornell and Schwertmann, 2003; Vodyanitskii, 2010). The weathering of primary minerals in the lithosphere releases  $\text{Fe}^{2+}$  ions, which are readily oxidized to form  $\text{Fe}^{3+}$  ions; the  $\text{Fe}^{3+}$  ions then hydrolyze to form Fe(III) oxides and (hydr)oxides with the groundwater at typical soil pH. This process is referred to as reconstructive transformation employing dissolution and reprecipitation (Mackay, 1960) and is the most common pathway for the iron cycle, while topotactic transformation is a structural change in the solid state that results from the modification of chemical characteristics (Cornell and Schwertmann,

2003). Intensive weathering accompanied by large amounts of O<sub>2</sub> and H<sub>2</sub>O increases the iron concentration in the pedosphere by drawing it from the lithosphere (Schwertmann, 1985). The aqueous iron ions speciate into Fe<sup>2+</sup> and Fe<sup>3+</sup> ions depending on the redox potential, and the concentration of hydroxide ion (pOH) determines the formation of iron (hydr)oxides. Cornell and Schwertmann (2003) summarized reconstructive transformation as follows: 1) the crystal growth of iron (hydr)oxides on the primary mineral, 2) pseudomorphosis, 3) amorphous coating on the primary mineral, and 4) diffusion interval between the release and oxidation of Fe(II) ions. Fe(III) oxide is prevalent in the soil environment, and amorphous Fe(III) (hydr)oxide mainly forms goethite, which is a thermodynamically stable hexagonal structure (Machala et al., 2007; Yusuf et al., 2010).

Fig. 2-1 summarizes the transformation of iron (hydr)oxide in the lithosphere, hydrosphere and pedosphere. The dehydration and dehydroxylation of goethite yields a topotactic transformation to hematite without organic matter and yields maghemite in the presence of organic matter (Cudennec and Lecerf, 2005). The dissolution of goethite leads to the formation of amorphous iron(III) (hydr)oxide again; spatiotemporal variability leads to crystallization into the various iron (hydr)oxides; and repeated circulation through the iron cycle distributes iron throughout the soil profile (Schwertmann, 1993, 1985). Except for goethite, which is distributed worldwide, iron (hydr)oxides can be divided into two groups: pure iron oxides (maghemite and hematite), which form under oxic and tropical conditions, and iron hydroxides (lepidocrocite and ferrihydrite), which form in cool

**Fig. 2-1** Abundance of iron (hydr)oxide in the climate zone and the common pathway of formation and transformation in the environment. The rectangular and hexagonal shape in the pedosphere indicate a cubic and hexagonal phase, and the color of the shape resembles the color of each iron (hydr)oxide. The size of the polygon shows the distribution following the climate zone. Round-edged rectangular and round mean the amorphous solid phase and ions in the aqueous phase, respectively. Colored and overlapping arrows show the chemical or physical reaction for transformation and simultaneous reaction in the transformation.



and temperate climates under anoxic conditions (Cornell and Schwertmann, 2003; Cudennec and Lecerf, 2005). Interestingly, maghemite and lepidocrocite both show cubic structure, while hematite and ferrihydrite are hexagonal (Cornell and Schwertmann, 2003). No topotactic transformation among goethite, lepidocrocite and ferrihydrite has been reported, but the reconstructive transformation has been observed (Cornell and Schwertmann, 2003; Cudennec and Lecerf, 2005; Schwertmann and Taylor, 1972). In contrast to the iron hydroxides, direct transformation among the iron oxides was observed, such as the topotactic transformation from maghemite to hematite caused by thermal oxidation and the opposite transformation caused by dehydroxylation with organic matter (MacHala et al., 2011; Petrovsk et al., 1996; Swaddle and Oltmann, 1980). The combination of dehydration and thermal events led to transformation from ferrihydrite to hematite (Cudennec and Lecerf, 2006), while dehydration alone caused transformation from lepidocrocite to maghemite (Cornell and Schwertmann, 2003; Cudennec and Lecerf, 2005).

Topotactic transformation is observed only within the iron hydroxides or iron oxides, while reconstructive transformation is more widely observed. Spatiotemporal variability in thermal events, redox potential, pH, background ions and organic matter governs the interconversion of iron (hydr)oxides (Cornell and Schwertmann, 2003; MacHala et al., 2011) and leads to perturbation in the behavior of oxyanions in soil because the transformation of iron (hydr)oxides determines their fundamental characteristics (Cornell and Schwertmann, 2003; MacHala et al., 2011; Udo and Rochelle, 2008; Weng et al., 2012). I found that most studies on

sorption experiments thoroughly characterized the iron (hydr)oxide properties, such as the pH, EC, surface area, point of net zero charge, morphology and crystal structure, before the adsorption experiment, but few studies observed the stability or integrity of the iron (hydr)oxides during the adsorption experiment. According to Bolanz et al. (2011, 2013a and 2013b), the presence of oxyanions, concentration and pH controlled the transformation of iron (hydr)oxides *via* various process, and much attention was dedicated to determining the stability of the iron (hydr)oxides in the adsorption experiments. Based on their studies, a high concentration (6 mM) of arsenate and phosphate blocked the transformation from ferrihydrite to others, but a high concentration (6 mM) of antimonate led to transformation to feroxyhyte. They also examined the effect of pH and observed transformation from ferrihydrite to hematite at pH 4 and to goethite at pH 12, while both transformation to both hematite and goethite was observed at pH 7. I also observed the transformation of goethite to bernalite at pH 10 and arsenate concentrations of 1-10 mM in an adsorption experiment (Han and Ro, 2018), and the bernalite showed higher arsenate adsorption capacity than the goethite without aggregation, which would facilitate massive colloidal transport. However, many previous sorption experiments did not include adequate attention to confirming structural stability and integrity, which could be one of the reasons for the conflicting results of sorption experiments.

### **2.2.3. Biological effect on iron (hydr)oxides**

Over 1.2 million species have been cataloged on Earth, and the number of species has been predicted to be approximately 8.7 million (Mora et al., 2011). Only

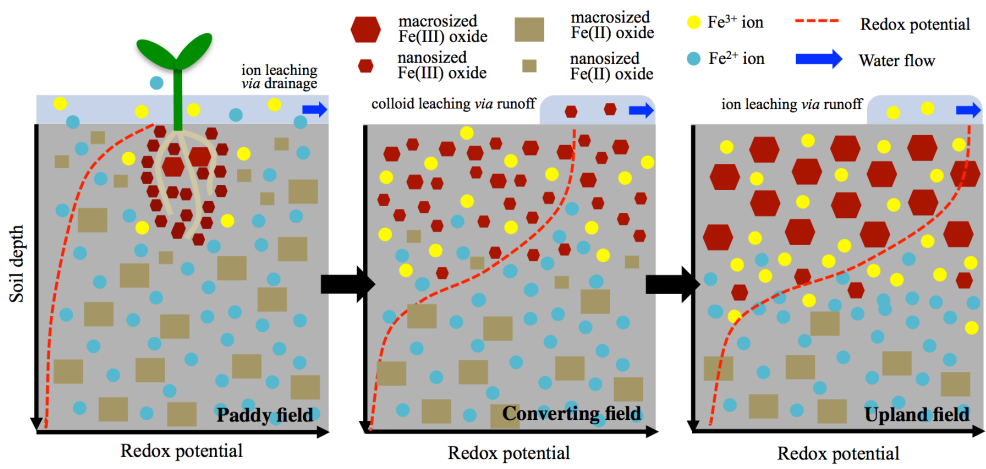
25 % of predicted species are oceanic organisms, while most of the rest interact with the soil (Mora et al., 2011). Among the various organisms, microbes and plants are the major mediators that influence the chemical and physical characteristics of soil (Baetz and Martinoia, 2014; Bais et al., 2006; Bertin et al., 2003). Uncountable interactions take place under the ground, but chemoautotrophic bacteria are known as a redox controller of metal (hydr)oxides and oxygen-containing molecules (Ilbert and Bonnefoy, 2013). Bacteria utilize metal oxides as electron acceptors in order to obtain energy. During the redox process, metal oxide transformations occur, and oxyanions at the surface immigrate to other sorption sites or precipitate with ions (Borer and Hug, 2014; Fakour and Lin, 2014). Not only the redox potential but also other environmental factors influence redox reactions; for example, pH and ion concentration affected weathering and dissolution (Dowling, 2002; Shi et al., 2011). Reactions involving bacteria directly transform the crystal structure of iron (hydr)oxide in the soil, while a plant influences the material belowground by inputting a massive amount of energy in the form of organic compounds (Baetz and Martinoia, 2014; Bais et al., 2006). Rhizodeposition is one of the ways by which plants survive and shape their neighboring environment. Various molecules have been identified as root exudates, such as organic acids, amino acids, sugars, proteins, inorganic ions, gases and phenolic compounds, and their functions are not yet fully understood; however, they act as nutrient sources, chemoattractants, chelators, acidifiers, detoxifiers, catalysts, growth promoters, growth inhibitors and defenders against pathogens (Baetz and Martinoia, 2014; Bais et al., 2006; Hütsch et al., 2002). The organic molecules involved in rhizodeposition vary significantly depending on

the plant cultivar, growth stage and environmental conditions; thus, determining a fundamental mechanism is very difficult (Aulakh et al., 2001; Bais et al., 2006). A few studies have been conducted to reveal the effects of root exudates on the oxyanion sorption of iron (hydr)oxides: 1) reductive dissolution by oxalate and ascorbate, 2) chelation, 3) competition at sorption sites, and 4) surface precipitation caused by hindering or facilitating sorption (Dakora and Phillips, 2002; Erbs et al., 2010; Panias et al., 1996; Reza et al., 2010; Zhu et al., 2011).

#### **2.2.4. Iron (hydr)oxide profile in upland vs. paddy**

As I discussed above, the redox condition is the key factor that governs iron (hydr)oxide transformation (Fan et al., 2014; Zhang et al., 2012). Upland fields and paddy fields are the typical land-use regime for crop cultivation with distinctive redox potentials (Zhou et al., 2014). There are few studies dealing with iron (hydr)oxide transformation in relation to the land-use regime (Fan et al., 2014; Kögel-Knabner et al., 2010; Takahashil et al., 1999). In the soil profile, the redox potential decreases with increasing depth (Mansfeldt, 2004; Reza et al., 2010), and the redox gradient yields complex and varied oxidation/reduction reactions in heterogeneous soil (Fakour and Lin, 2014; Fan et al., 2014). I schematically illustrated the redox potential change and iron (hydr)oxide transformation with interconversion from a paddy to an upland field (Fig. 2-2). Iron(II) oxide was mainly found in the upland field subsurface, while iron(III) oxide typically crystallized at the soil surface in the upland field (Cornell and Schwertmann, 2003). With increasing depth, the reduction potential governs chemical reactions by

**Fig. 2-2** Schematic diagram to describe iron (hydr)oxide transformation in the soil environment based on the land-use regime for crop cultivation. The hexagon and circle indicate iron (hydr)oxides in solid phase and iron ions in aqueous phase, respectively. The red dotted graph demonstrates redox potential change by soil depth.



reducing the oxygen-containing compounds or minerals sequentially. Conversion to a paddy field is achieved by flooding the upland field over enough time (Zhou et al., 2014). In the paddy field, the redox potential dramatically decreases with depth and time (Kögel-Knabner et al., 2010), and iron(III) oxide is hardly found because of its reduction by chemotrophic bacteria. An interesting phenomenon observed in rice cultivation in paddy fields is called the iron plaque (Chen et al., 2006). Previous studies identified the iron plaque as precipitates oxidized by the exudation of O<sub>2</sub> from the rice root, and it contributes to nutrient uptake (Chen et al., 2006; Huang et al., 2015). Iron(III) oxide is transformed into another phase *via* reconstructive transformation with no redox process, as the Fe<sup>2+</sup> ion from the dissolution of iron(III) oxide precipitates with various anions, such as siderite (with CO<sub>3</sub><sup>2-</sup>), troilite (with S<sup>2-</sup>), pyrite (with S<sub>2</sub><sup>2-</sup>) and vivianite (with PO<sub>4</sub><sup>3-</sup>). The reduction along the soil profile is easily observable because of the color change of iron (hydr)oxide from orange-brown to gray-black.

After the vegetative and reproductive stages of development, the ripening stage requires the soil to dry; thus, oxidation potential governs the ensuing chemical reactions (Aulakh et al., 2001). Thermodynamically unstable reduced compounds and minerals are rapidly oxidized upon contacting the atmosphere, and iron(III) oxide is formed (Cornell and Schwertmann, 2003; Takahashi et al., 1999). However, a very distinctive phenomenon observed between the converted field and the upland field is the size of iron(III) oxide in the soil profile (Anschutz and Penn, 2005; Schwertmann, 1993). The precipitation time during the reconstructive transformation determines the size of iron (hydr)oxides, and newly precipitated

iron(III) oxide is found to be nanosized. Based on environmental factors, this nanosized iron(III) oxide can be grown to macrosized particles or can remain nanosized (Hinkle et al., 2015; Iwasaki et al., 2011; Williams and Scherer, 2004). It is extremely important to describe the oxyanion dynamics in the soil because the nanosized particle causes colloidal transport (Borer and Hug, 2014; Zhang and Selim, 2007). As mentioned above, the iron (hydr)oxide has a positively charged surface complexed with organic matter and anions to result in a neutral surface charge, which causes high mobility by decreasing interaction with the soil component. This colloidal transport is one of the reasons for the massive leaching of nutrients from the soil to the water system (Borer and Hug, 2014; Riemsdijk et al., 2005; Zhang and Selim, 2007) and is thus a severe environmental problem worldwide (Smith et al., 2006; Smith and Schindler, 2009; Zamparas and Zacharias, 2014).

### **2.3. Structural configuration**

Several studies have attempted to reveal the structural configuration of oxyanions and organic acids on an iron (hydr)oxide surface. There are few experimental and theoretical methods for identifying this structural configuration. The surface complexation model is the most versatile method and is based on theoretical approximation combined with sorption data from batch experiments (Goldberg, 2013; Sharif et al., 2011). Theoretical calculation based on computational chemistry is a promising way to reveal the structural configuration (Acelas et al., 2013; Johnston and Chrysochoou, 2012; Kubicki et al., 2007), but it

is still unsuitable for simulating a multicomponent system because it requires excessive computational resources, and the structure must be confirmed by comparison with experimental data (Luengo et al., 2015; Yang et al., 2016). Spectroscopy is an applicable technique, and X-ray and infrared are common light sources for the experiments (Ferrari et al., 2004; Lefevre, 2004; Liu et al., 2015; Mudunkotuwa et al., 2014; Ona-Nguema et al., 2005). X-ray absorption spectroscopy (XAS) includes extended X-ray absorption fine structure (EXAFS) and X-ray absorption near edge structure (XANES), both techniques that enable us to see the local structure and oxidation number of the target element (Scott et al., 1992; Waychunas et al., 1993). Fourier-transform infrared spectroscopy (FTIR) equipped with attenuated total reflection (ATR) or diffuse reflectance (DRIFT) is frequently used to reveal the structural configuration of adsorption (Madejová, 2003; Mudunkotuwa et al., 2014).

### **2.3.1. Structural configuration of oxyanions**

Oxyanion adsorption on an iron (hydr)oxide surface can be classified into two complexes, an OS complex formed by electrostatic attraction, hydrogen bonding and configurational stabilization by interfacial water (Catalano et al., 2008) and an IS complex formed by covalent bonds (Sparks, 2003). The charge difference between the positively charged iron (hydr)oxide surface and the negatively charged oxyanion keeps the oxyanion near the surface in the interface (Adegoke et al., 2013; Sparks, 2003). The OS complex is a weak and exchangeable complex, whereas the IS complex is a strong and nonreversible complex (Sparks, 2003). The IS complex

can be specified based on the number of covalent bonds and on the number of ligands. As the number of covalent bonds increases, it is called monodentate, bidentate and tridentate, while as the number of ligands increases, it is called mononuclear, binuclear and trinuclear. For example, the oxyanion formed by two covalent bonds with two polyhedra is called a bidentate binuclear complex (BB).

Table 2-1 summarizes the dominant structural configurations of 9 oxyanions and 8 organic acids on 6 types of iron (hydr)oxides. Only 59 articles are cited in the table. We selected the articles that employed pure iron (hydr)oxides with descriptions of the crystal structure and complexation. For the oxyanions and iron (hydr)oxide, 7 elements (As, C, Cr, P, S, Se and Si) and 6 iron (hydr)oxides (goethite, lepidocrocite, ferrihydrite, hematite, maghemite and magnetite) were chosen based on abundance in the soil, deleterious effects on the environment, and number of published articles. Taking arsenate on goethite as an example, the keywords arsenate, goethite and complex were searched on Scopus within the article title, abstract and keywords; 79 articles were found, and the abstracts were carefully reviewed to determine the descriptions of the complexes. For the organic acids, numerous organic acids are present in the soil, and 19 organic acids and 24 amino acids were chosen from the previous literature summarizing root exudates (Dakora and Phillips, 2002); however, only a few studies have addressed the structural configuration of organic acids and amino acids on pure iron (hydr)oxide.

The subscripted number in Table 2-1 indicates the pH range in each experiment, the first subscripted letter denotes the experimental method, and the last subscripted letter denotes the sample preparation method. Further description is

**Table 2-1** The dominant structural configuration as a function of the pH of oxyanions and organic acids on six iron (hydr)oxides. Subscripted number and letter indicate the pH range and experimental method, respectively. Abbreviations: (For the method) *I* Infrared spectroscopy; *S* Surface complexation modeling; *T* Theoretical calculation; *X* X-ray spectroscopy, (For sample treatment) *F* Frozen sample; *D* Dried sample; *P* Paste sample; *A* Aqueous sample, (For complex) *OS* outer-sphere complex only; *IS* Inner-sphere complex without detailed configuration; *MM* inner-sphere monodentate mononuclear complex; *MB* inner-sphere monodentate binuclear complex; *MT* inner-sphere monodentate trinuclear complex; *BM* inner-sphere bidentate mononuclear complex; *BB* inner-sphere bidentate binuclear complex (bidentate bridging); *RS* ring structure of complex; *TH* inner-sphere tridentate hexanuclear complex.

	Goethite	Lepidocrocite	Ferrihydrite	Hematite	Maghemite	Magnetite
<b>Oxyanions</b>						
Arsenite	pH <sub>6,X/P</sub> : BB (Farquhar et al., 2002)	pH <sub>6,X/P</sub> : BB (Farquhar et al., 2002)	pH <sub>7,S/X/D</sub> : BM, BB (Ona-Nguema et al., 2005)	pH <sub>3,7/L/S/A</sub> : BB, MM (Brechtbühl and Christl, 2012)	pH <sub>8,X/D</sub> : BM, BB (Ona-Nguema et al., 2005)	pH <sub>5,X/P,D</sub> : TH (Liu et al., 2015)
	pH <sub>6,9,X/P</sub> : BB (Manning et al., 1998)	pH <sub>3,10,X/D</sub> : BB, MM (Ona-Nguema et al., 2005)		pH <sub>9,6,X/D</sub> : BM, BB (Ona-Nguema et al., 2005)	pH <sub>8,X/D</sub> : BM, BB (Morin et al., 2008)	pH <sub>7,2,X/D</sub> : BM, TH (Yuheng Wang et al., 2008)
	pH <sub>6,9,X/P</sub> : BB, MM (Fendorf et al., 1997)					
Arsenate	pH <sub>6,X/P</sub> : BB (Farquhar et al., 2002)	pH <sub>6,X/P</sub> : BB (Farquhar et al., 2002)	pH <sub>4,8,X/P</sub> : BM, BB (Neupane et al., 2014)	pH <sub>3,7/L/S/A</sub> : BB (Brechtbühl and Christl, 2012)	pH <sub>8,X/D</sub> : BB (Morin et al., 2008)	pH <sub>5,X/P,D</sub> : BB (Liu et al., 2015)
	pH <sub>8,X/P</sub> : BB, MM (Waychunas et al., 1993)	pH <sub>8,X/P</sub> : BB (Waychunas et al., 1993)				
	pH <sub>3,10,S</sub> : BB (Antelo et al., 2005)	pH <sub>7,X/P</sub> : BB (Randall et al., 2001)				
Carbonate	pH <sub>3,10,X,L,T/A,P</sub> : MT (Loring et al., 2009)	pH <sub>7,T,X/P</sub> : BB (Sherman and Randall, 2003)				
	pH <sub>4,T,X/P</sub> : BB (Sherman and Randall, 2003)					
	pH <sub>4,3,7/U/A</sub> : MM (Wijnja and Schulthess, 2001)			pH <sub>3,7/L/S/A</sub> : BB, MM (Brechtbühl and Christl, 2012)		pH <sub>6,5,8,5/U/A</sub> : BB and Holmgren, 2010)
Chromate	pH <sub>4,12/1,S/P</sub> : BB (Rahnamaie et al., 2007)		pH <sub>4,9,5/T,L/P</sub> : BB, MM (Johnston and Chrysochoou, 2012)	pH <sub>3,9,T,X,L/P</sub> : BB, MM (Johnston and Chrysochoou, 2014)		
	pH <sub>4,9,X/P</sub> : MM, BB, BM (Fendorf et al., 1997)					
	pH <sub>3,10,S</sub> : BB (Antelo et al., 2005)					
Phosphate	pH <sub>4,3,9/U/A</sub> : BB (Luengo et al., 2006)		pH <sub>4,9,S/U/A</sub> : BB (Arai and Sparks, 2001)	pH <sub>3,5,9/U/A</sub> : MM, BB (Elzinga and Sparks, 2007)		pH <sub>3,L,X/A,D</sub> : BB (Daou et al., 2007)
	pH <sub>5,8,5/U/A</sub> : BM (Tejedor-Tejedor and Anderson, 1990)		pH <sub>6,X/P</sub> : BB (Khare et al., 2007)			
	pH <sub>3,13,5/L/D</sub> : BM (Nilsson et al., 1996)					
Selenate	pH <sub>4,6/U/A</sub> : MM (Wijnja and Schulthess, 2000)					
	pH <sub>7,U/X,F</sub> : BB (Das et al., 2013)		pH <sub>7,U,X/A,F</sub> : BB (Das et al., 2013)			
	pH <sub>3,5,6,L,X/A,F</sub> : MM (Peak and Sparks, 2013)	pH <sub>7,U,X,F</sub> : BB (Das et al., 2013)	pH <sub>3,5,L,X/A,F</sub> : MM (Peak and Sparks, 2002)	pH <sub>3,5,L,X/A,F</sub> : MM (Peak and Sparks, 2002)	pH <sub>3,5,6,X,L/A,F</sub> : BB (Jordan et al., 2013)	pH <sub>2,12,S</sub> : OS (Martinez et al., 2006)
Selenite	pH <sub>3,8/U/A</sub> : BB (Das et al., 2013; Su and Suarez, 2000b)					
	pH <sub>3,11/T,S</sub> : BB (Hiemstra et al., 2007)			pH <sub>4,X/P</sub> : BB (Catalano et al., 2006)	pH <sub>3,5,8,X/P</sub> : BB, MM (Jordan et al., 2014)	pH <sub>7,12,S</sub> : MM (Kim et al., 2012)
						pH <sub>2,12,S</sub> : MM (Martinez et al., 2006)
Silicate	pH <sub>4,10,S</sub> : BB (Kersten and Vlasova, 2009)		pH <sub>4,U/A</sub> : BB (Swedlund et al., 2009)		pH <sub>7,11/U/A</sub> : BB (Yang et al., 2009)	pH <sub>7,11/U/A</sub> : BB (Yang et al., 2009)
Sulfate	pH <sub>3,9,S,T</sub> : MM (Rahnamaie et al., 2006)		pH <sub>4,X/D</sub> : BB (Zhu et al., 2013)	pH <sub>3,6,I</sub> : MM (Hug, 1997)		
	pH <sub>4,6,I</sub> : MM (Wijnja and Schulthess, 2000)		pH <sub>2,2,5,U/A,D</sub> : MM, BB (Eggleston et al., 1998)	pH <sub>2,2,5,U/A,D</sub> : MM, BB (Eggleston et al., 1998)		pH <sub>3,5,S</sub> : BB (Mansour et al., 2009)
			pH <sub>3,7,L,S</sub> : MM (Fukushi et al., 2013)	pH <sub>4,5/U/A</sub> : MM, BB (Lefèvre and Fedoroff, 2006)		
<b>Organic acids</b>						
Acetate	pH <sub>3,10/U/A</sub> : OS (Noren and Persson, 2007)					
Oxalate	pH <sub>2,5,9,T,X,U/A</sub> : RS-BM, OS (Persson and Axe, 2005)	pH <sub>3,9/U/A</sub> : RS-BM or RS-BB (Hug and Bahnemann, 2006)				
Citrate	pH <sub>3,10/U/A</sub> : IS, OS (Lindegren et al., 2009)					
Glutarate						
Malate						
Malonate	pH <sub>2,5,9,T,X,U/A</sub> : IS, OS (Persson and Axe, 2005)	pH <sub>3,9/U/A</sub> : IS (Hug and Bahnemann, 2006)				
Succinate						
Aspartate	pH <sub>3,11/L,T/A</sub> : RS-BB, OS (Yang et al., 2016)					pH <sub>2,7,T</sub> : RS-BM (Bürger et al., 2013)

included in the table caption. Arsenate and goethite are the most popular sorbate and sorbent, and arsenate sorption on a goethite surface is the most frequently studied experiment. The experimental method is quite different for each oxyanion because of the differing utility of XAS and of other methods. As, Cr and Se are mainly analyzed *via* XAS measurement within a hard X-ray regime ( $> 2$  keV), whereas lighter elements such as C, P and S are frequently measured with infrared spectroscopy (Newville, 2014). XAS can theoretically measure the soft X-ray region ( $< 2$  keV), where the Auger processes predominate over fluorescence, but Auger processes are less commonly measured (Josefsson et al., 2012; Newville, 2014). EXAFS and XANES measurement provides us with direct information of the local structure, coordination and oxidation state, but species transformation cannot be easily distinguished by protonation and deprotonation (Kubicki et al., 2007; Waychunas et al., 1993). In contrast, infrared spectroscopy offers only indirect evidence through vibration, but it enables us to interpret the species transformation from the protonation and deprotonation because it significantly alters the vibration mode of the complex, while the local structure shows no significant difference (Brechtbühl and Christl, 2012; Yang et al., 2016). All atomic distance by XAS and wavenumber of band by FTIR were summarized at Table 2-2 and 2-3, respectively.

#### 2.3.1.1 Arsenite and arsenate

The sorption of arsenite on 6 iron (hydr)oxides was studied in 7 papers at pH values ranging from 3 to 10. XAS was used in 6 papers (Farquhar et al., 2002; Liu et al., 2015; Manning et al., 1998; Morin et al., 2008; Ona-Nguema et al., 2005; Yuheng Wang et al., 2008), and FTIR and a surface complexation model (SCM)

were employed together in one paper. BB, bidentate mononuclear (BM) and monodentate mononuclear (MM) complexes similar to those of arsenate were identified, but tridentate hexanuclear complexes (TH) were proposed to describe arsenite on maghemite and magnetite surfaces (Auffan et al., 2008; Liu et al., 2015; Yuheng Wang et al., 2008). The nano effect, which occurs in nanosized maghemite smaller than 20 nm, caused TH and resulted in arsenite sorption on a six-membered iron octahedral ring in a TH configuration (Auffan et al., 2008). Wang et al. (2008) also identified a TH configuration of arsenite on the magnetite surface, and they found that a decrease in surface loading (SL) determined the structural transformation of arsenite from BM to TH and that the TH on the maghemite significantly decreased its solubility. Liu et al. (2015) confirmed the TH configuration and proposed that the interconversion between arsenate and arsenite occurs by redox fluctuation.

The sorption of arsenate on 6 iron (hydr)oxides was studied in 11 papers, and the pH of the sorption experiments ranged from 3 to 10. FTIR, SCM, computational chemistry (CC) and XAS were used in 2, 2, 2 and 9 papers, respectively, and multiple methods were applied in 3 papers. Based on the experimental results, 9 papers (Antelo et al., 2005; Brechbühl and Christl, 2012; Farquhar et al., 2002; Liu et al., 2015; Morin et al., 2008; Neupane et al., 2014; Randall et al., 2001; Sherman and Randall, 2003) suggested a BB complex as the structural configuration of arsenate sorption on 5 iron (hydr)oxides but not on goethite. The atomic distances calculated with EXAFS were 1.68 Å for As-O, and 2.85-3.65 Å for As-Fe. Most papers obtained an atomic distance for BB between

3.24-3.35 Å, whereas 4 papers (Farquhar et al., 2002; Fendorf et al., 1997; Loring et al., 2009; Waychunas et al., 1993) obtained an atomic distance ranging from 2.85-2.93 or 3.6-3.65 Å and a different coordination number. Neupane et al. (2014) and Waychunas et al. (1993) identified the As-Fe shell with a distance of 2.85-2.93 Å as a BM complex, whereas Fendorf et al. (1997) and Loring et al. (2009) described the As-Fe shell with a distance of 3.60-3.65 Å as an MM complex. Loring et al. (2009) also determined the As-Fe distance to be 3.29 Å at pH 3 and 10, but they reported the structure as a monodentate trinuclear complex (MT) because of their EXAFS and FTIR results. In this paper, the As-Co distance of pentaamminecobalt(III) arsenate was measured as a monodentate type (3.25 Å), and unprotonated, singly protonated and doubly protonated As-O stretching bands were observed in D<sub>2</sub>O. Liu et al. (2015) conducted an experiment to test the difference between a dried and paste sample on magnetite, but no difference was observed; however, the experiment confirmed that the MM complexes were identified only in the paste sample.

Fig. 1 shows a scatter plot of the adsorbed concentration per unit area ( $\Gamma_{As(V)}$ ,  $\mu\text{mol m}^{-2}$ ) against SL ( $\text{mmol m}^{-2}$ ) in arsenate sorption on six iron (hydr)oxides. I used 19 data points from EXAFS, and the minimum and maximum data were employed only when no significant difference was found in the midrange data. The scatter plot clearly showed that the MM is observed only in experiments with a relatively high SL and low  $\Gamma_{As(V)}$ , whereas no pH effect was observed (Fig. 2-3). Fendorf et al. (1997) reported that the addition of SL yielded a change in the structural configuration of the complex, and an MM complex gradually became

dominant at low SL and high pH. One possible explanation for the MM complex is the competition with background anions such as  $\text{NO}_3^-$  and  $\text{Cl}^-$  or with atmospheric  $\text{HCO}_3^-$  and  $\text{CO}_3^{2-}$  at high pH, as previous studies confirmed the competitive effect of such anions; thus, a similar effect could result from the increase in SL on the complexation (Brechtbühl and Christl, 2012; Frau et al., 2010). In addition, both experiments used 0.1 M  $\text{NaNO}_3$  to maintain the background solution, and the atmospheric conditions were not regulated. Another explanation for the MM complex is the ratio among the sorbate, sorbent and solution. Many researchers have reported a sorbent concentration effect, which enhanced the sorption per unit mass or area by increasing the SL (Guo et al., 2014; Zhao and Hou, 2012). The heightened concentration of sorbate per unit area could promote complex formation at the surface, and the competition for limited sorption sites would be increased (Das et al., 2013; Fendorf et al., 1997). Not only the competition and sorbent concentration effect but also the decrease in available sorption sites might yield the MM complex. Environmental changes in pH, aggregation, particulation, inducing organic matter, drying and freezing could alter the number of available sorption sites and the activity coefficient of the surface component (Dixit and Hering, 2003; Jordan et al., 2009a; Zhang and Selim, 2007), and the decreased activity coefficient of the surface component would increase the amount of complex because of the sorbent concentration effect caused by adsorbent particle-particle interaction (Guo et al., 2014; Zhao and Hou, 2012).

#### 2.3.1.2. Carbonate

Five studies on carbonate complexes have been conducted. Infrared

**Fig. 2-3** Scatter plot between  $\Gamma_{As}$  ( $\mu\text{mol m}^{-2}$ ) and SL ( $\mu\text{mol m}^{-2}$ ) for arsenate sorption on six iron (hydr)oxides using extended X-ray absorption fine structure spectroscopy results from previous papers ( $N=15$ ) (a), and scatter plot between competition effect and SL in the competition of arsenate with arsenite ( $N=45$ ) (b). BB, BM and MM denote the structural configuration of the inner-sphere complex as bidentate binuclear, bidentate mononuclear and monodentate mononuclear, respectively.

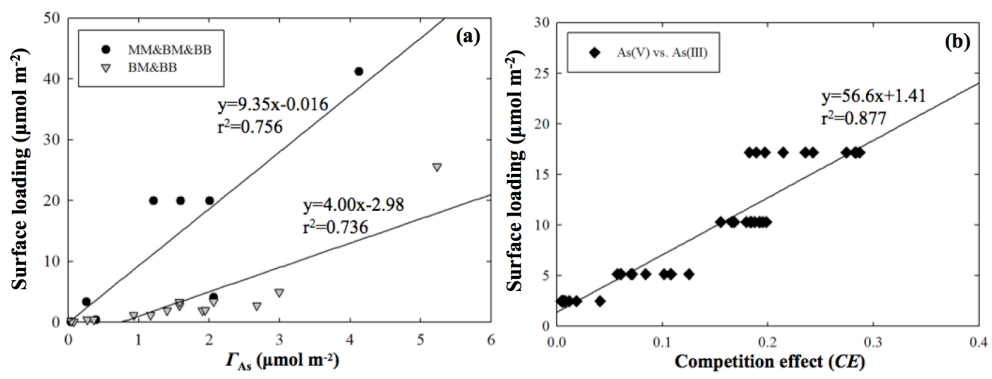


**Fig. 2-4** Scatter plot of arsenate on iron (hydr)oxides between pH and As-Fe distance measured by EXAFS studies. BB, BM and MM indicate bidentate binuclear, bidentate mononuclear and monodentate mononuclear complex, respectively. We found no pH effect on the structural configuration.

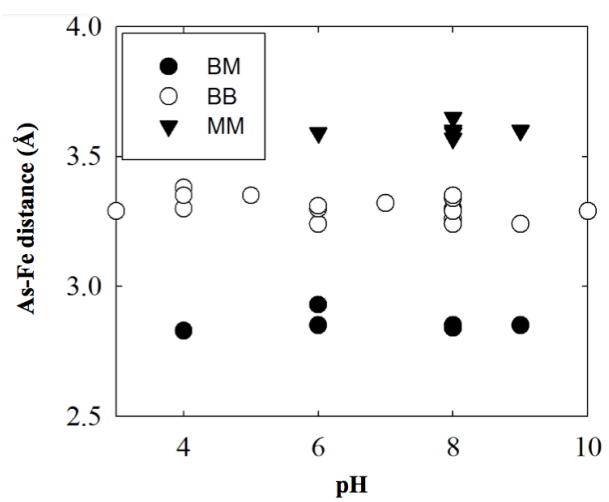


**Table 2-2** Summary of the atomic distance among oxyanion element, oxygen shell and iron shell using EXAFS studies.

Author	Iron (hydr)oxide	Oxyanion	Oxygen shell	Iron shell
(Das et al., 2013)	Ferrihydrite	Se(VI)	1.64	3.3
	Goethite	Se(VI)	1.65	3.31
	Lepidocrocite	Se(VI)	1.65	3.31
(Farquhar et al., 2002)	Goethite	As(V)	1.69	2.93/3.3
	Goethite	As(III)	1.78	3.31
	Lepidocrocite	As(V)	1.69	3.31
	Lepidocrocite.	As(III)	1.78	2.97/3.41
(Fendorf et al., 1997)	Goethite.	As(V)	1.66	2.85/3.24/3.6
	Goethite	Cr(VI)	1.68	2.91/3.29/3.63
(Johnston and Chrysochoou, 2012)	Hematite	Cr(VI)	1.64	3.32/3.51
(Liu et al., 2015)	Magnetite	As(V)	1.69	3.35
	Magnetite	As(III)	1.79	3.49
(Loring et al., 2009)	Goethite	As(V)	1.68	3.29
(Morin et al., 2008)	Maghemite	As(V)	1.69	3.35
	Maghemite	As(III)	1.77	2.90/3.45
(Ona-Nguema et al., 2005)	Ferrihydrite	As(III)	1.78	2.92/3.41
	Hematite	As(III)	1.76	2.89/3.36
	Goethite	As(III)	1.77	3.34/3.54
	Lepidocrocite	As(III)	1.78	3.38/3.58
	Ferrihydrite	As(III)	1.76	2.92/3.40
	Goethite	As(III)	1.78	3.31
	Lepidocrocite	As(III)	1.79	3.09/3.41
(Peak and Sparks, 2002)	Goethite	Se(VI)	1.64	3.31
	Hematite	Se(VI)	1.64	3.3
	Ferrihydrite	Se(VI)	1.64	3.3
(Randall et al., 2001)	Lepidocrocite	As(V)	1.69	3.32
(Yuheng Wang et al., 2008)	Magnetite	As(III)	1.79	3.53
(Waychunas et al., 1993)	Goethite	As(V)	1.663	3.3/3.65
	Lepidocrocite	As(V)	1.673	3.29

spectroscopy, theoretical calculations and SCM were used, and the pH range was 3-12. Wijnja and Schulthess (2001) identified bands at 1510, 1315 and 1068  $\text{cm}^{-1}$  with an  $\text{H}_2\text{O}$  background, and an additional band at 1462  $\text{cm}^{-1}$  appeared with a  $\text{D}_2\text{O}$  background; they assigned the carbonate complex on goethite as an MM complex. Brechbühl and Christl (2012) identified a band at 1522  $\text{cm}^{-1}$  as that of an MM complex and a band at 1463  $\text{cm}^{-1}$  as that of a BB complex, whereas bands at 1357 and 1063  $\text{cm}^{-1}$  were assigned for both MM and BB complexes. Hiemstra et al. (2004) interpreted the structural configuration by considering the relationship between the degree of splitting ( $\Delta\nu_3$ ) and the field strength of coordination. A large difference (300-340  $\text{cm}^{-1}$ ) in  $\Delta\nu_3$  indicated the BM complex, whereas a relatively small difference (80-120  $\text{cm}^{-1}$ ) revealed the MM complex. Bargar et al. (2005) reported the bands associated with aqueous carbonate species transformation and a carbonate complex at pH 3.6-8.2. Aqueous  $\text{HCO}_3^-$  showed bands at 1355, 1300 and 1000  $\text{cm}^{-1}$ , whereas  $\text{CO}_3^{2-}$  had only one band at 1393  $\text{cm}^{-1}$ . The bands at 1522, 1480, 1355 and 1320  $\text{cm}^{-1}$  were assigned to the BB complex on hematite. DFT (B3LYP/6-31G(d)) calculations obtained bands at 1529 and 1339  $\text{cm}^{-1}$  for the BB complex and at 1605 and 1271  $\text{cm}^{-1}$  for the MM complex. Roonasi and Holmgren (2010) found BB complex bands at 1545, 1485, 1335 and 1070  $\text{cm}^{-1}$ . All studies confirmed that the BM and BB complexes were dominated by a small contribution from the MM complex.

#### 2.3.1.3. Chromate

Three studies at pH values of 3-9.5 reported chromate sorption structures. Fendorf et al. (1997) reported MM, BB and BM complexes similar to those of

arsenate. The atomic distance was 1.89-1.69 Å for Cr-O and 2.91-3.63 Å for Cr-Fe. Johnston and Chrysochoou (2014) reported atomic distances of Cr-O and Cr-Fe as 1.64 and 3.22-3.51 Å, respectively. Fendorf et al. (1997) determined the atomic distances of the BB, BM and MM complexes to be 2.91, 3.29 and 3.63 Å, respectively, whereas Johnston and Chrysochoou (2014) determined the atomic distances of the BB and BM complexes to be 3.32 and 3.51 Å, respectively. They also identified the BB and BM complexes on the basis of theoretical calculations and IR spectroscopy. Aqueous chromate showed bands at 880 and 848 cm<sup>-1</sup> for CrO<sub>4</sub><sup>2-</sup> (*T<sub>d</sub>*), bands at 950 and 898 cm<sup>-1</sup> for HCrO<sub>4</sub><sup>-</sup> (*C<sub>3v</sub>*) and bands at 950, 882 and 772 cm<sup>-1</sup> for Cr<sub>2</sub>O<sub>7</sub><sup>2-</sup> (*C<sub>3v</sub>*). The chromate complex on ferrihydrite had bands at 950, 930, 885, 830 and 750 cm<sup>-1</sup> for pH 3.5 and at 910, 873 and 820 for pH 7.0. Based on the theoretical results, a nonprotonated MM complex was identified under the acidic condition, whereas protonated BB or BM complexes were dominant under the basic condition. We conclude that the BB complex is the dominant form in chromate, and an increase in the pH changes the complex from BB to MM with protonation.

#### 2.3.1.4. Phosphate

Nine studies revealed the structural configuration of phosphate on iron (hydr)oxides at pH values of 3-13. Two IR studies identified the MM complex at SL and high pH (Elzinga and Sparks, 2007; Kubicki et al., 2012). Otherwise, all studies reported a BB or BM complex for phosphate sorption. The BB complex was reported using SCM (Antelo et al., 2005; Arai and Sparks, 2001), while IR spectroscopy identified the BB or BM complex (Arai and Sparks, 2001; Daou et al., 2007; Luengo et al., 2006; Persson et al., 1996; Tejedor-Tejedor and Anderson,

1990). X-ray spectroscopy also revealed the BB complex (Daou et al., 2007; Khare et al., 2007). The aqueous band positions of phosphate were reported as approximately 1172, 1005 and 889  $\text{cm}^{-1}$  for  $\text{H}_3\text{PO}_4$  ( $C_{3v}$ ), 1159, 1077, 940 and 875  $\text{cm}^{-1}$  for  $\text{H}_2\text{PO}_4^-$  ( $C_{2v}$ ), 1078, 990 and 850  $\text{cm}^{-1}$  for  $\text{HPO}_4^{2-}$  ( $C_{3v}$ ) and 1011  $\text{cm}^{-1}$  for  $\text{PO}_4^{3-}$  ( $T_d$ ) (Elzinga and Sparks, 2007; Persson et al., 1996; Tejedor-Tejedor and Anderson, 1990). Tejedor-Tejedor and Anderson (1990) reported deprotonated BB bands at 1123, 1006 and 986  $\text{cm}^{-1}$  for  $\nu(\text{P}=\text{O})$ ,  $\nu_a(\text{P}-\text{OFe})$  and  $\nu_s(\text{P}-\text{OFe})$  or  $\nu(\text{P}-\text{OH})$ , protonated BB bands at 1094 and 1044  $\text{cm}^{-1}$  for  $\nu(\text{P}-\text{O})$ , and deprotonated MM bands at 1025 and 1001 for  $\nu(\text{P}-\text{O})$ . Arai and Sparks (2001) identified bands at 1100, 1040 and 1004 from pH 4.5 to 8.4, and they concluded that the BB complex is formed on the goethite surface. Luengo et al. (2006) assigned bands at 1092, 1047 and 952  $\text{cm}^{-1}$  to nonprotonated BB and 1122, 1012 and 933  $\text{cm}^{-1}$  to protonated BB. Persson et al. (1996) studied a dried sample using DRIFT-FTIR but observed a band position significantly different from the results of ATR-FTIR. Daou et al. (2007) measured dried magnetite using a transmission mode and identified BB bands at 1110, 1032, 962 and 816  $\text{cm}^{-1}$  by peak deconvolution at pH 3. Elzinga and Sparks (2007) reported the bands of a nonprotonated BB complex at 1117, 1007 and 964  $\text{cm}^{-1}$ , the bands of a monoprotated BB complex at 1075, 1030 and 936  $\text{cm}^{-1}$  and the bands of an MM complex at 1085, 1040 and 960  $\text{cm}^{-1}$ . Kubicki et al. (2012) employed two types of goethite, micro- and nanosized samples, from pH 4.2 to 8.0. Peak deconvolution identified bands at 1117, 1084, 1044, 1005 and 957  $\text{cm}^{-1}$  in nanosized goethite at pH 4.2 and bands at 1082, 1036, 1006, 966 and 935  $\text{cm}^{-1}$  at pH 8.0. In microsized goethite, the band positions were 1157, 1122, 1091, 1044 and

1009  $\text{cm}^{-1}$  at pH 4.2 and 1095, 1076, 1039 and 1005  $\text{cm}^{-1}$  at pH 8.0. Kubicki et al. (2012) also studied the effect of drying on complexation and found band positions completely different from those obtained by interfacial measurement. The theoretical results indicated that the surface structure led to alteration of the complex. Daou et al. (2007) employed X-ray photoemission spectroscopy (XPS) and Mossbauer spectroscopy for complex characterization, Khare et al. (2007) used a fingerprinting method with molecular orbital calculations, and both studies confirmed a BB complex. IR spectra results showed significant variation in the bands and their interpretation; thus, these results are still debatable for use in interpreting the complex. However, we inferred that phosphate showed dramatic changes with pH and SL, and the BB complex was identified as the most abundant phosphate complex on an iron (hydr)oxide surface.

#### 2.3.1.5. Selenate and selenite

Nine studies have been performed to examine selenate and selenite sorption on iron (hydr)oxide at pH values ranging from 3 to 12. Three studies identified an MM complex of selenate and selenite (Kim et al., 2012; Peak and Sparks, 2002; Wijnja and Schulthess, 2000), whereas the other five studies identified BB and BM complexes of selenate and selenite (Catalano et al., 2006; Das et al., 2013; Hiemstra et al., 2007; Jordan et al., 2014; Su and Suarez, 2000a). Martínez et al. (2006) revealed an OS complex of selenate, whereas an MM complex of selenite was calculated using SCM. Kim et al. (2012) also identified an MM complex of selenite using SCM. Hiemstra et al. (2007) employed SCM and theoretical calculations to study selenite sorption on goethite, and a BB complex

**Table 2-3** Summary of vibrational band position in each structural configuration from the previous literature.

Author	Oxyanion	Iron (hydr) oxide	Structural configuration	Band (cm <sup>-1</sup> )
(Wijnja and Schulthess, 2001)	C(IV)	goethite	MM	1510/1315/1068
	C(IV)	goethite	MM	1510/1462/1315/1068
(Brechtbühl and Christl, 2012)	C(IV)	hematite	MM	1522/1357/1063
	C(IV)	hematite	BB	1463/1357/1063
(Bargar et al., 2005)	C(IV)	Hematite	BB	1522/1480/1355/1320
(Roonasi and Holmgren, 2010)	C(IV)	Magnetite	BB	1545/1485/1335/1070
(Johnston and Chrysochoou, 2012)	Cr(VI)	ferrihydrate	MM	950/930/885/830/750
(Roonasi and Holmgren, 2010)	Cr(VI)	ferrihydrate	BB or BM	910/873/820
(Tejedor-Tejedor and Anderson, 1990)	P(V)	goethite	deprotonated B	1123/1006/986
	P(V)	goethite	protonated BB	1094/1044
	P(V)	goethite	deprotonated MM	1025/1001
(Arai and Sparks, 2001)	P(V)	ferrihydrate	BB	1100/1040/1004
(Luengo et al., 2006)	P(V)	goethite	nonprotonated BB	1092/1047/952
(Arai and Sparks, 2001)	P(V)	ferrihydrate	protonated BB	1122/1012/933
(Persson et al., 1996)	P(V)	Magnetite	BB	1110/1032/962/816
(Elzinga and Sparks, 2007)	P(V)	hematite	nonprotonated BB	1117/1007/964
	P(V)	hematite	monoprotonated BB	1075/1030/936
	P(V)	hematite	MM	1085/1040/960
(Kubicki et al., 2012)	P(V)	nanosized goethite	-	1117/1084/1044/1005/957
	P(V)	microsized goethite	-	1157/1122/1091/1044/1009
(Jordan et al., 2014)	Se(IV)	maghemite	BB	904/879/859/829
(Su and Suarez, 2000b)	Se(VI)	goethite	BB	910/880/820
(Peak and Sparks, 2002)	Se(VI)	hematite	MM	880/850/820
(Eggleston et al., 1998)	S(VI)	hematite	BB	1126/1042/980
(Zhu et al., 2013)	S(VI)	ferrihydrate	BB	1175/1121/1043
(Hug, 1997)	S(VI)	hematite	MM	1128/1055/975
(Wijnja and Schulthess, 2000)	S(VI)	goethite	MM	1130/1060/976

was identified. Catalano et al. (2006) used X-ray standing wave measurements on a BB complex at pH 4. Manceau and Charlet (1994) showed BB and BM complexes of selenite on ferrihydrite, while only a BB complex of selenite and selenate was identified on the goethite surface. The atomic distances of selenate and selenite were calculated to be 3.25-3.29 and 3.38 Å for the BB complex and 2.80-2.83 and 2.85 Å for the BM complex, respectively. Peak and Sparks (2002) identified an MM complex on goethite, ferrihydrite and hematite, and the atomic distance was 1.64-1.65 Å for Se-O and 3.3-3.31 Å for Se-Fe. They noted that the distance of 3.3-3.31 Å was intermediate between the distances associated with an MM and BB complex and that hydrogen bonding led to a contraction of the Se-Fe distance. Das et al. (2013) identified a BB complex on ferrihydrite, goethite and lepidocrocite even though the atomic distance resembled that found by Peak and Sparks (2002). Jordan et al. (2013) found a BB complex with an atomic distance at 3.38 Å, but the OS complex was abundant, while IS made only 15 % of the contribution to sorption. Jordan et al. (2014) reported BB and BM complexes of selenite on a maghemite surface, and the atomic distance was 1.71 Å for Se-O, 2.88-2.91 Å for BM and 3.36-3.38 Å for BB, respectively.

In IR spectroscopy, aqueous selenite ( $pK_{a1}=2.46$ ;  $pK_{a2}=7.3$ ) bands were observed at 849 and 825  $\text{cm}^{-1}$  for  $\text{HSeO}_3^-$  and at 851, 822 and 731  $\text{cm}^{-1}$  for  $\text{SeO}_3^{2-}$  (Duc et al., 2006). The selenate bands ( $pK_{a1}=-3$ ;  $pK_{a2}=1.9$ ) were observed at 867-873  $\text{cm}^{-1}$  (Das et al., 2013). Su and Suarez (2000b) identified a BB complex of selenate with bands at 910, 880 and 820  $\text{cm}^{-1}$ . Jordan et al. (2013) also reported a BB complex on maghemite, but the bands were at 904, 879, 859 and 829  $\text{cm}^{-1}$ . Peak

and Sparks (2002) revealed an MM complex on hematite, and the bands were at 880, 850 and 820  $\text{cm}^{-1}$ . For selenium, the MM, BB and BM complexes existed together, but the structural configuration changed with the environmental conditions.

#### 2.3.1.6. Silicate

Four studies were performed to examine the sorption of silicate on iron (hydr)oxide, all of which reported a BB or BM complex. Kersten and Vlasova (2009) performed batch adsorption experiments at various temperatures (10-75 °C). The percentage of adsorbed silicate decreased with time, and the maximum sorption occurred at pH 9. SCM identified two complexes, a nonprotonated BB complex and a deprotonated BB complex, and increasing the temperature yielded a decrease in the nonprotonated BB complex at acidic and neutral pH. Swedlund et al. (2009) observed the polymerization of silicate on a ferrihydrite surface. Aqueous  $\text{H}_4\text{SiO}_4$  ( $\text{pK}_{\text{a}1}=9.84$ ;  $\text{pK}_{\text{a}2}=13.2$ ) showed bands at 1090 and 939  $\text{cm}^{-1}$ , which were assigned to Si-O-H deformation and asymmetric Si-O stretching, respectively. Adsorbed silicate showed broad bands between 1200 to 750  $\text{cm}^{-1}$ , and band shifts were observed upon changes in time and silicate concentration. At low silicate concentration, the maximum intensity appeared at 943  $\text{cm}^{-1}$ , and it shifted to 1001  $\text{cm}^{-1}$  and finally to 1110  $\text{cm}^{-1}$  with increasing silicate concentration. The band shift resulted from the polymerization of monomeric silicate to oligomeric and finally to polymeric silicate. Yang et al. (2008) also observed a band shift upon the polymerization of silicate at pH 8.5 and 10.8, which are above and below the  $\text{pK}_{\text{a}1}$  of silicate. However, the polymerization rate was significantly lower at pH 10.8. Jolsterå et al. (2010) studied the SCM of silicate on maghemite at pH 3-11, and they

also found a BB complex or polynuclear silicate complex. In contrast to the situation for other oxyanions, polymerization is the key mechanism for understanding the dynamics of silicate in the environment, especially at high silicate concentration and pH. The band shift in the IR spectrum clearly confirmed the polymerization. Silicate is primarily sorbed as a BB complex and is strongly retained at the iron (hydr)oxide surface, forming an additional surface over the iron (hydr)oxides. In the soil environment, silicate is an abundant oxyanion due to the weathering of primary and secondary minerals; thus, understanding silicate dynamics is important.

#### 2.3.1.7. Sulfate

Eight studies have examined the complexation of sulfate on iron (hydr)oxide. Four studies identified an MM complex of sulfate (Fukushi et al., 2013; Hug, 1997; Rahnemaie et al., 2006; Wijnja and Schulthess, 2000), whereas two studies concluded that a BB complex is formed (Mansour et al., 2009; Zhu et al., 2013). Lefèvre and Fédoroff (2006) and Eggleston et al. (1998) measured both MM and BB complexes on hematite using ATR-FTIR. Rahnemaie et al. (2006) and Fukushi et al. (2013) used SCM to predict the complexation of sulfate and concluded that an MM complex is formed by comparing theoretical (BP86) and IR results. Mansour et al. (2009) identified a BB complex on magnetite at pH 3-5, whereas only an OS complex remained above pH 5. Zhu et al. (2013) employed EXAFS spectroscopy, the differential atomic pair distribution function (d-PDF) and ATR-FTIR measurement. Atomic distances of 1.46-1.47 Å for S-O and 3.18-3.19 Å for S-Fe were obtained with EXAFS, whereas atomic distances of 1.46-1.47 Å for

S-O and 3.24-3.27 Å for S-Fe were obtained with d-PDF. The IR bands at 1175, 1121, 1043  $\text{cm}^{-1}$  were assigned to  $\nu_3$  splitting, whereas the bands at 1102 and 977  $\text{cm}^{-1}$  were assigned to degenerate  $\nu_3$  and  $\nu_1$ , respectively. As a result, the BB complex was assigned under air-dried conditions. Previous studies observed the effect of drying on complexation was observed; thus, the sulfate possibly forms a complex of the MM type at the aqueous and solid interface. Eggleston et al. (1998) also confirmed a BB complex of sulfate on dried hematite. In the ATR-FTIR results, aqueous sulfate ( $\text{pK}_{\text{a}1}=-3$ ;  $\text{pK}_{\text{a}2}=1.99$ ) bands were observed at 1194, 1051 and 891  $\text{cm}^{-1}$  for  $\text{HSO}_4^-$  and 1102  $\text{cm}^{-1}$  for  $\text{SO}_4^{2-}$  ( $T_d$ ), whereas bands of adsorbed sulfate were found at 1126, 1042 and 980  $\text{cm}^{-1}$  for wet sample measurement. Hug (1997) and Wijnja and Schulthess (2000) also reported bands at 1128-1130, 1055-1060 and 975-976  $\text{cm}^{-1}$  as belonging to an MM complex. The studies confirmed that the dramatic increase in band intensity at 1200  $\text{cm}^{-1}$  was evidence of a BB complex. Based on these observations, we concluded that sulfate is primarily present as an MM complex under acidic conditions for all iron (hydr)oxides, and the drying effect and high pH yield a BB complex and an OS complex, respectively.

### **2.3.2. Structural configuration of organic acids**

It is well known that organic molecules mainly interact with the hydrophobic surface of soil organic matter and that ionizable organic molecules interact with the hydrophilic surface of soil minerals (Hyun and Lee, 2008). The sources of these organic molecules in the soil environment range from the decomposition of organic matter to the rhizodeposition of plants, both of which

introduce abundant and various organic molecules into the soil (Bais et al., 2006; Bertin et al., 2003). Previous studies found that 5-21 % of photosynthetic carbon is discharged into the rhizosphere through root exudates (Hütsch et al., 2002; Jones et al., 2009). For example, citrate, glutarate, oxalate, malonate, malate, succinate, acetate, lactate, glycolate, and formate have been reported as nutrient sources, chelators, acidifiers, and detoxifiers (Bais et al., 2006; Dakora and Phillips, 2002; Haichar et al., 2014), but their interaction with soil minerals is not fully understood (Dakora and Phillips, 2002). This section collects previous studies regarding the complexation of organic acids on an iron (hydr)oxide surface to reveal the competition effect (*CE*) on oxyanions.

A literature review found only 8 papers that describe the structural configuration of organic acids on an iron (hydr)oxide surface. A few studies focused on the structural configuration of organic acids on pure iron (hydr)oxide with a molecular-scale approach. IR spectroscopy was the main tool for describing the complexation. Norén and Persson (2007) studied the adsorption of acetate, benzoate and cyclohexanecarboxylate by varying the ionic strength and pH. They concluded that OS complexes dominated the sorption of three monocarboxylates on goethite and that two types of OS complex are involved in the sorption: hydrated OS and nonhydrated OS. Persson and Axe (2005) identified the structural configuration of oxalate and malonate on goethite using soft X-ray EXAFS, theoretical calculation (B3LYP, 6-31<sup>+</sup>G<sup>\*</sup>) and IR spectroscopy. They found that oxalate and malonate interacted with goethite *via* an OS and an IS complex, and the IS complex was favored at low pH. A ring structure-bidentate mononuclear (RS-BM) complex was identified for oxalate and malonate. Hug and Bahnemann (2006) studied oxalate and malonate sorption on lepidocrocite *via* IR spectroscopy by varying the pH from 3 to 9. RSs of the BM and BB complexes were assumed for oxalate, whereas no

specific complex was identified for malonate, but an IS complex of malonate was assumed because of the shifts in the asymmetric and symmetric carboxylate vibrations. Duckworth and Martin (2001) examined the sorption of oxalate, malonate, glutarate, succinate and adipate on hematite at pH 5. The oxalate, malonate and glutarate showed the RS of a BM or BB complex, whereas succinate and adipate formed an MM complex. They also found that the dissolution effect of organic acids on hematite, oxalate, glutarate, malonate and adipate increased the dissolution of the iron (hydr)oxide, whereas the dissolution of adipate and succinate resulted in no difference from the control. Lindegren et al. (2009) showed the molecular structure of citrate and tricarallylate on goethite and confirmed that only an IS complex was formed for both citrate and tricarallylate; however, they concluded that the IS complex was prevalent at high pH *via* a combination of hydroxyl and carboxylic groups. This result contradicted the findings of previous studies, which implied that the IS complex formed mainly at low pH, whereas the OS complex was dominant at high pH. Hwang and Lenhart (2008) examined the sorption of phthalate, malate, fumarate and succinate on hematite using ATR-FTIR. Phthalate, succinate and malate showed an IS complex at low pH and an OS complex at high pH, whereas fumarate showed only an OS complex. Yang et al. (2016) used ATR-FTIR and theoretical calculations to interpret aspartate sorption on goethite, and the RS-BB structure was the dominant sorption mechanism at pH 3. The OS complex prevailed above neutral pH *via* electrostatic attraction and hydrogen bonding. Bürger et al. (2013) also identified aspartate sorption on magnetite surface through theoretical calculation (force field simulation), and the results confirmed the RS-BM complex of aspartate, the quidentate trinuclear complex of glutamine and the RS-BB complex of glycine and leucine.

I recognized that the IS complex of an organic acid in various

configurations occurs primarily under acidic conditions, whereas the OS complex dominates under basic conditions. Therefore, organic acids not only compete with oxyanions for sorption sites but also change the sorption sites by the dissolution of iron from the surface. However, the specific mechanism has not been fully verified; thus, their interactions must be examined in order to elucidate the effect of organic acids on the bioavailability of oxyanions in the soil environment.

#### 2.4. COMPETITIVE SORPTION

In the real soil environment, various sorbates are always exposed to competition for a more stable condition, but present technology and knowledge can barely consider dual or ternary competition in a controlled environment. Twenty-one papers were selected that considered competitive sorption in a dual-solute system on pure iron (hydr)oxide (Table 2-4). All experiments with equal concentrations of simultaneously introduced oxyanions were included, but a few unequal and sequential experiments were also included because of the limited number of published articles. The articles were searched using the keywords oxyanion, iron (hydr)oxide and competitive sorption in the article title, abstract and keywords on Scopus, and the articles were reviewed to identify the experimental conditions. GraphClick software (Arizona, USA) was used for extracting data from the graphs. However, the available data varied substantially from case to case; thus, the competitive sorption ratio (*CSR*) from the previous study (Violante and Pigna, 2002) was applied, and two equations were used to compare the various experimental conditions from the articles. The *CSR* was expressed as follows:

$$\text{Competitive sorption ratio}_{A/B} (CSR_{A/B}) = q_{A,d}/q_{B,d} \quad (\text{Eq. 2-1})$$

where  $q_{A,d}$  and  $q_{B,d}$  are the sorbed concentrations of chemicals A and B in the dual system at equal initial concentrations. Eq. 2-1 shows only the sorption ratio of

chemical A to chemical B. A value of  $CSR$  above 1 indicates that the sorption of chemical A predominated over that of chemical B, and *vice versa*. If  $CSR_{A/B}$  is close to 1, then equal amounts of oxyanions A and B were sorbed, and no preferential sorption occurred. However, most studies did not provide both  $q_{A,d}$  and  $q_{B,d}$ ; thus, I modified the inhibition efficiency to obtain a reduced sorption percentage ( $RSP$ ) (Violante and Pigna, 2002; Zhu et al., 2011) and developed  $CE$  to compare the various sorption data using the limited data from the published articles.

$$\text{Reduced sorption percentage}_{A/B} (RSP_{A/B}) = q_{A,d}/q_{A,s} \times 100 \quad (\text{Eq. 2-2})$$

$$\text{Competition effect}_{A,B} (CE_{A,B}) =$$

$$(C_{A,d} + C_{B,d})/(C_{A,s} + C_{B,s}) - (q_{A,d} + q_{B,d})/(q_{A,s} + q_{B,s}) \quad (\text{Eq. 2-3})$$

In Eq. 2-2,  $q_{A,s}$  and  $q_{A,d}$  are the sorbed concentrations of chemical A in the single system and in the dual system with chemical B as the competitor at an equal initial concentration. A value of  $RSP_{A/B}$  close to 100 % means that the presence of chemical B did not affect the sorption of chemical A.  $RSP_{A/B}$  less than 100 % implied a  $CE$ , whereas a cosorption effect occurred above 100 %. However,  $RSP_{A/B}$  describes only the change in the sorption of chemical A, and no information is provided for chemical B. Moreover, the environmental conditions, such as SL, significantly affected the value of  $RSP$  (for example, close to 100 % at low SL). For that reason, the inverse value of  $RSP_{A/B}$  does not correlate with  $RSP_{B/A}$  and is not a mathematically correct equation, but it was the only data that could be extracted from the various experimental conditions. I understood the limitations and restrictions of employing  $RSP$  because the sorption data differed significantly among experiments, but I wanted to try to compare the results from the various

**Table 2-4** The dominant oxyanion species of competitive sorption among the various oxyanions and organic acids on each iron (hydr)oxide surface. The letter indicates the iron oxides. Abbreviations: Fh ferrihydrite; Gt goethite; Hm hematite; Lp lepidocrocite; Mm maghemite; Mn magnetite. The subscripted numbers and letters indicate the pH range and experimental method. Abbreviations: (For method) *B* batch experiment; *C* column experiment, *M* molecular modeling with infrared or XAFS measurement and *S* surface complexation modeling, (For chemical) As(III) arsenite; As(V) arsenate; C(IV) carbonate; Cr(VI) chromate; N(V) nitrate; P(V) phosphate; Se(VI) selenate, S(IV) sulfate; Si(IV) silicate; Ac. acetate; Fm. Formate; Ox. oxalate; Ct. citrate; Ast. Aspartate. P.E. and N.D. are abbreviations for promotive effect and no dominance, respectively.

	Arsenite	Arsenate	Carbonate	Chromate	Nitrate	Phosphate	Selenate	Silicate	Sulfate
<b>Arsenite</b>		Fh <sub>4-10B</sub> : N.D.(Jain and Loeppert, 2000)	Hm <sub>3-7B,M,S</sub> : As(III) (Brechtbühl and Christl, 2012)	-	-	Fh <sub>4-10B</sub> : N.D. (Jain and Loeppert, 2000) Fh <sub>5-6B</sub> : N.D. (Zhu et al., 2011)	Fh <sub>5-6B</sub> : As(III) (Zhu et al., 2011)	Gt <sub>1-1B</sub> : As(III) (Luxton et al., 2006) Gt <sub>8-8B</sub> : As(III) (Luxton et al., 2008)	Fh <sub>4-10B</sub> : As(III) (Jain and Loeppert, 2000) Fh <sub>5-6B</sub> : As(III) (Zhu et al., 2011)
<b>Arsenate</b>			Gt <sub>5-11</sub> : As(V) (Stachowicz et al., 2008) Hm <sub>3-7B,M,S</sub> : As(V) (Brechtbühl and Christl, 2012) Fh <sub>2-3B,M,S</sub> : As(V) (Brechtbühl and Christl, 2012) Fh <sub>8-9B</sub> : As(V) (Frau et al., 2010)	Gt <sub>3-5</sub> : As(V) (Khaodhiar et al., 2000)	Hm <sub>6B</sub> : As(V) (Youngran et al., 2007)	Gt <sub>5-9B</sub> : N.D. (Hongshao and Stanforth, 2001) Gt <sub>1-10</sub> : P(V) (Gao and Mucci, 2001) Fh <sub>4-10B</sub> : N.D. (Jain and Loeppert, 2000) Hm <sub>6B</sub> : N.D. (Youngran et al., 2007) Gt <sub>4-5-7B</sub> : N.D. (Violante and Pigna, 2002) Gt <sub>2-11B</sub> : N.D. (Manning and Goldberg, 1996) Fh <sub>4-10B</sub> : P(V) (Frau et al., 2010) Fh <sub>5-6B</sub> : N.D. (Zhu et al., 2011)	Hm <sub>6B</sub> : As(V) (Youngran et al., 2007) Fh <sub>5-6B</sub> : As(V) (Zhu et al., 2011)	Hm <sub>6B</sub> : As(V) (Youngran et al., 2007) Fh <sub>1-10B</sub> : As(V) (Frau et al., 2010)	Fh <sub>4-10B</sub> : As(V) (Jain and Loeppert, 2000) Hm <sub>6B</sub> : As(V) (Youngran et al., 2007) Fh <sub>1-10B</sub> : As(V) (Frau et al., 2010) Fh <sub>5-6B</sub> : As(V) (Zhu et al., 2011)
<b>Carbonate</b>				-	-	Gt <sub>7-11</sub> : P(V) (Rahnemaie et al., 2007)	Gt <sub>6-7B</sub> : Se(VI) (Wijnja and Schulthess, 2002)		Gt <sub>6-8B</sub> : P.E. (Wijnja and Schulthess, 2002)
<b>Chromate</b>					Mn <sub>4-8B</sub> : Cr(VI) (Meena and Arai, 2016)	Gt <sub>2-7</sub> : P(V) (Boukemara et al., 2016)	-	Gt <sub>4-8B</sub> : Cr(VI) (Garman et al., 2004)	Mn <sub>4-8B</sub> : Cr(VI) (Meena and Arai, 2016)
<b>Nitrate</b>						-	-	-	-
<b>Phosphate</b>							-		Gt <sub>2-9B</sub> : P(V) (Geelhoed et al., 1997) Gt <sub>3-8B</sub> : P(V) (Boukhalfa, 2010)
<b>Selenate</b>								Mn <sub>4-10B</sub> : Se(VI) (Jordan et al., 2009a) Hm <sub>4-11B,S</sub> : Se(VI) (Jordan et al., 2009b)	Gt <sub>5-8B</sub> : Se(VI) (Wijnja and Schulthess, 2002)
<b>Silicate</b>									-
<b>Acetate</b>		-	-	-	-		Gt <sub>6-7B</sub> : P.E. (Wijnja and Schulthess, 2002)		Gt <sub>5-7B</sub> : P.E. (Wijnja and Schulthess, 2002) Gt <sub>3-8B</sub> : S(VI) (Boukhalfa, 2010)
<b>Formate</b>		-	-	-	-				Gt <sub>6-7B</sub> : P.E. (Wijnja and Schulthess, 2002)
<b>Oxalate</b>	Fh <sub>3-6B</sub> : As(III) (Zhu et al., 2011)	Fh <sub>5-6B</sub> : As(V) (Zhu et al., 2011)	-	Gt <sub>4-11B</sub> : Cr(VI) (Mesure and Fish, 1992)	-				Gt <sub>3-8B</sub> : Ox. (Boukhalfa, 2010)
<b>Citrate</b>	Fh <sub>3-6B</sub> : As(III) (Zhu et al., 2011)	Fh <sub>5-6B</sub> : As(V) (Zhu et al., 2011)	-	-	-	Gt <sub>2-10B</sub> : P(V) (Geelhoed et al., 1998)			-
<b>Aspartate</b>		-	-	-	-	Gt <sub>3-6B,M</sub> : P(V) (Yang et al., 2016)			-
<b>Malate</b>	Fh <sub>3-6B</sub> : As(III) (Zhu et al., 2011)	Fh <sub>5-6B</sub> : As(V) (Zhu et al., 2011)	-	-	-				-
<b>Tartarate</b>	Fh <sub>3-6B</sub> : As(III) (Zhu et al., 2011)	Fh <sub>5-6B</sub> : As(V) (Zhu et al., 2011)	-	-	-				-

conditions, and to the best of our knowledge, *RSP* was the only available method.

The *CE* requires all the sorption data of chemicals A and B in single and dual systems.  $C_{A,s}$  and  $C_{A,d}$  are the initial concentrations of chemical A in the single and dual systems, respectively. I introduced the term  $(C_{A,d} + C_{B,d})/(C_{A,s} + C_{B,s})$  to compare the different conditions in the single and dual systems. The equal concentration experiment, where  $C_{A,s}=C_{B,s}=1$ , was selected, but different experimental conditions were found by introducing competition, such as  $C_{A,d}=C_{B,d}=0.5$  or  $C_{A,d}=C_{B,d}=1$ ; thus, this term was used for the comparison between two experimental conditions. A value of  $CE_{A,B}$  equal to 0 implies that no competition occurs; positive or negative values indicate competition between the two chemicals for limited sorption sites or increased sorption capacity *via* precipitation or cosorption. In most cases, *RSP* was employed to describe competitive sorption, whereas *CSR* and *CE* were used in only a few studies.

#### **2.4.1. Competitive sorption among oxyanions**

##### 2.4.1.1. Competition of arsenite

Arsenite (As(III)) and arsenate (As(V)) are known as the most problematic oxyanions because of their toxicity and worldwide distribution (Jain and Ali, 2000; Rosen and Liu, 2009; Tripathi et al., 2007). Their mobilization results in severe risks to human health where groundwater is used as drinking water (Vamerali et al., 2010; Zhang and Selim, 2007). Jain and Loeppert (2000) extensively studied the competitive sorption between arsenate and arsenite on ferrihydrite by varying the concentration (1.0-6.9 mM) and pH (4-10). The results were interesting because the

changes in concentration and pH led to dramatic changes in competitive sorption.  $CSR_{As(III)/As(V)}$  ranged from 0.57 to 52, and we found that an increase in either pH or concentration elevated  $CSR_{As(III)/As(V)}$ , which indicated that arsenite sorption was becoming more favorable.  $CE_{As(III),As(V)}$  ranged from 0.0 to 0.29 and increased with concentration. However,  $CE_{As(III),As(V)}$  decreased with increasing pH at high concentration (6.94 mM), and the surface polymerization of arsenite was assumed for this reason, but to the best of our knowledge, no verification was conducted. I considered the possibilities that the reason was polymerization, as the author claimed; the oxidation of arsenite to arsenate (Liu et al., 2015); or the formation of a nanosized As-Fe complex in aqueous solution *via* reductive dissolution (Farrell, 2017). Previous studies revealed that the activation energy for the transformation from ferrihydrite to goethite decreased with increasing pH (Yee et al., 2006). Arsenite and arsenate showed significant potential as competitors (Jain and Loeppert, 2000; Jönsson and Sherman, 2008) and exhibited species transformation through oxidation and reduction as previously reported (Fakour and Lin, 2014; Liu et al., 2015); thus, while the dynamics of arsenic are difficult to understand, a combination of causes can clearly lead to dramatic fluctuation (Appelo et al., 2002; Morin et al., 2008; Zhang and Selim, 2007).

Carbonate, phosphate, silicate and sulfate are the predominant oxyanions in the soil system due to the decomposition of organic matter and the dissolution of primary rock (Sparks, 2003). They are generally present in relatively high concentrations in the vadose zone rather than as trace elements (less than  $100 \mu\text{g g}^{-1}$ ), and they ubiquitously compete with oxyanions (Lefèvre and Fédoroff, 2006;

Luxton et al., 2008; Wijnja and Schulthess, 2001). Brechbühl and Christl (2012) studied the competitive sorption between arsenite and carbonate on hematite at unequal concentrations, and  $RSP_{As(III)/C(IV)}$  at a 30  $\mu\text{M}$  initial As concentration with 100 kPa  $\text{CO}_2$  decreased from 89 to 85 % as the pH increased from 3 to 5.4. Luxton et al. (2006) determined  $CSR_{As(III)/Si(V)}$  and  $CE_{As(III),Si(V)}$  to be 1.3-2.6 and -0.07-0.03, respectively, at pH 3-11. Luxton et al. (2008) determined  $RSP_{As(III)/Si(V)}$  to be 91-96 % at pH 4-8. Both studies confirmed that no competitive displacement was observed at equal concentrations. Jain and Loeppert (2000) examined the competitive sorption of phosphate or sulfate with arsenite, and  $CSR_{As(III)/P(V)}$  and  $RSP_{As(III)/S(VI)}$  were calculated to be 0.83-2.91 and 94-100 % at pH 4-10, respectively. Zhu et al. (2011) also revealed  $RSP_{As(III)/S(VI)}$ ,  $RSP_{As(III)/Se(VI)}$  and  $RSP_{As(III)/P(V)}$  at pH 5 to be 94.3, 95.3 and 56.8 %, respectively, and no significant difference was found at pH 6.

We summarize the average values of  $RSP$  between each chemical and its competitor in Table 2-5. A total of 352 data points were used at pH 2-12, and the pH range was separated into 2-6, 6-8 and 8-12. For arsenite, the  $RSP$  sequence for the entire pH range was as follows:  $\text{Si(V)}=\text{S(VI)}>\text{P(V)}=\text{As(V)}$ , and carbonate was excluded because it was not tested at equal concentrations (Table 2-5). Increases in  $RSP_{As(III)/As(V)}$  and  $RSP_{As(III)/P(V)}$  were observed with increasing pH, whereas  $RSP_{As(III)/S(VI)}$  and  $RSP_{As(III)/Si(V)}$  remained relatively constant. This result implied that arsenite is the dominant oxyanion for sorption on iron (hydr)oxide. Carbonate, silicate and sulfate showed no significant effect on arsenite at equal concentrations, whereas phosphate and arsenate acted as competitors. However, carbonate, silicate

and sulfate are more abundant than arsenite, and thus the competition would be significantly different in the real environment.

#### 2.4.1.2. Competition of arsenate

Three papers discussed the competitive sorption between arsenate and carbonate, but the authors did not provide enough data on the experimental conditions at equal concentration to calculate  $CSR$  and  $CE$  (Brechtbühl and Christl, 2012; Frau et al., 2010; Stachowicz et al., 2008). Frau et al. (2010) studied only the competition at pH 8.3, and the values of  $RSP_{As(V)/C(IV)}$  at 10 and 100 mM were 60 and 38 %, respectively. For sulfate and selenate, Jain and Loeppert (2000) found  $RSP_{As(V)/S(VI)}$  to range from 94 to 100 % at pH 4-10, whereas Frau et al. (2010) found  $RSP_{As(V)/S(VI)}$  to range from 77 to 104 % at pH 4-10. For silicate, Youngran et al. (2007) found  $RSP_{As(V)/Si(V)}$  to be 16.2 % at unequal concentrations. Zhu et al. (2011) showed that both  $RSP_{As(V)/S(VI)}$  and  $RSP_{As(III)/Se(VI)}$  at pH 6 were 100 % at equal concentrations, and increasing the concentration of the competitor showed no significant effect on the arsenate sorption. As a result, sulfate and selenate did not show a significant competitive effect; however, at high concentration, carbonate and silicate did compete with arsenate.

Chromate is a toxic oxyanion, whereas selenate is essential or toxic depending on the concentration (Babula et al., 2008; Goh and Lim, 2010). Chromate and selenate enter the environment mainly *via* anthropogenic activity such as mining and use in pigment (Babula et al., 2008). Khaodhiar et al. (2000) determined  $CSR_{As(V)/Cr(VI)}$  and  $CE_{As(V),Cr(VI)}$  to be 7.4-320 and -1.3-0.31 on goethite at pH 4.1-7.8.  $CSR$  and  $CE$  reached a maximum value at pH 6. At pH 4.0-6.7, a less

**Table 2-5** The average values of reduced sorption percent (*RSP*, %) among the oxyanions and organic acids by pH ranges. *RSP* denotes the ratio between the sorption amount of target oxyanion with competitor and the sorption amount of target oxyanion without competitor. The asterisk indicates a nonequal concentration between the chemical and competitor, otherwise equal concentrations were applied.

Oxyanion	Competitor	pH 2-6		pH 6-8		pH 8-12		Total	
		<i>N</i>	<i>RSP (%)</i>						
As(III)	As(V)	18	87.4	14	94.4	13	98.7	45	92.9
	C(IV)*	6	80.7	1	60.4	-	-	7	77.8
	P(V)	5	82.0	4	82.8	4	97.7	13	87.1
	S(VI)	5	96.4	4	99.4	3	100.3	12	98.5
	Se(VI)	1	95.3	1	97.8	-	-	2	96.5
	Si(IV)	6	100.7	3	101.2	3	102.4	12	101.2
As(V)	As(III)	18	85.5	14	74.2	13	61.5	45	75.1
	Cr(VI)	4	96.5	2	198.3	-	-	6	130.4
	P(V)	15	74.1	14	64.7	12	59.4	41	66.6
	S(VI)	5	95.6	6	98.6	8	94.1	19	95.7
	Se(VI)	-	-	1	100	-	-	1	100
C(IV)*	Se(VI)	-	-	4	70.8	-	-	4	70.8
Cr(VI)	As(V)	4	12.5	2	51.4	-	-	6	25.4
	N(V)	-	-	4	86.5	4	70.6	8	78.5
	S(VI)	1	61.3	3	66.2	4	56.9	8	60.9
	Si(IV)	1	96.9	2	58.2	-	-	3	71.1
P(V)	As(V)	8	63.8	6	68.9	5	65.2	19	65.8
	C(IV)	-	-	-	-	3	96.8	3	96.8
	Cr(VI)	4	95.9	-	-	-	-	4	95.9
	S(VI)	10	97.6	1	98.7	-	-	11	97.7
S(VI)	C(IV)*	1	107.7	6	130.7	-	-	7	127.4
	P(V)	9	12.3	3	4.3	-	-	12	10.3
Se(VI)	C(IV)	-	-	4	145.1	-	-	4	145.1
	S(VI)	-	-	3	85.8	-	-	3	85.8
	Si(IV)	4	104.4	4	101.3	5	85.4	13	96.1
Si(IV)	As(III)	4	91.7	2	93.4	3	105.5	9	96.7
	Cr(VI)	1	41.5	2	85.0	-	-	3	70.5
As(III)	Oxalate	1	88.4	1	92.2	-	-	2	90.3
	Malate	1	75.3	1	86.6	-	-	2	80.9
	Tartarate	1	73.6	1	86.4	-	-	2	80.0
	Citrate	1	72.3	1	80.3	-	-	2	76.3
As(V)	Oxalate	-	-	1	94.7	-	-	1	94.7
	Malate	-	-	1	88.1	-	-	1	88.1
	Tartarate	-	-	1	87.0	-	-	1	87.0
Cr(VI)	Oxalate	3	94.4	2	91.5	1	134.5	6	100.1
S(VI)	Acetate	6	93.3	3	61.2	-	-	9	82.6
	Formate	-	-	2	148.3	-	-	2	148.3
	Oxalate	4	44.6	-	-	-	-	4	44.6
Se(VI)	Acetate	1	96.5	3	162.6	-	-	4	146.1
P(V)	Citrate	5	82.7	-	-	-	-	5	82.7

significant  $CE$  was observed, whereas a negative  $CE_{As(V),Cr(VI)}$  suggested cosorption or precipitation at pH 7.8 . Youngran et al. (2007) determined  $RSP_{As(V)/Se(VI)}$  to be 91.4 % for  $As(V)=200 \mu\text{g L}^{-1}$  and  $Se(VI)=100 \mu\text{g L}^{-1}$ . According to this result, chromate and selenate showed no significant effect on the sorption of  $As(V)$ .

Nitrate and phosphate are the most common limiting nutrients for crop production, and thus, excessive amounts of these ions are introduced anthropogenically into the soil environment (Andrew et al., 2000; Riley et al., 2001; Zamparas and Zacharias, 2014). Competition among nutrients that are easily desorbed from the soil and their resulting discharge causes eutrophication in the water system (Arai and Sparks, 2007; Yin et al., 2013). Youngran et al. (2007) studied the competition of nitrate on hematite at pH 6 and found that  $RSP_{As(V)/N(V)}$  and  $RSP_{As(V)/P(V)}$  were 97 and 42 %, respectively, at unequal concentrations. Frau et al. (2010) determined  $RSP_{As(V)/P(V)}$  to be 13-28 and 19-23 %, respectively, at initial concentrations of 10 and 100 mM and pH 4-10. Zhu et al. (2011) also found  $RSP_{As(V)/P(V)}$  to be 58.9 % for pH 6. An interesting trend was observed: increasing pH led to an increase in  $RSP_{As(V)/P(V)}$  at a 10 mM initial concentration and *vice versa* at a 100 mM initial concentration. Hongshao and Stanforth (2001) determined  $CSR_{As(V)/P(V)}$  to be 0.95 and 1.02 at pH 3 and 5, respectively, whereas Jain and Loeppert (2000) determined  $CSR_{As(V)/P(V)}$  to be 0.7-1.0. Both studies confirmed that  $CSR_{As(V)/P(V)}$  increased with increasing pH. However, we also found a contrary result, in which  $CSR_{As(V)/P(V)}$  decreased with increasing pH. Gao and Mucci (2001) determined  $CSR_{As(V)/P(V)}$  and  $CE_{As(V),P(V)}$  to be 0.9-1.8 and 0.32-0.45, respectively, at pH 3-8.7. Violante and Pigna (2002) determined  $CSR_{As(V)/P(V)}$  and  $CE_{As(V),P(V)}$  to be

1.0-1.2 and 0-0.02 at pH 4-7, respectively. Manning and Goldberg (1996) found  $CSR_{As(V)/P(V)}$  and  $CE_{As(V),P(V)}$  to be 0.88-1.18 and 0.15-0.36, respectively, at pH 2.5-11.2.  $CSR_{As(V)/P(V)}$  and  $CE_{As(V),P(V)}$  increased with pH, and the latter result contradicts the results of the study by Jain and Loeppert (2000). No dominant sorption was found between arsenate and phosphate based on  $CSR_{As(V)/P(V)}$ , which ranged from 0.85 to 1.80 with an average value of 1.08, whereas the average value of  $CE_{As(V),P(V)}$  of 0.33 confirmed that arsenate and phosphate competed for the sorption sites of iron (hydr)oxide.

For arsenate, the *RSP* sequence for the entire pH range was as follows: Cr(VI)>S(VI)>As(III)>P(V). I also observed a promotive effect between arsenate and chromate at the circumneutral pH (Table 2-5). In contrast to the *RSP* sequence of arsenite, phosphate led to more desorption of arsenate than of arsenite, and  $RSP_{As(V)/As(III)}$  and  $RSP_{As(V)/As(III)}$  gradually decreased with increasing pH. I observed a decrease in  $RSP_{As(III)/As(V)}$  above and an inverse relationship between the *RSP* values of arsenate and arsenite was a reasonable conclusion. I also showed the effect of SL on *CE* (Fig. 2-3b). An increase in SL caused desorption of both oxyanions.

#### 2.4.1.3. Competition of carbonate

Rahnemaie et al. (2007) determined  $RSP_{P(V)/C(IV)}$  to be 96-97 % at pH 9.1-12.2 with initial concentrations of  $PO_4^{3-}=0.4$  mM and  $CO_3^{2-}=200$  mM. This result showed that carbonate did not affect phosphate sorption even at large differences in concentration. Wijnja and Schulthess (2001) determined  $RSP_{C(IV)/Se(VI)}$  to be 57-91 % at  $SeO_4^{3-}=CO_3^{2-}=1$  mM with pH 5-8, whereas  $RSP_{Se(VI)/C(IV)}$  was 99-187 % at  $SeO_4^{3-}=CO_3^{2-}=0.2$  mM and pH 6-8. The promotive effect was observed in  $RSP_{Se(VI)/C(IV)}$

and was caused by the generation of extra sorption sites by adsorbed  $\text{CO}_3^{2-}$ . A similar promotive effect was also observed in sulfate, and  $RSP_{S(VI)/C(IV)}$  was 77-195 % at pH 5.7-7.5.

#### 2.4.1.4. Competition of chromate

Meena and Arai (2016) determined  $RSP_{Cr(VI)/S(VI)}$  and  $RSP_{Cr(VI)/N(V)}$  to be 28-77 % and 18-106 %, respectively, at pH 4-12. The minimum value of  $RSP_{Cr(VI)/S(VI)}$  was at pH 11.3, and the maximum value of  $RSP_{Cr(VI)/N(V)}$  was at pH 9.2. Boukemara et al. (2016) found  $RSP_{P(V)/Cr(VI)}$  and  $RSP_{P(V)/S(VI)}$  to be 93-98 % and 97-101 %, respectively, at pH 2.6-5.9. These results indirectly implied that neither chromate nor sulfate showed a significant effect on phosphate. Garman et al. (2004) determined  $CSR_{Cr(VI)/Si(V)}$  and  $CE_{Cr(VI),Si(V)}$  to be 0.2-3.7 and 0.23-0.24, respectively, at pH 4-8.  $CSR_{Cr(VI)/Si(V)}$  was highest at pH 4 and lowest at pH 8. These results indicated that the pH dramatically influenced the competitive sorption between chromate and silicate, whereas the sorbed concentration under competition remained relatively constant. Chromate was less dominant against nitrate and sulfate than arsenite, arsenate and phosphate. Chromate did not compete with phosphate, but competition with silicate was clearly observed. For chromate, the  $RSP$  sequence for circumneutral pH was as follows:  $N(V) > Si(IV) > S(VI) > As(V)$  (Table 2-5). The effect of pH is difficult to address, but the  $RSP$  sequence showed a decreasing trend with increasing pH for nitrate, sulfate and silicate and *vice versa* for arsenate.

#### 2.4.1.5 Competition of phosphate or selenate

Two studies confirmed the competitive sorption between phosphate and

sulfate on goethite. Geelhoed et al. (1997) computed  $CSR_{P(V)/S(V)}$  and  $CE_{P(V)/S(V)}$  as 4.8-8.8 and 0.19-0.39 at pH 2.4-6.5, respectively. Boukhalifa (2010) determined  $RSP_{S(V)/P(V)}$  to be 2.7-22 % at pH 3.2-7.1, and the maximum and minimum were observed at pH 3.6 and 7.1, respectively. Both studies implied that sulfate exerted no competitive effect on phosphate. The sequence of  $RSP$  was as follows: C(IV)=Cr(VI)=S(VI)>As(V). The missing data hindered the interpretation of the results, but the data clearly showed that carbonate, chromate and sulfate caused no desorption of phosphate, whereas competition from arsenate led to the desorption of phosphate.

Three studies showed the competitive sorption of selenate with sulfate or silicate. Wijnja and Schulthess (2000) found  $RSP_{Se(VI)/S(V)}$  on goethite to be 67-98 % at pH 6-6.7. Jordan et al. (2009a) determined  $RSP_{Se(VI)/Si(V)}$  on magnetite to be 53-113 % at pH 4-9, and there was slightly enhanced sorption at low pH and a dramatic decrease at high pH. Jordan et al. (2009b) determined  $RSP_{Se(VI)/Si(V)}$  on hematite to be 84-100 % at pH 4-9; there was no enhanced sorption, and selenate competed only weakly with silicate at high pH. A dramatic change was observed in a narrow range around pH 6. Based on this observation, I concluded that selenate is dominant in competition with sulfate and silicate.

#### **2.4.2. Competitive sorption between oxyanions and organic acids**

As described above, organic acids are exuded by plant roots, and the resulting competition leads to changes in the bioavailability of ions (Dakora and Phillips, 2002). Six papers discussed competitive sorption between oxyanions and

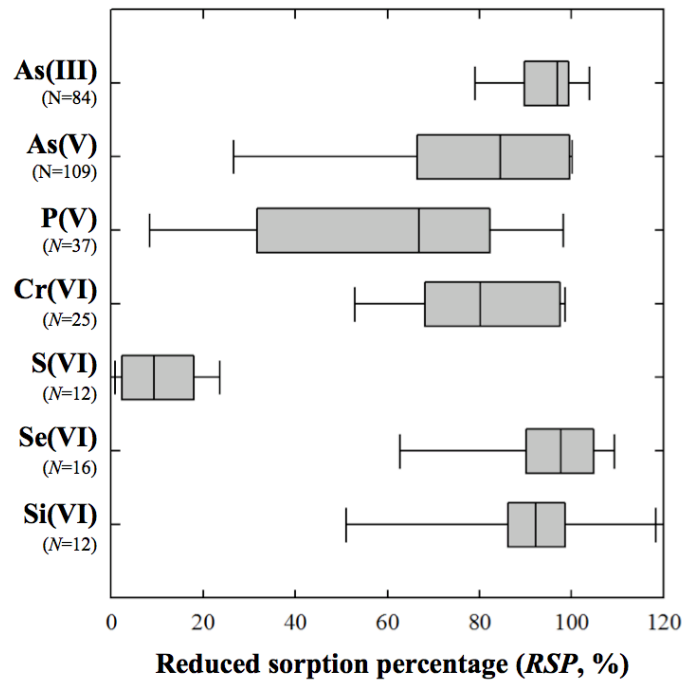
organic acids. Yang et al. (2016) studied the competitive sorption between aspartate and phosphate, and the ATR-FTIR spectra at pH 3 and 6 showed that phosphate dominates the sorption; however, no quantitative result was described. Wijnja and Schulthess (2002) examined the competitive sorption among selenate, sulfate, acetate (Ac) and formate (Fm). They found that  $RSP_{Se(VI)/Ac}$ ,  $RSP_{S(VI)/Fm}$  and  $RSP_{S(VI)/Ac}$  on goethite were 97-171, 137-160 and 98-141 %, respectively, at pH 5.6-7. The increase in  $RSP$  was explained by a promotive effect between the oxyanion and organic acids. Boukhalfa (2010) studied the competitive sorption of sulfate with acetate or oxalate (Ox) and found that  $RSP_{S(VI)/Ac}$  and  $RSP_{S(VI)/ox}$  were 19-103 and 0.5-62 %, respectively, at pH 3.4-7.3. The  $RSP$  dramatically decreased with increasing pH, and acetate showed no effect on sulfate sorption below pH 4 but acetate dominated the sorption sites, outcompeting sulfate, above pH 6.8. Oxalate showed an effect on sulfate at pH 3.2-4.3 and completely occupied the sorption sites above pH 4.8. The pH at which a sudden decrease in  $RSP_{S(VI)/Ox}$  occurred was near the  $pKa_2$  (4.2) of oxalate. Mesuere and Fish (1992) studied the competitive sorption of chromate with oxalate and found that  $CSR_{Cr(VI)/Ox}$  and  $CE_{Cr(VI),Ox}$  were 1.9-7.7 and -0.24-0.26, respectively, at pH 4 - 9.  $CSR_{Cr(VI),Ox}$  reached a maximum at pH 7.3.  $CE_{Cr(VI),Ox}$  was 0.25 at pH 4 but gradually decreased to -0.24 with increasing pH. Geelhoed et al. (1998) determined  $CSR_{P(V)/Ct}$  and  $CE_{P(V)/Ct}$  on goethite to be 3.4-6.0 and 0.35-0.43, respectively, at pH 2.5-5.6.  $CSR_{P(V)/Ct}$  reached a minimum at pH 3.7, whereas  $CE_{P(V)/Ct}$  gradually increased with increasing pH. Zhu et al. (2011) extensively studied the competitive sorption of arsenite and arsenate with oxalate, malate (Ml), tartrate (Tt) and citrate at circumneutral pH on ferrihydrite.  $RSP_{As(III)/Ox}$ ,

$RSP_{As(III)/Ml}$ ,  $RSP_{As(III)/Ti}$  and  $RSP_{As(III)/Cl}$  were 90.3, 80.9, 80.0 and 76.3 at pH 5 and 6, while  $RSP_{As(V)/Ox}$ ,  $RSP_{As(V)/Ml}$  and  $RSP_{As(V)/Ti}$  were 94.7, 88.1 and 87.0, respectively. Their results revealed that the increased concentration of organic acids and sequential addition of the solute cause changes in  $RSP$ , which implied that the relative concentration of solute and the sequence of addition affect competitive sorption. The  $CSR$  values of arsenite and arsenate with organic acids ranged from 72 to 94.7 %, indicating that the sorption of arsenite and arsenate was predominant over that of the organic acids. Not enough data was collected to interpret the competitive sorption between oxyanions and organic acids; thus, the results cannot be appropriately explained. However, we confirmed the occurrence of the promotive effect, the sudden desorption of oxyanions at certain pH values and a  $CE$  with increasing pH.

#### **2.4.3. Selectivity sequence using reduced sorption percentage**

A boxplot of  $RSP$  categorized by oxyanion is shown in Fig. 2-5. The average value was calculated using the  $RSP$  between a specific oxyanion and all competitors to describe the selectivity sequence at any pH. I could obtain a more meaningful result using  $CSR$  or  $CE$ , but the amount of data was not sufficient; thus, the  $RSP$  was employed. The sequence of the average  $RSP$  was as follows:  $As(III) > Si(IV) > Se(VI) > As(V) > P(V) > Cr(VI) > S(VI)$ . The collected data were not sufficient to calculate the sequence, because there were significant differences in the number of data points per oxyanion, in the conditions of the sorption experiments and in the concentrations of oxyanions introduced, but the results were meaningful

**Fig. 2-5** Box plot of the reduced sorption percentage (*RSP*, %) of each oxyanion with all other oxyanions. The lower (Q1) and upper (Q3) quartiles represent observations outside the 9 –91 percentile range. The line in the box shows the mean.



as a first trial of extracting a comparison of competitive sorption from experimental data under various conditions. Arsenate, arsenite, phosphate and chromate had 4-5 oxyanion competitors with 25-109 data points, whereas sulfate, selenate and silicate had only 2-3 oxyanion competitors with 12-16 data points. The significantly greater amount of data for certain competitors would suggest a more accurate affinity sequence. Previous studies identified the selectivity sequence on activated alumina as  $\text{OH}^- > \text{H}_2\text{AsO}_4^- > \text{Si}(\text{OH})_3^- > \text{F}^- > \text{HSeO}_3^- > \text{SO}_4^- > \text{CrO}_4^- > \text{HCO}_3^- > \text{Cl}^- > \text{NO}_3^- > \text{Br}^- > \text{I}^-$  (Clifford et al., 1986). Except for sulfate, the sequence of this review and the previous studies are significantly correlated; thus, I concluded that the present approach could possibly illuminate the selectivity sequence using the published literature, but the data were nonetheless greatly lacking.

#### **2.4.4. Surface site density from crystal structures of iron (hydr)oxides**

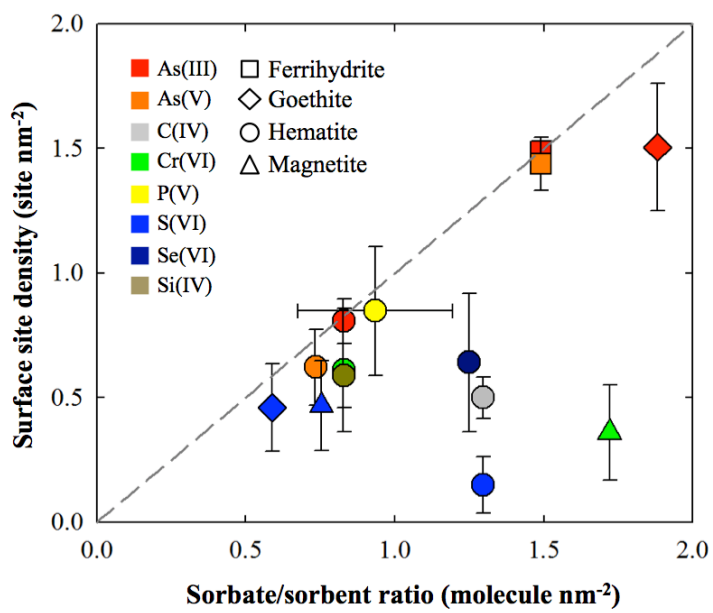
Fig. 2-6 shows the scatter plot of the *SL* and surface site density from the single sorption experiment on the oxyanions to describe the sorption differences caused by the crystal structure of the iron (hydr)oxides. To diminish the *SL* effect, I extracted *SL* data with 0.5-2.0 sites  $\text{nm}^{-2}$ , which was the surface site density when most of the sorbate was sorbed (>95 %). As discussed above, the pH, background ion, initial concentration and type of oxyanion and iron (hydr)oxide all affected the sorption; thus, the surface site density cannot be described accurately by the type of iron (hydr)oxide alone, but I could assume that the crystal structure affected the surface site density. Goethite was employed for 7 oxyanions, whereas ferrihydrite, hematite and magnetite were used for only 2 oxyanions. The dashed gray line

indicates the 1:1 line between SL and the surface site density, and positions close to the line indicate that the sorption percentage was near 100 %. Most of the data are near the line, which indicates that the differences in surface site density were caused by insufficient oxyanion input for saturation, but we found distinguishable patterns in carbonate, sulfate and selenate on goethite, arsenite on hematite and chromate on magnetite. For oxyanions with low selectivity, a sequence such as carbonate and sulfate would be explained by competition with background chloride and nitrate ions, but chromate, selenate and arsenite showed relatively high selectivity in both previous and present studies. This phenomenon could be caused by the physiochemical characteristics of the iron (hydr)oxides; thus, I need further studies to examine this effect.

## **2.5. CONCLUSIONS**

Iron (hydr)oxide is one of the key sorbents for oxyanions in the soil environment. The seasonal and spatial transformation of iron (hydr)oxide determines the bioavailability and leachability of oxyanions and ultimately influences the geocycling of the Earth. The structural configurations of oxyanion were clearly confirmed to be dependent on environmental factors, such as the crystal structure of iron (hydr)oxide, surface area, type of oxyanions, concentration, competing ions, pH and redox potential, and the sorption percentage is also linked to environmental factors. The reciprocal interactions among the environmental factors hamper estimation of the dynamics of oxyanions, which cause severe

**Fig. 2-6** Scatter plot between surface loading (molecule nm<sup>-2</sup>) and surface site density (site nm<sup>-2</sup>) from the single batch experiment. The color and shape of the symbols indicate the oxyanion and iron oxide, respectively. The gray dashed line shows the 1:1 line between the SL and the surface site density, where sorption percent was 100 %.



environmental problems such as eutrophication and metal poisoning worldwide.

For a better understanding of oxyanion behavior in the rhizosphere, the relationship between the structural configuration and sequence of *RSP* as result of competitive sorption was observed. Structures with higher denticity were higher in the selectivity sequence obtained using *RSP*. SL was observed to affect the structural configuration and *CE*; a higher SL led to a lower-denticity structure with a higher aqueous concentration caused by desorption. The organic acids not only compete with oxyanions but also can cause a promotive effect, dissolution and precipitation by forming IS complexes on the iron (hydr)oxide. The selectivity sequence using *RSP* was as follows:

As(III)>Si(IV)>Se(VI)>As(V)>P(V)>Cr(VI)>S(VI), and I observed the possibility of differences between the iron (hydr)oxides; however, the *RSP* sequence was clearly not theoretically valid and it was developed only to compare the competitive sorption results from various experimental condition.

Based on previous studies and our observations, I concluded that a change in environmental conditions leads to transformation of iron (hydr)oxides and of the structural configuration of the oxyanions on the iron (hydr)oxides, and both results contribute to the dynamics of oxyanions in the soil system. As a result, the availability and leachability of oxyanions could be altered. Plants use root exudation to address this alteration; organic molecules exude into the rhizosphere and subsequently affect the environmental condition, and this extremely complex and connected web of reactions determines the behavior of oxyanions in the soil system. Developments in analytical and theoretical chemistry have enabled us to see the

structural configuration of the complex at the atomic level, but many questions still remain. The following questions need to be answered to address environmental problems and to understand oxyanion behavior.

1. Based on our observations, the SL is the critical factor for the structural configuration of the complex. However, studies using EXAFS employ a paste or freeze-dried sample for examination. The sample pretreatment effect should be carefully identified to determine the actual structural configuration of the complex.

2. Several studies identified the MM complex of arsenate and phosphate using various methodologies, but the environmental conditions of the experiments were not sufficiently consistent to obtain a better understanding. Any undiscovered factors controlling the structural configuration of the MM complex should be determined. If the structural configuration could be changed on demand, this ability would be applicable to controlling the environmental problems caused by oxyanions.

3. Recent developments in computational chemistry lead us to interpret experimental data through comparison with theoretical calculations. This approach is applicable only to small molecular clusters for now, but advances in computation technology will enable us to address complex clusters, and we should accumulate data for better computation and interpretation.

4. The characteristics of laboratory-synthesized iron (hydr)oxides differed greatly case by case, which made interpretation of the results difficult. In addition, the available data were not sufficient to reach statistical conclusions. More data, a standard method and standard materials are essential for achieving compatibility and credibility of the experiments.

In ancient agriculture, limited oxyanions were a weighty matter, but we are now concerned with excessive abundance of oxyanions. The industrialization of cultivation brought us prosperity, but this prosperity is accompanied by severe problems. We should be prepared to solve these problems by understanding the dynamics of oxyanions and the interactions among plants, oxyanions and soil components.

## References

- Acelas, N.Y., Mejia, S.M., Mondragón, F., Flórez, E., 2013. Density functional theory characterization of phosphate and sulfate adsorption on Fe-(hydr)oxide: Reactivity, pH effect, estimation of Gibbs free energies, and topological analysis of hydrogen bonds. *Comput. Theor. Chem.* 1005, 16–24. doi:10.1016/j.comptc.2012.11.002
- Adegoke, H.I., Adekola, F.A., Fatoki, O.S., Ximba, B.J., 2013. Sorptive Interaction of Oxyanions with Iron Oxides : A Review. *Pol. J. Environ. Stud.* 22, 7–24.
- Andrew, S., Bob, F., Paul, W., 2000. Practical and innovative measures for the control of agricultural phosphorus losses to water. *J. Environ. Qual.* 29, 1–9.
- Anschutz, A.J., Penn, R.L., 2005. Reduction of crystalline iron(III) oxyhydroxides using hydroquinone: Influence of phase and particle size. *Geochem. Trans.* 6, 60–66. doi:10.1063/1.2037887
- Antelo, J., Avena, M., Fiol, S., López, R., Arce, F., 2005. Effects of pH and ionic strength on the adsorption of phosphate and arsenate at the goethite-water interface. *J. Colloid Interface Sci.* 285, 476–486. doi:10.1016/j.jcis.2004.12.032
- Appelo, C.A.J., Van Der Weiden, M.J.J., Tournassat, C., Charlet, L., 2002. Surface complexation of ferrous iron and carbonate on ferrihydrite and the mobilization of arsenic. *Environ. Sci. Technol.* 36, 3096–3103. doi:10.1021/es010130n
- Arai, Y., Sparks, D., 2007. Phosphate Reaction Dynamics in Soils and Soil Components: A Multiscale Approach. *Adv. Agron.* 94, 135–179. doi:10.1016/S0065-2113(06)94003-6
- Arai, Y., Sparks, D.L., 2001. ATR–FTIR Spectroscopic Investigation on Phosphate Adsorption Mechanisms at the Ferrihydrite–Water Interface. *J. Colloid Interface Sci.* 241, 317–326. doi:10.1006/jcis.2001.7773
- Auffan, M., Rose, J., Proux, O., Borschneck, D., Masion, A., Chaurand, P., Hazemann, J.L., Chaneac, C., Jolivet, J.P., Wiesner, M.R., Van Geen, A., Bottero, J.Y., 2008. Enhanced adsorption of arsenic onto maghemite nanoparticles: As(III) as a probe of the surface structure and heterogeneity. *Langmuir* 24, 3215–3222. doi:10.1021/la702998x
- Aulakh, M.S., Wassmann, R., Bueno, C., Kreuzwieser, J., Rennenberg, H., 2001. Characterization of Root Exudates at Different Growth Stages of Ten Rice (*Oryza sativa* L.) Cultivars. *Plant Biol.* 3, 139–148. doi:10.1055/s-2001-12905
- Babula, P., Adam, V., Opatrilova, R., Zehnalek, J., Havel, L., Kizek, R., 2008. Uncommon heavy metals, metalloids and their plant toxicity: A review. *Environ. Chem. Lett.* 6, 189–213. doi:10.1007/s10311-008-0159-9
- Baetz, U., Martinoia, E., 2014. Root exudates: the hidden part of plant defense. *Trends Plant Sci.* 19, 90–8. doi:10.1016/j.tplants.2013.11.006
- Bais, H.P., Weir, T.L., Perry, L.G., Gilroy, S., Vivanco, J.M., 2006. The role of root exudates in rhizosphere interactions with plants and other organisms. *Annu. Rev. Plant Biol.* 57, 233–266. doi:10.1146/annurev.arplant.57.032905.105159
- Bargar, J.R., Kubicki, J.D., Reitmeyer, R., Davis, J.A., 2005. ATR-FTIR spectroscopic characterization of coexisting carbonate surface complexes on hematite. *Geochim. Cosmochim. Acta* 69, 1527–1542. doi:10.1016/j.gca.2004.08.002
- Bertin, C., Yang, X., Weston, L.A., 2003. The role of root exudates and allelochemicals in the rhizosphere. *Plant Soil* 256, 67–83. doi:10.1023/A:1026290508166
- Bolanz, R.M., Majzlan, J., Ackermann, S., 2011. The effect of Sb(V) on the transformation of ferrihydrite to goethite, hematite, and ferrihydrite. *Mineral. Mag.* 75, 546–.
- Borer, P., Hug, S.J., 2014. Photo-redox reactions of dicarboxylates and  $\alpha$ -hydroxydicarboxylates at the surface of Fe(III)(hydr)oxides followed with in situ

- ATR-FTIR spectroscopy. *J. Colloid Interface Sci.* 416, 44–53. doi:10.1016/j.jcis.2013.10.030
- Boukhalifa, L., Boukhalifa, C., Reinert, L., Duclaux, L., 2016. Characterization of phosphate adsorption on goethite macroscopic and spectroscopic analyses. *J. Mater. Environ. Sci.* 7, 2541–2550.
- Boukhalifa, C., 2010. Sulfate removal from aqueous solutions by hydrous iron oxide in the presence of heavy metals and competitive anions. Macroscopic and spectroscopic analyses. *Desalination* 250, 428–432. doi:10.1016/j.desal.2009.09.070
- Brechbühl, Y., Christl, I., 2012. Competitive sorption of carbonate and arsenic to hematite: Combined ATR-FTIR and batch experiments. *J. Colloid Interface Sci.* 377, 313–321. doi:10.1016/j.jcis.2012.03.025
- Bürger, A., Magdans, U., Gies, H., 2013. Adsorption of amino acids on the magnetite-(111)-surface: A force field study. *J. Mol. Model.* 19, 851–857. doi:10.1007/s00894-012-1606-x
- Catalano, J.G., Park, C., Fenter, P., Zhang, Z., 2008. Simultaneous inner- and outer-sphere arsenate adsorption on corundum and hematite. *Geochim. Cosmochim. Acta* 72, 1986–2004. doi:10.1016/j.gca.2008.02.013
- Catalano, J.G., Zhang, Z., Fenter, P., Bedzyk, M.J., 2006. Inner-sphere adsorption geometry of Se(IV) at the hematite (100)-water interface. *J. Colloid Interface Sci.* 297, 665–671. doi:10.1016/j.jcis.2005.11.026
- Catalano, J.G., Zhang, Z., Park, C., Fenter, P., Bedzyk, M.J., 2007. Bridging arsenate surface complexes on the hematite (0 1 2) surface. *Geochim. Cosmochim. Acta* 71, 1883–1897. doi:10.1016/j.gca.2007.01.015
- Chen, R.F., Shen, R.F., Gu, P., Dong, X.Y., Du, C.W., Ma, J.F., 2006. Response of rice (*Oryza sativa*) with root surface iron plaque under aluminium stress. *Ann. Bot.* 98, 389–395. doi:10.1093/aob/mcl110
- Clifford, D., Subramonian, S., Sorg, T.J., 1986. Removing dissolved inorganic contaminants from water. *Environ. Sci. Technol.* 20, 1072–1080.
- Cornell, R.M., Schwertmann, U., 2003. *The iron oxides: structure, properties, reactions, occurrences, and uses.* Wiley-VCH.
- Cox, P.A., 1989. *The elements: their origin, abundance and distribution,* Oxford science publications. Oxford University Press.
- Cudennec, Y., Lecerf, A., 2006. The transformation of ferrihydrite into goethite or hematite, revisited. *J. Solid State Chem.* 179, 716–722. doi:10.1016/j.jssc.2005.11.030
- Cudennec, Y., Lecerf, A., 2005. Topotactic transformations of goethite and lepidocrocite into hematite and maghemite. *Solid State Sci.* 7, 520–529. doi:10.1016/j.solidstatesciences.2005.02.002
- Dakora, F.D., Phillips, D. a., 2002. Root exudates as mediators of mineral acquisition in low-nutrient environments. *Plant Soil* 245, 35–47. doi:10.1023/A:1020809400075
- Daou, T.J., Grenche, J.M., Thomas, F., Derory, a, Bernhardt, P., Legar, P., Pourroy, G., Legare, P., 2007. Phosphate Adsorption Properties of Magnetite-Based Nanoparticles Phosphate Adsorption Properties of Magnetite-Based Nanoparticles 19, 4494–4505. doi:10.1021/cm071046v
- Das, S., Jim Hendry, M., Essilfie-Dughan, J., 2013. Adsorption of selenate onto ferrihydrite, goethite, and lepidocrocite under neutral pH conditions. *Appl. Geochemistry* 28, 185–193. doi:10.1016/j.apgeochem.2012.10.026
- Dixit, S., Hering, J.G., 2003. Comparison of arsenic(V) and arsenic(III) sorption onto iron oxide minerals: Implications for arsenic mobility. *Environ. Sci. Technol.* 37, 4182–4189. doi:10.1021/es030309t

- Dowling, C.B., 2002. Geochemical study of arsenic release mechanisms in the Bengal Basin groundwater. *Water Resour. Res.* 38.
- Duc, M., Lefèvre, G., Fédoroff, M., 2006. Sorption of selenite ions on hematite. *J. Colloid Interface Sci.* 298, 556–563. doi:10.1016/j.jcis.2006.01.029
- Duckworth, O.W., Martin, S.T., 2001. Surface complexation and dissolution of hematite by C1-C6 dicarboxylic acids at pH = 5.0. *Geochim. Cosmochim. Acta* 65, 4289–4301. doi:10.1016/S0016-7037(01)00696-2
- Eggleston, C.M., Hug, S., Stumm, W., Sulzberger, B., Dos Santos Afonso, M., 1998. Surface Complexation of Sulfate by Hematite Surfaces: FTIR and STM Observations. *Geochim. Cosmochim. Acta* 62, 585–593. doi:10.1016/S0016-7037(97)00372-4
- Eick, M.J., Peak, J.D., Brady, W.D., 1999. The Effect of Oxyanions on the Oxalate-Promoted Dissolution of Goethite. *Soil Sci. Soc. Am. J.* 63, 1133–1141.
- Elzinga, E.J., Sparks, D.L., 2007. Phosphate adsorption onto hematite: An in situ ATR-FTIR investigation of the effects of pH and loading level on the mode of phosphate surface complexation. *J. Colloid Interface Sci.* 308, 53–70. doi:10.1016/j.jcis.2006.12.061
- Erbs, J.J., Berquó, T.S., Reinsch, B.C., Lowry, G. V., Banerjee, S.K., Penn, R.L., 2010. Reductive dissolution of arsenic-bearing ferrihydrite. *Geochim. Cosmochim. Acta* 74, 3382–3395. doi:10.1016/j.gca.2010.01.033
- Fakour, H., Lin, T., 2014. Effect of Humic Acid on As Redox Transformation and Kinetic Adsorption onto Iron Oxide Based Adsorbent ( IBA ). *Int. J. Environ. Res. Public Health* 11, 10710–10736. doi:10.3390/ijerph111010710
- Fan, J.X., Wang, Y.J., Liu, C., Wang, L.H., Yang, K., Zhou, D.M., Li, W., Sparks, D.L., 2014. Effect of iron oxide reductive dissolution on the transformation and immobilization of arsenic in soils: New insights from X-ray photoelectron and X-ray absorption spectroscopy. *J. Hazard. Mater.* 279, 212–219. doi:10.1016/j.jhazmat.2014.06.079
- Farquhar, M.L., Charnock, J.M., Livens, F.R., Vaughan, D.J., 2002. Mechanisms of arsenic uptake from aqueous solution by interaction with goethite, lepidocrocite, mackinawite, and pyrite: An X-ray absorption spectroscopy study. *Environ. Sci. Technol.* 36, 1757–1762. doi:10.1021/es010216g
- Farrell, J., 2017. Tridentate arsenate complexation with ferric hydroxide and its effect on the kinetics of arsenate adsorption and desorption. *Chemosphere* 184, 1209–1214. doi:10.1016/j.chemosphere.2017.06.099
- Fendorf, S., Eick, M.J., Grossl, P., Sparks, D.L., 1997. Arsenate and chromate retention mechanisms on goethite. 1. Surface structure. *Environ. Sci. Technol.* 31, 315–320. doi:10.1021/es950653t
- Ferrari, M., Mottola, L., Quaresima, V., 2004. Principles, techniques, and limitations of near infrared spectroscopy. *Can. J. Appl. Physiol.* 29, 463–487. doi:10.1139/h04-031
- Fine, P., Verosub, K.L., Singer, M.J., 1995. Pedogenic and lithogenic contributions to the magnetic susceptibility record of the Chinese loess/palaeosol sequence. *Geophys. J. Int.* 122, 97–107. doi:10.1111/j.1365-246X.1995.tb03539.x
- Frau, F., Addari, D., Atzei, D., Biddau, R., 2010. Influence of Major Anions on As ( V ) Adsorption by Synthetic 2-line Ferrihydrite . Kinetic Investigation and XPS Study of the Competitive Effect of Bicarbonate. *Water, Air, & Soil Pollut.* 205, 25–41. doi:10.1007/s11270-009-0054-4
- Fukushi, K., Aoyama, K., Yang, C., Kitadai, N., Nakashima, S., 2013. Surface complexation modeling for sulfate adsorption on ferrihydrite consistent with in situ infrared spectroscopic observations. *Appl. Geochemistry* 36, 92–103. doi:10.1016/j.apgeochem.2013.06.013

- Gao, Y., Mucci, A., 2001. Acid base reactions, phosphate and arsenate complexation, and their competitive adsorption at the surface of goethite in 0.7 M NaCl solution. *Geochim. Cosmochim. Acta* 65, 2361–2378. doi:10.1016/S0016-7037(01)00589-0
- Garman, S.M., Luxton, T.P., Eick, M.J., 2004. Kinetics of chromate adsorption on goethite in the presence of sorbed silicic acid. *J. Environ. Qual.* 33, 1703–1708. doi:10.2136/sssaj2002.0818
- Geelhoed, J.S., Hiemstra, T., Van Riemsdijk, W.H., 1998. Competitive interaction between phosphate and citrate on goethite. *Environ. Sci. Technol.* 32, 2119–2123. doi:10.1021/es970908y
- Geelhoed, J.S., Hiemstra, T., Van Riemsdijk, W.H., 1997. Phosphate and sulfate adsorption on goethite: Single anion and competitive adsorption. *Geochim. Cosmochim. Acta* 61, 2389–2396. doi:10.1016/S0016-7037(97)00096-3
- Geiss, C.E., Zanner, C.W., 2006. How abundant is pedogenic magnetite? Abundance and grain size estimates for loessic soil based on rock magnetic analyses. *J. Geophys. Res. Solid Earth* 111, 1–19. doi:10.1029/2006JB004564
- Georgiadis, M., Cai, Y., Solo-Gabriele, H.M., 2006. Extraction of arsenate and arsenite species from soils and sediments. *Environ. Pollut.* 141, 22–29. doi:10.1016/j.envpol.2005.08.028
- Gleyzes, C., Tellier, S., 2001. Arsenic characterisation in industrial soils by chemical extractions. *Environ. ...* 22, 27–38. doi:10.1080/09593332208618313
- Goh, K.H., Lim, T.T., 2010. Influences of co-existing species on the sorption of toxic oxyanions from aqueous solution by nanocrystalline Mg/Al layered double hydroxide. *J. Hazard. Mater.* 180, 401–408. doi:10.1016/j.jhazmat.2010.04.045
- Goldberg, S., 2013. Modeling Selenite Adsorption Envelopes on Oxides, Clay Minerals, and Soils using the Triple Layer Model. *Soil Sci. Soc. Am. J.* 77, 64–71. doi:10.2136/sssaj2012.0205
- Guo, Y., Hou, W., Liang, J., Liu, J., 2014. Sorbent concentration effect on adsorption of methyl orange on chitosan beads in aqueous solutions. *Chem. Res. Chinese Univ.* 30, 837–843. doi:10.1007/s40242-014-4042-x
- Haichar, F.E.Z., Santaella, C., Heulin, T., Achouak, W., 2014. Root exudates mediated interactions belowground. *Soil Biol. Biochem.* 77, 69–80. doi:10.1016/j.soilbio.2014.06.017
- Han, J., Ro, H.-M., 2018. Identification of Bernalite Transformation and Tridentate Arsenate Complex at Nano-goethite under Effects of Drying, pH and Surface Loading. *Sci. Rep.* 8, 8369. doi:10.1038/s41598-018-26808-4
- Hiemstra, T., Rahnemaie, R., Van Riemsdijk, W.H., 2004. Surface complexation of carbonate on goethite: IR spectroscopy, structure and charge distribution. *J. Colloid Interface Sci.* 278, 282–290. doi:10.1016/j.jcis.2004.06.014
- Hiemstra, T., Rietra, R.P.J.J., Riemsdijk, W.H. Van, 2007. Surface Complexation of Selenite on Goethite : MO / DFT Geometry and Charge Distribution. *Croat. Chem. ACTA* 80, 313–324.
- Hinkle, M.A.G., Wang, Z., Giammar, D.E., Catalano, J.G., 2015. Interaction of Fe(II) with phosphate and sulfate on iron oxide surfaces. *Geochim. Cosmochim. Acta* 158, 130–146. doi:10.1016/j.gca.2015.02.030
- Hongshao, Z., Stanforth, R., 2001. Competitive Adsorption of Phosphate and Arsenate on Goethite. *Environ. Sci. Technol.* 35, 4753–4757.
- Huang, Q., Yu, Y., Wang, Q., Luo, Z., Jiang, R., Li, H., 2015. Uptake kinetics and translocation of selenite and selenate as affected by iron plaque on root surfaces of rice seedlings. *Planta* 241, 907–916. doi:10.1007/s00425-014-2227-7

- Huang, X., Chaparro, J.M., Reardon, K.F., Zhang, R., Shen, Q., Vivanco, J.M., 2014. Rhizosphere interactions: root exudates, microbes, and microbial communities 1. *Botany* 275, 267–275.
- Hug, S.J., 1997. In Situ Fourier Transform Infrared Measurements of Sulfate Adsorption on Hematite in Aqueous Solutions. *J. Colloid Interface Sci.* 188, 415–422. doi:10.1006/jcis.1996.4755
- Hug, S.J., Bahnemann, D., 2006. Infrared spectra of oxalate, malonate and succinate adsorbed on the aqueous surface of rutile, anatase and lepidocrocite measured with in situ ATR-FTIR. *J. Electron Spectros. Relat. Phenomena* 150, 208–219. doi:10.1016/j.elspec.2005.05.006
- Hütsch, B.W., Augustin, J., Merbach, W., 2002. Plant rhizodeposition — an important source for carbon turnover in soils. *J Plant Nutr Soil Sci* 2624. doi:10.1002/1522-2624(200208)165
- Hwang, Y.S., Lenhart, J.J., 2008. Adsorption of C4-dicarboxylic acids at the hematite/water interface. *Langmuir* 24, 13934–13943. doi:10.1021/la801793p
- Hyun, S., Lee, L.S., 2008. Pentachlorophenol sorption by variable-charge soils in methanol-water mixture: pH effect at the low solvent volume fraction. *Chemosphere* 70, 503–10. doi:10.1016/j.chemosphere.2007.06.027
- Ilbert, M., Bonnefoy, V., 2013. Insight into the evolution of the iron oxidation pathways. *Biochim. Biophys. Acta - Bioenerg.* 1827, 161–175. doi:10.1016/j.bbabi.2012.10.001
- Iwasaki, T., Sato, N., Kosaka, K., Watano, S., Yanagida, T., Kawai, T., 2011. Direct transformation from goethite to magnetite nanoparticles by mechanochemical reduction. *J. Alloys Compd.* 509, 34–37. doi:10.1016/j.jallcom.2010.10.029
- Jain, A., Loeppert, R.H., 2000. Effect of competing anions on the adsorption of arsenate and arsenite by ferrihydrite. *J. Environ. Qual.* 29, 1422–1430. doi:10.2134/jeq2000.00472425002900050008x
- Jain, C., Ali, I., 2000. Arsenic: occurrence, toxicity and speciation techniques. *Water Res.* 34, 4304–4312.
- Johnson, D.L., 1971. Simultaneous Determination of Arsenate and Phosphate in Natural Waters. *Environ. Sci. Technol.* 5, 411–414. doi:10.1016/j.apmr.2010.12.011
- Johnson, M.G., McBride, M.B., 1989. Mineralogical and Chemical Characteristics of Adirondack Spodosols: Evidence for Para- and Noncrystalline Aluminosilicate Minerals. *Soil Sci. Soc. Am. J.* 53, 482. doi:10.2136/sssaj1989.03615995005300020030x
- Johnston, C.P., Chrysochoou, M., 2014. Mechanisms of chromate adsorption on hematite. *Geochim. Cosmochim. Acta* 138, 146–157. doi:10.1016/j.gca.2014.04.030
- Johnston, C.P., Chrysochoou, M., 2012. Investigation of chromate coordination on ferrihydrite by in situ ATR-FTIR spectroscopy and theoretical frequency calculations. *Environ. Sci. Technol.* 46, 5851–5858. doi:10.1021/es300660r
- Jolsterå, R., Gunneriusson, L., Forsling, W., 2010. Adsorption and surface complex modeling of silicates on maghemite in aqueous suspensions. *J. Colloid Interface Sci.* 342, 493–498. doi:10.1016/j.jcis.2009.10.080
- Jones, D.L., Nguyen, C., Finlay, R.D., 2009. Carbon flow in the rhizosphere: Carbon trading at the soil-root interface. *Plant Soil* 321, 5–33. doi:10.1007/s11104-009-9925-0
- Jönsson, J., Sherman, D.M., 2008. Sorption of As(III) and As(V) to siderite, green rust (fougerite) and magnetite: Implications for arsenic release in anoxic groundwaters. *Chem. Geol.* 255, 173–181. doi:10.1016/j.chemgeo.2008.06.036
- Jordan, N., Lomenech, C., Marmier, N., Giffaut, E., Ehrhardt, J.J., 2009a. Sorption of selenium(IV) onto magnetite in the presence of silicic acid. *J. Colloid Interface Sci.*

- 329, 17–23. doi:10.1016/j.jcis.2008.09.052
- Jordan, N., Marmier, N., Lomenech, C., Giffaut, E., Ehrhardt, J.J., 2009b. Competition between selenium (IV) and silicic acid on the hematite surface. *Chemosphere* 75, 129–134. doi:10.1016/j.chemosphere.2008.11.018
- Jordan, N., Ritter, a., Foerstendorf, H., Scheinost, a. C., Weiß, S., Heim, K., Grenzer, J., Mücklich, a., Reuther, H., 2013. Adsorption mechanism of selenium(VI) onto maghemite. *Geochim. Cosmochim. Acta* 103, 63–75. doi:10.1016/j.gca.2012.09.048
- Jordan, N., Ritter, A., Scheinost, A.C., Weiss, S., Schild, D., Hu, R., 2014. Selenium(IV) Uptake by Maghemite ( $\gamma$ -Fe<sub>2</sub>O<sub>3</sub>).
- Josefsson, I., Kunnus, K., Schreck, S., Föhlisch, A., De Groot, F., Wernet, P., Odelius, M., 2012. Ab initio calculations of X-ray spectra: Atomic multiplet and molecular orbital effects in a multiconfigurational scf approach to the L-edge spectra of transition metal complexes. *J. Phys. Chem. Lett.* 3, 3565–3570. doi:10.1021/jz301479j
- Kersten, M., Vlasova, N., 2009. Silicate adsorption by goethite at elevated temperatures. *Chem. Geol.* 262, 372–379. doi:10.1016/j.chemgeo.2009.02.002
- Khaodhiar, S., Azizian, M.F., Osathaphan, K., Nelson, P.O., 2000. Copper, chromium, and arsenic adsorption and equilibrium modeling in an iron-oxide-coated sand, background electrolyte system. *Water. Air. Soil Pollut.* 119, 105–120. doi:10.1023/A:1005109325539
- Khare, N., Martin, J.D., Hesterberg, D., 2007. Phosphate bonding configuration on ferrihydrite based on molecular orbital calculations and XANES fingerprinting. *Geochim. Cosmochim. Acta* 71, 4405–4415. doi:10.1016/j.gca.2007.07.008
- Kim, S.S., Min, J.H., Lee, J.K., Baik, M.H., Choi, J.W., Shin, H.S., 2012. Effects of pH and anions on the sorption of selenium ions onto magnetite. *J. Environ. Radioact.* 104, 1–6. doi:10.1016/j.jenvrad.2011.09.013
- Kögel-Knabner, I., Amelung, W., Cao, Z., Fiedler, S., Frenzel, P., Jahn, R., Kalbitz, K., Kölbl, A., Schloter, M., 2010. Biogeochemistry of paddy soils. *Geoderma* 157, 1–14. doi:10.1016/j.geoderma.2010.03.009
- Kubicki, J., Paul, K., Kabalan, L., Zhu, Q., 2012. ATR-FTIR and Density Functional Theory Study of the Structures, Energetics, and Vibrational Spectra of Phosphate Adsorbed onto Goethite. *Langmuir* 28, 14573–14587.
- Kubicki, J.D.J., Kwon, K.D., Paul, K.W., Sparks, D.L., 2007. Surface complex structures modelled with quantum chemical calculations: Carbonate, phosphate, sulphate, arsenate and arsenite. *Eur. J. Soil Sci.* 58, 932–944. doi:10.1111/j.1365-2389.2007.00931.x
- Lefevre, G., 2004. In situ Fourier-transform infrared spectroscopy studies of inorganic ions adsorption on metal oxides and hydroxides. *Adv. Colloid Interface Sci.* 107, 109–123. doi:10.1016/j.cis.2003.11.002
- Lefèvre, G., Fédoroff, M., 2006. Sorption of sulfate ions onto hematite studied by attenuated total reflection-infrared spectroscopy: Kinetics and competition with other ions. *Phys. Chem. Earth* 31, 499–504. doi:10.1016/j.pce.2006.04.001
- Lindegren, M., Loring, J.S., Persson, P., 2009. Molecular structures of citrate and tricarballoylate adsorbed on  $\alpha$ -FeOOH particles in aqueous suspensions. *Langmuir* 25, 10639–10647. doi:10.1021/la900852p
- Liu, C.H., Chuang, Y.H., Chen, T.Y., Tian, Y., Li, H., Wang, M.K., Zhang, W., 2015. Mechanism of Arsenic Adsorption on Magnetite Nanoparticles from Water: Thermodynamic and Spectroscopic Studies. *Environ. Sci. Technol.* 49, 7726–7734. doi:10.1021/acs.est.5b00381
- López-Arredondo, D.L., Leyva-González, M.A., González-Morales, S.I., López-Bucio, J.,

- Herrera-Estrella, L., 2014. Phosphate nutrition: improving low-phosphate tolerance in crops. *Annu. Rev. Plant Biol.* 65, 95–123. doi:10.1146/annurev-arplant-050213-035949
- Loring, J.S., Sandström, M.H., Norén, K., Persson, P., 2009. Rethinking arsenate coordination at the surface of goethite. *Chem. - A Eur. J.* 15, 5063–5072. doi:10.1002/chem.200900284
- Luengo, C., Brigante, M., Antelo, J., Avena, M., 2006. Kinetics of phosphate adsorption on goethite: Comparing batch adsorption and ATR-IR measurements. *J. Colloid Interface Sci.* 300, 511–518. doi:10.1016/j.jcis.2006.04.015
- Luengo, C. V., Castellani, N.J., Ferullo, R.M., 2015. Quantum chemical study on surface complex structures of phosphate on gibbsite. *Spectrochim. Acta Part A Mol. Biomol. Spectrosc.* doi:10.1016/j.saa.2015.03.013
- Luxton, T.P., Eick, M.J., Rimstidt, D.J., 2008. The role of silicate in the adsorption/desorption of arsenite on goethite. *Chem. Geol.* 252, 125–135. doi:10.1016/j.chemgeo.2008.01.022
- Luxton, T.P., Tadanier, C.J., Eick, M.J., 2006. Mobilization of Arsenite by Competitive Interaction with Silicic Acid. *Soil Sci. Soc. Am. J.* 70, 204–214. doi:10.2136/sssaj2005.0101
- MacHala, L., Tuček, J., Zbořil, R., 2011. Polymorphous transformations of nanometric iron(III) oxide: A review. *Chem. Mater.* 23, 3255–3272. doi:10.1021/cm200397g
- Machala, L., Zboril, R., Gedanken, A., 2007. Amorphous iron(III) oxide--a review. *J. Phys. Chem. B* 111, 4003–4018. doi:10.1021/jp064992s
- Mackay, A.L., 1960. Some aspects of the topochemistry of the iron oxides and hydroxides. *Proc. 4th. Int. Symp. React. Solids, Amsterdam.*
- Madejová, J., 2003. FTIR techniques in clay mineral studies. *Vib. Spectrosc.* 31, 1–10.
- Manceau, A., Charlet, L., 1994. The Mechanism of Selenate Adsorption on Goethite and Hydrrous Ferric Oxide. *J. Colloid Interface Sci.* 168, 87–93. doi:10.1006/jcis.1994.1396
- Manning, B.A., Fendorf, S.E., Goldberg, S., Goldberg, S., 1998. Surface Structures and Stability of Arsenic (III) on Goethite: Spectroscopic Evidence for Inner-Sphere Complexes Surface Structures and Stability of Arsenic (III) on Goethite: Spectroscopic Evidence for Inner-Sphere Complexes 2383–2388. doi:10.1021/es9802201
- Manning, B.A., Goldberg, S., 1996. Modeling Competitive Adsorption of Arsenate with Phosphate and Molybdate on Oxide Minerals. *Soil Sci. Soc. Am. J.* 60, 121. doi:10.2136/sssaj1996.03615995006000010020x
- Mansfeldt, T., 2004. Redox potential of bulk soil and soil solution concentration of nitrate, manganese, iron, and sulfate in two Gleysols. *J. Plant Nutr. Soil Sci.* 167, 7–16. doi:10.1002/jpln.200321204
- Mansour, C., Lefèvre, G., Pavageau, E.M., Catalette, H., Fédoroff, M., Zanna, S., 2009. Sorption of sulfate ions onto magnetite. *J. Colloid Interface Sci.* 331, 77–82. doi:10.1016/j.jcis.2008.11.009
- Martínez, M., Giménez, J., De Pablo, J., Rovira, M., Duro, L., 2006. Sorption of selenium(IV) and selenium(VI) onto magnetite. *Appl. Surf. Sci.* 252, 3767–3773. doi:10.1016/j.apsusc.2005.05.067
- Masscheleyn, P.P.H., Delaune, R.D., Patrick, W.H., 1991. Effect of redox potential and pH on arsenic speciation and solubility in a contaminated soil. *Environ. Sci. Technol.* 25, 1414–1419. doi:10.1021/es00020a008
- Meena, A.H., Arai, Y., 2016. Effects of common groundwater ions on chromate removal by

- magnetite: importance of chromate adsorption. *Geochem. Trans.* 1–13. doi:10.1186/s12932-016-0033-9
- Meharg, A. a. A., Hartley-Whitaker, J., Hartley-Whitaker, J., 2002. Arsenic uptake and metabolism in arsenic resistant and nonresistant plant species. *New Phytol.* 154, 29–43.
- Mesuere, K., Fish, W., 1992. Chromate and oxalate adsorption on goethite. 2. Surface complexation modelling of competitive adsorption. *Environ. Sci. Technol.* 26, 2365–2370.
- Michael Bolanz, R., Bl??ss, U., Ackermann, S., Ciobot??, V., R??sch, P., Tarcea, N., Popp, J., Majzlan, J., 2013. The effect of antimonate, arsenate, and phosphate on the transformation of ferrihydrite to goethite, hematite, feroxyhyte, and tripuhyite. *Clays Clay Miner.* 61, 11–25. doi:10.1346/CCMN.2013.0610102
- Mir, K. a., Rutter, A., Koch, I., Smith, P., Reimer, K.J., Poland, J.S., 2007. Extraction and speciation of arsenic in plants grown on arsenic contaminated soils. *Talanta* 72, 1507–1518. doi:10.1016/j.talanta.2007.01.068
- Mora, C., Tittensor, D.P., Adl, S., Simpson, A.G.B., Worm, B., 2011. How many species are there on earth and in the ocean? *PLoS Biol.* 9, 1–8. doi:10.1371/journal.pbio.1001127
- Morin, G., Ona-Nguema, G., Wang, Y., Menguy, N., Juillot, F., Proux, O., Guyot, F., Calas, G., Brown, G.E., 2008. Extended X-ray absorption fine structure analysis of arsenite and arsenate adsorption on maghemite. *Environ. Sci. Technol.* 42, 2361–2366. doi:10.1021/es072057s
- Mudunkotuwa, I. a, Minshid, A. Al, Grassian, V.H., 2014. ATR-FTIR spectroscopy as a tool to probe surface adsorption on nanoparticles at the liquid-solid interface in environmentally and biologically relevant media. *Analyst* 139, 870–81. doi:10.1039/c3an01684f
- Neupane, G., Donahoe, R.J., Arai, Y., 2014. Kinetics of competitive adsorption/desorption of arsenate and phosphate at the ferrihydrite-water interface. *Chem. Geol.* 368, 31–38. doi:10.1016/j.chemgeo.2013.12.020
- Newville, M., 2014. Fundamentals of XAFS. *Rev. Mineral. Geochemistry* 78, 33–74. doi:10.2138/rmg.2014.78.2
- Nilsson, N., Persson, P., Lövgren, L., Sjöberg, S., 1996. Competitive surface complexation of o-phthalate and phosphate on goethite ( $\alpha$ -FeOOH) particles. *Geochim. Cosmochim. Acta* 60, 4385–4395. doi:10.1016/S0016-7037(96)00258-X
- Norén, K., Persson, P., 2007. Adsorption of monocarboxylates at the water/goethite interface: The importance of hydrogen bonding. *Geochim. Cosmochim. Acta* 71, 5717–5730. doi:10.1016/j.gca.2007.04.037
- Ona-Nguema, G., Morin, G., Juillot, F., Calas, G., Brown, G.E., 2005. EXAFS analysis of arsenite adsorption onto two-line ferrihydrite, hematite, goethite, and lepidocrocite. *Environ. Sci. Technol.* 39, 9147–9155. doi:10.1021/es050889p
- Panias, D., Taxiarchou, M., Paspaliaris, I., Kontopoulos, a., 1996. Mechanisms of dissolution of iron oxides in aqueous oxalic acid solutions. *Hydrometallurgy* 42, 257–265. doi:10.1016/0304-386X(95)00104-O
- Pantsar-Kallio, M., Manninen, P.K.G., 1997. Speciation of mobile arsenic in soil samples as a function of pH. *Sci. Total Environ.* 204, 193–200.
- Peak, D., Sparks, D.L., 2002. Mechanisms of selenate adsorption on iron oxides and hydroxides. *Environ. Sci. Technol.* 36, 1460–1466. doi:10.1021/es0156643
- Persson, P., Axe, K., 2005. Adsorption of oxalate and malonate at the water-goethite interface: Molecular surface speciation from IR spectroscopy. *Geochim. Cosmochim. Acta* 69, 541–552. doi:10.1016/j.gca.2004.07.009
- Persson, P., Nilsson, N., Sjöberg, S., 1996. Structure and Bonding of Orthophosphate Ions at

- the Iron Oxide-Aqueous Interface. *J. Colloid Interface Sci.* 177, 263–275. doi:10.1006/jcis.1996.0030
- Petrovsk, E., Krop, V., Dekkers, M.J., Ambafiello, A., 1996. Transformation of Hematite to maghemite as observed by changed in magnetic parameters: Effects of mechanical activation? *Geophys. Res. Lett.* 23, 1477–1480.
- Rahnemaie, R., Hiemstra, T., van Riemsdijk, W.H., 2007. Carbonate adsorption on goethite in competition with phosphate. *J. Colloid Interface Sci.* 315, 415–425. doi:10.1016/j.jcis.2007.07.017
- Rahnemaie, R., Hiemstra, T., van Riemsdijk, W.H., 2006. Inner- and outer-sphere complexation of ions at the goethite-solution interface. *J. Colloid Interface Sci.* 297, 379–388. doi:10.1016/j.jcis.2005.11.003
- Randall, S.R., Sheerman, D.M., Ragnarsdottir, K.V., 2001. Sorption of As(V) on green rust (Fe4(II)Fe2(III)(OH)12SO4·3H2O) and lepidocrocite(-FeOOH): Surface complexes from EXAFS spectroscopy. *Geochim. Cosmochim. Acta* 65, 1015–1023.
- Reza, a. H.M.S., Jean, J.S., Lee, M.K., Liu, C.C., Bundschuh, J., Yang, H.J., Lee, J.F., Lee, Y.C., 2010. Implications of organic matter on arsenic mobilization into groundwater: Evidence from northwestern (Chapai-Nawabganj), central (Manikganj) and southeastern (Chandpur) Bangladesh. *Water Res.* 44, 5556–5574. doi:10.1016/j.watres.2010.09.004
- Riemsdijk, W.H. Van, Weng, L., Hiemstra, T., 2005. Ion - Colloid - Colloid Interactions.
- Riley, W., Ortiz-Monasterio, I., Matson, P., 2001. Nitrogen leaching and soil nitrate, nitrite, and ammonium levels under irrigated wheat in Northern Mexico. *Nutr. Cycl. ...* 61, 223–236.
- Roonasi, P., Holmgren, A., 2010. An ATR-FTIR study of carbonate sorption onto magnetite. *Surf. Interface Anal.* 42, 1118–1121. doi:10.1002/sia.3382
- Rosen, B.P., Liu, Z., 2009. Transport pathways for arsenic and selenium: A minireview. *Environ. Int.* 35, 512–515. doi:10.1016/j.envint.2008.07.023
- Schwertmann, U., 1993. Relations between iron oxides, soil color, and soil formation. *Proc. a Symp. Soil Color* 51–69. doi:10.2136/sssaspecpub31.c4
- Schwertmann, U., 1985. The Effect of Pedogenic Environments on Iron Oxide Minerals, in: Stewart, B.A. (Ed.), *Advances in Soil Science*. Springer New York, New York, NY, pp. 171–200. doi:10.1007/978-1-4612-5046-3\_5
- Schwertmann, U., Taylor, R.M., 1972. The transformation of lepidocrocite to goethite. *Clays Clay Miner.* 20, 151–158. doi:10.1346/CCMN.1972.0200307
- Scott, R. a., Yamashita, S., Taniguchi, K., Nomoto, S., Yamaguchi, T., Wakita, H., 1992. X-ray Absorption Spectroscopy. *X??Ray Spectrom.* 21, 91–97. doi:10.1002/xrs.1300210209
- Sharif, M.S.U., Davis, R.K., Steele, K.F., Kim, B., Hays, P.D., Kresse, T.M., Fazio, J.A., 2011. Surface complexation modeling for predicting solid phase arsenic concentrations in the sediments of the Mississippi River Valley alluvial aquifer, Arkansas, USA. *Appl. Geochemistry* 26, 496–504. doi:10.1016/j.apgeochem.2011.01.008
- Shaw, S., Pepper, S.E., Bryan, N.D., Livens, F.R., 2005. The kinetics and mechanisms of goethite and hematite crystallization under alkaline conditions, and in the presence of phosphate. *Am. Mineral.* 90, 1852–1860. doi:10.2138/am.2005.1757
- Sherman, D.M., Randall, S.R., 2003. Surface complexation of arsenic(V) to iron(III) (hydr)oxides: Structural mechanism from ab initio molecular geometries and EXAFS spectroscopy. *Geochim. Cosmochim. Acta* 67, 4223–4230. doi:10.1016/S0016-7037(03)00237-0

- Shi, Z., Krom, M.D., Bonneville, S., Baker, A.R., Bristow, C., Drake, N., Mann, G., Carslaw, K., McQuaid, J.B., Jickells, T., Benning, L.G., 2011. Influence of chemical weathering and aging of iron oxides on the potential iron solubility of Saharan dust during simulated atmospheric processing. *Global Biogeochem. Cycles* 25. doi:10.1029/2010GB003837
- Shi, Z., Li, F., Yao, S., 2010. Effect of small organic acid anions on the adsorption of phosphate anions onto synthetic goethite from aqueous solution. *Adsorpt. Sci. Technol.* 28, 885–893. doi:10.1260/0263-6174.28.10.885
- Smith, V.H., Joye, S.B., Howarth, R.W., 2006. Eutrophication of freshwater and marine ecosystems. *Limnol. Oceanogr.* 51, 351–355. doi:10.4319/lo.2006.51.1\_part\_2.0351
- Smith, V.H., Schindler, D.W., 2009. Eutrophication science: where do we go from here? *Trends Ecol. Evol.* 24, 201–7. doi:10.1016/j.tree.2008.11.009
- Sparks, D.L., 2003. *Environmental soil chemistry*. Academic Press.
- Sparks, D.L., 2000. New frontiers in elucidating the kinetics and mechanisms of metal and oxyanion sorption at the soil mineral/water interface. *J. Plant Nutr. Soil Sci.* 163, 563–570. doi:10.1002/1522-2624(200012)163:6<563::aid-jpln563>3.0.co;2-0
- Srivastava, D.N., Perkas, N., Gedanken, A., Felner, I., 2002. Sonochemical synthesis of mesoporous iron oxide and accounts of its magnetic and catalytic properties. *J. Phys. Chem. B* 106, 1878–1883. doi:10.1021/jp015532w
- Stachowicz, M., Hiemstra, T., van Riemsdijk, W.H., 2008. Multi-competitive interaction of As(III) and As(V) oxyanions with Ca<sup>2+</sup>, Mg<sup>2+</sup>, PO<sub>3</sub><sup>4-</sup>, and CO<sub>2</sub><sup>3-</sup> ions on goethite. *J. Colloid Interface Sci.* 320, 400–414. doi:10.1016/j.jcis.2008.01.007
- Stumm, W., Morgan, J.J., 1981. *Aquatic chemistry: an introduction emphasizing chemical equilibria in natural waters*. Wiley.
- Su, C., Suarez, D.L., 2000a. Selenate and Selenite Sorption on Iron Oxides. *Soil Sci. Soc. Am. J.* 64, 101. doi:10.2136/sssaj2000.641101x
- Su, C., Suarez, D.L., 2000b. Selenate and Selenite Sorption on Iron Oxides: An Infrared and Electrophoretic Study. *Soil Sci. Soc. Am. J.* 64, 101–111.
- Swaddle, T. wilson, Oltmann, P., 1980. Kinetics of the magnetite-maghemite-hematite transformation, with special reference to hydrothermal. *Can. J. Chem.* 58, 1763–1772.
- Swedlund, P.J., Miskelly, G.M., McQuillan, A.J., 2009. An attenuated total reflectance IR study of silicic acid adsorbed onto a ferric oxyhydroxide surface. *Geochim. Cosmochim. Acta* 73, 4199–4214. doi:10.1016/j.gca.2009.04.007
- Takahashil, T., Park, C.-Y., Nakajima, H., Sekiya, H., Toriyama, K., 1999. Ferric iron transformation in soils with rotation of irrigated rice-upland crops and effect on soil tillage properties. *Soil Sci. Plant Nutr.* 45, 163–173. doi:10.1080/00380768.1999.10409332
- Tejedor-Tejedor, M., Anderson, M., 1990. The protonation of phosphate on the surface of goethite as studied by CIR-FTIR and electrophoretic mobility. *Langmuir* 6, 602–611. doi:10.1021/la00093a015
- Templeton, D.M., Fujishiro, H., 2017. Terminology of elemental speciation – An IUPAC perspective. *Coord. Chem. Rev.* 352, 424–431. doi:10.1016/j.ccr.2017.02.002
- Timmons, D.R., Dylla, A.S., 1981. Nitrogen Leaching as Influenced by Nitrogen Management and Supplemental Irrigation Level. *J. Environ. Qual.* 10, 421–426.
- Tripathi, R.D., Srivastava, S., Mishra, S., Singh, N., Tuli, R., Gupta, D.K., Maathuis, F.J.M., 2007. Arsenic hazards: strategies for tolerance and remediation by plants. *Trends Biotechnol.* 25, 158–165. doi:10.1016/j.tibtech.2007.02.003
- Tu, S., Ma, L., Luongo, T., 2004. Root exudates and arsenic accumulation in arsenic hyperaccumulating *Pteris vittata* and non-hyperaccumulating *Nephrolepis exaltata*.

- Plant Soil 258, 9–19.
- Udo, S., Rochelle, M.C., 2008. Iron Oxides in the Laboratory. Preparation and Characterization, Wiley-vch.
- Vamerli, T., Bandiera, M., Mosca, G., 2010. Field crops for phytoremediation of metal-contaminated land. A review. *Environ. Chem. Lett.* 8, 1–17. doi:10.1007/s10311-009-0268-0
- Violante, A., Pigna, M., 2002. Competitive sorption of arsenate and phosphate on different clay minerals and soils. *Soil Sci. Soc. Am. J.* 66, 1788–1796. doi:10.2136/sssaj2002.1788
- Vodyanitskii, Y.N., 2010. Iron hydroxides in soils: A review of publications. *Eurasian Soil Sci.* 43, 1244–1254. doi:10.1134/S1064229310110074
- Wang, Y., He, Y., Zhang, H., Schroder, J., Li, C., Zhou, D., 2008. Phosphate Mobilization by Citric, Tartaric, and Oxalic Acids in a Clay Loam Ultisol. *Soil Sci. Soc. Am. J.* 72, 1263.
- Wang, Y., Morin, G., Ona-Nguema, G., Menguy, N., Juillot, F., Aubry, E., Guyot, F., Calas, G., Brown, G.E., 2008. Arsenite sorption at the magnetite-water interface during aqueous precipitation of magnetite: EXAFS evidence for a new arsenite surface complex. *Geochim. Cosmochim. Acta* 72, 2573–2586. doi:10.1016/j.gca.2008.03.011
- Waychunas, G. A., Rea, B. A., Fuller, C. C., Davis, J. A., 1993. Surface chemistry of ferrihydrite: Part 1. EXAFS studies on geometry of coprecipitated and adsorbed arsenate. *Geochim. Cosmochim. Acta* 57, 2251–2269. doi:10.1016/0016-7037(93)90567-G
- Weng, L., Van Riemsdijk, W.H., Hiemstra, T., 2012. Factors Controlling Phosphate Interaction with Iron Oxides. *J. Environ. Qual.* 41, 628–635. doi:10.2134/jeq2011.0250
- Wijnja, H., Schulthess, C.P., 2002. Effect of Carbonate on the Adsorption of Selenate and Sulfate on Goethite. *Soil Sci. Soc. Am. J.* 66, 1190–1197. doi:10.2136/sssaj2002.1190
- Wijnja, H., Schulthess, C.P., 2001. Carbonate Adsorption Mechanism on Goethite Studied with ATR – FTIR, DRIFT. and Proton Coadsorption Measurements. *Soil Sci. Soc. Am. J.* 65, 324–330.
- Wijnja, H., Schulthess, C.P.C., 2000. Vibrational Spectroscopy Study of Selenate and Sulfate Adsorption Mechanisms on Fe and Al (Hydr)oxide Surfaces. *J. Colloid Interface Sci.* 229, 286–297. doi:10.1006/jcis.2000.6960
- Williams, A.G.B., Scherer, M.M., 2004. Spectroscopic evidence for Fe(II)-Fe(III) electron transfer at the iron oxide-water interface. *Environ. Sci. Technol.* 38, 4782–4790. doi:10.1021/es049373g
- Yang, X., Roonasi, P., Holmgren, A., 2008. A study of sodium silicate in aqueous solution and sorbed by synthetic magnetite using in situ ATR-FTIR spectroscopy. *J. Colloid Interface Sci.* 328, 41–47. doi:10.1016/j.jcis.2008.08.061
- Yang, X., Roonasi, P., Jolsterå, R., Holmgren, A., 2009. Kinetics of silicate sorption on magnetite and maghemite: An in situ ATR-FTIR study. *Colloids Surf., A* 343, 24–29. doi:10.1016/j.colsurfa.2009.01.041
- Yang, Y., Wang, S., Xu, Y., Zheng, B., Liu, J., 2016. Molecular-Scale Study of Aspartate Adsorption on Goethite and Competition with Phosphate. *Environ. Sci. Technol.* 50, acs.est.5b05450. doi:10.1021/acs.est.5b05450
- Yee, N., Shaw, S., Benning, L.G., Nguyen, T.H., 2006. The rate of ferrihydrite transformation to goethite via the Fe(II) pathway. *Am. Mineral.* 91, 92–96. doi:10.2138/am.2006.1860
- Yin, H., Kong, M., Fan, C., 2013. Batch investigations on P immobilization from

- wastewaters and sediment using natural calcium rich sepiolite as a reactive material. *Water Res.* 47, 4247–4258. doi:10.1016/j.watres.2013.04.044
- Youngran, J., FAN, M., Van Leeuwen, J., Belczyk, J.F., 2007. Effect of competing solutes on arsenic(V) adsorption using iron and aluminum oxides. *J. Environ. Sci.* 19, 910–919. doi:10.1016/S1001-0742(07)60151-X
- Yusuf, S.M., Mukadam, M.D., De Teresa, J.M., Ibarra, M.R., Kohlbrecher, J., Heinemann, a., Wiedenmann, a., 2010. Structural and magnetic properties of amorphous iron oxide. *Phys. B Condens. Matter* 405, 1202–1206. doi:10.1016/j.physb.2009.11.040
- Zamparas, M., Zacharias, I., 2014. Restoration of eutrophic freshwater by managing internal nutrient loads. A review. *Sci. Total Environ.* 496, 551–62. doi:10.1016/j.scitotenv.2014.07.076
- Zhang, C., Ge, Y., Yao, H., Chen, X., Hu, M., 2012. Iron oxidation-reduction and its impacts on cadmium bioavailability in paddy soils: A review. *Front. Environ. Sci. Eng. China* 6, 509–517. doi:10.1007/s11783-012-0394-y
- Zhang, H., Selim, H.M., 2007. Colloid mobilization and arsenite transport in soil columns: effect of ionic strength. *J. Environ. Qual.* 36, 1273–80. doi:10.2134/jeq2006.0373
- Zhao, L.X., Hou, W.G., 2012. The effect of sorbent concentration on the partition coefficient of pollutants between aqueous and particulate phases. *Colloids Surf., A* 396, 29–34. doi:10.1016/j.colsurfa.2011.12.026
- Zhou, W., Lv, T.F., Chen, Y., Westby, A.P., Ren, W.J., 2014. Soil physicochemical and biological properties of paddy-upland rotation: A review. *Sci. World J.* 2014. doi:10.1155/2014/856352
- Zhu, J., Pigna, M., Cozzolino, V., Caporale, A.G., Violante, A., 2011. Sorption of arsenite and arsenate on ferrihydrite : Effect of organic and inorganic ligands. *J. Hazard. Mater.* 189, 564–571. doi:10.1016/j.jhazmat.2011.02.071
- Zhu, M., Northrup, P., Shi, C., Billinge, S.J.L., Sparks, D.L., Waychunas, G.A., 2013. Structure of Sulfate Adsorption Complexes on Ferrihydrite. *Environ. Sci. Technol. Lett.* 1, 97–101. doi:10.1021/ez400052r

(This page intentionally left blank)

# CHAPTER 3. EXPERIMENTAL PROCEDURES

## List of contents

<b>CHAPTER 3. EXPERIMENTAL PROCEDURES .....</b>	<b>3-1</b>
List of contents .....	3-1
Abstract .....	3-2
3.1. Introduction .....	3-3
3.2. Theoretical calculation using computational chemistry .....	3-5
3.2.1. Definition and history .....	3-5
3.2.2. Principle and methods .....	3-6
3.2.3. Density functional theory .....	3-7
3.3. Experimental measurement using ATR-FTIR .....	3-8
3.3.1. Importance of interfacial measurement .....	3-8
3.3.2. History and technique .....	3-9
3.3.3. Principle and consideration .....	3-10
3.3.4. Experimental procedure .....	3-19
3.4. Spectral Interpretation of ATR-FTIR .....	3-23
3.4.1. Spectrum correction .....	3-24
3.4.2. Band identification .....	3-25
3.4.3. Data interpretation .....	3-32
3.5. Experimental measurement using XAS .....	3-35
3.5.1. History and technique .....	3-35
3.5.2. Principle and consideration .....	3-38
3.6. Spectral interpretation of XAS .....	3-40
3.6.1. Spectrum reduction .....	3-40
3.6.2. Structure identification .....	3-40
3.7. Sorbent characterization .....	3-44
3.6.1. Elemental composition .....	3-45
3.6.2. Morphological characterization .....	3-45
3.6.3. Crystal structure identification .....	3-46
3.6.4. Electrochemical characterization .....	3-47
References .....	3-48

## **Abstract**

This chapter summarizes advantage and limitation in computational chemistry, infrared and X-ray spectroscopy to understand a rhizospheric interaction among organic acids, oxyanions, and metal oxides. Since organic acids and metal oxides determine dynamics of oxyanions in the soil environment, knowledge of fundamental mechanisms is a prerequisite for understanding the interactions at soil-water interface. Attenuated total reflectance-Fourier transform infrared spectroscopy (ATR-FTIR) is a powerful tool to measure the interfacial reactions. However, the ATR-FTIR measurements are abstruse, because the optical characteristics for measurements are variable depending on the experimental setup. Besides, spectral overlapping is a primary obstacle to the analysis of the interfacial reaction; thus, it is essential to detect and to deconvolute bands for signal interpretation. In this review, I explained the fundamental principle for spectrum processing, and four band identification methods, such as derivative spectroscopy, two-dimension correlation spectroscopy, multivariate curve resolution, and computational chemistry with an example of aqueous phosphate speciation. As a result, spectrum processing and computational chemistry improved interpretation and spectral deconvolution of overlapped spectra in a relatively simple system, but it was still unsatisfactory for the problems in a more complex system like nature. Nevertheless, I believed that our challenge would contribute practically to developing adequate analytical procedures, signal processing and protocols that could help to improve interpretation and to understand the interfacial interactions of oxyanions in natural systems.

## **Keywords**

ATR-FTIR, Computational spectroscopy, EXAFS, Organic acid, Oxyanion, Metal oxide

### 3.1. INTRODUCTION

Recent studies have reported that the various organic acids from the plant-derived root exudate lead the desorption of oxyanions from the sorption site in the soil by the competition or the dissolution of metal (hydr)oxides, where the oxyanions mainly adsorbed. The desorption and dissolution increase the bioavailability of oxyanions in the rhizosphere, but no direct evidence has not provided yet (Baetz and Martinoia, 2014; Bais et al., 2006; Kim et al., 2010). The reason could be categorized as 1) previous approaches on soil characterization are mainly performed with dried samples. The bioavailable phosphate in soil existed as low fraction, it easily precipitates with multi-valent cations or the metal (hydr)oxide could be formed during the drying process. The process leads the difference of phosphate in soil between the dried and wet samples (Fan et al., 2014; McGeehan et al., 1998). 2) The bioavailable phosphate mainly adsorbed on the surface of clay mineral and metal (hydr)oxide at low abundance with high heterogeneity, and it makes hard to analyze the structural configuration of phosphate in the soil. 3) X-ray absorption spectroscopy (XAS) is the most promising analytical tool to reveal the structural configuration of phosphate even at low concentration, but the X-ray easily break down the organic acids; thus, it is hard to observe the competitive adsorption of organic acids and oxyanions on the metal (hydr)oxides, but it is still a versatile tool to identify the structural configuration of oxyanions on the metal (hydr)oxides. These reasons make the direct measurement of the chemical reaction between organic acids and oxyanions on the metal (hydr)oxides difficult.

Raman, infrared, electron paramagnetic resonance and nuclear magnetic resonance are suggested to analyze the interactions instead of XAS, and attenuated total reflectance-Fourier transform infrared spectroscopy (ATR-FTIR) enables us to

measure the change in the vibration energy at the real time and solid-solution interface. (Hind et al., 2001; Mudunkotuwa et al., 2014). A molecular structure and mass of individual component determine the absorption of infrared beam, and the problem is the overlapped bands caused by the vibrational mode, complexity of system and similarity of component (Shi and Yan, 2014). In the past, it was not able to interpret the overlapped spectra in the complex system, but interpreting the simple system was mainly studied, and recent approach on isotope study enables us to identify the band shift caused by the difference in the atomic mass of stable isotope (Max and Chapados, 2009). These approaches were still not enough to deconvolute the complexly overlapped spectra.

However, recent development in the computation and quantum mechanics leads us to calculate the theoretical molecular orbitals by Schrödinger equation with approximations. Lately, many commercial or academic software for computational chemistry have been developed, and anyone who has ability on the calculation using the computer and has knowledge on the computational chemistry can easily obtain the electronic structure of molecule or complex. For example, the adsorbed structure of oxyanion on the metal (hydr)oxide (Kubicki et al., 2012; Watts et al., 2014). The development in computational chemistry led a significant advance in the interpretation of overlapped spectra using *in situ* ATR-FTIR studies and the interpretation of structural configuration using XAS because the theoretical calculation yields the spectroscopic characteristics and structure of the complex. As the result, the theoretical vibration mode and position could be calculated, and it is possible to use this information for characterizing individual structural configuration by the band deconvolution (Carabante and Grahn, 2010; Kubicki et al., 2012).

There is dramatic increase in the studies combining the infrared

spectroscopy and computational chemistry to identify the structural configuration at the solid-solution interface. The development in the computation and theory of electronic structure enable us to understand the structural configuration of the complex in the simple system. Approaches to deal with more complex system has been achieved in the various fields of studies, and the oxyanion dynamics in the heterogeneous soil system is the one of the utmost targets for soil scientists. In this study, I extensively reviewed the fundamental theory, history, application, advantage and disadvantage of computational chemistry and *in situ* ATR-FTIR and XAS to conduct a study for rhizospheric interactions, the reason and methods for metal (hydr)oxide characterization by the transformation in the experiment. I also summarized how to deal with the overlapped spectra in the infrared spectroscopy and how to interpret the structural configuration from the infrared and X-ray spectroscopy.

### **3.2. Theoretical calculation using computational chemistry**

#### 3.2.1. Definition and history of computational chemistry

Computational chemistry is one of the theoretical chemistry, and it uses computing simulation to solve chemical problems. Since Heitler and London conducted the first theoretical calculation in 1927, and the computational chemistry was settled as one of the fields of study with the development in the computer technology in the 1940s. The first calculation using *ab initio* Hartree-Fock method was performed at MIT in 1956, an empirical calculation using Hückel method was conducted in 1964, from the 1970s to present, numerous studies and methods have been developed with a significant advance in the computer. Walter Kohn and John Pople received the Nobel prize in 1998 by developing a density functional theory

and computational method in quantum mechanics, and it announced the real beginning of computational chemistry. Martin Karplus, Michael Levitt, and Arieh Warshel received the Nobel prize in 2013 again, for the development of multiscale models for complex chemical systems, and it gained much attention in the computational chemistry.

### 3.2.2. Principle and methods

It is possible to understand a wave nature of electron by solving Schrödinger equation mathematically, and many computations and approximation methods should be employed to solve the equation (Schrödinger, 1926). Based on the approximation method, we can categorize as *ab initio* and empirical method. The main difference in two type of approximation is the utilization of empirical or semi-empirical parameter for the computation of orbital function, and *ab initio* method employs no such parameter, but empirical method employs the parameters (Kim et al., 2012). Hartree Fock molecular orbital theory (HF) and density functional theory (DFT) are the typical methods in *ab initio*, and it employs self-consistent field for the computation. For example, one orbital function of electrons is proposed, a potential field of a electron is computed first, and base on the computation, the other potential field of electron is substantially computed. And the computation would be repeated until the newly computed potential field of electron matches with the previous version (Blinder, 1965).

The HF is the simplest equation in *ab initio* method, and firstly proposed by Douglas Rayner Hartree in 1927, and Vladimir Fock applied Pauli exclusion principle. HF is not describing the repulsive force of electrovalence, and it only considers the average effect (Froese Fischer, 1987). On the other hand, DFT was developed from Thomas-Fermi model by Liewellyn Thomas and Enrico Fermi, and

modified by Walter Kohn and Pierre Hohenberg, it utilizes Born-Oppenheimer approximation, which is fixing the nuclear and computing the motion of a electron. From the Born-Oppenheimer approximation, it dramatically decreases the load on the computation. To put it briefly, the DFT saves the load on computation by replacing wave function of a electron with density function. The empirical method can be categorized as a semi-empirical and empirical method with the utility of parameters, and it is effective to reduce the load on computation especially with the high number of atoms in the molecule (Kim et al., 2012; VandeVondele et al., 2012). In case of an excessive number of atom in the molecule, classical mechanics is frequently employed instead of quantum dynamics.

### 3.2.3. Density functional theory

Even a simple system, numerous computation should be performed to solve the Schrödinger equation; various approximations for effective computation and high level of computing resource are essential. Among the numerous approximations, an exchange-correlation functional method proposed by Axel Becke and modified Chengteh Lee, Weitao Yang and Robert G. Parr is the one of common methods (B3LYP). The B3LYP is improved from HF method, and it showed a similar result with less time-consuming in the previous studies (Stephens et al., 1994; VandeVondele et al., 2012). The solution from the computation with approximations can be used to predict the various characteristics of a molecule, such as molecular geometry, vibrational frequency, atomization and ionization energy, electronic and magnetic characteristics and reaction pathway (Becke, 1993; Kim et al., 2012; Stephens et al., 1994). There is several softwares implementing the computational chemistry with academic, commercial and non-commercial licenses. ADF, GAMESS, Gaussian, NWchem and Spartan are the most known

software. Each software has difference in license, approximation, basis set and theory, computing way; thus, it is essential to choose appropriate software for the objective in the study.

### **3.3. Experimental measurement using ATR-FTIR**

#### **3.3.1. Importance of solid-solution interfacial measurement**

The chemical reaction at the solid-solution interface is critical to interpreting the adsorption and dynamics of pollutant and nutrient in the soil environment (Gunnarsson, 2002; Violante, 2013). The oxyanions go through various reactions, such as adsorption, desorption, chemical transformation and precipitation in the soil environment, and it finally leached out from the soil to water system (Hwang and Lenhart, 2008; Selim and Zhang, 2013). Irreversible change in the oxyanion dynamics caused by environmental perturbation could affect the whole pathway in the ecosystem, and the perturbed cycle would lead significant effect on the human. For that reason, it is essential to understand the reaction at the solid-solution interface (Gunnarsson, 2002; Hind et al., 2001), and various methodologies have being developed to measure the interfacial reaction.

Atomic force microscopy, electron energy loss spectroscopy, electron paramagnetic resonance, low energy electron diffraction, X-ray absorption spectroscopy and X-ray photoemission spectroscopy are the most advanced technique to identify the structural configuration of complex (Hind et al., 2001; Lefevre, 2004; Mudunkotuwa et al., 2014); however, there are advantage and disadvantage in each technique. The techniques utilizing electron require a high level of vacuum condition, and the reaction at solid-solution interface could not be determined such techniques, and the sample should be pretreated by the drying or

freezing, which causes the phase transition. There are three problems utilizing X-ray: 1) the low intensity for the measurement by the water absorption; 2) even if we utilize the synchrotron, which provides high intensity with water, it could affordable signal to noise ratio for the interpretation, but the organic molecules can be easily degraded during the measurement (Cerkez et al., 2015; Mudunkotuwa et al., 2014). For that reason, it is essential to measure the solid-solution interfacial measurement without degrading the organic molecules and transition the phase of sample.

### 3.3.2. History and technique

William Herschel discovered the infrared radiation in 19th century, and first type of infrared spectrophotometer utilized a prism or monochromator. In the late 19th century, Albert Abraham Michelson invented an interferometer using a beam splitter, and it caused a great advance in the spectroscopy. It still had a problem that an interferogram measured at time-domain could not convert to frequency-domain. But the problem was solved by Peter Fellgett in 1949 by applying Fourier transform for the conversion and it is was the first development of Fourier transform infrared spectroscopy (FTIR). A commercial FTIR was introduced to the scientists in 1960s, and the FTIR have led the great advance in the scientific research since. Numerous analytical methods using FTIR have been developed, and transmission, diffuse reflectance, photoacoustic, attenuated total reflectance and specular reflectance are the most typical methods (Fig. 3-1).

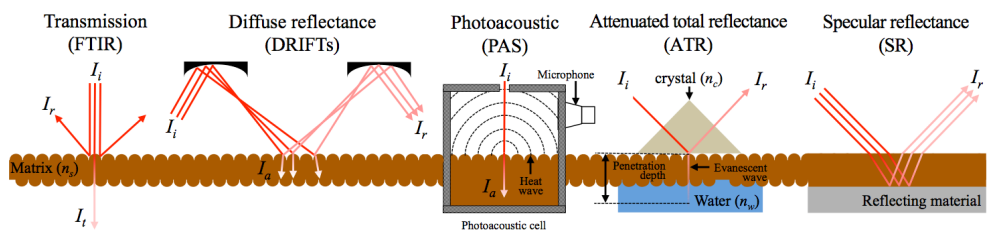
Each analytical method has advantage and disadvantage; the transmission method could be categorized into a solid measurement using KBr and solid-solution mixture measurement by transmitting IR in a thin mixture. The KBr method could not measure the interfacial reaction, and solid-solution mixture measurement requires few  $\mu\text{m}$ -sized thickness to transmit the IR and homogeneous dispersion of sample, it

is not applicable for interfacial measurement. Diffuse reflectance method irradiates IR beam on the sample and the detector measured the adsorbed and diffused IR beam by condensing, and it has an advantage that it does not require any pretreatment, but the water contained sample led low intensity at the detector; thus, the interfacial measurement is difficult. The photoacoustic method detects the vibration from the IR absorption by a microphone, and it typically utilized in the high absorbing materials such as an organic matter and biochar, and it needs additional resonator to detect interfacial measurement (Bekiaris et al., 2015). The specular reflection method measures the difference between the intensity of initial IR beam and absorbed and reflected beam on the sample and reflecting materials. It easily measures the coating or film on the metal surface with high smoothness, but it is not applicable to interfacial measurement with aggregated particle sample (Amma et al., 2015). The attenuated total reflection (ATR) method requires the formation of a film of target sorbent on the crystal surface, the IR beam goes through the internal of crystal, and the total reflection occurs at the interface between the crystal and solid film. During the total reflection, the evanescent wave was generated at a certain depth of penetration ( $d_p$ ) to the sample film and solution with the IR absorption, and the difference in absorption between the intensity of initial and final IR beam yields the spectra. The ATR method only employs few  $\mu\text{m}$ -sized  $d_p$ ; thus, the sample should be less than  $d_p$ , but it enables us to measure the interfacial reaction at a real-time.

### 3.3.3. Principle and consideration

The fundamental principle of solid-solution interfacial measurement using ATR-FTIR is causing total reflection at the crystal and solid interface by incident of IR beam on the crystal, the few  $\mu\text{m}$ -sized evanescent waves from the crystal passes

**Fig. 3-1** Fundamental schematic diagram of analysis technique using Fourier transform infrared spectroscopy.  $I_i$ ,  $I_r$ ,  $I_a$ , and  $I_t$  indicate initial, reflected, absorbed and transmitted infrared, respectively.



through the solid sample and solution with absorption, and it goes back to the crystal (Gunnarsson, 2002; Hebert et al., 2004). For that reason, the formation of total reflection is the key in ATR-FTIR studies, and the schematic diagram was illustrated in Fig. 3-2 with the associated parameters. In the solid-solution interface measurement, the angle of incident IR beam ( $\theta_i$ ) and reflective indexes of crystal, metal (hydr)oxide and water ( $n_c$ ,  $n_s$  and  $n_w$ ) determines the IR beam pathways, which are the specular reflection, total reflection and transmission. The temperature, pressure and  $\theta_i$  are constant during the experiment, the ratio between the metal (hydr)oxide and crystal ( $n_s/n_c$ ) determines the critical angle ( $\theta_{cs}$ ). If  $n_s < n_c$  and  $\theta_i > \theta_{cs}$ , the total reflection occurs, the evanescent wave comes from the interface between the crystal and metal (hydr)oxide, and the depth of penetration by the total reflection ( $d_{p,cs}$ ) can be calculated using Eq. 3-1 (Hamers et al., 2011; Hase et al., 2010).

$$d_{p,cs} = \lambda/2 \cdot \pi \cdot n_c \left( \sin^2 \theta_i - \left( \frac{n_s}{n_c} \right)^2 \right)^{\frac{1}{2}} \quad \text{(Eq. 3-1)}$$

Based on the Eq. 3-1, the  $d_{p,cs}$  increase with the increase of wavelength ( $\lambda$ ) and  $n_s/n_c$  or decrease of  $\theta_i$ . The molecules in the path of evanescent wave absorb the IR beam, and the decreased intensity after total reflection ( $I_{ATR-r}$ ) goes to the detector, and the difference between the initial intensity of IR beam ( $I_i$ ) and  $I_{ATR-r}$  yields the absorbance.

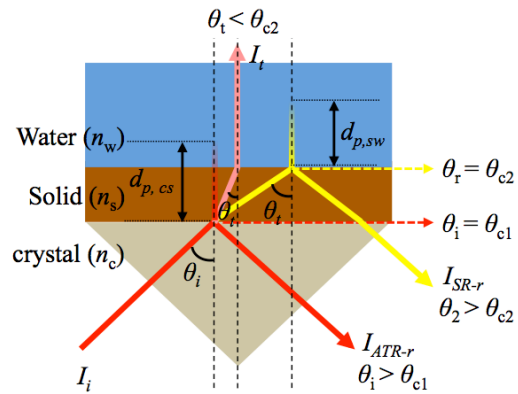
The number of total reflection categorizes as single ATR and multiple ATR. The single ATR illustrated in Fig. 3-2 uses small a crystal to generate total reflection one time, and it usually employs for qualitative measurement or extreme condition measurement using a diamond, which is expensive material. The multiple ATR uses a rod-shaped crystal to generate multiple total reflection to increase the path of  $d_p$ , the quantitative measurement could be achieved than the single ATR. The crystals made with zinc selenide (ZnSe) and amorphous material transmitting

infrared radiation (AMTIR) typically employs in multiple ATR, but the hardness of these materials is lower than the quartz, which is abundant in the soil sample. The quartz sometimes damages the crystal for adhesion process, and it cause diffuse reflection in ATR, which decrease the signal to noise ratio (S/N).

Table 1 summarizes the calculated  $d_p$  as function of crystal and metal (hydr)oxides, the reflective index of crystal is ranged from 2.2 to 4.0 at  $\lambda = 10 \mu\text{m}$  condition (Mudunkotuwa et al., 2014), and the reflective index of metal (hydr)oxide in the review is ranged from 1.65 to 3.1 (Su and Suarez, 2000; Szekeres and Tombácz, 2012; Wei et al., 2014). If the reflective indexes of crystal and metal (hydr)oxide are similar ( $n_c \approx n_s$  and  $\theta_i < \theta_{cs}$ ), the total reflection could not be occurred at the crystal-metal (hydr)oxide interface and the IR beam tranmits to metal (hydr)oxides. The transmitted IR beam reaches the interface between the metal (hydr)oxide and water, total reflection occurs under  $n_w < n_s$  and  $\theta_r > \theta_{sw}$  conditions. This phenomenon is similar to the specular reflection illustrated in Fig. 3-1, and the water act as reflecting materials, and total reflection is happened at the metal (hydr)oxide and water interface. Besides, the penetration depth at metal (hydr)oxides and water interface ( $d_{p,sw}$ ) can be differed by  $\theta_i$  and  $n$ ; the evanescent wave passes through the water molecules, which has a great absorbability of IR beam. For that reason, the intensity after specular reflection ( $I_{SR-r}$ ) significantly decreases compared with  $I_{ATR-r}$ . Decrease in  $\lambda$  dramatically increase the  $d_p$ , and it would lead no measurable intensity of IR beam at the detector (Fang et al., 2013; Hebert et al., 2004; Parikh et al., 2008).

As we can see in Fig. 3-2, there is a difference in the position between the  $I_{ATR-r}$  and  $I_{SR-r}$ , and the increase of a number of total reflection and sample thickness would accelerate the difference between the path position, and the IR beam could not reach the detector properly under certain conditions (Hamers et al., 2011)

**Fig. 3-2** Schematic diagram showing optical pathway during internal reflection at solid-liquid interface measurement using *in situ* ATR-FTIR.  $n_c$ ,  $n_s$ , and  $n_w$  indicate refractive index of crystal, solid, and water, and  $\theta_i$  and  $\theta_t$  mean angle of incident from crystal to solid, and from solid to water.  $I_i$ ,  $I_{ATR-r}$ ,  $I_{ATR-r}$ ,  $I_{SR-r}$ , and  $I_r$  indicate infrared intensity of initial, ATR refracted, SR refracted and transmitted.



$n_c, n_s, n_w$  = refractive index of crystal, solid, and water  
 $\theta_i$  = angle of incident from crystal to solid  
 $\theta_t$  = angle of incident from solid to water  
 $\theta_{c1}$  = critical angle between crystal and solid =  $\sin^{-1}(n_2/n_1)$   
 $\theta_{c2}$  = critical angle between solid and water =  $\sin^{-1}(n_3/n_2)$   
 $I_i, I_{ATR-r}, I_{ATR-t}, I_{SR-r}, I_r$  = IR intensity of initial, ATR refracted,  
 SR refracted and transmitted  
 $n_1 \sin(\theta_1) = n_2 \sin(\theta_2)$   
 $d_p$  = depth of penetration

**Table 3-1** Penetration depth between crystal material and metal oxide ( $T=25\text{ }^{\circ}\text{C}$ , pressure=1 atm,  $n_w=1.33$ ,  $\lambda=10\text{ }\mu\text{m}$ ,  $\theta_i=45^{\circ}$ )

metal oxide \ crystal		ZnS	KRS-5	ZnSe	AMTIR	Si	Ge
	LWL ( $\text{cm}^{-1}$ )	850	250	525	625	1500	780
	<i>working pH</i>	5-9	5-8	5-9	1-9	1-12	1-14
	<i>n</i> *	2.2	2.37	2.4	2.5	3.4	4.0
Air	1.00	1.34	1.18	1.16	1.09	0.73	0.60
Water	1.33	1.86	1.51	1.46	1.33	0.79	0.63
Boehmite ( $\text{Al}(\text{OH})_2$ )	1.65	1.97 **	5.43	4.01	2.51	0.91	0.69
Periclase ( $\text{MgO}$ )	1.735	1.97 **	1.56 **	1.51 **	4.70	0.96	0.71
Corundum ( $\text{Al}_2\text{O}_3$ )	1.765	1.97 **	1.56 **	1.51 **	16.1	0.98	0.72
Manganosite ( $\text{MnO}$ )	2.16	1.97 **	1.56 **	1.51 **	1.37 **	1.51	0.87
Goethite ( $\text{FeOOH}$ )	2.2	1.97 **	1.56 **	1.51 **	1.37 **	1.64	0.90
Wüstite ( $\text{FeO}$ )	2.32	1.97 **	1.56 **	1.51 **	1.37 **	2.53	0.98
Magnetite ( $\text{Fe}_3\text{O}_4$ )	2.42	1.97 **	1.56 **	1.51 **	1.37 **	0.79 **	1.09
Maghemite ( $\gamma\text{-Fe}_2\text{O}_3$ )	2.7	1.97 **	1.56 **	1.51 **	1.37 **	0.79 **	1.89
Hematite ( $\text{Fe}_2\text{O}_3$ )	2.9	1.97 **	1.56 **	1.51 **	1.37 **	0.79 **	0.64 **
Ferrihydrite ( $\text{Fe}_2\text{O}_3$ )	3.1	1.97 **	1.56 **	1.51 **	1.37 **	0.79 **	0.64 **

\* Refractive index of crystal and metal oxide

\*\* Penetration depth by total reflection at metal oxide and pure water interface under  $n_s \approx n_c$ ,  $n_w < n_s$ ,  $\theta_i < \theta_{cs}$ , and  $\theta_r > \theta_{sw}$  conditions

*LWL* long wavelength cutoff of of the ATR crystal, *working pH* safe pH range for any damage on crystal, *ZnS* zinc sulphide, *KRS-5* thallium bromo-iodide (TlBr-TII), *ZnSe* zinc selenide, *AMTIR* amorphous material transmitting infrared radiation ( $\text{Ge}_{33}\text{As}_{12}\text{Se}_{55}$ ), *Si* Silicon, *Ge* Germanium

However, we can adjust the optic condition to reach the IR beam to the detector in most circumstance, we can obtain the optimum experimental condition by correcting the experimental parameters. As I illustrated in Fig. 3-2, the angle of incident from metal (hydro)oxide to water could be decreased under certain conditions ( $n_3 \approx n_2$  and  $\theta_i < \theta_{c2}$ ), the IR beam would transmit to water without the formation of evanescent wave. No transmission occurs at  $\theta_i = 45^\circ$  condition, but the decrease of  $\theta_i$  generates the transmission, and no ATR study was available under such condition.

Not only the experimental condition but also the optical characteristics of FTIR affects the measurement, the dependence of  $d_p$  on the wavenumber and  $n_s$  is illustrated in Fig. 3-3. Fig. 3-3a shows the exponential increase of  $d_p$  as a function of  $\theta_i$  and wavenumber in the mid-IR beam range ( $4000 - 500 \text{ cm}^{-1}$ ), which are located above the long wavelength cutoff point. When  $\theta_i$  is low, the dramatic increase of  $d_p$  was observed; thus, the IR beam intensity to the detector significantly decreases. On the other hand, When  $\theta_i$  is high, the  $d_p$  is decreased. If the sample thickness is lower than  $d_p$ , the evanescent wave could not reach the interface between the metal (hydr)oxide and water, the absorbance from the adsorbed complex could not be obtained (Hind et al., 2001; Lefevre, 2004; Wijnja and Schulthess, 2000).

Fig. 3-3b illustrates the difference of  $d_p$  varying  $n_s$  at  $1000 \text{ cm}^{-1}$  and ZnSe crystal. The dramatic increase of  $d_{p,cs}$  was observed when  $n_s$  is ranged from 1 to 2. This phenomenon is named as an evanescent wave coupling, which is observable when the medium with low  $n$  has existed with the medium with high  $n$  on both side, the evanescent wave is delivered through the medium with low  $n$  even the total reflection occurs. The evanescent wave coupling blocks the evanescent wave return, and absorbance from the evanescent wave could not be detected (Taga et al., 1994). If  $\theta_i$  is low, the formation of evanescent wave is only occurred at low  $n_s$ ; the

evanescent wave would not be formed at  $n_s > 1$  condition. If the condition is  $\theta_i > 35^\circ$ , the evanescent wave coupling would happen with increase of  $n_s$ ; thus, the evanescent wave at the metal (hydr)oxide and water interface would be formed. In this case, the  $\theta_i$  would be differed by the  $n_s$ , but the ratio of refractive index between the water and metal (hydr)oxide ( $n_w/n_s$ ); thus, the  $d_{p,sw}$  is constant under varying  $n_s$  condition.

As I discussed above, the  $d_p$  is a function of  $n$ ,  $\theta_i$  and  $\lambda$ , and no evanescent wave could not be formed at a certain condition, setting an appropriate experimental condition by understanding the crystal and metal (hydr)oxide is critical in the ATR-FTIR experiment (Hamers et al., 2011). In addition, the metal (hydr)oxides have various values of  $n_s$  as a function of  $\lambda$ , the researcher should be aware of the whole inter-correlated knowledge to set up the experimental parameters before designing the experiment (Lefevre, 2004; Madejová, 2003; Mudunkotuwa et al., 2014)

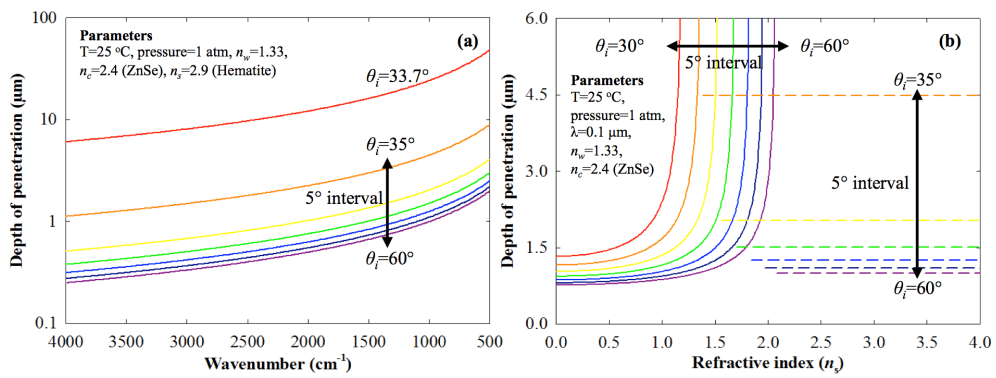
#### 3.3.4 Experimental procedure

If the fundamental theory was understood and the experimental parameter was set, the physical characteristics of metal (hydr)oxides should be considered for further experiment. The iron (hydr)oxide is the one of abundant metal (hydr)oxide in the soil environment, and six types of synthesis in laboratory have being reported: 1) Hydrolysis of acidic solutions of Fe(III) salts, 2) Oxidative hydrolysis of Fe(II) salts, 3) phase transformation, 4) Gel-sol method, 5) Hydrothermal precipitation and 6) Decomposition of metal chelate (Udo and Rochelle, 2008). In the ATR-FTIR experiment, the film formation method using the monodispersed particles is typically employed, and the monodispersed particles are formed by nucleation and crystal growth in the solution. The size of particle is critical factor controlling the

surface area, the shape of particle also determines the adsorption because each facet has different thermodynamic stability of surface complex (Kubicki et al., 2012); thus, the synthesis and utilization of monodispersed particle is the important parameter in ATR-FTIR experiment (Lefevre, 2004; Mudunkotuwa et al., 2014; Müller and Lefèvre, 2011).

The iron (hydr)oxides in the soil environment have shown various types of crystal structure and morphology, but the rod and sphere with the size of few micron and submicron are commonly found. The  $d_p$  of experiment usually less than few  $\mu\text{m}$  as I discussed above, and if the particle size is larger than the  $d_p$ , no information on the surface complex could not be acquired. In addition, the adhesion of metal (hydr)oxide on the crystal is a critical factor for interfacial measurement, and the increase of particle size would lead difficulty in the film formation, because of less coagulation occurs in the particle (Glotch and Rossman, 2009; Udo and Rochelle, 2008). The increase of particle size also yield the decrease of number of pore in the film, but the size of each pore would be increased. The water and air saturate the pore space, it would cause the decrease of stability in the film on the crystal, and the film would be detached from the crystal eventually. However, the water and air saturation in the pore space without decreasing the film stability would form the evanescent wave at the crystal and metal (hydr)oxide interface at  $n_c \approx n_s$  condition (Hamers et al., 2011; Mudunkotuwa et al., 2014). For that reason, I recommend to synthesis or purchase the monodispersed particle, it should be dispersed in the solvent at the appropriate concentration, and it should be spread on the crystal at uniform thickness (Carabante and Grahn, 2010; Kubicki et al., 2012). The drying of nanoparticle on the crystal easily makes the film, but the solution condition such as pH and ionic strength determines the film stability, and we should maximize the film stability by controlling the environmental condition such as

**Fig. 3-3** Theoretically calculated depth of penetration ( $d_p$ ) as function of wavenumber (a) and refractive index (b). The color difference means 5° interval at angle of incident ( $\theta_i$ ).



adjusting pH and adding coagulant, but the environmental condition should not have any influence on the adsorption study.

If the film is adequately formed, the reactor should be placed on the top of the ATR crystal plate to hold solution on the film. Many researchers produced own reactors, or there is commercial reactor from the several manufacturers. After the saturation of solution on the film is saturated, the stability of the film should be assessed before the experiment, and the ATR-FTIR experiment is ready. There are several methods to observe reaction; the kinetic study is frequently used to measure the time-dependent sorption at real time (Kira et al., 2014; Rakshit et al., 2016; Tofan-Lazar and Al-Abadleh, 2012). It also possible to monitor the absorbance by perturbing the environmental condition, such as pH, ionic strength and competing ion (Brechtbühl and Christl, 2012; Carabante and Grahn, 2010; Du et al., 2014; Lindgren and Persson, 2009; Waiman et al., 2013). The equilibrium study is also possible, but it depends on the condition of FTIR instrument (Elzinga and Sparks, 2007; Kubicki et al., 2012; Sabur and Al-Abadleh, 2015). There are several methods have been developed, and I proposed how to measure the preferential adsorption on the binary mixture condition, and Elzinga et al. (2012) examined how the microbe interact with metal (hydr)oxide.

#### **3.4. Spectral interpretation of ATR-FTIR**

In the ATR-FTIR experiment equipped with ZnSe, the spectrum of mid-IR is ranged in  $4000\text{-}650\text{ cm}^{-1}$ , and various vibrations occur at the range. The binding vibration is commonly found in the range of  $1200\text{-}600\text{ cm}^{-1}$ , and it is called as fingerprint region because inorganic molecule with oxygen usually shows the absorption at the range. However, the increase of  $\lambda$  dramatically increase the  $d_p$ , it is

hard to get significant intensity at the range less than  $800\text{ cm}^{-1}$ , and the increase of system complexity causes more overlapped bands, which it makes hard to interpret the spectra. To diminish such problem, a deuterium water used to shift the absorption bands, or experimental condition such as  $\theta_i$  and  $n_c$  could be controlled to change the  $d_p$ . In addition, there are several methods to identify the bands using mathematical or quantum chemical approach such as derivative spectroscopy, two-dimensional correlation spectroscopy (2D-COS), multivariate curve resolution (MCR) and computational chemistry.

#### 3.4.1. Spectrum correction

Before interpreting the measured spectra, it is essential to correct the spectra, and there are several correction methods, but I explained two types in this review. As a first, smoothing should be performed to eliminate the noise effect. In the ATR-FTIR measurement, the intensity of IR beam at the detector is significantly lower than other methods; thus, the noise could be observed in the most experimental condition, and these effects should be removed, but it should be performed without changing the band information from the original spectrum. The other correction is the ATR correction. As I discussed above, the  $d_p$  dramatically increases with the decrease of wavenumber, and the path length also increased (Madejová, 2003; Mudunkotuwa et al., 2014) (Fig. 3-3a). Even if the constant absorption occurs, the intensity at the detector decreased as a result. For that reason, the ATR method has more absorbability at lower wavenumber because of the increase of  $d_p$ , and there is band shift to lower wavenumber. Kramer-Kronig correction is one of ATR correction to diminish such effect (Huang and Urban, 1992). Under the conditions with the significant difference between  $n_c$  and  $n_s$ , and low value of  $\theta_i$ , the effect occurs critically, but the common conditions at ZnSe

( $n_c=2.4$ ) and  $\theta_i=45^\circ$  could not be observed.

### 3.4.2. Band identification

After the spectrum corection, the band identification should be assessed to interpret the absorption by the vibration of a molecule, and it is easily performed for a simple system, but it is almost impossible for a complex system, because the number of overlapped bands is increased geometrically. In this review, I summarize four methods for band identification, which are derivative spectroscopy, (2D-COS), multivariate curve resolution (MCR) and computational chemistry.

#### 3.4.2.1. Derivative spectroscopy

The derivative spectroscopy is the classical method for band identification by a differential calculus of a spectrum. The 1<sup>st</sup> derivative of the spectrum can be calculated using Eq. 3-2 (Griffiths and Hubbard, 1991; Owen, 1995; Rieppo et al., 2012).

$$dA/d\lambda = f'(\lambda) \quad \text{(Eq. 3-2)}$$

and the result from the 1<sup>st</sup> derivative of spectrum could be calculated, and the number of applied differential calculus (n) determines the n<sup>th</sup> derivative. In Fig. 3-4a, It shows the spectra of phosphate at pH 4.5 and 7.0 using ATR-FTIR with 2nd derivate, and the minimum at  $dA^2/dx^2$  indicates the band position. As a result, I confirmed five band positions in the spectra. This method is easily applicable for band identification for the simple system, but it is hard to applicable for the complex system, where the overlapped bands are severe. Besides, the ATR-FTIR experiment by changing environmental conditions or time series, individual identification should be assessed, and it would be difficult.

### 3.4.2.2. Two-dimensional correlation spectroscopy

The 2D-COS is the method calculating the intensity of spectra using the frequency, wavenumber, and wavelength of an electromagnetic wave; it is firstly introduced for NMR study in the 1980s. This method enables us to identify synchronous and asynchronous of the spectral signal with changing of the system (Noda, 2015, 2009; Pazderka and Kopecky Jr, 2008; Planinšek et al., 2006). The change in the signal could be triggered by the external perturbation or physical change of sample, and the 2D-COS mathematically analyzes the change in the signal using crosscorrelation. The two versions of 2D map is the result of the method, and it is named as 2D correlation spectrum, which is synchronous and asynchronous. The synchronous and asynchronous spectra are calculated with Eq. 3-3 and 3-4, respectively.

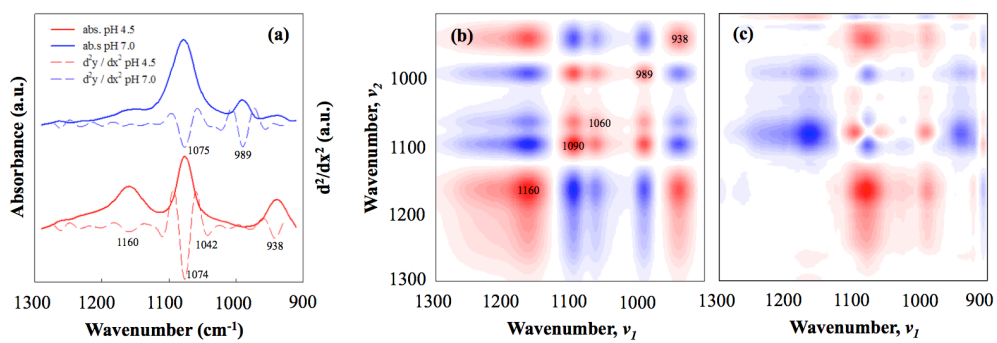
$$\Phi(v_1, v_2) = \frac{1}{(m-1)} \sum_{j=1}^m \tilde{A}_j(v_1) \cdot \tilde{A}_j(v_2) \quad (\text{Eq. 3-3})$$

$$\Psi(v_1, v_2) = \frac{1}{(m-1)} \sum_{j=1}^m \tilde{A}_j(v_1) \cdot \sum_{k=1}^m N_{jk} \cdot \tilde{A}_j(v_2) \quad (\text{Eq. 3-4})$$

where  $\Phi$  and  $\Psi$  are the synchronous and asynchronous spectra, respectively. The  $\tilde{A}_j(v)$  is the reference spectrum of the system, and it is commonly averaged spectrum for the observation.  $v_1$  and  $v_2$  are an arbitrary pair of two dynamic spectral signals, measured separately at wavenumbers, The  $m$  is the last value of spectra, and  $N_{jk}$  is the element of the  $j$ -th row and  $k$ -th column in Hilbert-Noda transformation matrix. As a result, the synchronous spectra ( $\Phi(v_1, v_2)$ ) indicates a synchronism at the certain perturbation condition.

For better understanding, Fig. 3-4b and 3-4c show synchronous and asynchronous correlation spectrum of aqueous phosphate by perturbing the pH condition from 4.5 to 7 using ATR-FTIR with time-series measurement. In the Fig. 3-4b, five band positions were identified, and it is easily observed at the point of

**Fig. 3-4** Example of peak identification in aqueous phosphate speciation measured by *in situ* ATR-FTIR using derivative spectroscopy under pH 5.5 and 8.0 (a) and synchronous (b) and asynchronous correlation spectrum (c) from pH 5.5 to pH 8.0 using two dimensions correlation spectroscopy. Solid and dotted line indicate absorbance and  $d^2/dx^2$ , respectively. Number indicates identified peak positions.



$\nu_1 = \nu_2$ . The band was identified at 1160, 1090, 1060, 989 and 938  $\text{cm}^{-1}$ , which is significantly different position compared with the result of derivative spectroscopy. It is also possible to identify the sequence of band appearance, and autopeak and crosspeak could be determined using synchronous correlation spectrum. The autopeak is that the two peaks increase together while the crosspeak is that the two peaks are inverse correlation during the perturbation. It is easily identified in the synchronous correlation spectrum by drawing correlation square. If  $\Phi(\nu_1, \nu_2)$  is positive (red), it is the autopeak while if  $\Phi(\nu_1, \nu_2)$  is negative (blue), it is crosspeak. For example with bands at 1160 and 1090  $\text{cm}^{-1}$ , it is negative; thus it is crosspeak, which has an inverse correlation between two peak, and band at 1160 and 938  $\text{cm}^{-1}$  is autopeak, which increase simultaneously.

The asynchronous correlation spectrum does not indicate the autopeak, but it only informs the crosspeak. The difference between synchronous and asynchronous correlation spectra is that the presence of symmetry based on the diagonal line. The crosspeak in the asynchronous spectrum is only observed by the difference in the signal at  $\nu_1$  and  $\nu_2$ , and it is useful to identify the sequence of the change of overlapped spectra. The  $\Psi(\nu_1, \nu_2)$  can be positive or negative; it shows the sequence of bands. If  $\Psi(\nu_1, \nu_2)$  is positive (red), the band of  $\nu_1$  changed first, and then  $\nu_2$  band is changed sequentially, *vice versa* in the negative (blue) (Noda, 2015, 2009). For example in Fig. 3-4c, the  $\Psi(1160, 1090)$  is negative; thus, the change in the band at 1090  $\text{cm}^{-1}$  comes first, then the change in the band at 1160  $\text{cm}^{-1}$  comes later. Based on this approach, it is possible to identify the band and sequence of appearance together.

#### 3.4.2.3. Multivariate curve resolution

The MCR is the mathematical signal processing method to extract

individual signal from the complexly overlapped signal without prior background, and it is proposed by William H. Lawton and Edward A. Sylvestre in 1971 (de Juan and Tauler, 2006; Lawton and Sylvestre, 1971; Ruckebusch et al., 2004). The MCR method enables us to separate the individual signals from the mixture of signal by the experiment without previous knowledge of the model; thus, it is possible to conduct the analysis using the experimental data only, but better interpretation would be released with prior knowledge and background for the experiment (Kessler and Kessler, 2006; Tauler, 2005).

The fundamental theory of MCR method is separating the two-way data matrix ( $D(m \times n)$ ) as two matrixes, which is  $C(m \times k)$  and  $S^T(k \times n)$ , and  $k$  species of the unknown mixture of pure concentration profiles and pure spectra can be calculated according to Eq. 3-5 (Ruckebusch and Blanchet, 2013):

$$D = CS^T + E \quad (\text{Eq. 3-5})$$

where  $E(m \times n)$  is the error matrix including the residual variation of data. MCR-ALS is the most commonly employed method among the MCR, and it embedded alternating least squares algorithms, which is proposed by Romà Tauler in 1995 (Jaumot et al., 2015; Ruckebusch and Blanchet, 2013; Tauler, 2005). The most important point analyzing MCR is to set constraints (Jaumot et al., 2015; Ruckebusch and Blanchet, 2013), and it should be done by the fundamental knowledge on the chemistry and physics of the experimental data. There are mainly four constraints, which are non-negativity, unimodality, closure and hard-modeling (Ruckebusch et al., 2004). For example with non-negativity, if we have data matrix by measuring absorbance as a function of time and there is no self-luminescent and no external light, the absorbance could not be the negative value in this experimental setup. As a result, the value of absorbance should be greater than zero, and it could not be calculated as negative.

Fig. 3-5a shows the evolved spectra of phosphate species transformation in the aqueous phase by changing pH from 4.5 to 7 using ATR-FTIR, and Fig. 3-5b and 5c indicate MCR optimized spectra and MCR optimized concentrations profile, respectively. The protocol of MCR-ALS method is pretreatment of spectrum matrix by correction, smoothing, and normalization, and then set up the initial estimates and number of the component for the analysis (Felten et al., 2015). For the setup the initial estimates and component, singular value decomposition (SVD) is applied, and analyzer should setup the parameter based on the SVD; then, I got the MCR optimized spectra and concentration profile.

The two spectra in Fig. 3-5b are similar with the spectra in Fig. 3-4, which used for derivative spectroscopy, because the series of spectra has only consisted with two molecules ( $\text{H}_2\text{PO}_4^-$  and  $\text{HPO}_4^{2-}$ ) and the band in each spectrum is autpeak. Fig. 3-5c indicates the concentration change from MCR-ALS analysis by changing pH condition, and I clearly identified the distribution of each phosphate species upon the pH. Based on the MCR analysis, we can extract important individual bands from the complexly overlapped spectra.

#### 3.4.2.4. Computational chemistry

In the Fig. 3-5b, the red and blue bar indicate the band position of aqueous  $\text{H}_2\text{PO}_4^-$  and  $\text{HPO}_4^{2-}$  calculated with DFT (B3LYP, 6-31G) (VandeVondele et al., 2012), and the DFT result clear confirmed the overlapped bands of  $\nu_a(\text{PO}^{2-})$  and  $\nu_s(\text{PO}^-)$  in 1090 and 1080  $\text{cm}^{-1}$  position. Previously discussed methods (derivative spectroscopy, 2D-COS and MCR-ALS) identified the overlapped band in other position, but it was impossible to separate the closely appeared band at 1090-1080  $\text{cm}^{-1}$ . In this case, I can theoretically calculate the vibrational frequency of each species, it is possible to identify the overlapped bands (Klahn et al., 2004;

Rudolph Dieter; Irmer, Gert, 2006). Fig. 3-6a and 3-6b show the deconvoluted peak by a peak fitting and predicted vibrational frequencies by the DFT study at pH 5.5 and 8. Tachyon supercomputer was employed for the computation in Korea Institute of Science and Technology Information, and Gaussian 09 (Gaussian, USA) and Avogadro (USA) were used for the computation and input generator, respectively (Frisch et al., 2009; Hanwell M.D. Lonie D.C., Vandermeersch, T., Zurek E., Hutchison, G., 2012). The B3LYP function with 6-31G(d,p) basis set was utilized for geometry optimization and frequency analysis with five water molecules (VandeVondele et al., 2012), but the water molecules were not visualized for better visibility of figures. The green arrows indicate the direction and intensity of the vibration in Fig 3-6a and 3-6b, and it is clearly observable the transition of intensity in vibration mode by pH changes. Based on the computational chemistry, it is possible to verify the experimental result with theoretical calculation, and it also identify the closely appeared bands. But, it is very hard to match the experimental data and theoretical value by saving the computational resource or simplifying the molecular structure; thus, there is always the possibility of error from the theoretical calculation (Bhandari et al., 2010; Klahn et al., 2004; Watts et al., 2014; Yaguchi et al., 2016).

#### 3.4.3. Data interpretation

Based on the approaches we described above, it is important to understand the structural configuration by the environmental changes. The absorbance of each band in Fig. 3-4a, the concentration profile in Fig. 3-5c and the deconvoluted peak area in Fig 3-6c show the information how the phosphate species transformed by the pH change. The proposed methods enable us to identify the individual band from the complexly overlapped spectra, and it is also possible to calculate the distribution

**Fig. 3-5** Contour map of aqueous phosphate speciation measured by pH change using *in situ* ATR-FTIR (a), two identified spectrum and its experimental peak position calculated using DFT (b), pH versus concentration graph fitted by MCR-ALS (c). Red and blue bar in (b) indicate theoretically calculated peak position using DFT (B3LYP, 6-31G).

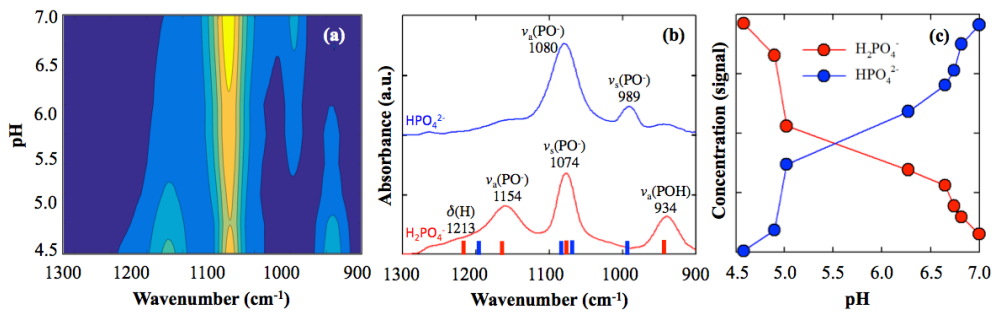
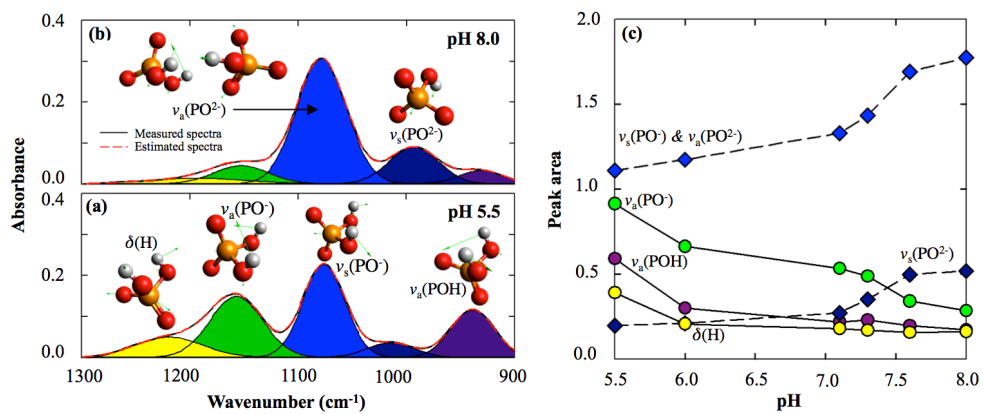


**Fig. 3-6** Peak deconvolution spectrum at pH 5.5 (a) and 8.0 (b), and the assigned vibrational mode for each deconvoluted peak, and deconvoluted peak area change as function of pH (c). Black solid and red dotted lines indicate measured spectra and estimated spectra for (a) and (b), and black solid and black dotted lines in (c) indicate spectrum of  $\text{H}_2\text{PO}_4^-$  and  $\text{HPO}_4^{2-}$ , respectively.



of each band by calculating the concentration profile or peak area. In this review, the simple aqueous phosphate solution was demonstrated to improve the understanding, but if the metal (hydr)oxide is added in this protocol, we can also identify the geometry and calculate the distribution and fraction of phosphate complex. I expected that the further development in the signal processing and infrared spectroscopy would analyze the complex reaction in the soil environment eventually, and the process to reach there will enable us to understand the interfacial reactions of numerous contributors.

### **3.5. Experimental measurement using XAS**

The XAS is one of the most powerful tools to characterize the chemical and physical properties of atoms, and its surrounding environment using X-ray beam generated by synchrotron radiation, which provides an incomparable flux of light than X-ray instrument in a laboratory (Newville, 2014). The invention of XAS studies has accelerated the characterization on the nano-scale reactions, and it has provided us better insight to understand the reactions in nature (Kuzmin and Chaboy, 2014). Besides, the XAS is applied for both amorphous and crystallized structure, and it is element specific and sensitive to high dilutions. The complex on the solid-solution interface is also measurable using XAS; thus numerous studies already conducted in the multidisciplinary fields of studies, such as chemistry, physics, biology, earth, material and environmental science (Kuzmin and Chaboy, 2014; Newville, 2014; Yano and Yachandra, 2009).

#### **3.5.1. History and technique in XAS**

Since Röntgen's discovery of X-ray, X-ray based analytical chemistry had developed, and X-ray diffraction (XRD) was the first widespread scientific tool for the

environmental study to identify the crystal structure of solid-state sample (Mottana and Marcelli, 2013). The XRD improves the understanding of the soil and geological process, but it could not get any information on the amorphous materials and liquid solution. The characteristics of XAS could not receive the attention, but the development in the particle accelerator; it enables us to characterize any materials in any phases (Mottana and Marcelli, 2013; Newville, 2014). The XAS (also referred as X-ray absorption fine structure can be categorized as X-ray absorption near-edge structure (XANES) and extended X-ray absorption fine structure (EXAFS) by measuring and analyzing the different incident energy on the sample, and the XANES provides us the local electronic structure, and the EXAFS enables us to identify the structural configuration fo target element and it's surrounding.

The first XAS spectrum using synchrotron radiation was recorded in 1974, and the XANES was introduced by Antonio Biancoconi and Jo Stohr in 1980s (Mottana and Marcelli, 2013), and it is also called as near edge X-ray absorption fine structure (NEXAFS) in surface and molecular science generally. Farrel W. Lytle introduced the EXAFS in 1999, and he developed his theory by cooperation with Dale E. Sayers and Edward A. Stern (Mottana and Marcelli, 2013). Recent development in the computation, it is possible to analyze the XAS spectrum without perfect understanding the fundamental theory and difficult calculation.

### 3.5.2. Principle and consideration in XAS

The fundamental principle of XAS is that the X-ray interacts with the magnetic field, and the materials emitted by X-ray absorbs the X-ray by scattering or transmits, and the absorption is caused by the excitation of an electron with a transition to higher energy state. The absorption coefficient is calculated with Lambert's law of absorption (Eq. 3-6):

$$I = I_0 \cdot e^{-\mu t} \tag{Eq. 3-6}$$

where  $I_0$  and  $I$  are the x-ray intensity incident on a sample and the x-ray intensity after the absorption by the sample, respectively.  $t$  is the thickness of a sample, and  $\mu$  is the absorption coefficient. It is for the measurement using transmission mode, and there is an additional fluorescent mode for the detection. There are two mechanisms for the decay of excited atomic state by the x-ray absorption, which is x-ray fluorescence and Auger effect. In the soft x-ray region ( $< 2\text{KeV}$ ), the Auger emission is dominant while the fluorescence is mainly occurred in hard x-ray region ( $> 2\text{KeV}$ ). Based on the instrument setup on XAFS, the x-ray region would be differed, and 7D beamline in Pohang accelerator laboratory is used for the XAFS measurement in this study, only hard x-ray region was investigated (5-30 KeV). The K edge of phosphorus, iron, and arsenic is 2.145, 7.112 and 11.867 KeV, respectively; thus, the K edge of iron and arsenic was investigated in this study by fluorescence mode more frequently than transmission.

The XANES analyzes the region near the absorption edge, and the white line in the absorption edge indicates the bonding of target atom and oxygen, and it indicates the oxidation states by comparing the sample with reference materials or theoretical calculations. However, the EXAFS analysis is more abstruse than the XANES analysis. The EXAFS interprets the oscillation above the absorption edge and EXAFS function  $\chi(E)$  with following Eq. 3-7:

$$\chi(E) = (\mu(E) - \mu_0(E)) / \Delta\mu_0(E) \quad \text{(Eq. 3-7)}$$

where  $\mu(E)$  is the measured absorption coefficient while  $\mu_0(E)$  is background function representing the absorption of an isolated atom.  $\Delta\mu_0(E)$  is the difference between before and after the absorption in absorption edge. The  $\chi(E)$  is frequently converted to the wave number of the photo-electron ( $k$ ) by following Eq. 3-8:

$$k = \sqrt{2m(E - E_0) / \hbar^2} \quad \text{(Eq. 3-8)}$$

where  $E_0$  is the absorption edge energy, and  $m$  is the electron mass. The EXAFS is

oscillatory, it decays with the increase of  $k$ , and it is multiplied by a power of  $k^2$  or  $k^3$  to emphasize the oscillation. The  $\chi(k)$  can be calculated with following Eq. 3-9:

$$\chi(k) = -\sum_j \frac{N_j f_j(k) e^{-2k^2 \sigma_j^2}}{k R_j^2} \cdot \sin[2k R_j^2 + \delta_j(k)] \quad (\text{Eq. 3-9})$$

where  $f(k)$  and  $\delta(k)$  are the atom scattering properties,  $N$  is the number of neighboring atoms,  $R$  is the distance to the neighboring atom,  $\sigma^2$  is the disorder in the neighbor distance. It is hard to understand the equation, but it is possible to determine the parameters ( $N$ ,  $R$ , and  $\sigma^2$ ) by solving the equation.

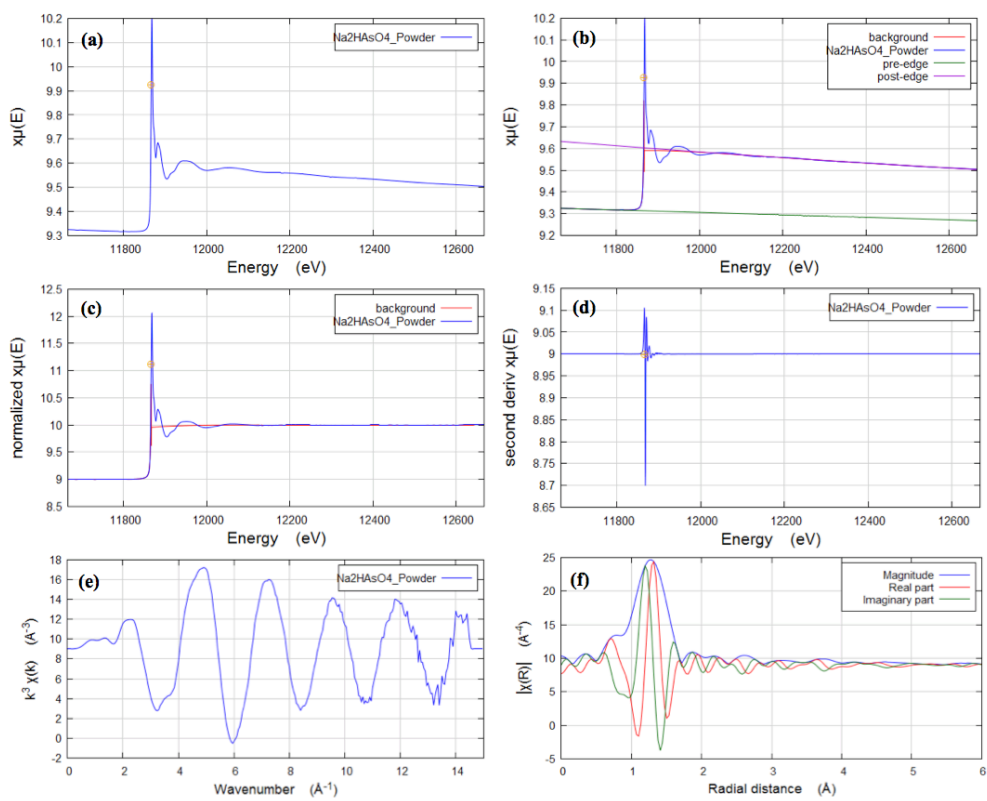
### 3.6. Spectral interpretation of XAFS

#### 3.6.1. Spectrum reduction

A data reduction should be performed for analyzing the XAFS spectra for XANES or EXAFS with transmission or fluorescence mode. First, the measured intensity should be converted to  $\mu(E)$  by the Eq. 3-6 (Fig. 3-7a), and the subtraction of pre-edge function should be performed from  $\mu(E)$  to remove the effect such as absorption from other edge and noise from instrument (Fig. 3-7b) (Newville, 2014). The  $E_0$  should be determined by calculating the derivative of  $\mu(E)$  or with other functions (Fig. 3-7d), and the  $\mu(E)$  should be normalized for XANES analysis (Fig. 3-7c). And the background function should be applied to remove the post-edge, and the EXAFS analysis should be conducted for further analysis (Kuzmin and Chaboy, 2014; Ravel et al., 2014). A Fourier transform from  $k$ -space to  $R$ -space is frequently employed to show the number of neighboring atoms and its distance from the target element (Fig. 3-7e and 3-7f). The XAFS software easily conducts all the data reduction process.

#### 3.6.2. Structure identification

**Fig. 3-7** Data reduction process of XAFS spectra using  $\text{Na}_2\text{HAsO}_4$  powder as an example. Raw data of XAFS spectra (a), background, pre-edge and post-edge identification using Athena software (b), normalized spectra with background (c), 2<sup>nd</sup> derivative of spectra for  $E_0$  identification, conversion to  $k^3$ -space (e), and Fourier transform to  $R$ -space (d).



For the XAFS study in the environmental science, it is still hard to estimate the structural configuration (Paktunc, 2004). There are two types of approach, and if we know or predict the structure, FeFF calculation shows the theoretical EXAFS spectrum from the known or predicted structure (Newville, 2014; Paktunc, 2004). The comparison between the theoretical and experimental EXAFS spectra enables us to confirm the structure as the easy way. In case of material science and engineering, this approach is frequently employed, but it is not able to the most the researchers who analyze the environmental samples. On the contrary, if we have only experimental EXAFS spectra, and it is impossible to identify the structure, the most of environmental samples are heterogeneous, and various complexes could co-exist in a sample (Paktunc, 2004). The adsorption study with trace element on the surface is more abstruse because of a low concentration of target element in the sample (Ravel et al., 2014; Yano and Yachandra, 2009).

To solve such problems, there are commonly four types of techniques, which are fingerprinting, linear combination fitting (LCF), principal component analysis (PCA) and modeling (Calvin, 2014). If we found the distance of intense bands, we just compare the distance with previous studies, and it is called as the fingerprinting method, and it is similar with the XRD analysis. The LCF is frequently used for calculating the individual fraction of mixture sample, and it should be awarded that the individual structure of the sample, but in most case, it is not applicable for adsorption study. The PCA is applicable when the data is series set, and the mathematical calculation identifies the individual component from the series-change. The modeling is the most frequently used for characterizing the structural configuration of the adsorbed complex (Calvin, 2014; Newville, 2014).

The modeling could be categorized into two types by employing the experimental or theoretical structure. If we use the experimental structure obtained

from other studies such as XRD and TEM, we could conduct the shell fitting by estimating parameters such as  $N$ ,  $\Delta R$ , and  $\sigma^2$ . For example, the scorodite is commonly used for shell fitting on arsenate sorption on the iron (hydr)oxides, and two single scatterings of As-Fe are calculated in 3.35 and 3.39 Å, and the shell fitting fits the spectra by varying the parameters. And, we also calculate the optimized geometry of complex based on the computational chemistry, which is described above. Based on the theoretical structure, we also conduct the shell fitting, and if there is several complex together, we can combine the modeling and LCF together to estimate the fraction of each complex; however, it is hard to estimate the theoretical structures, and the limitation on the computing resource and time only allows us to predict the more simple version of structure than the real structure. The combination of appropriate techniques would yield better interpretation, and further development in computational chemistry would enable us to understand the real reaction in the environment.

### **3.7. Sorbent characterization**

In this study, the nano-sized iron (hydr)oxides were used for the experiment, and its transformation have reported from the numerous studies; thus it should be carefully assessed to interpret a solid explanation (Bolanz et al., 2011; Han and Ro, 2018). For example, the nanosized bernalite formation from the goethite was observed in the TEM analysis at pH 10 with the presence of arsenate, and it showed higher adsorption capacity of arsenate than the goethite by EDS analysis (Han and Ro, 2018). Numerous studies have analyzed the sorption characteristics on the sorbents, but the development in the nano-technology has identified the importance of stability recently. For that reason, we should carefully

observe the change in the sorbent characteristics during the experiment to extract a meaningful conclusion.

### 3.6.1. Elemental composition

In this study, the closed system was employed for the experiment; thus, the elemental composition should be constant over the time. There are several methods to quantify the elemental concentration and composition, but spectroscopic analysis by the atomic absorption spectroscopy (AA) or inductively coupled plasma spectroscopy (ICP) equipped with optical (ICP-OES) or mass detector (ICP-MS) is mainly employed, but the sample should be digested as aqueous or gas phase, which means the pretreatment is essential for the characterization. X-ray fluorescence (XRF) also frequently used, and it has an advantage that no pretreatment for characterization is necessary. Recent development in laser-induced breakdown spectroscopy (LIBS) equipped with optical or mass detector also enables us to measure the elemental composition without the pretreatment, but the method should be verified for further analysis. X-ray photoelectron spectroscopy (XPS) is a surface-sensitive quantification method with the information on the chemical and electronic states of the element. The EDS or XRF detector equipped with TEM or SEM provides us the elemental composition of local area, but it needs lots of extrapolation or measurement to characterize the elemental composition statistically.

### 3.6.2. Morphological characterization

The morphology is the critical factor governing the adsorption characteristics and stability of nanosized metal (hydr)oxides. The surface area is determined by the size of particle, and it also determines the colloidal properties of nanoparticles. The BET isotherm by adsorbing N<sub>2</sub> or CO<sub>2</sub> provides us the

information on the surface area. The electron microscopy is mainly employed for the morphological characterization because the light limited the resolution of traditional microscopy (approximately 0.2  $\mu\text{m}$ ). The electron microscopy provides us much higher resolution (approximately  $< 0.5 \text{ \AA}$  in TEM), which is enough to identify the individual atom in the structure. Based on the detection way of an electron, electron microscopy can be categorized into transmission, scanning or scanning transmission electron microscopy (TEM, SEM, and STEM).

The TEM provides us an image with high resolution for morphological characterization and diffractogram by the diffraction, which contains the information on crystal structure while the SEM enables us to observe the morphology of aggregates, for example, the film formation in the ATR-FTIR study. The STEM equipped with additional scanning coils from the TEM, and it combines the advantages. The electron microscopy equipped with an additional detector for the spectroscopic mapping, such as energy dispersive X-ray spectroscopy (EDS or EDXS) and electron energy loss spectroscopy (EELS) and the XRF also equipped in the SEM for elemental quantification. The combination of image and mapping provides us the detailed information on the adsorption, and it is useful to characterize the preferential sorption in the mixture sorbents. Besides, there is a particle size analyzer by low-angle laser light scattering, dynamic light scattering, and photosedimentation methods, but the methods are only applicable for the nanoparticles with high stability. Single-particle ICP-MS (SP-ICP-MS) is also used for size characterization and quantification of nanoparticles (Mitrano et al., 2012).

### 3.6.3. Crystal structure identification

The crystal structure of metal (hydr)oxides determines the morphological and adsorption characteristics simultaneously; thus the identification of crystal

structure is essential to evaluate the stability of metal (hydr)oxides. As I described above, the electron diffraction using TEM or electron backscatter diffraction (EBSD) using SEM is the way to measure the crystal structure with the morphological characterization simultaneously. In addition, the XRD is the most common method for the determination, and the crystal structure is easily measurable, but it needs more samples than the diffraction using electron microscopy, which would be the obstacles in the nanoparticle study. As I discussed, the UV-Vis, IR, Raman, and NMR spectroscopy also identify the change of crystal structure in certain conditions, and there are several synchrotron-based methods for crystal structure, such as photoemission, magnetic and scattering spectroscopy. The difference in the crystal structure also could be detected by thermal methods, such as differential thermal and thermogravimetric analysis.

#### 3.6.4. Electrochemical characterization

The electrochemical properties of metal (hydr)oxides plays important role in the stability. Point of net zero charge (PNZC) is the most important factor controlling the colloidal properties in the solution. The solution pH after mixing with metal (hydr)oxides also the critical factor for adsorption study, because the most oxyanions have shown the pH-dependent sorption on the metal (hydr)oxides. Electrical conductivity (EC) could be the indirect index in the change of solute concentration and composition, because the EC is the function of concentration and valency of ions, and the fluctuation on the pH and EC could be monitored real-time by installing the probe in the reactor. For example, the dissolution of goethite ( $\text{FeOOH}$ ) as ferric ion requires 3 protons; thus, the pH would be decreased, and the EC would be increased by the dissolved ions.

## References

- Amma, S.I., Luo, J., Pantano, C.G., Kim, S.H., 2015. Specular reflectance (SR) and attenuated total reflectance (ATR) infrared (IR) spectroscopy of transparent flat glass surfaces: A case study for soda lime float glass. *J. Non. Cryst. Solids* 428, 189–196. doi:10.1016/j.jnoncrysol.2015.08.015
- Baetz, U., Martinoia, E., 2014. Root exudates: the hidden part of plant defense. *Trends Plant Sci.* 19, 90–8. doi:10.1016/j.tplants.2013.11.006
- Bais, H.P., Weir, T.L., Perry, L.G., Gilroy, S., Vivanco, J.M., 2006. The role of root exudates in rhizosphere interactions with plants and other organisms. *Annu. Rev. Plant Biol.* 57, 233–266. doi:10.1146/annurev.arplant.57.032905.105159
- Becke, A.D., 1993. Density-functional thermochemistry. III. The role of exact exchange. *J. Chem. Phys.* 98, 5648. doi:10.1063/1.464913
- Bekiaris, G., Bruun, S., Peltre, C., Houot, S., Jensen, L.S., 2015. FTIR-PAS: A powerful tool for characterising the chemical composition and predicting the labile C fraction of various organic waste products. *Waste Manag.* 39, 45–56. doi:10.1016/j.wasman.2015.02.029
- Bhandari, N., Hausner, D.B., Kubicki, J.D., Strongin, D.R., 2010. Photodissolution of ferrihydrite in the presence of oxalic acid: An in situ ATR-FTIR/DFT study. *Langmuir* 26, 16246–16253. doi:10.1021/la101357y
- Blinder, S., 1965. Basic concepts of self-consistent-field theory. *Am. J. Phys.* 33, 431. doi:10.1119/1.1971665
- Bolanz, R.M., Majzlan, J., Ackermann, S., 2011. The effect of Sb(V) on the transformation of ferrihydrite to goethite, hematite, and ferroxhyte. *Mineral. Mag.* 75, 546-.
- Brechbühl, Y., Christl, I., 2012. Competitive sorption of carbonate and arsenic to hematite: Combined ATR-FTIR and batch experiments. *J. Colloid Interface Sci.* 377, 313–321. doi:10.1016/j.jcis.2012.03.025
- Calvin, S., 2014. XAFS for Everyone, Igarss 2014. doi:10.1007/s13398-014-0173-7.2
- Carabante, I., Grahn, M., 2010. In situ ATR-FTIR studies on the competitive adsorption of arsenate and phosphate on ferrihydrite. *J. Colloid Interface Sci.* 351, 523–531. doi:10.1016/j.jcis.2010.07.064
- Cerkez, E.B., Bhandari, N., Reeder, R.J., Strongin, D.R., 2015. Coupled Redox Transformation of Chromate and Arsenite on Ferrihydrite. *Environ. Sci. Technol.* 49, 2858–2866. doi:10.1021/es505666w
- de Juan, A., Tauler, R., 2006. Multivariate Curve Resolution (MCR) from 2000: Progress in Concepts and Applications. *Crit. Rev. Anal. Chem.* 36, 163–176. doi:10.1080/10408340600970005
- Du, J., Jing, C., Duan, J., Zhang, Y., Hu, S., 2014. Removal of arsenate with hydrous ferric oxide coprecipitation: Effect of humic acid. *J. Environ. Sci. (China)* 26, 240–247. doi:10.1016/S1001-0742(13)60437-4
- Elzinga, E.J., Huang, J.-H., Chorover, J., Kretzschmar, R., 2012. ATR-FTIR spectroscopy study of the influence of pH and contact time on the adhesion of *Shewanella putrefaciens* bacterial cells to the surface of hematite. *Environ. Sci. Technol.* 46, 12848–55. doi:10.1021/es303318y
- Elzinga, E.J., Sparks, D.L., 2007. Phosphate adsorption onto hematite: An in situ ATR-FTIR investigation of the effects of pH and loading level on the mode of phosphate surface complexation. *J. Colloid Interface Sci.* 308, 53–70. doi:10.1016/j.jcis.2006.12.061
- Fan, J.X., Wang, Y.J., Liu, C., Wang, L.H., Yang, K., Zhou, D.M., Li, W., Sparks, D.L., 2014. Effect of iron oxide reductive dissolution on the transformation and

- immobilization of arsenic in soils: New insights from X-ray photoelectron and X-ray absorption spectroscopy. *J. Hazard. Mater.* 279, 212–219. doi:10.1016/j.jhazmat.2014.06.079
- Fang, V., Kennedy, J., Futter, J., Manning, J., 2013. A review of near infrared reflectance properties of metal oxide nanostructures.
- Felten, J., Hall, H., Jaumot, J., Tauler, R., de Juan, A., Gorzsás, A., 2015. Vibrational spectroscopic image analysis of biological material using multivariate curve resolution–alternating least squares (MCR-ALS). *Nat. Protoc.* 10, 217–240. doi:10.1038/nprot.2015.008
- Frisch, M.J., Trucks, G.W., Schlegel, H.B., Scuseria, G.E., Robb, M. a., Cheeseman, J.R., Montgomery, J. a., Vreven, T., Kudin, K.N., Burant, J.C., Millam, J.M., Iyengar, S.S., Tomasi, J., Barone, V., Mennucci, B., Cossi, M., Scalmani, G., Rega, N., Petersson, G. a., Nakatsuji, H., Hada, M., Ehara, M., Toyota, K., Fukuda, R., Hasegawa, J., Ishida, H., Nakajima, T., Honda, Y., Kitao, O., Nakai, H., Klene, M., Li, X., Knox, J.E., Hratchian, H.P., Cross, J.B., Adamo, C., Jaramillo, J., Gomperts, R., Stratmann, R.E., Yazyev, O., Austin, A.J., Cammi, R., Pomelli, C., Ochterski, J., Ayala, P.Y., Morokuma, K., Voth, G. a., Salvador, P., Dannenberg, J.J., Zakrzewski, V.G., Dapprich, S., Daniels, A.D., Strain, M.C., Farkas, O., Malick, D.K., Rabuck, A.D., Raghavachari, K., Foresman, J.B., Ortiz, J.V., Cui, Q., Baboul, A.G., Clifford, S., Cioslowski, J., Stefanov, B.B., Liu, G., Liashenko, A., Piskorz, P., Komaromi, I., Martin, R.L., Fox, D.J., Keith, T., Al-Laham, M. a., Peng, C.Y., Nanayakkara, A., Challacombe, M., Gill, P.M.W., Johnson, B., Chen, W., Wong, M.W., Gonzalez, C., Pople, J. a., 2009. Gaussian 09W Tutorial. an Introd. To Comput. Chem. Using G09W Avogadro Softw. 34.
- Froese Fischer, C., 1987. General Hartree-Fock program. *Comput. Phys. Commun.* 43, 355–365. doi:10.1016/0010-4655(87)90053-1
- Glotch, T.D., Rossman, G.R., 2009. Mid-infrared reflectance spectra and optical constants of six iron oxide/oxyhydroxide phases. *Icarus* 204, 663–671. doi:10.1016/j.icarus.2009.07.024
- Griffiths, T.R., Hubbard, H.V.S.A., 1991. Absorption spectrum of single-crystal UO<sub>2</sub>: Identification of and effect of temperature on the peak positions of essentially all optical transitions in the visible to near infrared regions using derivative spectroscopy. *J. Nucl. Mater.* 185, 243–259. doi:10.1016/0022-3115(91)90510-E
- Gunnarsson, M., 2002. Surface Complexation at the Iron Oxide/Water Interface.
- Hamers, R.J., Stavis, C., Pokhrel, A., Franking, R., Ruther, R.E., Wang, X., Cooperrider, M.C., Zheng, H., Carlisle, J.A., Butler, J.E., 2011. Characterization of molecular and biomolecular layers on diamond thin films by infrared reflection-absorption spectroscopy. *Diam. Relat. Mater.* 20, 733–742. doi:10.1016/j.diamond.2011.03.022
- Han, J., Ro, H., 2018. Identification of Bernalite Transformation and Tridentate Arsenate Complex at Nano- goethite under Effects of Drying , pH and Surface Loading. *Sci. Rep.* 1–10. doi:10.1038/s41598-018-26808-4
- Hanwell M.D. Lonie D.C., Vandermeersch, T., Zurek E., Hutchison, G., C.D.E., 2012. Avogadro: An Advanced Semantic Chemical Editor, Visualisation, and Analysis Platform. *J. Chem. Informatics* 4, 1–17.
- Hase, M., Scheffelmaier, R., Hayden, S., Rivera, D., 2010. Quantitative in situ attenuated total internal reflection fourier transform infrared study of the isotherms of Poly(sodium 4-styrene sulfonate) Adsorption to a TiO<sub>2</sub> Surface over a range of cetylpyridinium bromide monohydrate concentration. *Langmuir* 26, 5534–5543. doi:10.1021/la903787t

- Hebert, G.N., Odom, M.A., Bowman, S.C., Strauss, S.H., 2004. Attenuated Total Reflectance FTIR Detection and Quantification of Low Concentrations of Aqueous Polyatomic Anions. *Anal. Chem.* 76, 781–787. doi:10.1021/ac034915i
- Hind, A.R., Bhargava, S.K., McKinnon, A., 2001. At the solid/liquid interface: FTIR/ATR--the tool of choice. *Adv. Colloid Interface Sci.* 93, 91–114. doi:10.1016/S0001-8686(00)00079-8
- Huang, J.B., Urban, M.W., 1992. Evaluation and Analysis of Attenuated Total Reflectance FT-IR Spectra Using Kramers-Kronig Transforms. *Appl. Spectrosc.* 46, 1666–1672. doi:10.1366/0003702924926970
- Hwang, Y.S., Lenhart, J.J., 2008. Adsorption of C4-dicarboxylic acids at the hematite/water interface. *Langmuir* 24, 13934–13943. doi:10.1021/la801793p
- Jaumot, J., de Juan, A., Tauler, R., 2015. MCR-ALS GUI 2.0: New features and applications. *Chemom. Intell. Lab. Syst.* 140, 1–12. doi:10.1016/j.chemolab.2014.10.003
- Kessler, W., Kessler, R.W., 2006. Multivariate curve resolution: A method of evaluating the kinetics of biotechnological reactions. *Anal. Bioanal. Chem.* 384, 1087–1095. doi:10.1007/s00216-005-0077-7
- Kim, K., Owens, G., Naidu, R., 2010. Effect of root-induced chemical changes on dynamics and plant uptake of heavy metals in rhizosphere soils. *Pedosphere* 20, 494–504. doi:10.1016/S1002-0160(10)60039-2
- Kim, N., Yoon, S., Park, G., 2012. Introduction to Computational Chemistry Namseok. *KIC News* 15, 23–27.
- Kira, O., Linker, R., Shaviv, A., 2014. A Novel Method Combining FTIR-ATR Spectroscopy and Stable Isotopes to Investigate the Kinetics of Nitrogen Transformations in Soils. *Soil Sci. Soc. Am. J.* 78, 54. doi:10.2136/sssaj2013.08.0358dgs
- Klahn, M., Mathias, G., Kotting, C., Nonella, M., Schlitter, J., Gerwert, K., Tavan, P., 2004. IR Spectra of Phosphate Ions in Aqueous Solution: Predictions of a DFT / MM Approach Compared with Observations. *J. Phys. Chem. A* 108, 6186–6194.
- Kubicki, J., Paul, K., Kabalan, L., Zhu, Q., 2012. ATR-FTIR and Density Functional Theory Study of the Structures, Energetics, and Vibrational Spectra of Phosphate Adsorbed onto Goethite. *Langmuir* 28, 14573–14587.
- Kuzmin, A., Chaboy, J., 2014. EXAFS and XANES analysis of oxides at the nanoscale. *IUCrJ* 1, 571–589. doi:10.1107/S2052252514021101
- Lawton, W.H., Sylvestre, E.A., 1971. Self Modeling Curve Resolution. *Technometrics* 13, 617–633. doi:10.1080/00401706.1971.10488823
- Lefevre, G., 2004. In situ Fourier-transform infrared spectroscopy studies of inorganic ions adsorption on metal oxides and hydroxides. *Adv. Colloid Interface Sci.* 107, 109–123. doi:10.1016/j.cis.2003.11.002
- Lindegren, M., Persson, P., 2009. Competitive adsorption between phosphate and carboxylic acids: Quantitative effects and molecular mechanisms. *Eur. J. Soil Sci.* 60, 982–993. doi:10.1111/j.1365-2389.2009.01171.x
- Madejová, J., 2003. FTIR techniques in clay mineral studies. *Vib. Spectrosc.* 31, 1–10.
- Max, J.-J., Chapados, C., 2009. Isotope effects in liquid water by infrared spectroscopy. III. H<sub>2</sub>O and D<sub>2</sub>O spectra from 6000 to 0 cm<sup>-1</sup>. *J. Chem. Phys.* 131, 184505. doi:10.1063/1.3258646
- McGeehan, S.L., Fendorf, S.E., Naylor, D. V., 1998. Alteration of arsenic sorption in flooded-dried soils. *Soil Sci. Soc. Am. J.* 62, 828–833.
- Mitrano, D.M., Barber, A., Bednar, A., Westerhoff, P., Higgins, C.P., Ranville, J.F., 2012. Silver nanoparticle characterization using single particle ICP-MS (SP-ICP-MS) and

- asymmetrical flow field flow fractionation ICP-MS (AF4-ICP-MS). *J. Anal. At. Spectrom.* 27, 1131. doi:10.1039/c2ja30021d
- Mottana, A., Marcelli, A., 2013. The historical development of X-ray Absorption Fine Spectroscopy and of its applications to Materials Science 1–46. doi:10.1007/978-94-017-9645-3\_15
- Mudunkotuwa, I. a, Minshid, A. Al, Grassian, V.H., 2014. ATR-FTIR spectroscopy as a tool to probe surface adsorption on nanoparticles at the liquid-solid interface in environmentally and biologically relevant media. *Analyst* 139, 870–81. doi:10.1039/c3an01684f
- Müller, K., Lefèvre, G., 2011. Vibrational characteristics of outer-sphere surface complexes: Example of sulfate ions adsorbed onto metal (Hydr)oxides. *Langmuir* 27, 6830–6835. doi:10.1021/la200514z
- Newville, M., 2014. Fundamentals of XAFS. *Rev. Mineral. Geochemistry* 78, 33–74. doi:10.2138/rmg.2014.78.2
- Noda, I., 2015. Techniques of two-dimensional ( 2D ) correlation spectroscopy useful in life. *Biomed. Spectrosc. Imaging* 4, 109–127. doi:10.3233/BSI-150105
- Noda, I., 2009. Generalized Two-Dimensional Correlation Spectroscopy. *Front. Mol. Spectrosc.* 367–381. doi:10.1016/B978-0-444-53175-9.00013-1
- Owen, A.J., 1995. Uses of Derivative Spectroscopy. *Spectroscopy* 8.
- Paktunc, D., 2004. A computer program for analysing complex bulk XAFS spectra and for performing significance tests. *J. Synchrotron Radiat.* 11, 295–298. doi:10.1107/S0909049504003681
- Parikh, S.J., Lafferty, B.J., Sparks, D.L., 2008. An ATR-FTIR spectroscopic approach for measuring rapid kinetics at the mineral/water interface. *J. Colloid Interface Sci.* 320, 177–185. doi:10.1016/j.jcis.2007.12.017
- Pazderka, T., Kopecky Jr, V., 2008. 2D correlation spectroscopy and its application in vibrational spectroscopy using Matlab. *Tech. Comput. Prague* 978–80.
- Planinšek, O., Planinšek, D., Zega, A., 2006. Surface analysis of powder binary mixtures with ATR FTIR spectroscopy. *Int. J. Pharm.* 319, 13–19. doi:10.1016/j.ijpharm.2006.03.048
- Rakshit, S., Sallman, B., Davantès, A., Lefèvre, G., 2016. Tungstate (VI) sorption on hematite: An in situ ATR-FTIR probe on the mechanism. *Chemosphere* 1–7. doi:10.1016/j.chemosphere.2016.11.007
- Ravel, B., Group, S.S., Measurement, M., Division, S., Contact, L., Synchrotron, N., Source, L., 2014. A challenging EXAFS analysis problem.
- Rieppo, L., Saarakkala, S., Närhi, T., Helminen, H.J., Jurvelin, J.S., Rieppo, J., 2012. Application of second derivative spectroscopy for increasing molecular specificity of Fourier transform infrared spectroscopic imaging of articular cartilage. *Osteoarthr. Cartil.* 20, 451–9. doi:10.1016/j.joca.2012.01.010
- Ruckebusch, C., Blanchet, L., 2013. Multivariate curve resolution: A review of advanced and tailored applications and challenges. *Anal. Chim. Acta* 765, 28–36. doi:10.1016/j.aca.2012.12.028
- Ruckebusch, C., Duponchel, L., Huvenne, J.P., Saurina, J., 2004. Multivariate curve resolution of step-scan FTIR spectral data. *Vib. Spectrosc.* 35, 21–26. doi:10.1016/j.vibspec.2003.11.002
- Rudolph Dieter; Irmer, Gert, W.W.. F., 2006. Vibrational Spectroscopic Studies and Density Functional Theory Calculations of Speciation in the CO<sub>2</sub>-Water System . *Appl. Spectrosc.* 60, 130–144.
- Sabur, M.A., Al-Abadleh, H.A., 2015. Surface interactions of monomethylarsonic acid with

- hematite nanoparticles studied using ATR-FTIR : adsorption and desorption kinetics. *Can. J. Chem.* 93, 1297–1304. doi:10.1139/cjc-2015-0350
- Schrödinger, E., 1926. An undulatory theory of the mechanics of atoms and molecules. *Phys. Rev.* 28, 1049–1070. doi:10.1103/PhysRev.28.1049
- Selim, H.M., Zhang, H., 2013. Modeling Approaches of Competitive Sorption and Transport of Trace Metals and Metalloids in Soils: A Review. *J. Environ. Qual.* 42, 640. doi:10.2134/jeq2012.0323
- Shi, Q.-T., Yan, W., 2014. Adsorption of arsenate on lanthanum-impregnated activated alumina: In situ ATR-FTIR and two-dimensional correlation analysis study. *Chinese Chem. Lett.* 26, 200–204. doi:10.1016/j.ccl.2014.12.009
- Stephens, P.J., Devlin, F.J., Chabalowski, C.F., Frisch, M.J., 1994. Ab Initio Calculation of Vibrational Absorption and Circular Dichroism Spectra Using Density Functional Force Fields. *J. Phys. Chem.* 98, 11623–11627. doi:10.1021/j100096a001
- Su, C., Suarez, D.L., 2000. Selenate and Selenite Sorption on Iron Oxides. *Soil Sci. Soc. Am. J.* 64, 101. doi:10.2136/sssaj2000.641101x
- Szekeres, M., Tombácz, E., 2012. Surface charge characterization of metal oxides by potentiometric acid–base titration, revisited theory and experiment. *Colloids Surf., A* 414, 302–313. doi:10.1016/j.colsurfa.2012.08.027
- Taga, K., Kellner, R., Kainz, U., Sleytr, U., 1994. In Situ Attenuated Total Reflectance FT-IR Analysis of an Enzyme-Modified Mid-Infrared Fiber Surface Using Crystalline Bacterial Surface Proteins. *Anal. Chem.* 66, 35–39. doi:10.1021/ac00073a008
- Tauler, R., 2005. Multivariate Curve Resolution : theory and applications. Constraints.
- Tofan-Lazar, J., Al-Abadleh, H., 2012. Kinetic ATR-FTIR Studies on Phosphate Adsorption on Iron (Oxyhydr)oxides in the Absence and Presence of Surface Arsenic: Molecular-Level Insights into the Ligand Exchange Mechanism. *J. Phys. Chem. A* 116, 10143–10149.
- Udo, S., Rochelle, M.C., 2008. *Iron Oxides in the Laboratory. Preparation and Characterization*, Wiley-vch.
- VandeVondele, J., Tröster, P., Tavan, P., Mathias, G., 2012. Vibrational spectra of phosphate ions in aqueous solution probed by first-principles molecular dynamics. *J. Phys. Chem. A* 116, 2466–74. doi:10.1021/jp211783z
- Violante, A., 2013. Elucidating mechanisms of competitive sorption at the mineral/water interface. *Adv. Agron.* 118, 111–176. doi:10.1016/B978-0-12-405942-9.00003-7
- Waiman, C. V, Avena, M.J., Regazzoni, A.E., Zanini, G.P., 2013. A real time in situ ATR-FTIR spectroscopic study of glyphosate desorption from goethite as induced by phosphate adsorption: Effect of surface coverage. *J. Colloid Interface Sci.* 394, 485–489. doi:10.1016/j.jcis.2012.12.063
- Watts, H., Tribe, L., Kubicki, J., 2014. Arsenic Adsorption onto Minerals: Connecting Experimental Observations with Density Functional Theory Calculations. *Minerals* 4, 208–240. doi:10.3390/min4020208
- Wei, S., Tan, W., Liu, F., Zhao, W., Weng, L., 2014. Surface properties and phosphate adsorption of binary systems containing goethite and kaolinite. *Geoderma* 213, 478–484. doi:10.1016/j.geoderma.2013.09.001
- Wijnja, H., Schulthess, C.P.C., 2000. Vibrational Spectroscopy Study of Selenate and Sulfate Adsorption Mechanisms on Fe and Al (Hydr)oxide Surfaces. *J. Colloid Interface Sci.* 229, 286–297. doi:10.1006/jcis.2000.6960
- Yaguchi, M., Uchida, T., Motobayashi, K., Osawa, M., 2016. Speciation of Adsorbed Phosphate at Gold Electrodes: A Combined Surface-Enhanced Infrared Absorption Spectroscopy and DFT Study. *J. Phys. Chem. Lett.* 7, 3097–3102.

doi:10.1021/acs.jpcllett.6b01342

Yano, J., Yachandra, V.K., 2009. X-ray absorption spectroscopy. *Photosynth. Res.* 102, 241–254. doi:10.1007/s11120-009-9473-8

(This page intentionally left blank)

# **CHAPTER 4. IDENTIFICATION OF BERNALITE TRANSFORMATION AND TRIDENTATE ARSENATE COMPLEX AT NANO-GOETHITE UNDER DRYING, pH AND SURFACE LOADING**

## **List of contents**

<b>CHAPTER 4. IDENTIFICATION OF BERNALITE TRANSFORMATION AND TRIDENTATE ARSENATE COMPLEX AT NANO-GOETHITE UNDER DRYING, pH AND SURFACE LOADING</b>	<b>4-1</b>
List of contents	4-1
Abstract	4-2
4.1. Introduction	4-3
4.2. Material and methods	4-5
4.2.1. Physiochemical characterization	4-6
4.2.2. Batch experiment	4-6
4.2.3. High-resolution transmission electron microscopy	4-10
4.2.4. X-ray absorption spectroscopy measurement	4-10
4.2.5. Density functional theory calculation	4-13
4.2.6. Statistical analysis	4-14
4.3. Result and discussion	4-17
4.3.1. Sorption isotherm and aqueous iron concentration	4-17
4.3.2. Transformation at pH 10 with arsenate	4-18
4.3.3. EXAFS, DFT result and linear combination fitting	4-26
4.3.4. pH and surface loading effect on structural configuration	4-39
4.3.5. Drying effect on structural configuration	4-47
4.4. Environmental implication	4-49
References	4-53

## **Abstract**

The structural configuration of arsenate on the iron (hydr)oxide determines its leachability and bioavailability in the soil environment. It is important to understand how the stability of iron hydroxide and structural configuration of arsenate complexes varies in response to changes in environmental conditions. Therefore, we investigated the effects of drying, pH and surface loadings on the stability of goethite and structural configuration of arsenate through batch experiments and TEM and XAS measurements with DFT calculation. As the result, we observed no significant transformation of goethite under the most conditions, but TEM analysis confirmed a partial formation of bernalite in the presence of arsenate at pH 10, and the bernalite showed 2.18 times higher arsenate sorption than the goethite. Linear combination fitting of EXAFS spectrum with DFT calculations revealed that tridentate and bidentate complexes were dominant under low surface loading and pH in the sedimented samples, while monodentate complexes were abundant under high surface loading and pH. Based on our result, we concluded that the formation of arsenic rich colloidal could attribute the mobilization in the soil environment, and the density of available sorption site and the concentration of solute interactively cause the transition of the structural configuration.

## **Keywords**

Tridentate complex, EXAFS, DFT, Arsenate, Linear combination fitting, Surface loading

#### 4.1. Introduction

Arsenic is one of the most notorious elements in the earth because of its abundance, toxicity and usage worldwide (Jain and Ali, 2000; Leermakers et al., 2006). Over 20 countries have suffered from groundwater contamination by arsenic originating from the natural and anthropogenic sources, such as mining, agricultural chemicals and wood preservatives (Smedley and Kinniburgh, 2002; Zhang and Selim, 2006), which have accelerated arsenic contamination in the soil environment (Hyun et al., 2012; Singh et al., 2015; Zhang and Selim, 2006). Arsenic accumulation poses a serious threat to human and ecosystems health (Han et al., 2014; Hughes, 2002; Jain and Ali, 2000; Leermakers et al., 2006), since arsenate (major oxyanion form of arsenic) resembles phosphate and can block phosphate metabolism, causing various problems to humans (Hughes, 2002; Li et al., 2007; Ratnaike, 2003). However, it is extremely difficult to diminish such problems due to its distinctive dynamics in the soil environment such as species transformation, methylation, transport, precipitation and adsorption (Diaz-Bone et al., 2011; Leermakers et al., 2006; Rosen and Liu, 2009).

The soil is a heterogeneous aggregate of various materials, such as phyllosilicate, metal (hydr)oxide and organic matter. Among them, nanosized iron (hydr)oxides are reported as the key component to retain oxyanions, due to their relative abundance (4<sup>th</sup> abundant element), high surface area and charged surface (Claudio et al., 2017; Cornell and Schwertmann, 2003). In addition, the crystal structure and morphology also determine characteristics and govern the arsenate dynamic in the soil environment (Fan et al., 2014; Gotoh and Patrick, 1974; Michael Bolanz et al., 2013). Not only the sorbent characteristics but also the interaction between the arsenate and sorbent are important. There are two main

types of interaction, inner-sphere complex is adsorption through covalent bonds, while outer-sphere complex is adsorption by electrostatic attraction, dispersion interaction and hydrophobic effect. In addition, the inner-sphere complex can be a monodentate, bidentate or tridentate, and the structural configuration of inner-sphere complex is essential, because it determines the leachability and bioavailability of the arsenate in the soil environment (Loring et al., 2009; Rahnemaie et al., 2006; Sherman and Randall, 2003; Xu et al., 2006).

Numerous studies have attempted to reveal the structural configuration of arsenate on the iron oxides, but it is still controversial. A bidentate binuclear (BB) complex has been confirmed as the major structural configuration of arsenate on the iron oxides (Antelo et al., 2005; Farquhar et al., 2002; Fendorf et al., 1997; Gao et al., 2013; Morin et al., 2008; Neupane et al., 2014; Randall et al., 2001; Waychunas et al., 1993), but few studies also identified bidentate mononuclear (BM) (Fendorf et al., 1997; Neupane et al., 2014) and monodentate mononuclear (MM) complexes (Fendorf et al., 1997; Loring et al., 2009; Waychunas et al., 1993). Previous studies confirmed the transition of structural configuration by the environmental condition, Elzinga and Sparks (Elzinga and Sparks, 2007), Waychunas et al. (Waychunas et al., 1993), He et al. (He et al., 2009) and Abdala et al. (Abdala et al., 2015) reported the pH and surface loading effect on the transition, while Gu et al. (Gu et al., 2016) reported the drying effect. From the literature, it is clear that the transition of structural configuration is highly dependent on the environmental condition, but the inter-connection among the environmental conditions was not fully addressed yet.

In addition, the interpretation of adsorbed arsenate using extended X-ray absorption fine structure (EXAFS) technique is quite challenging because it has a relatively low signal to noise ratio and it is extremely difficult to construct a model

structure. For that reason, most of studies employed a scorodite as model structure for the shell fitting analysis. However, when we carefully reviewed the previous studies, we found a slight peak shifting around 2.4-2.7 Å by changing pH, surface loading and competition from the shell fitting results with the scorodite, and the studies reported that the multiple scattering was the reason. However, we observed the residual of fit decrease with pH and surface loading increase, and we thought that there is a possibility of unknown complex overlapped with the multiple scattering. In addition, recent studies also reported the possibility of a tridentate complex. Auffan et al.(Auffan et al., 2008) and Liu et al.(Liu et al., 2015) identified a tridentate hexanuclear complex of arsenite on maghemite and magnetite nanoparticles by X-ray absorption spectroscopy (XAS). And, Farrell(Farrell, 2017) showed the thermodynamic stability of the tridentate arsenate complex using density functional theory (DFT) calculation and the As-Fe distance was 2.41 Å in tridentate complex with one hydroxide cluster.

For that reason, the objectives of this study were to evaluate the stability of goethite, to examine the possibility of arsenate tridentate complex, and to identify the effect of drying, pH and surface loading on the stability and structural configuration of arsenate on nano-goethite. To do so, we confirmed the structural transformation of nano-goethite with environmental changes, determined the structural configuration of arsenate on the nano-goethite surface including a tridentate complex, and simulated the effect of pH and surface loading on arsenate complexation using a macroscale batch experiment and nanoscale high resolution transmission electron spectroscopy (HRTEM) and XAS measurements with the DFT calculation.

## **4.2. Materials and Methods**

#### 4.2.1. Physiochemical characterization

A rod-shaped nano-goethite (US3162) was purchased from US Research Nanomaterials (USA). To understand the crystal structure, we employed XRD using D8 Advance (Bruker, Germany) with Cu K $\alpha$  radiation from 5 to 90°. The XRD spectrum was compared to previous data from the American mineralogist crystal structure database (Downs and Hall-Wallace, 2003). Point of net zero charge was measured using the drift method (Yang et al., 2004), and pH was potentiometrically measured using Orion 5 Star (Thermo, USA) in 1:200 (W/V). A Brunauer-Emmett-Teller (BET) isotherm with N<sub>2</sub> gas was applied to measure surface area using ASAP 2010 (Micromeritics, USA) at 77 K. All characteristics of nano-goethite were summarized in Table 4-1, and the XRD diffractogram is illustrated in Fig. 4-1.

#### 4.2.2. Batch experiment

To evaluate the adsorption capacity of arsenate on the goethite surface, we employed batch experiments at various pH and arsenate concentrations. Briefly, 50 mL of arsenate solution at different concentrations (0, 0.1, 1, 5 and 10 mM) were mixed with 0.25 g of dried goethite in a 50 mL C-tube. All solutions contained 0.1 M of NaCl to maintain ionic strength. We employed a Langmuir isotherm to characterize the sorption behavior of arsenate on the nano-goethite with varying pH (4, 7 and 10), and we also conducted an iron dissolution experiment with or without arsenate concentration. After 48 h of incubation using a vertical shaker (Daehan, Korea) at 200 rpm at room temperature, we transferred the 10 mL samples to the 15 mL C-tube for further XAS analysis. We centrifuged the samples at 4,200 RCF for 1 h, and the 35 mL of supernatant was filtered with a 0.2- $\mu$ m PTFE syringe filter (Advantec, Japan). The supernatant readily acidified, and we used inductively coupled plasma optical emission spectroscopy (ICP-OES, Icap-7200, Thermo,

**Fig. 4-1** X-ray diffraction spectrum of goethite sample (black dot) and reference of goethite (blue bar, AMCSD-0003165) and bernalite (red bar, AMCSD-0001607) from the American mineralogist crystal structure database.

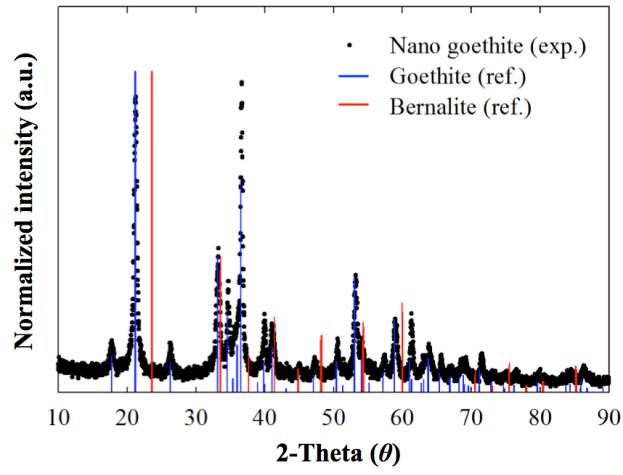


**Table 4-1** Physiochemical characteristics of nano-goethite.

Characteristics	Value
pH	6.13 (0.17)
EC ( $\mu\text{S cm}^{-1}$ )	0.137 (0.01)
PNZC	5.66
SA ( $\text{m}^2 \text{g}^{-1}$ )	83.9
Shape	rod
Size (nm)	50.3 x 10.8

EC electrical conductivity ( $\mu\text{S cm}^{-1}$ ); PNZC point of net zero charge; SA surface area ( $\text{m}^2 \text{g}^{-1}$ )  
pH and EC were measured at 1:200 (g:mL).

PNZC and SA were measured by drift method and  $\text{N}_2$ -BET method at 77 K, respectively.

The value in the parenthesis indicate standard deviation of triplicates

USA) to measure the arsenic and iron concentration in the solution. The centrifuged solid samples were oven-dried at 105 °C (24 h) for XAS measurement. The adsorbed arsenate was calculated by subtracting the initial amount from the aqueous amount. We schematically illustrated the procedure in Fig. 4-2. All reagents were purchased from Sigma-Aldrich (USA) with at least 98% purity.

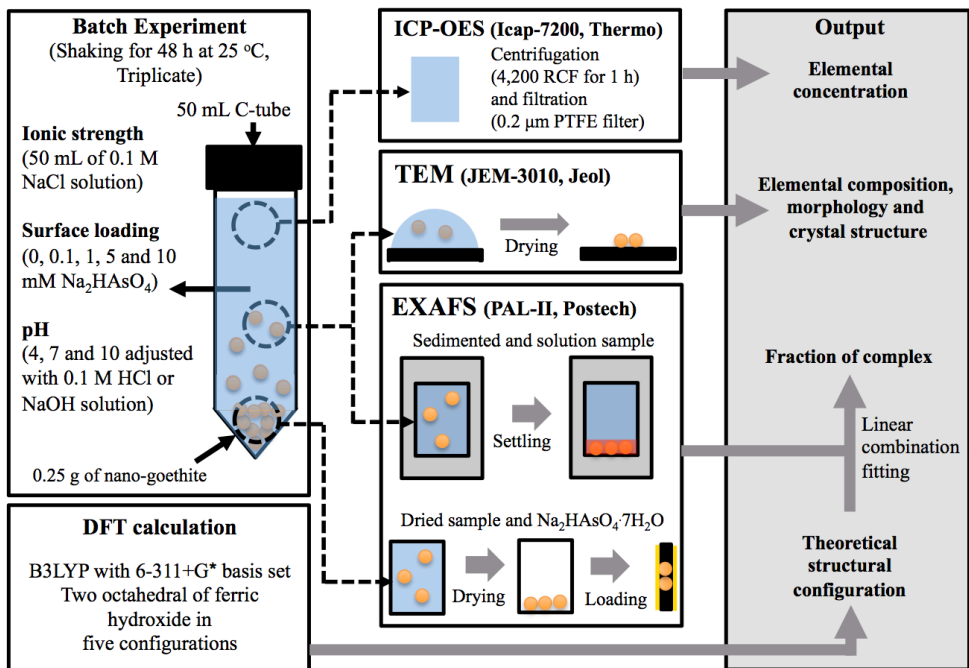
#### 4.2.3. High-resolution transmission electron microscopy

The shape, size, crystal structure and elemental composition of the nano-goethite at each treatment were analyzed by high resolution transmission electron spectroscopy (HRTEM) using a JEM-3010 (Jeol, Japan), and the digital image and elemental composition were obtained using a Gatan digital camera and energy dispersive spectroscopy (EDS), respectively. We put one drop of sample from the XAS sample (without acidification) into a carbon film on a copper grid, and it dried overnight in a dust-free chamber. The sample grid was placed in a 60-mm Petri dish (SPL, Korea) and sealed with Parafilm for subsequent analysis. We employed Digital Micrograph software (Gatan, USA) to analyze the shape and size calculations, and we used CrysTBox software (Institute of Physics Academy of Science, Czech Republic) to interpret the SAED pattern (Klinger et al., 2016).

#### 4.2.4. X-ray absorption spectroscopy measurement

Synchrotron-based XANES and EXAFS measurements were performed on the 7D beamline of the Pohang Accelerator Laboratory (PLS-II, 3.0 GeV, 360 mA). The XAS spectra were collected in transmission and fluorescence mode for the dried samples but only fluorescence mode for the sedimented samples. We employed a Si(111) double crystal monochromator at room temperature with helium purging, and we measured the K edge of As at 11.867 keV. We employed

**Fig. 4-2** Schematic illustration for the batch experiment, DFT calculation, ICP-OES, TEM and EXAFS measurement and the output from the interpretation.



the dried sample and sedimented sample to evaluate the drying effect on the structural configuration. The dried samples were ground for sample loading with kapton tape, and we used the handmade holder for the sedimented sample, which has an inside volume of 5 (width) x 20 (height) x 10 (depth) mm; we injected aqueous samples. The surface was sealed with kapton tape, and the samples were sedimented for 1 h before the XAS measurement. We used a sedimented goethite volume greater than the beam size, which was approximately 1 x 4 mm. We used  $\text{NaH}_2\text{AsO}_4 \cdot 7\text{H}_2\text{O}$  as the reference materials and measured 10 mM of aqueous arsenate at pH 4 and 10 for background. We employed the Demeter software package (version, 0.9.25)(Ravel and Newville, 2005) for normalization and background correction, and the spectra were converted to frequency ( $k$ ) space weighted by  $k^3$ . The  $k^3$ -weighted spectra were Fourier transformed to the R space using a Hanning window with  $k$  ranging from 3-11  $\text{\AA}^{-1}$ . Structural configuration from DFT calculations was employed for FEFF calculations using FEFF8.5 lite(Newville et al., 2009) to obtain the theoretical EXAFS spectrum.

#### 4.2.5. Density functional theory calculation

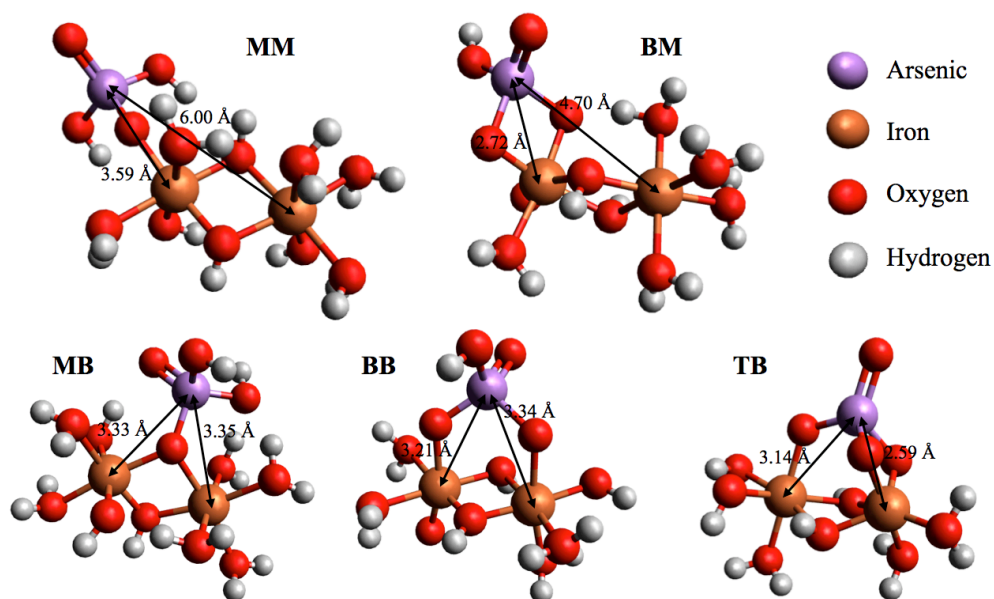
All calculations were conducted using the DFT in Gaussian 09 software through a Tachyon 2 supercomputer at the supercomputing center of the Korean Institute of Science and Technology Information (KISTI). The input file was generated with Avogadro software(Hanwell M.D. Lonie D.C., Vandermeersch, T., Zurek E., Hutchison, G., 2012). To calculate the geometry of arsenate on nano-goethite, we employed the density functional theory method B3LYP with the 6-311+G\* basis set. The nano-goethite was simulated with a dual octahedral configuration of ferric hydroxide, which has been used in several DFT studies of arsenate binding for iron hydroxides(Adamescu et al., 2014; Farrell, 2017; Sherman

and Randall, 2003). We proposed five clusters for the calculation without considering the protonation of oxyanion and ferric hydroxide; thus, all clusters have a net charge of zero. We simulated the BB, BM, MB, MM and TB complexes with dual ferric hydroxides (Fig. 4-3).

#### 4.2.6. Statistical analysis

We used LCF instead of shell fitting, and the reasons for that is: 1) We have no information on the scattering path of aqueous or precipitated arsenate, and it is difficult to predict the structure, but we have experimental EXAFS spectra of aqueous or precipitated arsenate; 2) there is the limitation on the variables to fit the spectra. We employed 5 DFT calculated structures with one aqueous or precipitated arsenate. We conducted shell fitting by assuming  $\Delta E_0=0$  and  $\sigma^2=0.0003$  (to reduce number of variables), and it showed similar result with LCF, but the fitting result was not suitable because of relatively high uncertainty with high number of variables; 3) Working in R-space allows us to selectively ignore higher coordination shells (Newville, 2014). The measured spectrum from EXAFS and calculated DFT spectrum were Fourier-transformed to R-space using the Athena software (Ravel and Newville, 2005) (Ravel and Newville, 2005), and the spectra were normalized and exported as CSV files within the R+ $\Delta R$  range from 1 to 4 Å. We conducted LCF analyses to semi-quantify the distribution of the complex with the pH and concentration changes. The protocol for LCF was derived from the study of Paktunc (2004) (Paktunc, 2004). We employed Marquardt-Levenberg algorithm for the least-squares fit (Marquardt, 1963). There are plenty of XAS data-analysis programs such as SIXPACK (Webb, 2005), Artemis (Ravel and Newville, 2005) and WinXAS (Ressler, 1997), and they enable us to do comprehensive data analysis, but the programs could not deal with the complex mixed spectra such as environmental

**Fig. 4-3** Optimized geometry by DFT calculation of B3LYP with 6-311+G\* basis set. The M, B and T as the first letter indicate dentation number—monodentate, bidentate and tridentate while the second letter show the number of nuclei—mononuclear and binuclear, respectively. The number indicates the atomic distance between As and Fe.



and geological samples, which are complex mixtures and essential to quantify the contribution of each component (Paktunc, 2004). The fraction of the complex making up the experimental EXAFS spectrum is calculated by solving a mass balance equation (Paktunc, 2004). We used Sigmaplot 10 (Systat, USA) to calculate the fraction with the LCF with least-squares fit, and we constrained the fraction to  $> 0$  and employed 500 fits with 2,000 iterations.

### 4.3. Results and Discussion

#### 4.3.1. Sorption isotherm and aqueous iron concentration

The arsenate adsorption on the goethite was measured by varying initial arsenate concentration (0, 0.1, 1, 5 and 10 mM) and pH (4, 7 and 10) for 48 h. We fitted the experimental data with Langmuir isotherm, and the result is illustrated in Fig. 4-4a. As a result, we found that the maximum adsorption capacities ( $\Gamma_{max}$ ) at pH 4, 7 and 10 were 2.24, 2.13 and 1.79 site  $\text{nm}^{-2}$ , while the Langmuir constant ( $K_L$ ) was 10.2, 4.70 and 2.09 L site $^{-1}$ , respectively. The adjusted coefficient of determination was 0.994, 0.978 and 0.992 for pH 4, 7 and 10, respectively. The increase in pH yielded the desorption of arsenate, and the difference in  $\Gamma_{max}$  dramatically increased at the change from pH 7 to 10 compared to the change from pH 4 to 7. Consistent with previous studies, the values were 1.49, 2.31 and 1.43 site  $\text{nm}^{-2}$ , respectively. We also found that  $K_L$  dramatically decreased with pH increase and was 10.2, 4.70 and 20.9 L site $^{-1}$  for pH 4, 7 and 10, respectively. The difference in  $K_L$  was higher at the change from pH 4 to 7 than from pH 7 to 10. Based on our result, we concluded that the pH significantly decreased the  $\Gamma_{max}$  and  $K_L$ , which implied that fewer surfaces were available, and less energy was favorable for arsenate sorption.

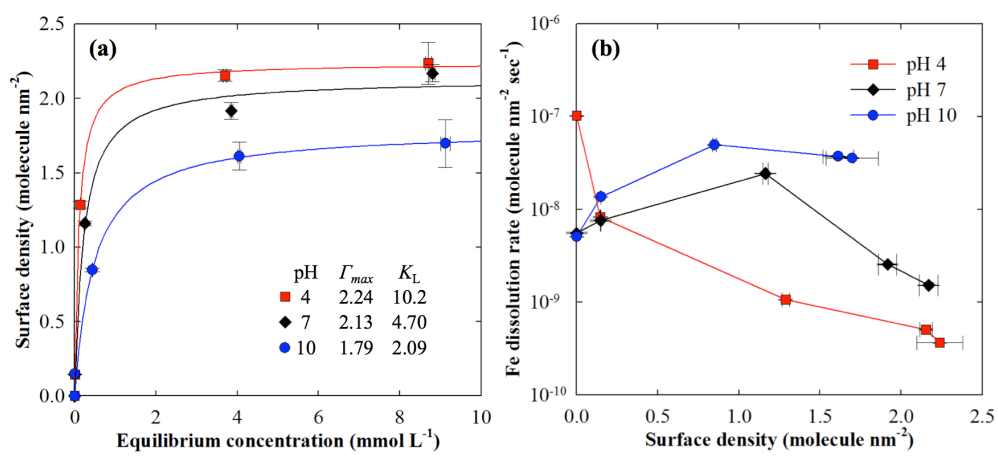
The dissolution rate of iron ( $\text{DR}_{\text{Fe}}$ ) with or without arsenate showed an

interesting result (Fig. 4-4b). We found a decrease of  $DR_{Fe}$  with arsenate increase at pH 4, caused by inner-sphere (IS) complexation. Once the IS complex forms at the surface, the complex needs more energy to dissolve iron from goethite; therefore,  $DR_{Fe}$  decreased with a surface density increase in arsenate (Erbs et al., 2010; Fan et al., 2014). The result showed a decrease in  $DR_{Fe}$  with a pH increase without arsenate and corresponded to previous studies (Gotoh and Patrick, 1974; Violante and Gaudio, 2006), but the  $DR_{Fe}$  pattern completely differed with arsenate concentration at pH 7 and 10. There was a maximum  $DR_{Fe}$  at 1 mM treatment of arsenate; it gradually decreased at pH 7 with arsenate increase, with no significant decrease at pH 10. We hypothesized two possible mechanisms for the explanation: formation of an aqueous arsenate-ferric ion complex and formation of a few nanosized iron precipitates with high surface charge. To test these, we used a UV-Vis spectrophotometer to determine the arsenate-ferric ion complex based on a previous study (Yang et al., 2015), and we confirmed the arsenate-ferric ion complex by measuring absorbance peak at 280 nm under pH 4 and 7 (data not shown). However, we could not find the arsenate-ferric ion complex in the aqueous phase at pH 10, but we observed background increase at Vis range, which indicated the formation of crystallized structure; thus, we utilized HRTEM to confirm the formation of nanosized iron precipitates.

#### 4.3.2. Transformation at pH 10 with arsenate

We measured HRTEM for all treatments with arsenate concentration (0 - 10 mM) and pH (4 - 10), and we observed three distinctive features in the treatments: square-shaped, rod-shaped and spherical particles. To identify each structure, we measured the selected area electron diffraction (SAED) pattern and element composition using HRTEM-EDS. As a result, we identified square-shaped

**Fig. 4-4** Langmuir sorption isotherm of arsenate (0, 0.1, 1, 5 and 10 mM initial concentration) on nano-goethite plotted with surface density at pH 4 (red), 7 (black) and 10 (blue) (a).  $\Gamma_{max}$  and  $K_L$  are the maximum surface density and Langmuir coefficient, respectively. Scatter plot between surface density and Fe dissolution rate (molecule nm<sup>-2</sup> sec<sup>-1</sup>) to explain co-presence of arsenate and pH effect on Fe dissolution rate (b). Error bars indicate standard deviation of three replicates.

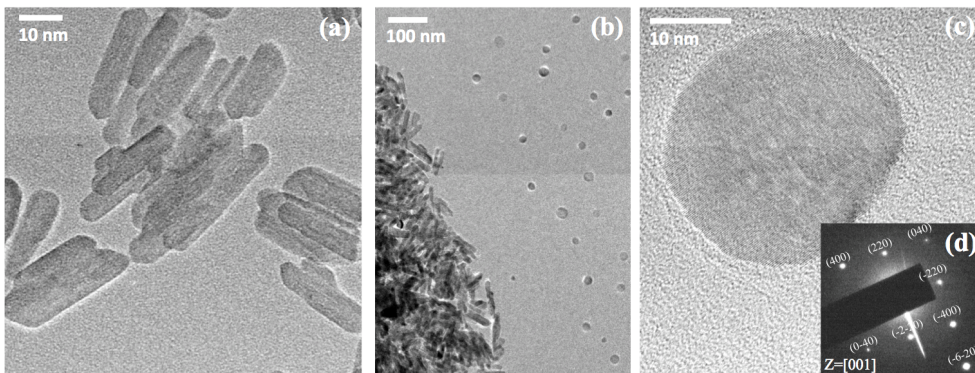


particles as a NaCl precipitate, because the EDS showed an approximately equal atomic ratio of Na and Cl elements with high abundance, and the size of square-shaped particle was varied from 30 - 200 nm, approximately. We classified rod-shaped particles as goethite (Fig. 4-5a) because the HRTEM image was identical to the specification sheet from the manufacturer, and the element composition of iron and oxygen was  $\text{Fe}_1\text{O}_{2.05}$ , which matches goethite's composition. The size of goethite was  $10.8 (\pm 2.1) \times 50.3 (\pm 11.9)$  nm ( $n = 151$ ), and we could not detect a significant decrease in size for all treatments; however, we found an increase in  $\text{DR}_{\text{Fe}}$ , which implied that goethite was dissolved into ferric ions, but the level of  $\text{DR}_{\text{Fe}}$  did not lead to a significant difference in size, because the dissolved ferric ion from the goethite was ranged from  $0.38 \times 10^{-4} \%$  to  $1.1 \times 10^{-2} \%$ . We also found that the degree of aggregation among the nano-size goethite increased with increased pH and arsenate concentration, but we were not able to quantify the aggregation in this experiment.

We assumed that the 48 hr incubation time would not yield any precipitation or transformation in the most conditions, but we observed spherical nanoparticles with  $27.3 (\pm 5.2)$  nm diameter ( $n = 158$ ) in the treatments with pH 10 and arsenate concentration (1-10 mM). We found that the abundance of spherical nanoparticles increased with arsenate concentration, and we could not find any in treatments at pH 10 with low arsenate concentration (0 - 0.1 mM). Based on the result, we presume that the spherical nanoparticle is dependent on arsenate and pH. Based on the literature review, we found several studies describing the transformation of goethite to other iron (hydr)oxide minerals in alkaline solution (Bolanz et al., 2011; Cudennec and Lecerf, 2006; Iwasaki et al., 2011; Michael Bolanz et al., 2013). The inter-transformation among the various iron (hydr)oxides is a well-known phenomenon in the environment, and the

transformation plays a key role in maintaining the ecosystem by retaining nutrients and pollutants and involving oxidation and reduction (Fakour and Lin, 2014; Fan et al., 2014; Michael Bolanz et al., 2013). For that reason, we suspected contamination during the experiment or drying process. We purchased new reagents, repeated the experiment, and used a tightly sealed box for drying with purified ambient air; however, the spherical nanoparticle was still found at pH 10 with high arsenate concentration. We measured the elemental composition using HRTEM-EDS, and O/Fe ratio of nano-goethite from 10 mM arsenate treatment was 2.19 ( $\pm 0.31$ ), 2.15 ( $\pm 0.15$ ) and 2.10 ( $\pm 0.42$ ) for pH 4, 7 and 10, while the spherical nanoparticle was 3.20 ( $\pm 0.27$ ). Without arsenate, the O/Fe ratio was 2.05 ( $\pm 0.09$ ), and we concluded that the arsenate complex on the surface was the reason for the oxygen concentration decrease on the goethite surface with increased pH. However, a distinctive elemental composition was found in spherical nanoparticles at pH 10, which was approximately 1.5-fold higher than goethite. We also found trace levels (less than 1% in atomic percent) of chromium, silica, and sulfur in all treatments, but the element was also detected in nanoparticle-free spots with EDS; thus, we excluded their contribution in the spherical nanoparticles. In the HRTEM analysis, we found rod-shaped goethite as large aggregates, but the spherical nanoparticle was only observed outside of the goethite aggregates, and the inter-particle distance was relatively constant without aggregation (Fig. 4-5b). This was hard to explain, but we presume that the formation from aqueous ions occurred during drying or inter-particle repulsion of previously formed nanoparticles by the high surface charge. During the drying process, the water volume decreases and it decreases the relative concentration of aqueous ions; thus, precipitation occurred, and numerous studies reported a drying effect on precipitation (Abdelwahed et al., 2006; Lin et al., 2005). However, in this case, the goethite aggregate holds the water longer by

**Fig. 4-5** HRTEM image of rod-shaped goethite (a) and spherical bernalite by transformation from goethite (c), their distribution at pH 10 with 10 mM arsenate concentration (b), and selected area electron diffraction pattern of spherical bernalite at  $Z = [001]$  (d). We only found bernalite at pH 10 with arsenate concentration, and the abundance of bernalite increased with arsenate concentration.



surface charge, so the precipitated nano-particle should form near the goethite aggregate. Ahn and Lee (2015) reported the formation of close-packed nanoparticles by partial drying, which can cause constant distance without aggregation. Both reactions could contribute to the phenomenon, but it was impossible to identify the specific mechanism for the formation of spherical nanoparticles. To identify the crystal structure, we tried to measure it using the fast Fourier transform function of digital micrograph software. We obtained d-spacings of 1.89, 2.69 and 2.71 Å from the spherical nanoparticle, and it was impossible to find the matched crystal structure from the reported transformation. We considered hematite the primary candidate because the thermal dehydration easily transformed the goethite to hematite *via* maghemite, and several studies have already discussed the formation of hematite (Bolanz et al., 2011; Vu et al., 2010). Ralph et al. (Michael Bolanz et al., 2013) examined the effect of antimonate, arsenate and phosphate on the transformation of iron (hydr)oxides, and the result showed that arsenate and phosphate favored hematite formation over goethite from the ferrihydrite, but no transformation occurred at high concentration (above 2.25 mM). In our laboratory, we also had 30-nm hematite purchased from US nano (US3160, USA), and it had similar d-spacing values, 1.84, 2.51 and 2.70 Å, by X-ray diffraction (XRD) analysis. However, the elemental composition and discordance in the [110] plane verified that the spherical nanoparticle was not hematite. Based on literature studies on the minor abundant iron (hydr)oxides, we found that bernalite (Fe(OH)<sub>3</sub>) was in accordance with the elemental composition (Birch et al., 1993). To characterize the crystal structure, we employed SAED pattern analysis. Fig. 4-5d shows the SAED pattern of spherical nanoparticles at the [001] axis. Based on the elemental composition and SAED pattern analysis, we confirmed the bernalite as the spherical nanoparticle. In addition, the EDS result showed that more arsenate was adsorbed

onto the bernalite surface because the As:Fe ratio on the goethite was 0.099, 0.093 and 0.083 for the treatments at pH 4, 7 and 10 in 10 mM arsenate, respectively, but 0.181 for bernalite. This implied that bernalite had higher sorption capacity per unit area; however, only 0.0025% of iron from the total iron weight (calculated from  $DR_{Fe}$ ) was assumed to involve bernalite nanoparticle formation as maximum; thus, we ignored the bernalite effect on the arsenate adsorption in further EXAFS measurements. However, the formation of bernalite in real environment would be significant because of the colloidal transportation in the presence of arsenate and high pH condition.

#### 4.3.3. EXAFS, DFT result and linear combination fitting

We tried to measure the XAS spectrum for 0.1, 1 and 10 mM arsenate concentrations at pH 4, 7 and 10 with dried and sedimented samples, but we could not measure the spectrum in the 0.1 mM treatment because we could not obtain a significant signal-to-noise ratio. We illustrated the experimental and theoretical As K-edge  $k^3$ -weighted EXAFS spectra of sedimented and dried samples in Fig. 4-6 and Fig. 4-7, respectively. We also showed As K-edge  $k^3$ -weighted spectrum of experimental and theoretical EXAFS in Fig. 4-8 and Fig. 4-9. We observed no difference in X-ray absorption near edge structure (XANES) for all treatments (Fig. 4-10), which indicated that no change was observed in the oxidation/reduction status of arsenate. We also measured the spectra of 10 mM arsenate solutions at pH 4 and 10 and the spectrum of  $Na_2HAsO_4 \cdot 7H_2O$  reagent to identify the background of aqueous and precipitated arsenate. We used the aqueous and precipitated spectra as references for further linear combination fitting (LCF). We found slight difference in the aqueous arsenate spectrum at pH 4 and 10, and there was difference by the multiple scattering path changed by the symmetry of arsenate

**Fig. 4-6** Fourier transform magnitude of As K-edge  $k^3$ -weighted EXAFS spectra in sedimented samples at various pH values (4, 7, 10) and concentrations (1, 10 mM) (a), experimental spectra of arsenate solution and  $\text{Na}_2\text{HAsO}_4 \cdot 7\text{H}_2\text{O}$  powder as the references, and theoretical spectra of five configurations by DFT calculation (b). The black line, red dotted line and grey line indicate the spectrum of experiment data, fit result and DFT calculation, respectively.

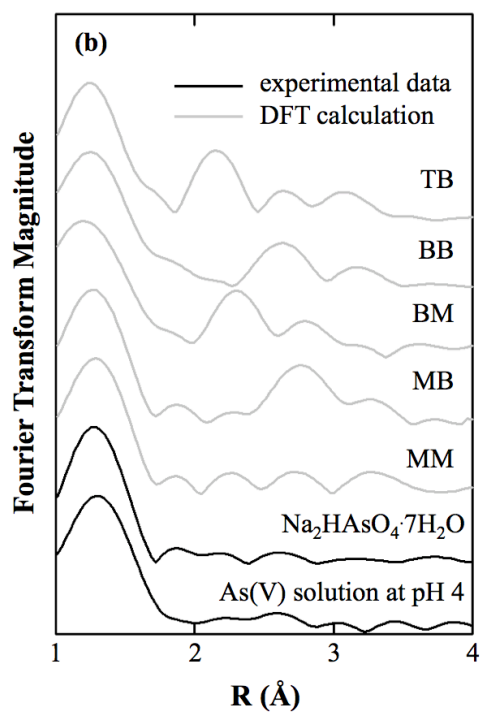
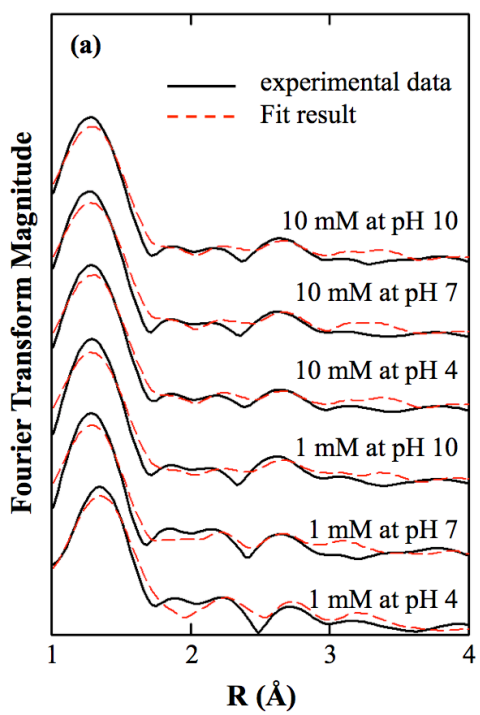


**Fig. 4-7** Fourier transform magnitude from As K-edge  $k^3$ -weighted EXAFS spectra of dried samples under various pH (4, 7 and 10) and surface loading (1 and 10 mM). The black solid line and red dashed line indicate the spectra of experimental data and fit result from linear combination fitting analysis, respectively.

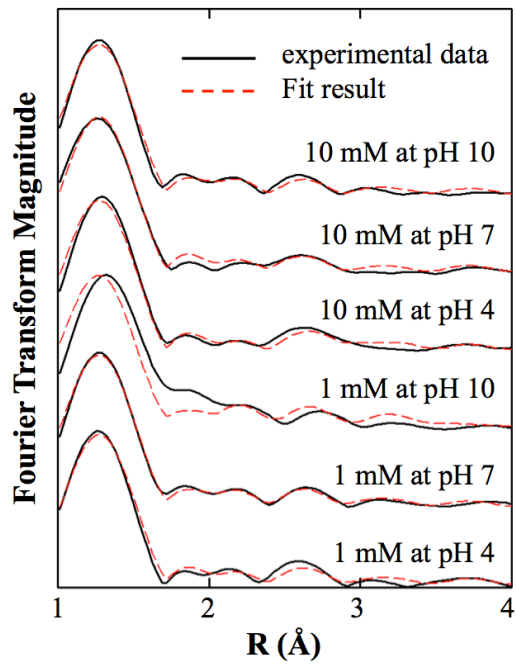


**Fig. 4-8** As K-edge  $k^3$ -weighted EXAFS spectra (a) and the corresponding Fourier transform magnitude (b) of 10 mM aqueous arsenate at pH 4 (red), 7 (black) and 10 (blue). 10 mM aqueous arsenate at pH 4 and 10 were measured by EXAFS, and 10 mM aqueous arsenate at pH 7 was merged with experimental spectrum of pH 4 and 10.

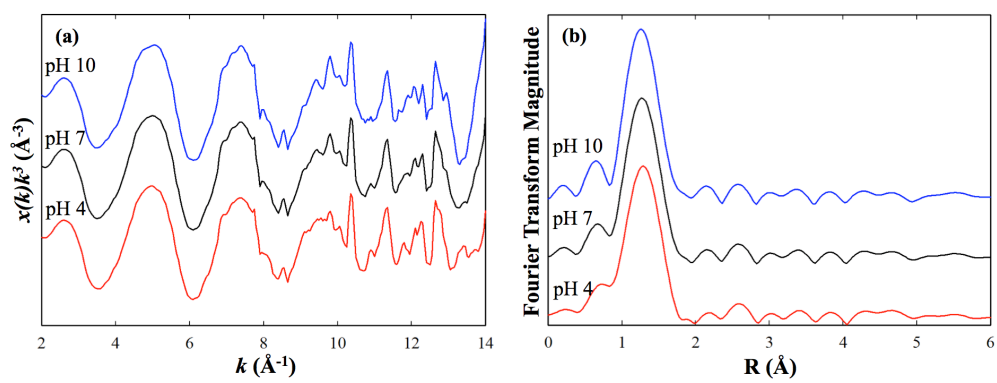


**Fig. 4-9** Experimental As K-edge  $k^3$ -weighted EXAFS spectra of 1 mM (dotted line) and 10 mM arsenate (solid line) on the goethite at pH 4 (red), 7 (black) and 10 (blue) under different sample phase (sedimented (top) and dried (middle)), and theoretical As K-edge  $k^3$ -weighted EXAFS spectra of five clusters of the complex from DFT calculation (bottom).

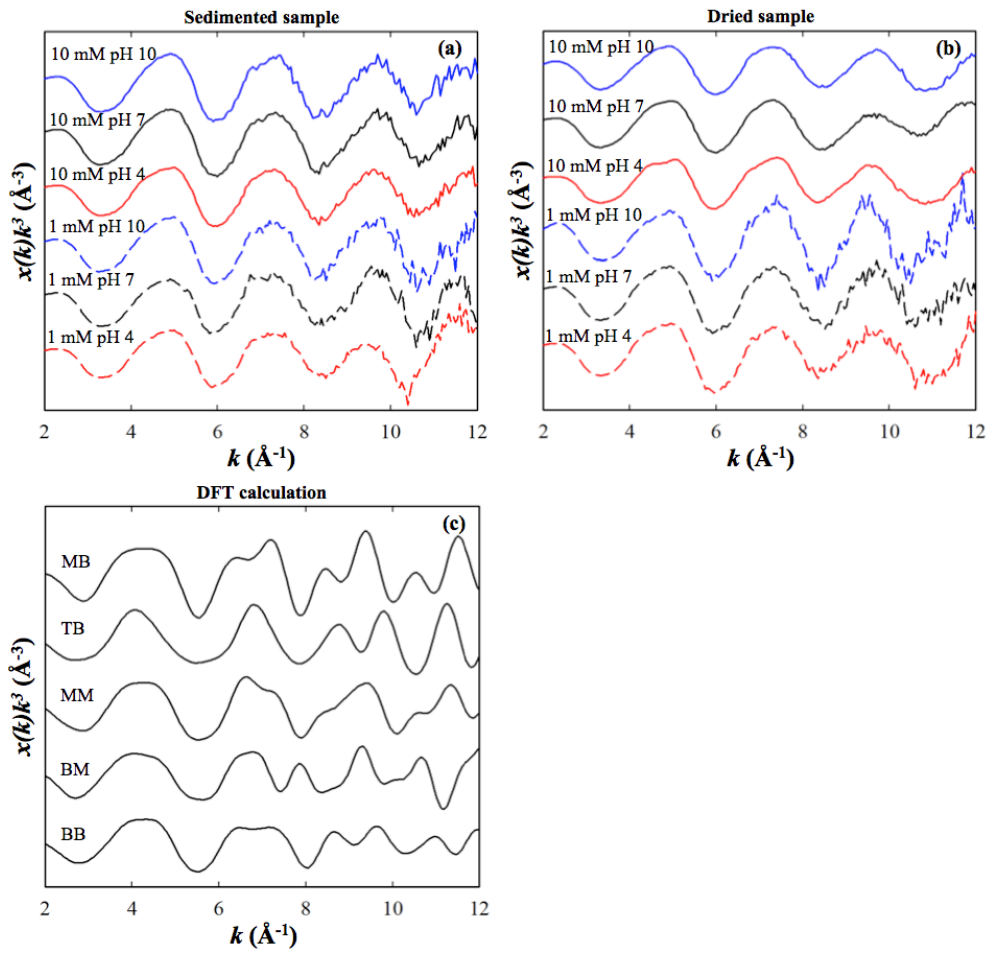
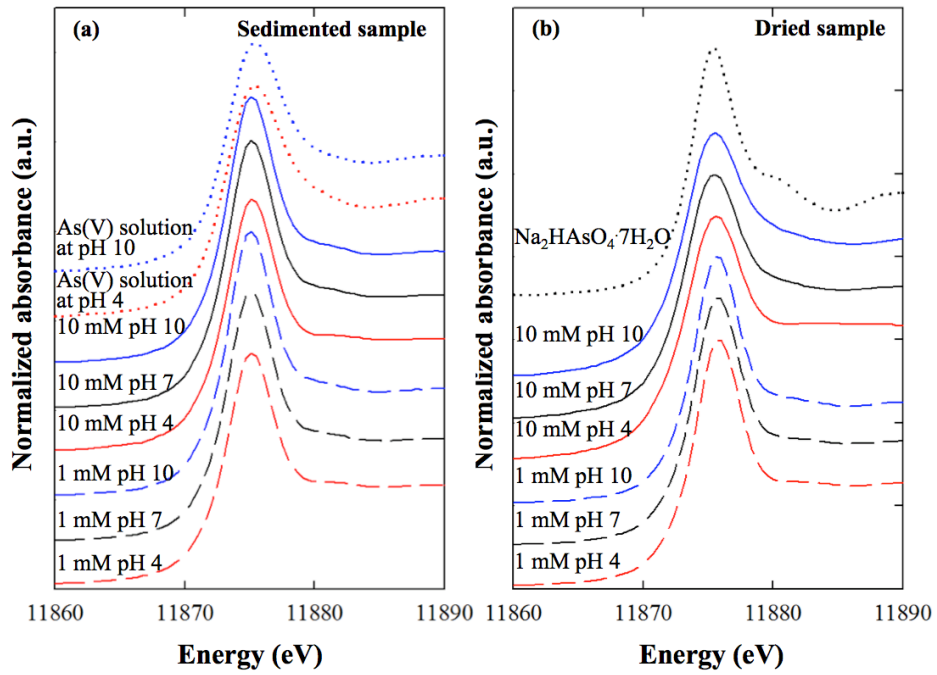


**Fig. 4-10** As K-edge XANES spectra of 1 mM (dashed line) and 10 mM arsenate (solid line) on the goethite at pH 4 (red), 7 (black) and 10 (blue) under different sample phase (sedimented (a) and dried (b)), and the aqueous arsenate (dotted line) and precipitate (dotted line).



protonation (Fig. 4-8); thus, we merged aqueous spectrum at pH 4 and 10 to generate aqueous spectrum at pH 7, where  $\text{H}_2\text{AsO}_4^-$  and  $\text{HAsO}_4^{2-}$  existed as similar concentration ( $\text{p}K_{a2}=6.94$ ). Based on the optimized geometry from the DFT, we calculated the theoretical spectrum of BB, BM, MB, MM and TB complexes (Fig. 4-3). The M, B and T as the first letter indicate dentation number—monodentate, bidentate and tridentate, respectively. The M and B as in the second letter show the number of nuclei—mononuclear and binuclear, respectively. The first shell distance between arsenic and oxygen was 1.65-1.72 Å, consistent with previous experiments and calculations. Based on the calculation, the atomic distances among the arsenic and two iron atoms was 3.59 and 6.00 Å for the MM complex, 3.33 and 3.35 Å for the MB complex, 2.72 and 4.70 Å for the BM complex, 3.21 and 3.34 Å for the BB complex, and 2.59 and 3.14 Å for the TB complex.

Our experimental result showed that more distinctive differences were found in 1 mM treatment than 10 mM treatment, and we found significant shifts and transitions in the spectrum (Fig. 4-11); however, it was difficult to identify the specific sorption mechanism among the overlapped spectra. For that reason, we utilized the LCF with the theoretical spectra of five clusters and the experimental spectrum of aqueous and precipitated samples as the independent variables, and we set the spectrum of each treatment as the dependent variable. We also used Fourier-transformed R space from 1 to 4 Å for the analysis, because the EXAFS spectrum had slightly different features before the first shell, caused by the strong whiteline of arsenate. The Rbkg function of Athena software (Ravel and Newville, 2005) was not able to completely remove this effect. In addition, we only employed one arsenic and two iron atoms with several oxygen atoms for the DFT calculation, and thus, the calculation did not have sufficient geometry for distances more than 4 Å from the center atom of arsenic. The results for LCF and analysis of variance (ANOVA) are summarized in Table 4-2. The probability of ANOVA was <0.0001

**Table 4-2** Results from batch experiment and linear combination fitting of EXAFS spectra acquired in sedimented and dried samples.

Experimental condition			Batch experiment				Linear combination fitting of EXAFS spectra							R-factor
Phase	Conc. (mM)	pH	Aqueous As ( $\mu\text{mol}$ )	adsorbed As ( $\mu\text{mol}$ )	$\Gamma$ ( $\text{N nm}^{-2}$ )	$\Gamma/\Gamma_{\text{max}} \times 100$	Fraction							
							MM	MB	BB	BM	TB	Solution	Powder	
Sedimented	1	4	6.61 (0.098)	44.8 (0.786)	1.29 (0.022)	57.4%	0.091 (0.052)	0.000 (0.029)	0.357 (0.054)	0.000 (0.035)	0.411 (0.027)	0.141 (0.043)	-	0.00585
Sedimented	1	7	12.5 (0.142)	40.4 (0.549)	1.16 (0.016)	54.5%	0.090 (0.072)	0.004 (0.042)	0.000 (0.077)	0.000 (0.049)	0.295 (0.037)	0.612 (0.060)	-	0.00041
Sedimented	1	10	21.6 (0.179)	29.6 (0.429)	0.849 (0.012)	47.4%	0.156 (0.056)	0.137 (0.033)	0.087 (0.062)	0.000 (0.039)	0.058 (0.029)	0.562 (0.047)	-	0.00402
Sedimented	10	4	435 (3.75)	77.9 (4.92)	2.24 (0.141)	99.9%	0.418 (0.045)	0.000 (0.026)	0.000 (0.049)	0.032 (0.032)	0.038 (0.024)	0.513 (0.038)	-	0.00028
Sedimented	10	7	440 (3.28)	75.6 (2.01)	2.17 (0.058)	102%	0.408 (0.055)	0.010 (0.032)	0.000 (0.060)	0.259 (0.038)	0.046 (0.028)	0.276 (0.047)	-	0.00014
Sedimented	10	10	456 (5.57)	59.1 (5.63)	1.70 (0.162)	94.8%	0.345 (0.048)	0.040 (0.028)	0.000 (0.053)	0.108 (0.035)	0.040 (0.025)	0.468 (0.040)	-	0.00007
Dried	1	4	0.661 (0.010)	44.8 (0.786)	1.29 (0.022)	57.4%	0.000 (0.031)	0.005 (0.016)	0.070 (0.028)	0.014 (0.022)	0.019 (0.015)	-	0.891 (0.053)	0.01725
Dried	1	7	1.25 (0.014)	40.4 (0.549)	1.16 (0.016)	54.5%	0.003 (0.018)	0.005 (0.009)	0.069 (0.016)	0.000 (0.012)	0.057 (0.009)	-	0.866 (0.031)	0.00535
Dried	1	10	2.16 (0.018)	29.6 (0.429)	0.849 (0.012)	47.4%	0.174 (0.096)	0.000 (0.048)	0.098 (0.084)	0.020 (0.066)	0.109 (0.046)	-	0.600 (0.162)	0.00181
Dried	10	4	43.5 (0.375)	77.9 (4.92)	2.24 (0.141)	99.9%	0.000 (0.030)	0.075 (0.017)	0.027 (0.030)	0.000 (0.022)	0.000 (0.015)	-	0.899 (0.049)	0.00062
Dried	10	7	44.0 (0.328)	75.6 (2.01)	2.17 (0.058)	102%	0.000 (0.029)	0.000 (0.015)	0.060 (0.027)	0.034 (0.022)	0.000 (0.015)	-	0.906 (0.048)	0.00053
Dried	10	10	45.6 (0.557)	59.1 (5.63)	1.70 (0.162)	94.8%	0.000 (0.027)	0.000 (0.013)	0.037 (0.024)	0.000 (0.018)	0.044 (0.013)	-	0.919 (0.046)	0.00027

*Aqueous As* arsenate mol in aqueous phase after batch experiment measured by ICP-OES, and the difference in sedimented (50 mL solution) and dried (5 mL supernatant) sample is caused by the volume difference of sample; *Adsorbed As* adsorbed arsenate on the goethite by subtracting from total to aqueous concentration;  $\Gamma$  ( $\text{N nm}^{-2}$ ) surface density;  $\Gamma/\Gamma_{\text{max}} \times 100$  surface coverage percent calculated with Langmuir isotherm parameter; *MM* monodentate mononuclear complex; *MB* monodentate binuclear complex; *BB* bidentate binuclear complex; *BM* bidentate mononuclear complex; *TB* tridentate binuclear complex; The value in parenthesis indicates standard error of estimate;  $R\text{-factor} = \Sigma(\text{data-fit})^2/\Sigma(\text{data})^2$ .

for all treatments while  $F$  was ranged from 224 to 6439. The adjusted  $r^2$  and standard error of estimate for LCF were within 0.919-0.997 and 0.016-0.083, respectively.

The LCF result of sedimented and dried sample was illustrated in Fig. 4-12 and Fig. 4-13, and listed in Table 4-2. It shows that the distribution of the complex changed with pH and arsenate concentration. The fraction indicated the relative abundance of each complex. It did not imply the concentration, because we already normalized the EXAFS spectrum, and we also used different sample thicknesses and densities for the measurement. Thus, it only implied the relative distribution of complexes from the result. We used six independent variables: five from the DFT calculation and one from the experiment of arsenate solution. We denoted the spectrum of arsenate solution as OS+Aq., because we could not separate the outer-sphere complex and aqueous arsenate using EXAFS. In the dried sample, we used the precipitate instead of OS+Aq..

#### 4.3.4. pH and surface loading effect on structural configuration

First, we tried to find out the pH and surface loading effect. In the 1 mM treatment, we found significant increases in the OS+Aq., MM and MB complex with pH increase, but the TB and BB were decreased with pH increase while no BM complex was observed. In the 10 mM treatment, the TB and BM complex showed no significant change with pH at low fraction, while the MM complex was dominant for all pH range, and the MM complex was slightly decreased at pH 10. Interestingly, the OS+Aq. and BB showed the opposite distribution with pH increase, the BB complex showed maximum fraction at pH 7. We found dramatic transition in the structural configuration with both pH and arsenate surface loading.

Obviously, we identified, for the first time, the formation of the TB

complex. As we mentioned above, we observed the peak shifting at 2.5-2.7 Å, and we initially identified the peaks from the multiple scattering of As-O-O-As based on the previous studies (Catalano et al., 2011; Sherman and Randall, 2003; Zhang et al., 2011). However, we looked up the normalized spectrum and found significant peak shifts in 1 mM treatments and less fluctuation in 10 mM treatments (Fig. 4-11). We carefully reviewed numerous papers and we found that a few theoretical studies reported the possibility of a tridentate complex between arsenate and iron (hydr)oxide. Farrell (Farrell, 2017) discussed the higher thermodynamic stability of a tridentate complex compared to a mono- or bidentate complex, and Waychunas (Stollenwerk and Welch, 2003; Waychunas et al., 1993) suggested a face-sharing tridentate complex with a similar As-Fe distance to a bidentate complex. In addition, we also found several studies that identified a tridentate complex (Auffan et al., 2008; Kirsch et al., 2008; Liu et al., 2015; Wang et al., 2008), but not the arsenate. Thus, we included the tridentate complex for DFT calculation and statistical analysis and found significant abundance of TB complex in the treatment at pH 4 and 7 with 1 mM arsenate.

The fraction of OS+Aq. was relatively low at pH 4 and increased at pH 7 under 1 mM treatment; then, it decreased at pH 10 (Table 4-2). From the batch experiment, only 57, 54 and 47% of surface sites were occupied ( $I/I_{max}$ ), and 13, 25 and 43% of arsenate remained in the solution phase at pH 4, 7 and 10, respectively. The difference between the fraction from EXAFS study and aqueous arsenate concentration from batch experiment was mainly caused by the outer-sphere complex, which was not distinguishable by EXAFS, and numerous studies reported that the decrease in the OS complex with pH increase was due to the change in the surface charge. Thus, the decrease in the IS complex led to a dramatic increase in the OS+Aq. from pH 4 to 7, while a decrease in the OS complex caused a decrease

**Fig. 4-11** Fourier transform magnitude from As K-edge  $k^3$ -weighted EXAFS spectra of sedimented and dried samples at pH 4 (red), 7 (black) and 10 (blue) at 1 and 10 mM arsenate surface loading. The dashed gray and dashed black lines are the spectrum of the 10 mM arsenate solution at pH 4 and  $\text{Na}_2\text{HAsO}_4 \cdot 7\text{H}_2\text{O}$  powder, respectively.

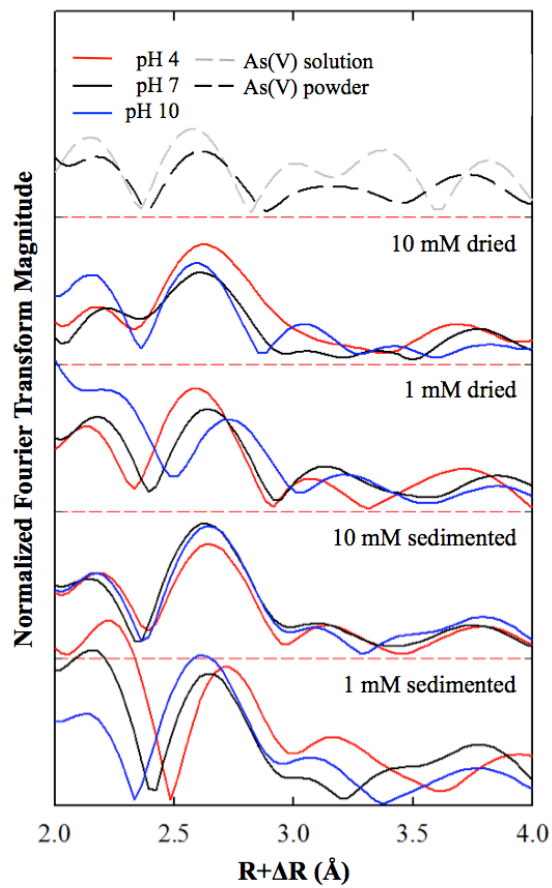


**Fig. 4-12** Distribution of five configurations of the complex by pH and arsenate concentration. The fraction resulted from the LCF and implied relative abundance of each configuration, but not the mean concentration. White, blue, black and red indicate dentation status, and the circle, triangle, square and diamond show the degree of nucleation.

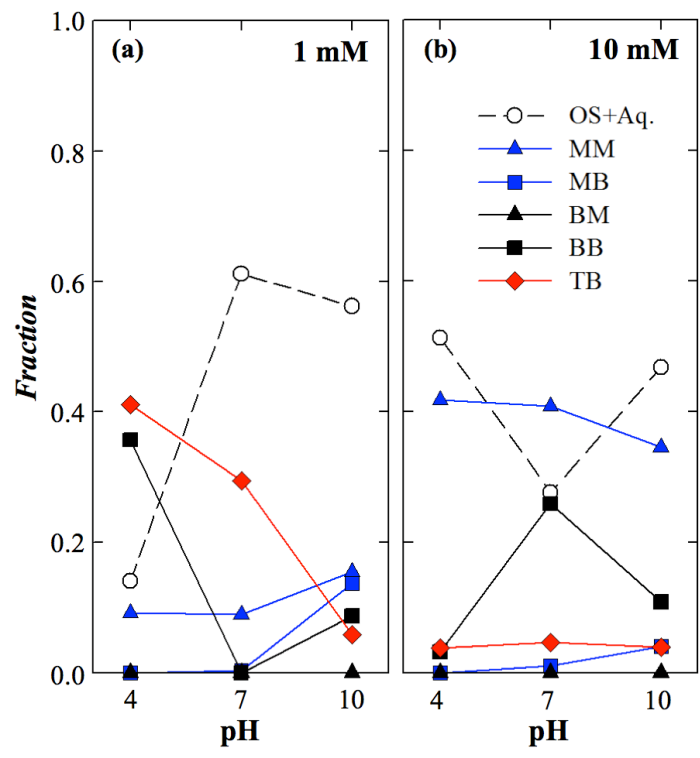
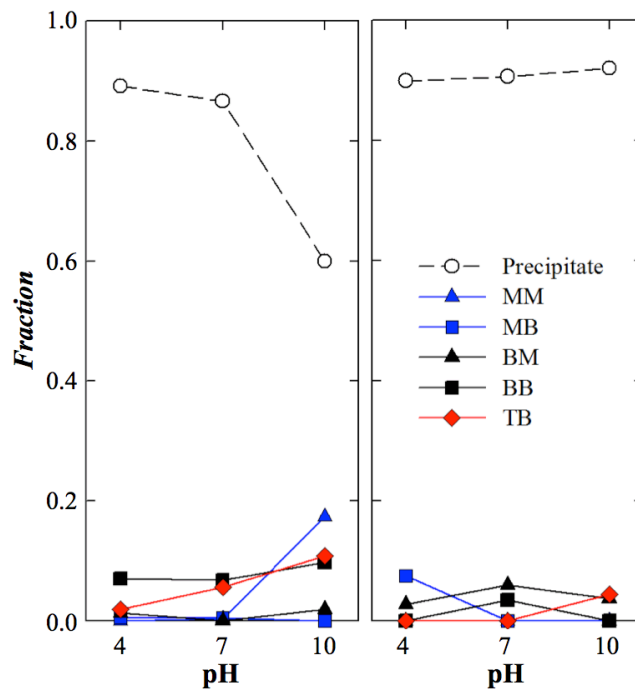


**Fig. 4-13** Distribution of five configurations of the complex and precipitated arsenate (using  $\text{NaH}_2\text{AsO}_4 \cdot 7\text{H}_2\text{O}$ ) at pH 4, 7 and 10 and arsenate concentration (1 and 10 mM) after drying. The fraction was calculated by linear combination fitting and it implied relative abundance of each configuration, but not the mean concentration. White, blue, black and red indicate number of dentation, and the circle, triangle, square and diamond show the number of nucleation.



in OS+Aq. from pH 7 to 10. Interestingly, we found a sudden decrease of OS+Aq. with an increase in BB complex at pH 7 under the 10 mM treatment. We assumed that both  $\text{H}_2\text{AsO}_4^-$  and  $\text{HAsO}_4^{2-}$  are dominant at pH 7 and PNZC of goethite was 5.66; thus, the combination of arsenate speciation and surface charge might lead to this the result. In addition, we observed the similar adsorption at pH 4 and 7 in the 10 mM arsenate treatment in the batch experiment, and the ferric arsenate complex or the surface precipitation might cause the BB complex.

The MM complex was observed at all treatments but was mainly found in the 10 mM arsenate treatments. The MM complex in 1 mM treatment increased with pH increase, but the pH effect was the opposite in the 10 mM treatment. Recent studies reported that surface loading determines the complex; Waychunas et al.(Waychunas et al., 1993) initially reported the presence of MM complex and surface loading effect; Elzinga and Sparks(Elzinga and Sparks, 2007) also reported a surface loading effect using ATR-FTIR, and Abdala et al.(Abdala et al., 2015) reported that the MM complex of phosphate had high surface loading, while the BM and BB complexes were found with low surface loading. For that reason, we explained that more competition at the limited sorption site led to the formation of MM complex. A high concentration of arsenate caused more competition on the sorption site, and pH increase changed the positively charged surface of goethite to a neutral or negatively charged surface, which could limit the sorption sites. As a result, both surface loading and pH caused the formation of MM complex.

#### 4.3.5. Drying effect on structural configuration

Unlike to the sedimented samples, LCF result of dried samples showed the relatively higher abundance of arsenate precipitate in all treatments. The fraction of precipitate was calculated as 0.60-0.92, and the 1 mM treatment at pH 10 showed

minimum value of precipitate fraction while the 10 mM treatment at pH 10 showed maximum value. The fraction of precipitate in the 1 mM treatment was 0.891, 0.866 and 0.600, while the fraction of precipitate in the 10 mM treatment was 0.899, 0.906 and 0.919 at pH 4, 7 and 10, respectively. We found opposite trend in the fraction of precipitate, and we presumed the reason from the batch experiment. In table 4-2, the aqueous As in the 1 mM treatment was 0.661, 1.25 and 2.16 at pH 4, 7 and 10, while the adsorbed As was 44.8, 40.4 and 29.6  $\mu\text{mol}$ , respectively. We dried out the sample (0.25 g) with 5 mL of solution, the fraction of precipitate at pH 4 and 7 would be increased by the precipitation from aqueous arsenate and outer-sphere complex, but the outer-sphere complex of arsenate at pH 10 dramatically decreased by the repulsion from the negatively charged surface while small amount of aqueous arsenate was precipitated; thus the fraction of precipitate was significantly decreased. As a consequence, the fraction of inner-sphere complex was increased. In the 10 mM treatment, the aqueous As was dramatically increased (21.1-65.8 times) from the 1 mM treatment, the fraction of precipitate showed more than 0.899. We assumed that the amount of desorbed outer-sphere complex from pH 4 to 10 was less than the amount of increased aqueous arsenate; thus, the fraction of precipitate was increased with pH increase.

However, the fraction of inner-sphere complex was low to discuss the distribution of the structural configuration, and we also only employed  $\text{Na}_2\text{HAsO}_4 \cdot 7\text{H}_2\text{O}$  as the precipitate; thus, it was not enough to explain the possible structural configuration and precipitation in the arsenate and iron hydroxide containing system. For example, we only employed di-sodium arsenate, but the precipitate can contain mono-sodium at low pH or tri-sodium at high pH. In addition, the ferric arsenate in various atomic ratio and configuration could be precipitated such as the bernalite, which was confirmed the formation at high pH

with the arsenate presence in this study. For that reason, our approach using  $\text{Na}_2\text{HAsO}_4 \cdot 7\text{H}_2\text{O}$  as the only precipitate might be not enough to explain the drying effect, however, the LCF employing the reference of precipitate as many as possible would yield more explainable data in the future.

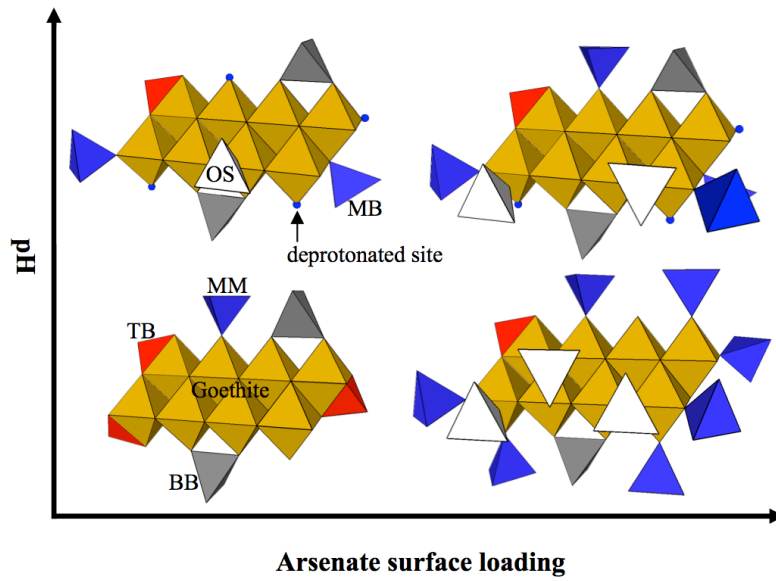
#### 4.4. Environmental implication

In this study, we evaluated the structural configuration of arsenate with changes in concentration, drying and pH using a batch experiment and HRTEM and EXAFS measurements with DFT calculation. We confirmed the formation of nanosized bernalite only in the presence of arsenate at pH 10 using HRTEM measurements, and the bernalite showed 46% of increase in As:Fe ratio compared to nano-goethite at pH 10. However, the formation of bernalite might enhance the colloidal transport of arsenate in the waste water treatment using iron (hydr)oxide or in the pH-increasing amendment treated soil environment. In addition, we found that the TB and BB complex was dominant at low pH and low surface loading, while MM and MB were observed in the high pH and high surface loading conditions (Fig. 4-14). The density of available sorption site gradually decrease with pH increase, and the bidentate and tridentate complex are dominant with less competition at low surface loading because there is plenty of neighboring sorption site. However, the increase of pH or surface loading decrease the available sorption site or the available sorption site per arsenate; thus, the MM complex are dominant with high competition at high surface loading because there is no enough sorption site to occupy.

These results may help us to understand the effect of environmental conditions on the structural configuration of arsenate at the goethite-water interface. However, because this result only employed a single arsenate and two octahedral

ferric hydroxides as the model sorbate for the DFT calculation, there is a significant discordance from reality. Employing a more detailed structure for nano-goethite might lead to more accurate results for the interpretation. In addition, a denser experimental setup would yield a more persuasive result for this experiment.

**Fig. 4-14** Schematic illustration for the transition of structural configuration by the change of pH and surface loading conditions. The white tetrahedral indicated outer-sphere complex, while blue, grey and red tetrahedral showed the monodentate, bidentate and tridentate complexes, respectively. The brown octahedral sheet is the goethite.



## References

- Abdala, D.B., Northrup, P.A., Arai, Y., Sparks, D.L., 2015. Surface loading effects on orthophosphate surface complexation at the goethite/water interface as examined by extended X-ray Absorption Fine Structure (EXAFS) spectroscopy. *J. Colloid Interface Sci.* 437, 297–303. doi:10.1016/j.jcis.2014.09.057
- Abdelwahed, W., Degobert, G., Stainmesse, S., Fessi, H., 2006. Freeze-drying of nanoparticles: Formulation, process and storage considerations. *Adv. Drug Deliv. Rev.* 58, 1688–1713. doi:10.1016/j.addr.2006.09.017
- Adamescu, A., Hamilton, I.P., Al-Abadleh, H.A., 2014. Density functional theory calculations on the complexation of p-arsanilic acid with hydrated iron oxide clusters: Structures, reaction energies, and transition states. *J. Phys. Chem. A* 118, 5667–5679. doi:10.1021/jp504710b
- Ahn, S., Joon Lee, S., 2015. Dehydration-mediated cluster formation of nanoparticles. *Sci. Rep.* 5, 1–12. doi:10.1038/srep11383
- Antelo, J., Avena, M., Fiol, S., López, R., Arce, F., 2005. Effects of pH and ionic strength on the adsorption of phosphate and arsenate at the goethite-water interface. *J. Colloid Interface Sci.* 285, 476–486. doi:10.1016/j.jcis.2004.12.032
- Auffan, M., Rose, J., Proux, O., Borschneck, D., Masion, A., Chaurand, P., Hazemann, J.L., Chaneac, C., Jolivet, J.P., Wiesner, M.R., Van Geen, A., Bottero, J.Y., 2008. Enhanced adsorption of arsenic onto maghemite nanoparticles: As(III) as a probe of the surface structure and heterogeneity. *Langmuir* 24, 3215–3222. doi:10.1021/la702998x
- Birch, W.D., Pring, A., Reller, A., Schmalte, H.W., 1993. Bernalite, Fe(OH)<sub>3</sub>, a New Mineral From Broken-Hill, New-South-Wales - Description and Structure. *Am. Mineral.* 78, 827–834.
- Bolanz, R.M., Majzlan, J., Ackermann, S., 2011. The effect of Sb(V) on the transformation of ferrihydrite to goethite, hematite, and ferroxhyte. *Mineral. Mag.* 75, 546–.
- Catalano, J.G., Luo, Y., Otemuyiwa, B., 2011. Effect of aqueous Fe(II) on arsenate sorption on goethite and hematite. *Environ. Sci. Technol.* 45, 8826–8833. doi:10.1021/es202445w
- Claudio, C., Di Iorio, E., Liu, Q., Jiang, Z., Barrón, V., 2017. Iron oxide nanoparticles in soils: Environmental and agronomic importance. *J. Nanosci. Nanotechnol.* 17, 4449–4460. doi:10.1166/jnn.2017.14197
- Cornell, R.M., Schwertmann, U., 2003. *The iron oxides: structure, properties, reactions, occurrences, and uses.* Wiley-VCH.
- Cudennec, Y., Lecerf, A., 2006. The transformation of ferrihydrite into goethite or hematite, revisited. *J. Solid State Chem.* 179, 716–722. doi:10.1016/j.jssc.2005.11.030
- Diaz-Bone, R. a., Raabe, M., Awibus, S., Keuter, B., Menzel, B., Küppers, K., Widmann, R., Hirner, A. V., 2011. Investigation of biomethylation of arsenic and tellurium during composting. *J. Hazard. Mater.* 189, 653–659. doi:10.1016/j.jhazmat.2010.12.011
- Downs, R., Hall-Wallace, M., 2003. The American Mineralogist crystal structure database. *Am. Mineral.* 88, 247–250.
- Elzinga, E.J., Sparks, D.L., 2007. Phosphate adsorption onto hematite: An in situ ATR-FTIR investigation of the effects of pH and loading level on the mode of phosphate surface complexation. *J. Colloid Interface Sci.* 308, 53–70. doi:10.1016/j.jcis.2006.12.061
- Erbs, J.J., Berquó, T.S., Reinsch, B.C., Lowry, G. V., Banerjee, S.K., Penn, R.L., 2010. Reductive dissolution of arsenic-bearing ferrihydrite. *Geochim. Cosmochim. Acta* 74, 3382–3395. doi:10.1016/j.gca.2010.01.033

- Fakour, H., Lin, T., 2014. Effect of Humic Acid on As Redox Transformation and Kinetic Adsorption onto Iron Oxide Based Adsorbent ( IBA ). *Int. J. Environ. Res. Public Health* 11, 10710–10736. doi:10.3390/ijerph111010710
- Fan, J.X., Wang, Y.J., Liu, C., Wang, L.H., Yang, K., Zhou, D.M., Li, W., Sparks, D.L., 2014. Effect of iron oxide reductive dissolution on the transformation and immobilization of arsenic in soils: New insights from X-ray photoelectron and X-ray absorption spectroscopy. *J. Hazard. Mater.* 279, 212–219. doi:10.1016/j.jhazmat.2014.06.079
- Farquhar, M.L., Charnock, J.M., Livens, F.R., Vaughan, D.J., 2002. Mechanisms of arsenic uptake from aqueous solution by interaction with goethite, lepidocrocite, mackinawite, and pyrite: An X-ray absorption spectroscopy study. *Environ. Sci. Technol.* 36, 1757–1762. doi:10.1021/es010216g
- Farrell, J., 2017. Tridentate arsenate complexation with ferric hydroxide and its effect on the kinetics of arsenate adsorption and desorption. *Chemosphere* 184, 1209–1214. doi:10.1016/j.chemosphere.2017.06.099
- Fendorf, S., Eick, M.J., Grossl, P., Sparks, D.L., 1997. Arsenate and chromate retention mechanisms on goethite. 1. Surface structure. *Environ. Sci. Technol.* 31, 315–320. doi:10.1021/es950653t
- Gao, X., Root, R.A., Farrell, J., Ela, W., Chorover, J., 2013. Effect of silicic acid on arsenate and arsenite retention mechanisms on 6-L ferrihydrite: A spectroscopic and batch adsorption approach. *Appl. Geochemistry* 38, 110–120. doi:10.1016/j.apgeochem.2013.09.005
- Gotoh, S., Patrick, W.H., 1974. Transformation of Iron in a Waterlogged Soil as Influenced by Redox Potential and pH1. *Soil Sci. Soc. Am. J.* 38, 66. doi:10.2136/sssaj1974.03615995003800010024x
- Gu, C., Wang, Z., Kubicki, J.D., Wang, X., Zhu, M., 2016. X-ray Absorption Spectroscopic Quantification and Speciation Modeling of Sulfate Adsorption on Ferrihydrite Surfaces. *Environ. Sci. Technol.* 50, 8067–8076. doi:10.1021/acs.est.6b00753
- Han, J., Kim, J., Kim, M., Moon, D.H., Sung, J.-S., Hyun, S., 2014. Chemical extractability of As and Pb from soils across long-term abandoned metallic mine sites in Korea and their phytoavailability assessed by Brassica juncea. *Environ. Sci. Pollut. Res. Int.* 22, 1270–8. doi:10.1007/s11356-014-3441-3
- Hanwell M.D. Lonie D.C., Vandermeersch, T., Zurek E., Hutchison, G., C.D.E., 2012. Avogadro: An Advanced Semantic Chemical Editor, Visualisation, and Analysis Platform. *J. Chem. Informatics* 4, 1–17.
- He, G., Zhang, M., Pan, G., 2009. Influence of pH on initial concentration effect of arsenate adsorption on TiO<sub>2</sub> surfaces: Thermodynamic, DFT, and EXAFS interpretations. *J. Phys. Chem. C* 113, 21679–21686. doi:10.1021/jp906019e
- Hughes, M.F., 2002. Arsenic toxicity and potential mechanisms of action. *Toxicol. Lett.* 133, 1–16. doi:10.1016/S0378-4274(02)00084-X
- Hyun, S., Kim, J., Kim, D.-Y., Moon, D.H., 2012. Effect of seepage conditions on chemical attenuation of arsenic by soils across an abandoned mine site. *Chemosphere* 87, 602–7. doi:10.1016/j.chemosphere.2012.01.013
- Iwasaki, T., Sato, N., Kosaka, K., Watano, S., Yanagida, T., Kawai, T., 2011. Direct transformation from goethite to magnetite nanoparticles by mechanochemical reduction. *J. Alloys Compd.* 509, 34–37. doi:10.1016/j.jallcom.2010.10.029
- Jain, C., Ali, I., 2000. Arsenic: occurrence, toxicity and speciation techniques. *Water Res.* 34, 4304–4312.
- Kirsch, R., Scheinost, A.C., Rossberg, A., Banerjee, D., Charlet, L., 2008. Reduction of

- antimony by nano-particulate magnetite and mackinawite. *Mineral. Mag.* 72, 185–189. doi:10.1180/minmag.2008.072.1.185
- Klinger, M., Polivka, L., Šteger, A., Tyunina, M., 2016. Quantitative analysis of structural inhomogeneity in nanomaterials using transmission electron microscopy. *J. Appl. Crystallogr.* 49, 762–770. doi:10.1107/S1600576716003800
- Leermakers, M., Baeyens, W., De Gieter, M., Smedts, B., Meert, C., De Bisschop, H.C., Morabito, R., Quevauviller, P., 2006. Toxic arsenic compounds in environmental samples: Speciation and validation. *TrAC - Trends Anal. Chem.* 25, 1–10. doi:10.1016/j.trac.2005.06.004
- Li, C.X., Feng, S.L., Shao, Y., Jiang, L.N., Lu, X.Y., Hou, X.L., 2007. Effects of arsenic on seed germination and physiological activities of wheat seedlings. *J. Environ. Sci.* 19, 725–732.
- Lin, H.-Y., Chen, Y.-W., Wang, W.-J., 2005. Preparation of nanosized iron oxide and its application in low temperature CO oxidation. *J. Nanoparticle Res.* 7, 249–263. doi:10.1007/s11051-005-4717-9
- Liu, C.H., Chuang, Y.H., Chen, T.Y., Tian, Y., Li, H., Wang, M.K., Zhang, W., 2015. Mechanism of Arsenic Adsorption on Magnetite Nanoparticles from Water: Thermodynamic and Spectroscopic Studies. *Environ. Sci. Technol.* 49, 7726–7734. doi:10.1021/acs.est.5b00381
- Loring, J.S., Sandström, M.H., Norén, K., Persson, P., 2009. Rethinking arsenate coordination at the surface of goethite. *Chem. - A Eur. J.* 15, 5063–5072. doi:10.1002/chem.200900284
- Marquardt, D.W., 1963. An Algorithm for Least-Squares Estimation of Nonlinear Parameters. *J. Soc. Ind. Appl. Math.* 11, 431–441. doi:10.1137/0111030
- Michael Bolanz, R., Blöchl, U., Ackermann, S., Ciobotaru, V., Rössler, P., Tarcea, N., Popp, J., Majzlan, J., 2013. The effect of antimonate, arsenate, and phosphate on the transformation of ferrihydrite to goethite, hematite, ferrioxhyte, and tripuyite. *Clays Clay Miner.* 61, 11–25. doi:10.1346/CCMN.2013.0610102
- Morin, G., Ona-Nguema, G., Wang, Y., Menguy, N., Juillot, F., Proux, O., Guyot, F., Calas, G., Brown, G.E., 2008. Extended X-ray absorption fine structure analysis of arsenite and arsenate adsorption on maghemite. *Environ. Sci. Technol.* 42, 2361–2366. doi:10.1021/es072057s
- Neupane, G., Donahoe, R.J., Arai, Y., 2014. Kinetics of competitive adsorption/desorption of arsenate and phosphate at the ferrihydrite-water interface. *Chem. Geol.* 368, 31–38. doi:10.1016/j.chemgeo.2013.12.020
- Newville, M., 2014. Fundamentals of XAFS. *Rev. Mineral. Geochemistry* 78, 33–74. doi:10.2138/rmg.2014.78.2
- Newville, M., Kas, J.J., Rehr, J.J., 2009. Improvements in modeling EXAFS with many-pole self-energy and FEFF 8.5. *J. Phys. Conf. Ser.* 190. doi:10.1088/1742-6596/190/1/012023
- Paktunc, D., 2004. A computer program for analysing complex bulk XAFS spectra and for performing significance tests. *J. Synchrotron Radiat.* 11, 295–298. doi:10.1107/S0909049504003681
- Rahnemaie, R., Hiemstra, T., van Riemsdijk, W.H., 2006. Inner- and outer-sphere complexation of ions at the goethite-solution interface. *J. Colloid Interface Sci.* 297, 379–388. doi:10.1016/j.jcis.2005.11.003
- Randall, S.R., Sheerman, D.M., Ragnarsdottir, K.V., 2001. Sorption of As(V) on green rust (Fe<sub>4</sub>(II)Fe<sub>2</sub>(III)(OH)<sub>12</sub>SO<sub>4</sub>·3H<sub>2</sub>O) and lepidocrocite (FeOOH): Surface complexes from EXAFS spectroscopy. *Geochim. Cosmochim. Acta* 65, 1015–1023.

- Ratnaike, R.N., 2003. Acute and chronic arsenic toxicity. *Postgrad. Med. J.* 79, 391–396. doi:10.1136/pmj.79.933.391
- Ravel, B., Newville, M., 2005. ATHENA, it ARTEMIS, it HEPHAESTUS: data analysis for X-ray absorption spectroscopy using IFEFFIT. *J. Synchrotron Radiat.* 12, 537–541. doi:10.1107/S0909049505012719
- Ressler, T., 1997. WinXAS : A New Software Package not only for the Analysis of Energy-Dispersive XAS Data. *Le J. Phys. IV* 7, C2-269-C2-270. doi:10.1051/jp4/1997195
- Rosen, B.P., Liu, Z., 2009. Transport pathways for arsenic and selenium: A minireview. *Environ. Int.* 35, 512–515. doi:10.1016/j.envint.2008.07.023
- Sherman, D.M., Randall, S.R., 2003. Surface complexation of arsenic(V) to iron(III) (hydr)oxides: Structural mechanism from ab initio molecular geometries and EXAFS spectroscopy. *Geochim. Cosmochim. Acta* 67, 4223–4230. doi:10.1016/S0016-7037(03)00237-0
- Singh, R., Singh, S., Parihar, P., Singh, V.P., Prasad, S.M., 2015. Arsenic contamination, consequences and remediation techniques: A review. *Ecotoxicol. Environ. Saf.* 112, 247–270. doi:10.1016/j.ecoenv.2014.10.009
- Smedley, P.L., Kinniburgh, D.G., 2002. A review of the source, behaviour and distribution of arsenic in natural waters. *Appl. Geochemistry* 17, 517–568. doi:10.1016/S0883-2927(02)00018-5
- Stollenwerk, K.G., Welch, A.H., 2003. Arsenic in Ground Water, in: *Arsenic in Ground Water: Geochemistry and Occurrence*. KLUWER ACADEMIC PUBLISHERS, pp. 67–100. doi:10.1007/b101867
- Violante, A., Gaudio, S.D.E.L., 2006. Coprecipitation of Arsenate with Metal Oxides : Nature , Mineralogy , and Reactivity of Aluminum Precipitates. *Environ. Sci. Technol.* 40, 4961–4967.
- Vu, H.P., Shaw, S., Brinza, L., Benning, L.G., 2010. Crystallization of hematite (Fe<sub>2</sub>O<sub>3</sub>) under alkaline condition: The effects of Pb. *Cryst. Growth Des.* 10, 1544–1551. doi:10.1021/cg900782g
- Wang, Y., Morin, G., Ona-Nguema, G., Menguy, N., Juillot, F., Aubry, E., Guyot, F., Calas, G., Brown, G.E., 2008. Arsenite sorption at the magnetite-water interface during aqueous precipitation of magnetite: EXAFS evidence for a new arsenite surface complex. *Geochim. Cosmochim. Acta* 72, 2573–2586. doi:10.1016/j.gca.2008.03.011
- Waychunas, G. A., Rea, B. A., Fuller, C. C., Davis, J. A., 1993. Surface chemistry of ferrihydrite: Part 1. EXAFS studies on geometry of coprecipitated and adsorbed arsenate. *Geochim. Cosmochim. Acta* 57, 2251–2269. doi:10.1016/0016-7037(93)90567-G
- Webb, S.M., 2005. SIXPack a Graphical User Interface for XAS Analysis Using IFEFFIT. *Phys. Scr. T115*, 1011–1014. doi:10.1238/Physica.Topical.115a01011
- Xu, N., Christodoulatos, C., Braida, W., 2006. Modeling the competitive effect of phosphate, sulfate, silicate, and tungstate anions on the adsorption of molybdate onto goethite. *Chemosphere* 64, 1325–1333. doi:10.1016/j.chemosphere.2005.12.043
- Yang, J., Chai, L., Yue, M., Li, Q., 2015. Complexation of arsenate with ferric ion in aqueous solutions. *RSC Adv.* 5, 103936–103942. doi:10.1039/C5RA21836E
- Yang, Y., Chun, Y., Sheng, G., Huang, M., 2004. pH-Dependence of Pesticide Adsorption by Wheat-Residue-Derived Black Carbon. *Langmuir* 20, 6736–6741. doi:10.1021/la049363t
- Zhang, H., Selim, H.M., 2006. Modeling the Transport and Retention of Arsenic (V) in Soils. *Soil Sci. Soc. Am. J.* 70, 1677. doi:10.2136/sssaj2006.0035
- Zhang, M., Pan, G., Zhao, D., He, G., 2011. XAFS study of starch-stabilized magnetite

nanoparticles and surface speciation of arsenate. *Environ. Pollut.* 159, 3509–3514.  
doi:10.1016/j.envpol.2011.08.017

(This page intentionally left blank)

# **CHAPTER 5. INTERPRETING COMPETITIVE ADSORPTION OF ARSENATE AND PHOSPHATE ON SYNTHETIC NANO-IRON (HYDR)OXIDES: EFFECT OF PH AND SURFACE LOADING**

## **List of contents**

<b>CHAPTER 5. INTERPRETING COMPETITIVE ADSORPTION OF ARSENATE AND PHOSPHATE ON SYNTHETIC NANO-IRON (HYDR)OXIDES: EFFECT OF PH AND SURFACE LOADING .....</b>	<b>5-1</b>
List of contents .....	5-1
Abstract .....	5-2
5.1. Introduction .....	5-4
5.2. Material and methods .....	5-6
5.2.1. Physiochemical characterization .....	5-6
5.2.2. Batch experiment .....	5-9
5.2.3. Data analysis and fitting .....	5-13
5.3. Result and discussion .....	5-14
5.3.1. Physiochemical characteristics .....	5-14
5.3.2. Adsorption result and competitive sorption ratio .....	5-15
5.3.3. Competition effect .....	5-26
5.3.4. Iron (hydr)oxide stability with presence of oxyanions.....	5-36
5.4. Conclusion .....	5-41
References .....	5-43

## Abstract

Arsenate and phosphate have similar properties due to their electrochemical structures, but their environmental impacts are unique. The abundance and competition of arsenate and phosphate determine their bioavailability and leachability; thus, it is essential to understand their fate in the soil environment. In this study, the effects of pH and surface loading on the competitive adsorption of arsenate and phosphate on four iron (hydr)oxides were evaluated by employing the Langmuir isotherm, competitive sorption ratio (*CSR*) and competition effect (*CE*). The stability and transformation of the iron (hydr)oxides were also assessed. Various adsorption patterns were observed in the single and mixed treatments by controlling the addition oxyanions, pH, surface loading and type of iron (hydr)oxides. Arsenate was preferentially adsorbed at a low pH, whereas phosphate showed the opposite trend. The  $CE_{As(V),P(V)}$  was close to zero at low surface density (no competition) and sequentially changed to negative or positive values with increasing surface density, indirectly indicating the sequential development of promotive and competitive effects. Transformation in goethite was identified at a high pH with the presence of oxyanions, except that no transformation was observed upon the addition of oxyanions and with pH change. However, the stability of the iron (hydr)oxides decreased at a low pH and with the presence of phosphate, arsenate or both. The hematite showed a significant promotive effect regardless of the pH. Our study revealed that the pH, surface loading and type of iron (hydr)oxides are intercorrelated and simultaneously affect the adsorption characteristics of oxyanions and the stability of iron (hydr)oxides.

**Keywords**

Iron (hydr)oxide, arsenate, phosphate, Langmuir isotherm, competitive sorption ratio, competitive effect

## 5.1. Introduction

Arsenic and phosphorus are in group VII of the periodic table and have similar electrochemical properties; however, their environmental impacts are extremely different (Luengo et al., 2007; Woolson et al., 1971). Arsenic has been known as a poison throughout history (Vahidnia et al., 2007), and phosphorus had acted as a limiting nutrient for agricultural productivity worldwide (Elser et al., 2007). Recent anthropogenic activities in agriculture and mining have accelerated arsenic contamination in over 20 countries, and overfertilization with phosphorus has caused severe eutrophication of water systems worldwide (Barberis et al., 1995; Elser et al., 2007; Jain and Ali, 2000; Leermakers et al., 2006). Arsenate and phosphate are the major species of arsenic and phosphorus in the oxic rhizosphere (Lu and Zhu, 2010; Masscheleyn et al., 1991; Truog, 1930). They are the most notorious elements controlling the fate of arsenic and phosphorus in the soil environment because the fluctuation of environmental conditions not only causes the transition of oxyanion species but also leads to the transformation of soil components and dramatically changes the sorption characteristics (Han and Ro, 2018; Kwon et al., 2010; Michael Bolanz et al., 2013).

Various elements coexist in the soil environment, and their competition for adsorption onto the soil components determines their bioavailability and leachability (Liu et al., 2017; Scheckel et al., 2009; Zhang and Selim, 2008). Thus, it is essential to understand their competitive adsorption under environmental changes (Violante, 2013). Arsenate and phosphate have relatively high affinity for metal (hydr)oxides, but controversial results regarding their competition and structural configuration were found in previous studies. For example, the As(V)/P(V) ratio calculated in the previous literature showed significantly different

competitive sorption patterns (Fig. 5-1) (Carabante and Grahn, 2010; Frau et al., 2010; Goh and Lim, 2010; Hongshao and Stanforth, 2001; Jain and Loeppert, 2000; Zhang and Selim, 2008). In addition, numerous studies confirmed a bidentate complex as a major structural configuration of arsenate and phosphate on iron (hydr)oxides (Antelo et al., 2005; Brechbühl and Christl, 2012; Farquhar et al., 2002; Liu et al., 2015; Neupane et al., 2014; Sherman and Randall, 2003; Tejedor-Tejedor and Anderson, 1990), but a few studies have identified the presence of a monodentate complex (Fendorf et al., 1997; Loring et al., 2009; Waychunas et al., 1993) or the transition of a monodentate to a tridentate complex upon changing the environmental conditions (Han and Ro, 2018).

Previous studies showed diverse results in the adsorption of arsenate and phosphate on iron (hydr)oxides; the results were controversial, and a comparison of published data is challenging due to diverse interpretations and experimental setup conditions (for example, pH, ionic strength, solution/solid ratio and surface loading) (Abdala et al., 2015; Han and Ro, 2018; Kim et al., 2012; Li et al., 2015; Puls et al., 1991). We found that there is no simple equation to quantify the degree of competition to compare and interpret numerous studies. Recent studies by Bolanz et al. (2013) showed that the presence of oxyanions, their concentration and the pH control the iron (hydr)oxide transformation *via* various processes, but previous adsorption experiments focused on the stability of iron (hydr)oxides. Most studies synthesized the iron (hydr)oxides in their laboratories, allowing for a scientific result with proper sorbent characterization but possibly generating impurities in the sorbent. Dai et al. (2018) studied the effect of impurities on iron (hydr)oxide formation and showed that the surface of the nanoparticle was enriched with impure ions, altering the adsorption characteristics. Therefore, four commercial and nanosized iron (hydr)oxides, goethite, hematite, maghemite and magnetite, were

selected to compare the adsorption characteristics and obtain results that allow for comparison with other studies.

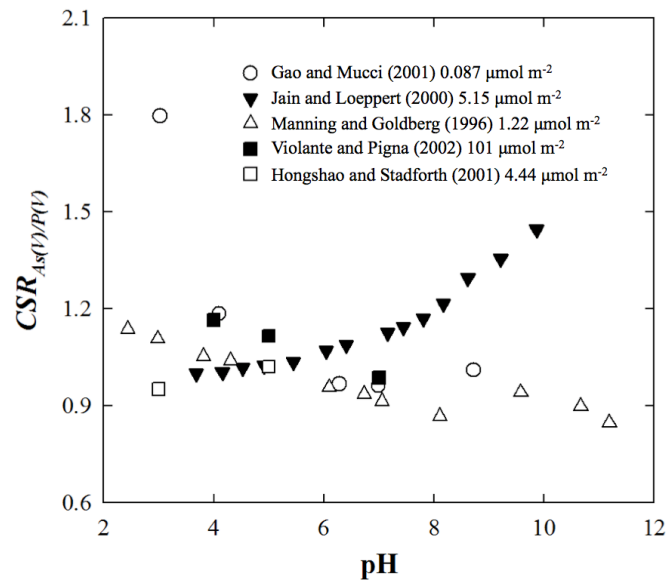
In this study, single and mixed adsorption isotherms of arsenate and phosphate were investigated. The commercial and nanosized goethite, hematite, maghemite and magnetite were employed to evaluate the competitive adsorption characteristics. The adsorption data were compared using two simple equations to interpret the sorption mechanism during the competitive sorption. In addition, the structural stability of the iron (hydr)oxides was evaluated under environmental changes (competing ion, pH and surface loading) by measuring the iron dissolution rate and morphological transformation *via* transmission electron microscopy analysis.

## **5.2. Materials and Methods**

### 5.2.1. Physiochemical characterization

The nanosized iron (hydr)oxides were obtained from Sigma-Aldrich (USA) and US Research Nanomaterials (USA). We measured the pH, electrical conductivity (EC), point of net zero charge (PNZC), surface area (SA), crystal structure and elemental composition of each of the iron (hydr)oxides. The pH and EC were measured using an Orion 5 Star (Thermo, USA) in a 1:200 (W/V) dilution. The PNZC was measured using the pH drift method (Tewari and Campbell, 1976). The SA was obtained using an ASAP 2010 (Micromeritics, USA) with the BET isotherm (N<sub>2</sub> and 77 K). To identify the crystal structure, X-ray diffraction (XRD) and high-resolution transmission electron microscopy (HRTEM) were employed. A D8 Advance (Bruker, Germany) with CuK $\alpha$  radiation from 5 to 90° was employed for XRD, and a JEM-3010 (Jeol, Japan) was used for HRTEM measurement. The

**Fig. 5-1** Scatter plot of pH and competitive sorption ratio ( $CSR_{As(V)/P(V)}$ ) of arsenate and phosphate from the previous studies. The number in the legend indicates surface loading. All studies were conducted in equal addition of arsenate and phosphate.



diffraction pattern was compared with the reference from the American Mineralogist Crystal Structure Database. A Gatan digital camera and an energy dispersive spectroscopy (Gatan, USA) were employed in the HRTEM to characterize the morphology and elemental concentration. For sample preparation for the HRTEM, one drop of the sample was placed onto a carbon film on a copper grid (C300-25, Ted Pella Inc., USA) and dried overnight in a clean chamber. The sample grid was placed in a 60-mm Petri dish (SPL, Korea) and sealed with parafilm for further analysis. Digital Micrograph software (Gatan, USA) was used to analyze the HRTEM image. The characteristics of the iron (hydr)oxides are summarized in Table S1, and the XRD diffraction patterns of the iron (hydr)oxides, including the reference, are illustrated in Fig. 5-2. The pH, EC, PNZC and SA measurements were conducted at least in triplicate.

#### 5.2.2. Batch experiment

For the sorption isotherm, a single-batch experiment of arsenate or phosphate and a dual-batch experiment of arsenate and phosphate were conducted by varying the pH (4, 7 and 10) and surface loading (0, 0.1, 1, 5 and 10 mM) in triplicate. Briefly, 50 mL of oxyanion solution at different concentrations was mixed with 0.25 g of dried iron (hydr)oxide in a 50-mL conical tube. The initial pH of solution was adjusted to the target pH by adding 1 M HCl or NaOH, and the pH of the mixture was controlled every 12 h. All solutions contained 0.1 M NaCl to maintain the ionic strength under the soil environment, and a vertical shaker (Daehan, Korea) was used at 200 rpm at room temperature ( $25\text{ }^{\circ}\text{C} \pm 2\text{ }^{\circ}\text{C}$ ) for 48 h of incubation. After the incubation, the sample was centrifuged at 4,200 RCF for 1 h, and 20 mL of supernatant was filtered with a 0.2- $\mu\text{m}$  PTFE syringe filter (Advantec, Japan). The supernatant was acidified with a drop of 10 M HCl solution, and

**Table 5-1** Physiochemical characteristics of iron (hydr)oxides.

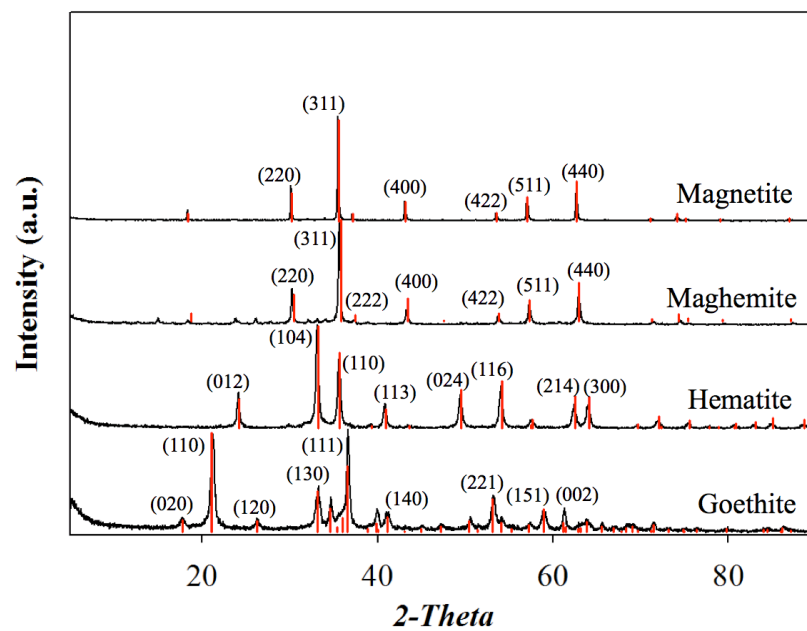
Iron oxide	Formula	Manufacturer (Catalog #)	Shape	Crystal structure	pH	EC	PNZC	Measured SA (m <sup>2</sup> g <sup>-1</sup> )	Calculated SA (m <sup>2</sup> g <sup>-1</sup> )	Cell volume (nm <sup>3</sup> )	Proposed size (nm)	Measured size (nm)
Goethite	FeOOH	US-Nano (US3162)	Rod	isometric	5.72	0.13	5.66	84.0	103.4	0.1386	50x10	50.3x10.8 (n=151)
Hematite	Fe <sub>2</sub> O <sub>3</sub>	US-Nano (US3160)	Spherical	trigonal	9.02	0.11	9.41	37.8	38.1	0.3027	50	58.1 (n=103)
Maghemite	Fe <sub>2.67</sub> O <sub>4</sub>	Sigma-Aldrich (544884)	Spherical	isometric	5.11	0.14	4.66	35.6	24.7	0.5825	30	53.7 (n=116)
Magnetite	Fe <sub>3</sub> O <sub>4</sub>	Sigma-Aldrich (637106)	Spherical	orthomorph	5.34	0.08	4.63	9.30	15.4	0.5906	50-100	109.4 (n=135)

*pH* proton concentration, *EC* electric conductivity (μS cm<sup>-1</sup>), *PZC* point of net zero charge, *SA* surface area (m<sup>2</sup> g<sup>-1</sup>)

*pH* and *EC* were measured at 1:200 (g:mL).

*PNZC* and *SA* were measured by the drift method and N<sub>2</sub>-BET method at 77K, respectively.

**Fig. 5-2** Measured XRD spectrum (black line) and reference position (red bar) of nanosized goethite (0004538), hematite (0017806), maghemite (0020585) and magnetite (0020645). The numbers in the figure indicate the Miller indexes, and the codes from the American mineralogist crystal structure database are shown next to the iron (hydr)oxides.



inductively coupled plasma-optical emission spectrometry (Icap-7200, Thermo, USA) was employed to measure the oxyanion and iron concentration in the solution. The adsorbed concentration was calculated by subtracting the initial concentration from the aqueous concentration. The iron dissolution rate was calculated by dividing the surface area and reaction time by the total amount of iron in the solution determined from the ICP-OES measurement. All reagents were obtained from Sigma-Aldrich (USA) and were at least 98% pure.

### 5.2.3. Data analysis and fitting

The Langmuir isotherm was used to evaluate the sorption characteristics of the iron (hydr)oxides. The Langmuir model is expressed as follows:

$$\Gamma_{eq} = (\Gamma_{max} \cdot K_L \cdot C_{eq}) / (1 + K_L \cdot C_{eq}) \quad \text{(Eq. 5-1)}$$

where  $\Gamma_{eq}$  and  $C_{eq}$  are the equilibrium concentrations of oxyanions in the adsorbed surface (molecule nm<sup>-2</sup>) and solution (mM), respectively, and  $\Gamma_{max}$  and  $K_L$  are the maximum surface density (molecule nm<sup>-2</sup>) and Langmuir constant (L mmol<sup>-1</sup>), respectively. The isotherm fitting was conducted with the dynamic fit wizard function in Sigmaplot 10 (Systat, USA), and we constrained  $0 < \Gamma_{max} < 100$  and  $0 < K_L < 1,000$  and employed 1,000 fits with 2,000 iterations.

Two equations were employed, the competitive sorption ratio (*CSR*) and the competitive effect (*CE*), to better understand the competition between arsenate and phosphate (Violante and Pigna, 2002; Zhu et al., 2011). The *CSR* was obtained from the study of Violante and Pigna (2002), and we developed the *CE* to compare the adsorption difference between single and mixed treatments. The equations are expressed as follows:

$$CSR_{As(V)/P(V)} = \Gamma_{As(V),d} / \Gamma_{P(V),d} \quad \text{(Eq. 5-2)}$$

$$CE_{As(V),P(V)} = \frac{C_{As(V),d} + C_{P(V),d}}{C_{As(V),s} + C_{P(V),s}} - \frac{\Gamma_{As(V),d} + \Gamma_{P(V),d}}{\Gamma_{As(V),s} + \Gamma_{P(V),s}} \quad \text{(Eq. 5-3)}$$

where  $\Gamma_{As(V),d}$  and  $\Gamma_{P(V),d}$  are the adsorbed arsenate and phosphate in the dual-batch experiment, respectively, and  $\Gamma_{As(V),s}$  and  $\Gamma_{P(V),s}$  are the adsorbed arsenate and phosphate in the single-batch experiment, respectively.  $C_{As(V),d}$  and  $C_{P(V),d}$  are the initial concentrations in the dual-batch experiment, and  $C_{As(V),s}$  and  $C_{P(V),s}$  are the initial concentrations in the single-batch experiment. The *CSR* indicates the preference between the oxyanions on the sorbent during the competitive adsorption; a  $CSR_{As(V)/P(V)}$  greater than 1 indicates that the adsorption of arsenate is more predominant than that of phosphate, and *vice versa*. If the  $CSR_{As(V)/P(V)}$  is close to 1, no preferential sorption was favored. We developed the *CE* to quantitatively demonstrate the change in adsorption *via* promotion or competition; a *CE* close to zero implies that no competitive effect occurs; positive or negative values indicate competitive or promotive effects, respectively. All calculations were conducted in Excel software (Microsoft, USA).

### 5.3. Results and Discussion

#### 5.3.1. Physiochemical characteristics

The physiochemical characteristics of goethite, hematite, maghemite and magnetite are summarized in Table S1. The pH values of goethite, hematite, maghemite and magnetite were 5.72, 9.02, 5.11 and 5.34, and the PNZC values were 5.66, 9.41, 4.66 and 4.63, respectively. The EC was 0.08-0.14  $\mu\text{S cm}^{-1}$ , and the SAs from the BET isotherm were 84, 38, 36 and 9.3  $\text{m}^2 \text{g}^{-1}$  for goethite, hematite, maghemite and magnetite, respectively. The cell volume and SA were theoretically calculated from the TEM-measured size of each crystal structure, 0.5825, 0.3027, 0.5906 and 0.1386  $\text{nm}^3$  for the cell volume and 103.4, 38.1, 24.7 and 15.4  $\text{m}^2 \text{g}^{-1}$  for the SA of goethite, hematite, maghemite and magnetite, respectively. There was a

minor difference in the proposed size of the nanosized iron (hydr)oxide and the TEM measurement result, with a rod shape found for the goethite and a spherical shape for the hematite, maghemite and magnetite; the sizes were 50.3 x 10.8, 58.1, 53.7 and 109.4 nm, respectively (Fig. 5-3).

XRD measurement was conducted to confirm the crystal structure of the iron (hydr)oxides, and the results are illustrated in Fig. 5-2. The measured XRD pattern was compared with the previously reported pattern from the American mineralogist crystal structure database, showing a significant match with each crystal structure from the database. The XRD patterns between the maghemite and magnetite were significantly similar, which has been reported in previous studies (Dar and Shivashankar, 2014; Ruíz-Baltazar et al., 2015). Small peaks at 21.9 and 25.4° were found, showing the difference between the two crystal structures. Based on our observations, nanosized goethite, hematite, maghemite and magnetite without unknown sample contamination were confirmed.

### 5.3.2. Adsorption results and competitive sorption ratio

The batch experiment results at the maximum concentration (10 mM) are illustrated for four iron (hydr)oxides and three pH conditions (Fig. 5-4). The adsorbed oxyanion concentrations per gram of iron (hydr)oxide ( $q_s$ ) for arsenate, phosphate and the mixture on the goethite were 0.34, 0.37 and 0.31 mmol g<sup>-1</sup>, respectively, at pH 4; 0.35, 0.32 and 0.26 mmol g<sup>-1</sup>, respectively, at pH 7; and 0.29, 0.23 and 0.27 mmol g<sup>-1</sup>, respectively, at pH 10. The  $q_s$  values for arsenate, phosphate and the mixture on the hematite were 0.29, 0.23 and 0.17 mmol g<sup>-1</sup>, respectively, at pH 4; 0.20, 0.20 and 0.21 mmol g<sup>-1</sup>, respectively, at pH 7; and 0.06, 0.13 and 0.13 mmol g<sup>-1</sup>, respectively, at pH 10. For the maghemite, the  $q_s$  values for arsenate, phosphate and the mixture were 0.17, 0.28 and 0.28 mmol g<sup>-1</sup>,

respectively, at pH 4; 0.18, 0.19 and 0.15 mmol g<sup>-1</sup>, respectively, at pH 7; and 0.07, 0.14 and 0.07, respectively, at pH 10. For the magnetite, they were 0.08, 0.14 and 0.09 mmol g<sup>-1</sup>, respectively, at pH 4; 0.11, 0.16 and 0.11 mmol g<sup>-1</sup>, respectively, at pH 7; and 0.01, 0.15 and 0.06 mmol g<sup>-1</sup>, respectively, at pH 10. The maximum  $q_s$  was observed in the goethite treatments at pH values of 4 and 7, and the minimum  $q_s$  was observed in the maghemite treatment at pH 10. General patterns in  $q_s$  were observed: a gradual decrease with increasing pH and a significant correlation between the  $q_s$  value and the surface area of the adsorbent; the general patterns were described in previous studies (Dixit and Hering, 2003; Mahmood et al., 2014; Roberts et al., 2004).

A distinctive pattern was observed in which the goethite and magnetite showed higher average values in the single treatments than in the mixed treatments at all pH conditions, but hematite showed lower average values in the single treatments than in the mixed treatments at all pH conditions. The maghemite showed similar results to those of hematite at pH 4 but showed the opposite results at pH 7 and 10. In addition, the  $q_s$  of phosphate did not gradually decrease with increasing pH in the magnetite treatment, and the single arsenate and mixed treatments showed maximum  $q_s$  at pH 7, whereas there was no significant difference for phosphate. The  $q_s$  of phosphate in the hematite, maghemite and magnetite was higher than the  $q_s$  of arsenate, except for the hematite at pH 4, and the  $q_s$  of arsenate was higher than that of phosphate in the goethite at pH 7 and 10, whereas the opposite pattern was observed at pH 4. The results show that the arsenate, phosphate and their mixture showed different adsorption characteristics on the iron hydroxides and that the pH controlled the adsorption characteristics. To better explain the adsorption isotherm, the  $q_s$  was converted to surface density ( $\Gamma_s$ ) to address the effects of SA and surface loading. The terms surface loading and

**Fig. 5-3** HRTEM image of nano-sized goethite (a), hematite (b), maghemite (c) and magnetite (d).

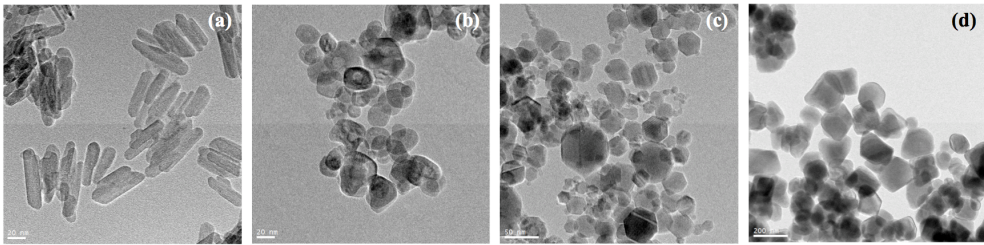


**Fig. 5-4** Stacked bar graph of the adsorbed oxyanion per unit mass in the arsenate, phosphate and mixture treatments under 10 mM of total oxyanion input on the goethite, hematite, maghemite and magnetite at pH values of 4, 7 and 10. Error bar indicates standard error from the Langmuir fitting result. An asterisk (\*) indicates that the average value of the adsorbed oxyanions from two single treatments is significantly higher than the sum of the adsorbed oxyanions from the mixture treatment, and two asterisks (\*\*) indicates the opposite.

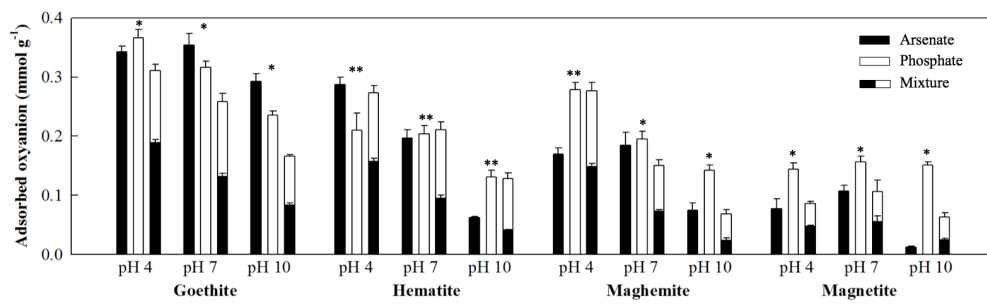


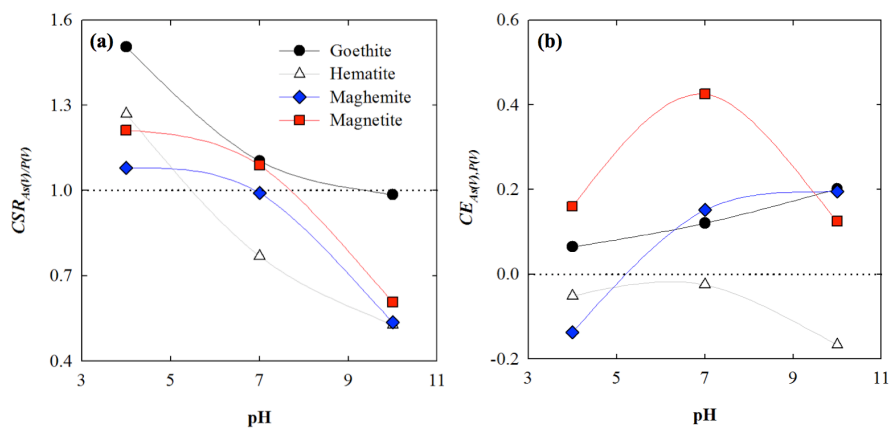
**Table 5-2** Langmuir fitting results with different oxyanion inputs, pH values and iron oxides.  $\Gamma_{max}$  and  $K_L$  are the maximum surface density and Langmuir constant, respectively. Values in parenthesis and Adj.  $R^2$  indicate the standard error and the adjusted coefficient of determination of the Langmuir fitting. The  $\Gamma_{max}$  value in magnetite at pH 7 was caused by unsaturated curve.

Target	Matrix	pH	Goethite			Hematite			Maghemite			Magnetite		
			$\Gamma_{max}$	$K_L$	Adj. $R^2$	$\Gamma_{max}$	$K_L$	Adj. $R^2$	$\Gamma_{max}$	$K_L$	Adj. $R^2$	$\Gamma_{max}$	$K_L$	Adj. $R^2$
As(V)	As(V) only	4	2.45 (0.07)	8.39 (1.43)	0.994	4.83 (0.20)	1.66 (0.34)	0.994	3.01 (0.18)	3.23 (1.16)	0.978	5.66 (1.09)	6.69 (0.52)	0.877
		7	2.45 (0.14)	3.42 (1.10)	0.978	3.46 (0.22)	1.26 (0.36)	0.983	3.50 (0.37)	0.672 (0.27)	0.970	100 (633)	0.078 (0.05)	0.932
		10	2.27 (0.09)	1.43 (0.28)	0.992	0.98 (0.03)	578 (142)	0.987	1.41 (0.20)	1.12 (0.71)	0.911	0.748 (0.08)	31.9 (26.9)	0.859
P(V)	P(V) only	4	2.56 (0.10)	8.10 (1.85)	0.989	3.41 (6.20)	2.48 (0.80)	0.980	4.86 (0.21)	2.27 (0.51)	0.989	9.66 (0.68)	1.75 (0.66)	0.972
		7	2.24 (0.08)	6.75 (1.55)	0.990	3.38 (0.22)	1.59 (0.52)	0.977	3.54 (0.23)	1.72 (0.57)	0.977	11.4 (0.63)	0.90 (0.21)	0.988
		10	1.72 (0.05)	3.13 (0.54)	0.994	2.11 (0.19)	3.01 (1.78)	0.949	2.40 (0.15)	2.20 (0.77)	0.978	11.6 (0.34)	0.47 (0.05)	0.998
As(V)	As(V) + P(V)	4	1.31 (0.04)	44.8 (9.01)	0.992	2.54 (0.09)	8.70 (1.74)	0.992	2.60 (0.10)	728 (.154)	0.991	2.85 (0.10)	290 (90.3)	0.985
		7	0.934 (0.04)	59.0 (23.1)	0.988	1.56 (0.09)	5.90 (2.13)	0.977	1.22 (0.04)	1894 (754)	0.989	4.28 (0.60)	1.09 (0.57)	0.946
		10	0.591 (0.02)	957 (578)	0.979	0.71 (0.02)	1325 (336)	0.990	0.404 (0.08)	-6.34 (2.30)	0.820	1.75 (0.21)	1.96 (1.05)	0.936
P(V)	As(V) + P(V)	4	0.870 (0.03)	34.8 (12.5)	0.989	2.00 (0.11)	3.31 (0.92)	0.984	2.41 (0.14)	1.88 (0.48)	0.987	2.35 (0.12)	43.9 (20.5)	0.967
		7	0.846 (0.06)	23.5 (13.5)	0.966	2.03 (0.12)	2.80 (0.82)	0.982	1.23 (0.13)	6.30 (4.35)	0.931	3.93 (0.65)	0.76 (0.41)	0.948
		10	0.600 (0.00)	14.6 (0.79)	0.999	1.35 (0.13)	3.89 (2.04)	0.946	0.754 (0.03)	39.2 (17.4)	0.978	2.88 (0.20)	1.20 (0.33)	0.985

surface density indicate the total amount of oxyanion per SA of sorbent and the adsorbed amounts of oxyanion per SA of sorbent, respectively.

The Langmuir adsorption parameters ( $\Gamma_{max}$  and  $K_L$ ) were fitted at pH 4, 7 and 10 in the arsenate, phosphate and mixed treatments. The  $\Gamma_{max}$  values of the arsenate treatment at pH 7 were 2.45, 3.46, 3.50 and 100 molecule nm<sup>-2</sup> for goethite, hematite, maghemite and magnetite, respectively, and the  $\Gamma_{max}$  values of the phosphate treatment at pH 7 were 2.24, 3.38, 3.54 and 11.4 molecule nm<sup>-2</sup>, respectively. In the mixed treatment at pH 7, the  $\Gamma_{max}$  values of arsenate were 0.846, 2.03, 1.23 and 3.93 molecule nm<sup>-2</sup> for goethite, hematite, maghemite and magnetite, respectively, and the  $\Gamma_{max}$  values of phosphate were 0.846, 2.03, 1.23 and 3.93 molecule nm<sup>-2</sup>, respectively. The adjusted coefficient of determination was 0.820 to 0.999. An unexpected error was found in the  $\Gamma_{max}$  of the arsenate treatment at pH 7 on the magnetite because the maximum constraint for the fitting was reached. An unsaturated fitting curve was observed, and precipitation was assumed based on the unsaturated curves; thus, HRTEM and XRD analysis were conducted to identify the precipitates. However, the size measurement and XRD showed no significant difference (data not shown). Based on the results and previous studies, it is presumed that the unsaturated curve was caused by surface precipitation or reduction of arsenate to arsenite with the oxidation of magnetite. Numerous studies reported precipitation of arsenate on the surface of iron (hydr)oxides, but no study has confirmed the coprecipitation at circumneutral pH. Precipitation was also not detectable in our HRTEM and XRD analysis. Numerous studies reported that reduction of arsenate to arsenite could increase the adsorption (Jain and Loeppert, 2000; Liu et al., 2015), but there was insufficient information to measure the reduction (for example, X-ray absorption near-edge spectroscopy). In addition, the magnetite easily oxidizes under ambient conditions, and the transformation is not easily detected if maghemite is formed or if only a thin surface is transformed (Schwaminger et al., 2017).

**Fig. 5-5** Line and scatter plot of the pH and competitive sorption ratio (*CSR*) (a) and the pH and competitive effect (*CE*) (b) calculated for interpreting the competitive sorption between arsenate and phosphate. *CSR* and *CE* were calculated with  $\Gamma_{max}$  from the Langmuir isotherm fitting result. A value greater than 1 in  $CSR_{As(V)/(P)}$  indicates that Arsenate is more predominant than phosphate and *vice versa*. The value close to zero in  $CE_{As(V),P(V)}$  implies that no competitive effect was observed, while positive and negative values show the competitive or promotive effect, respectively.



With increasing pH from 4 to 10, the  $\Gamma_{max}$  decreased or was similar in most treatments, but the  $\Gamma_{max}$  in all magnetite treatments and arsenate treatments on maghemite increased or increased then decreased. In contrast, the  $K_L$  decreased or decreased then increased with increasing pH from 4 to 10 in most treatments, except for arsenate and the mixed treatment on goethite and phosphate and the mixed treatment on maghemite. However, the trends in competitive adsorption in response to a change in pH are complicated; thus,  $\Gamma_{max}$  was applied in eq. (2) to interpret the results more easily, as illustrated in Fig. 5-5a. As described above, the  $CSR$  and  $CE$  indicate the preferential adsorption and competitive effects, respectively, and the black dotted line indicates that no such effect occurred, i.e., the value for the  $CSR$  was 1 and for the  $CE$  was 0. Interestingly, more preferential sorption of arsenate than phosphate at pH 4 was observed, but the  $CSR_{As(V)/P(V)}$  gradually decreased with increasing pH. The  $CSR_{As(V)/P(V)}$  values were 1.50, 1.27, 1.08 and 1.21 for goethite, hematite, maghemite and magnetite, respectively, at pH 4 and decreased to 0.98, 0.53, 0.54 and 0.61 at pH 10, respectively. Based on the observation, it was confirmed that the arsenate was more preferentially adsorbed onto the iron (hydr)oxides at the low pH conditions, but phosphate was preferred at the high pH conditions for all the iron (hydr)oxides except goethite.

As noted above, previous studies reported controversial results (Fig. 5-1). Based on the previous studies, the  $CSR_{As(V)/P(V)}$  was calculated. Several studies confirmed the increase in the  $CSR_{As(V)/P(V)}$  with increasing pH, such as 0.95-1.02 at pH 3-5 on goethite according to Hongshao and Stanforth (2001) and 1.0-1.45 at pH 3.7-9.9 on ferrihydrite according to Jain and Loeppert (2000). In contrast, opposite patterns have also been found; Gao and Mucci (2001) reported  $CSR_{As(V)/P(V)}$  values of 0.9-1.8 at pH 3-8.7 on goethite, Violante and Pigna (2002) reported 1.0-1.2 at pH 4-7 on ferrihydrite, and Manning and Goldberg (1996) found 0.88-1.18 at pH 2.5-

11.2 on goethite. No significant correlation among the  $CSR_{As(V)/P(V)}$  pattern, type of iron (hydr)oxide and experimental condition was found from the previous studies; however, we observed an interesting pattern for interpreting the relationship between surface loading and  $CSR_{As(V)/P(V)}$  (Fig. 5-6). The  $CSR$  of each pH was close to 1 at low surface loading for all iron (hydr)oxides, and the pattern of the  $CSR$  with increasing pH was distinctive at the high surface loading condition. In addition, the maghemite and magnetite showed similar patterns, possibly due to the transformation of the magnetite surface to maghemite. The arsenate was more preferentially adsorbed on the iron (hydr)oxide surface at low pH, and phosphate was dominant at high pH, as shown by our observation and previous studies. The surface loading also showed different  $CSR_{As(V)/P(V)}$  patterns for each of the iron (hydr)oxides.

### 5.3.3. Competitive effect

We observed a relatively uniform pattern in the  $CSR_{As(V)/P(V)}$  results, but the  $CE_{As(V),P(V)}$  results showed a more ambiguous pattern.  $\Gamma_{max}$  was applied in eq. (3) to interpret the results (Fig. 5-5b), and the surface loading effect determined using  $q_s$  is illustrated in Fig. 5-6. The  $CE_{As(V),P(V)}$  values at pH 4, 7 and 10 were 0.06, 0.12 and 0.20, respectively for goethite; -0.05, -0.02 and -0.17, respectively, for hematite; -0.13, 0.15 and 0.20, respectively, for maghemite; and 0.16, 0.42 and 0.12, respectively, for magnetite. We hypothesized that an increase in pH would lead to an increase in the  $CE_{As(V),P(V)}$  because more deprotonated sorption sites would be available due to the increased amount of hydroxyl ion, which does not apply to the adsorption sites of oxyanions. In our results, the pattern of the  $CE_{As(V),P(V)}$  agreed with the hypothesis for the goethite and maghemite treatments, but we observed all negative  $CE_{As(V),P(V)}$  values in the hematite treatment and a maximum at pH 7 in the

**Fig. 5-6** Line and scatter plot of surface loading and competitive sorption ratio (*CSR*) on goethite, hematite, maghemite and magnetite. A value greater than 1 in  $CSR_{As(V)/(P)}$  indicates that As(V) is predominant *versus* phosphate and *vice versa*.

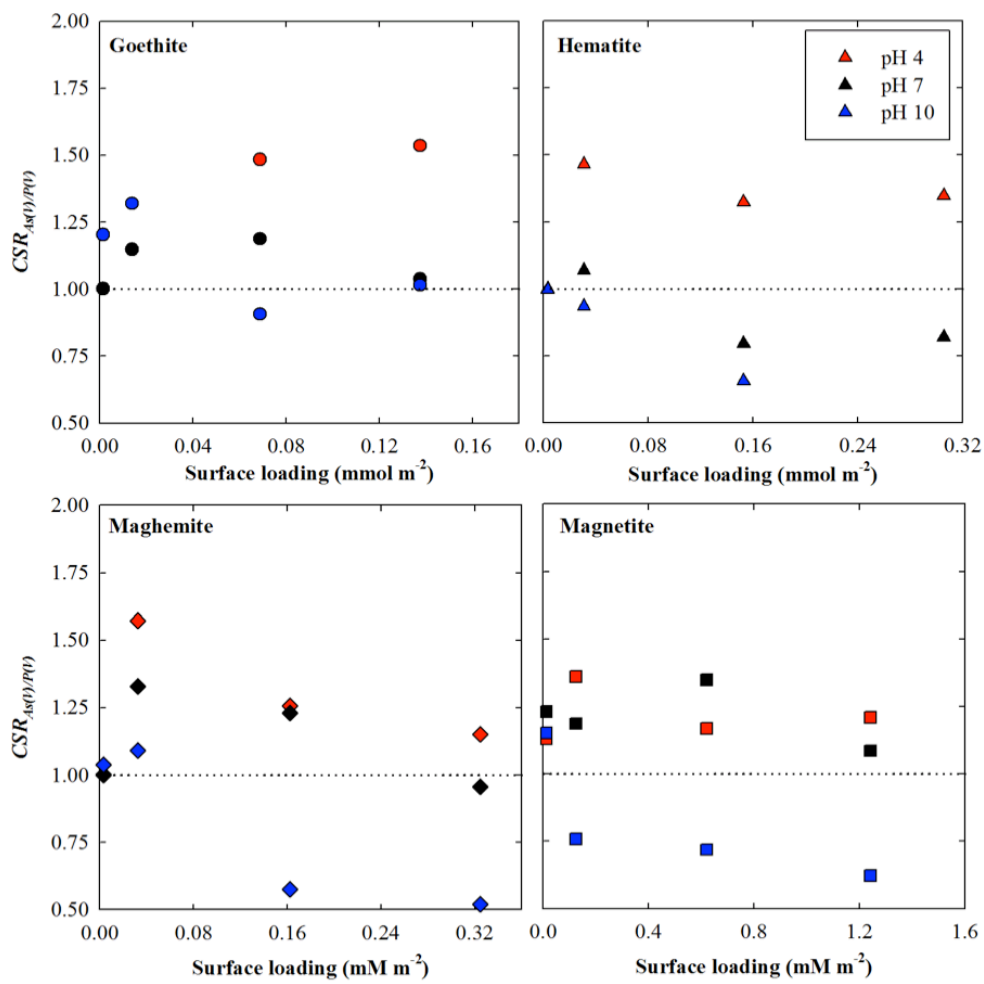
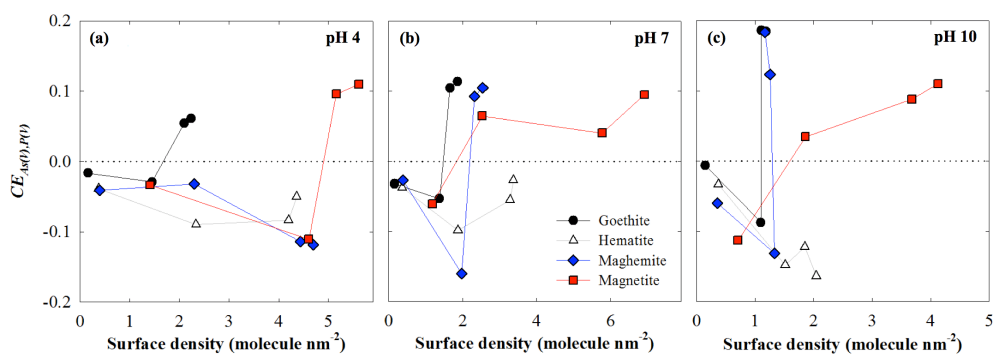


**Fig. 5-7** Line and scatter plot of surface density (molecule nm<sup>-2</sup>) and competitive effect (*CE*) of arsenate and phosphate on goethite, hematite, maghemite and magnetite at pH values of 4 (a), 7 (b) and 10 (c). *CE* was calculated with experimental sorption data, and the dotted line indicates zero in  $CE_{As(V),P(V)}$ , which implies that no competitive effect is observed. The cross point of the dotted line and solid line was defined as the surface density without the competitive and promotive effects ( $\Gamma_{CE=0}$ ).



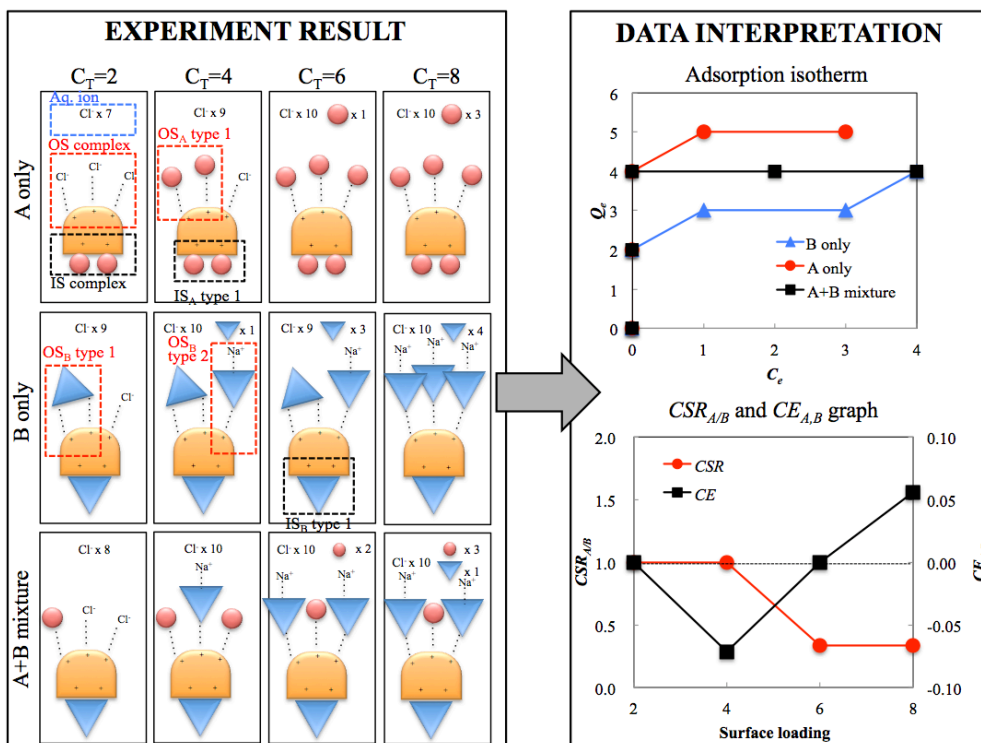
magnetite treatment, which caused the unsaturated curve described above. To explain the results, we considered the surface loading effect because we also hypothesized that increased surface loading would lead to competition for adsorption sites. The relationship between the surface density and  $CE_{As(V),P(V)}$  is illustrated in Fig. 5-7 to interpret the surface loading effect.

We found an interesting phenomenon in the goethite, maghemite and magnetite in which the  $CE_{As(V),P(V)}$  was close to zero at low surface density and became negative with increasing surface density. In addition, a dramatic increase was observed at certain points except for hematite; the crossing point of the dotted line and solid line was defined as  $T_{CE=0}$ , where the competitive and promotive effects were offset (Fig. 5-7). This phenomenon was also observed in previous studies by calculating the  $CE_{As(V),P(V)}$  and was explained by the competition for limited sorption sites. At low surface density, excess adsorption sites were available for both oxyanions; thus, no competitive or promotive effects occurred. However, an increase in surface density led to more adsorption capacity in the mixed treatment than the sum of the single treatments for arsenate and phosphate, which could be explained by the difference in the adsorption mechanisms of both oxyanions on the iron (hydr)oxide surface.

Previous studies confirmed that each oxyanion has a different thermodynamic stability on the plane of the crystal structure. For example, Kubicki et al. (2012) identified the adsorption energies of phosphate as monodentate and bidentate configurations through molecular dynamic simulation, and the results suggested that the bidentate configuration was favorable in the (101), (010) and (100) planes, whereas the monodentate configuration was more stable in the (210) and (001) planes. Kubicki et al. (2007) also showed that the Gibbs free energy of

adsorption ( $\Delta G_{\text{ads}}$ ) for monoprotonated and biprotonated arsenate on bioctahedral ferric hydroxide and biprotonated arsenate showed lower  $\Delta G_{\text{ads}}$  than the monoprotonated arsenate complex. Based on the simulation results, it was inferred that the speciation and structural configuration of each oxyanion would lead to a thermodynamically preferential adsorption mechanism on each plane of the iron (hydr)oxide surface, and the overlaid result was only observable from the various adsorption mechanisms. Based on the inference, a sudden decrease in  $CE_{As(V),P(V)}$  could be explained as a result of the difference in the thermodynamic stabilities of the structural configuration for each oxyanion on each iron (hydr)oxide surface, i.e., the promotive effect derived from the difference in the sorption mechanisms of each oxyanion. The promotive and competitive effects are illustrated in Fig. 5-8. In the figure, chemicals A and B are the oxyanions, which are mono- and divalent ions and have two and three sorption mechanisms *via* inner- and outer-sphere complexations. At low surface loading ( $C_T=2$ ), there is unoccupied space in the sorbent; thus, no competitive effect ( $CE_{A,B}=0$ ) or preferential sorption ( $CSR_{A/B}=1$ ) was observed. At  $C_T=4$ , we observed two types of sorption mechanisms for chemical A, three types for chemical B, and three types for the A+B mixture. It was assumed that the IS complex of chemical A ( $IS_A$ ) is not thermodynamically favorable when competing with the IS complex of chemical B with the bidentate configuration ( $IS_B$ ); thus, only the  $OS_A$  complex was found in the A+B mixture, but both the IS and OS complexes were found in chemical B. In addition, chemical B has two OS complex types, the electrostatic pair interaction with the sorbent ( $OS_{B\text{-type 1}}$ ) and the electrostatic pair with the sorbent and  $Na^+$  ion ( $OS_{B\text{-type 2}}$ ). In the A+B mixture, four chemicals were observed at the surface, and 7 chemicals were observed in the A and B treatments; thus, the  $CE_{A,B}$  was calculated as -0.07, which indicates the promotive effect of changing the adsorption mechanism of chemical B.

**Fig. 5-8** Schematic illustration for the isotherm adsorption, competitive sorption ratio (*CSR*) and competitive effect (*CE*) on two chemicals, A and B, with increasing surface loading. IS and OS denote the inner- and outer-sphere complex, respectively. We assumed that chemical A has only one type of IS and OS interaction with the sorbent, while chemical B has two types of OS interaction with one IS interaction.



There was no preferential sorption because all chemicals were adsorbed.

In our experiment, a dramatic increase in the  $CE_{As(V),P(V)}$  was observed with the promotive effect, and  $\Gamma_{CE=0}$  was defined as where the degrees of the promotive effect and competitive effect are equal. In Fig. 5-8,  $C_T=6$  describes  $\Gamma_{CE=0}$ , but the surface loading was used instead of the surface density because the difference in surface loading could not be shown in this example. At this point, the promotive effect is equal to the  $C_T=4$  condition; however, competition was introduced, and the competitive effect counterbalanced the promotive effect. The  $CSR_{A/B}$  decreased to 0.33 because more chemical B was adsorbed on the surface than chemical A. After  $\Gamma_{CE=0}$ , an increase in the  $CE_{A,B}$  was also observed due to the change in the OS complex in chemical B. With increasing concentration,  $OS_{B-type 2}$  is more favorable for all OS complexes; thus, three  $OS_{B-type 2}$  were formed, and nine chemicals were adsorbed in the single treatments of A and B, whereas only four chemicals were adsorbed in the A+B mixed treatment. As a result,  $CE_{A,B}$  increased to 0.06.

With the interpretation of the example, it is possible to explain the experimental results. Similar patterns were observed in goethite and magnetite at all pH conditions:  $CE_{As(V),P(V)}$  was zero at low surface density and decreased with increasing surface density; then, it increased after  $\Gamma_{CE=0}$ . The  $\Gamma_{CE=0}$  values of goethite at pH 4, 7 and 10 were 1.8, 1.7 and 1.2 molecule  $nm^{-2}$ , respectively, and the  $\Gamma_{CE=0}$  values of magnetite were 4.9, 1.9 and 1.7 molecule  $nm^{-2}$ , respectively. The  $\Gamma_{CE=0}$  values of maghemite at pH 7 and 10 were 2.3 and 1.4, respectively. An increase in pH led to a decrease in  $\Gamma_{CE=0}$ , and we observed that the degree of the decrease significantly differed depending on the iron (hydr)oxide and pH. The results show that there are no promotive or competitive effects when the surface is unsaturated with a low concentration of chemicals and that increasing the surface loading from the low concentration leads to a greater increase in the total adsorbed

concentration than the sum of the individually adsorbed concentrations. This phenomenon is called a promotive effect because there is an increase in the adsorbed concentration. Then, the  $\Gamma_{CE=0}$  point appears, where the promotive effect and competitive effect are counterbalanced. At high surface loading, the total adsorbed concentration is less than the sum of the individually adsorbed concentrations, and the competitive effect would be greater than the promotive effect; thus, a positive value should be obtained.

#### 5.3.4. Iron oxide stability with the presence of oxyanions

The adsorption characteristics and the stability of the sorbent are crucial to estimate the bioavailability and leachability of oxyanions in the soil environment. There are three main types of iron in the aqueous phase after the centrifugation and filtration, colloidal iron oxide less than 200 nm (because a 0.2  $\mu\text{m}$  filter was used), aqueous iron-oxyanion complexes and iron ions. However, quantification of their abundance was not possible due to difficulty in obtaining measurements. Thus, the results were interpreted using three rules from previous studies. Numerous studies reported the effect of pH on iron dissolution and revealed that more ferric ions would be released at a low pH condition (Cornell and Schwertmann, 2003; Panias et al., 1996; Schwertmann, 1991). If the solution pH was close to the PNZC of the colloidal particle, then the precipitation would increase; thus, the concentration of colloidal iron oxide would decrease. In contrast, if the solution pH was not close to the PNZC, then the colloidal particles would increase. Ferric arsenate or the ferric phosphate complex have been reported as a pathway of interaction between iron oxide and aqueous phosphate in the soil environment (Du et al., 2014; Jia and Demopoulos, 2008; Wang et al., 2016). Yang et al. (2015) revealed that increasing pH led to the ferric arsenate complex above pH 2.38, and the formation of the

FeAsO<sub>4</sub> complex from Fe<sup>3+</sup> and H<sub>2</sub>AsO<sub>4</sub><sup>-</sup> ions yielded -448.2 kJ mol<sup>-1</sup> of Gibbs free energy, indicating the thermodynamic stability of the ferric arsenate complex. For this reason, the iron dissolution rate at a high pH condition was mainly caused by the ferric arsenate complex.

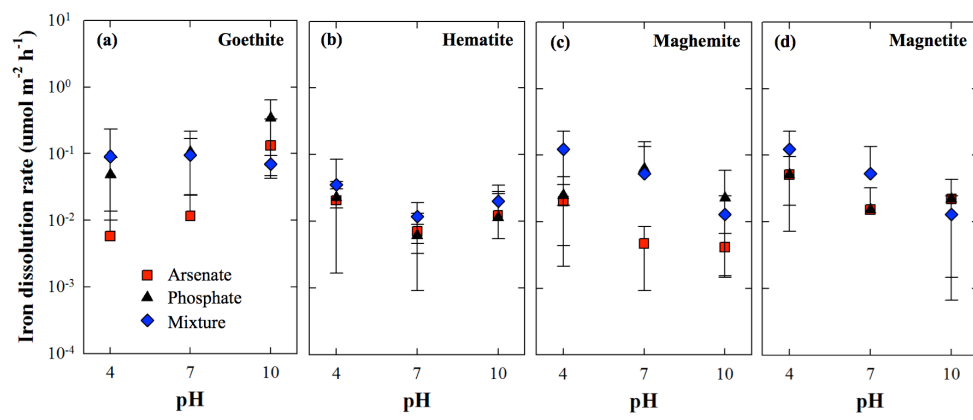
The iron dissolution rate is demonstrated in Fig. 5-9 for the single arsenate or phosphate treatments and the mixed treatment in goethite, hematite, maghemite and magnetite at a 10-mM concentration. The iron dissolution rates at different concentrations were also measured, but illustration of the concentration effect was too complex; thus, the pH and oxyanion input types were focused on. To summarize the concentration effect, in most conditions, a higher concentration of the arsenate, phosphate or mixed treatments led to a decrease in the iron dissolution rate, except for goethite (data not shown). Regarding the effect of the pH and oxyanion, the maximum iron dissolution rate was observed at pH 4, except for goethite, and was 0.021, 0.020 and 0.042 μmol m<sup>-2</sup> h<sup>-1</sup> for hematite, maghemite and magnetite, respectively, under phosphate treatment. Interestingly, goethite showed a maximum iron dissolution rate at pH 10 with the mixed treatment, and bernalite formation was observed with the presence of arsenate or phosphate, which was identified in previous studies (Han and Ro, 2018). From the HRTEM measurement, we identified the size of the bernalite formation as approximately 30 nm at the high pH condition with high concentrations of arsenate, phosphate or the mixture, which was the reason for the high iron dissolution rate in goethite at pH 10.

In most conditions, except for the goethite treatment with a high pH, the iron dissolution rates of the arsenate treatments were lower than or similar to those of the phosphate or mixed treatments. The phosphate and mixed treatments showed no significant difference for hematite and magnetite, and the minimum iron dissolution rate occurred at pH 7. A general pattern was observed, showing a

decrease in the iron dissolution rate with increasing pH, mainly caused by the reduction in ferric ion dissolution from the iron (hydr)oxide surface. An increase in the iron dissolution rate with increasing pH was observed in the hematite and magnetite, and it was inferred that the formation of ferric arsenate or ferric phosphate resulted in the increase in the iron dissolution rate with increasing pH. The iron dissolution rate of the mixture in maghemite and magnetite showed similar patterns that were distinctive from that in the presence of arsenate. The arsenate treatments showed a lower iron dissolution rate than the phosphate or mixture treatments, but the iron dissolution rates of the arsenate and phosphate treatments were similar for magnetite. Similar results were found in previous studies. Khoe and Robins (1988) measured the formation constant of ferric arsenate and ferric phosphate as -1.34 and 0.78, respectively. Kuzin et al. (2013) observed an increase in the iron dissolution rate with the addition of phosphate, whereas Paige et al. (1997) observed a decrease in the iron dissolution rate with the presence of arsenate, caused by surface precipitation. Based on previous studies, the combination of the rate of ferric-oxyanion formation and surface precipitation controls the iron dissolution rate. In addition, the magnetite and maghemite did not show significant differences, and it was presumed that the reduction of arsenate and oxidation of the magnetite surface led to such an effect.

An extremely distinctive pattern of the iron dissolution rate was observed as a function of pH, iron (hydr)oxide and surface loading, and the individual patterns were difficult to explain based on the current study. However, bernalite as a colloidal iron hydroxide has been found, which would cause the previously reported colloidal mobilization of arsenate and phosphate (Zhang and Selim, 2007), and a high level of phosphate would facilitate the iron dissolution compared with the arsenate-rich conditions in most treatments. The hematite showed relatively

**Fig. 5-9** The average of iron dissolution rates ( $\text{nmol m}^{-2} \text{h}^{-1}$ ) at 10 mM of the arsenate (red), phosphate (blue) and mixture (black) treatments as a function of pH on goethite (a), hematite (b), maghemite (c) and magnetite (d). The error bar indicates the standard deviation of the iron dissolution rates at a 10-mM oxyanion concentration.



superior stability with the change in pH and oxyanion than the other iron (hydr)oxides. In addition, our results suggest that the oxyanion could work as a protector or a destroyer of nanosized iron (hydr)oxide in the soil environment. Environmental problems, such as soil acidification or nutrient depletion, would decrease the stability of iron (hydr)oxide in the soil, which would thus accelerate soil degradation by releasing the iron (hydr)oxide from the soil.

#### 4 Conclusion

In this study, adsorption isotherms were determined by changing the pH of four synthetic nanosized iron (hydr)oxides, and the results were compared by employing the *CSR* and newly proposed *CE* to better interpret the competitive adsorption in this study and previous studies. Single or mixed treatments of arsenate and phosphate yielded different results as a function of the pH and the type of iron hydroxide. Arsenate was preferentially adsorbed at a low pH, and phosphate was dominant at a high pH. The  $CE_{As(V),P(V)}$  was close to zero at low surface density and sequentially changed to a negative then positive value with increasing surface density due to promotive and competitive effects. Transformation from goethite to bernalite was identified at high pH with the presence of an oxyanion, and the iron (hydr)oxides showed resistance upon the addition of an oxyanion and a change in pH. In the presence of phosphate, arsenate or both and at low pH, the stability of iron (hydr)oxide decreased.

In the real environment, oxyanions always compete with each other at different concentrations, pH values and adsorbents, but the detailed mechanisms of competition are not fully understood. However, our investigation revealed that the environmental variables are interconnected, and this significantly affects the

adsorption characteristics of oxyanions in the soil environment. The hematite showed a significant promotive effect regardless of the pH, and it could more effectively reduce problems caused by overfertilization compared to the other iron (hydr)oxides. We focused on the competitive adsorption at equal concentrations of arsenate and phosphate; in the future, the competitive adsorption at nonequal concentrations with a more complex composition must be described to interpret the natural phenomenon in the soil environment.

## References

- Abdala, D.B., Northrup, P.A., Arai, Y., Sparks, D.L., 2015. Surface loading effects on orthophosphate surface complexation at the goethite/water interface as examined by extended X-ray Absorption Fine Structure (EXAFS) spectroscopy. *J. Colloid Interface Sci.* 437, 297–303. doi:10.1016/j.jcis.2014.09.057
- Antelo, J., Avena, M., Fiol, S., López, R., Arce, F., 2005. Effects of pH and ionic strength on the adsorption of phosphate and arsenate at the goethite-water interface. *J. Colloid Interface Sci.* 285, 476–486. doi:10.1016/j.jcis.2004.12.032
- Barberis, E., Ajmone Marsan, F., Scalenghe, R., Lammers, A., Schwertmann, U., Edwards, A.C., Maguire, R., Wilson, M.J., Delgado, A., Torrent, J., 1995. European soils overfertilized with phosphorus: Part 1. Basic properties. *Fertil. Res.* 45, 199–207. doi:10.1007/BF00748590
- Bolan, R.M., Wierzbicka-Wieczorek, M., Čaplovičová, M., Uhlík, P., Göttlicher, J., Steininger, R., Majzlan, J., 2013. Structural Incorporation of As 5+ into Hematite. *Environ. Sci. Technol.* 47, 9140–9147. doi:10.1021/es305182c
- Brechbühl, Y., Christl, I., 2012. Competitive sorption of carbonate and arsenic to hematite: Combined ATR-FTIR and batch experiments. *J. Colloid Interface Sci.* 377, 313–321. doi:10.1016/j.jcis.2012.03.025
- Carabante, I., Grahn, M., 2010. In situ ATR-FTIR studies on the competitive adsorption of arsenate and phosphate on ferrihydrite. *J. Colloid Interface Sci.* 351, 523–531. doi:10.1016/j.jcis.2010.07.064
- Cornell, R.M., Schwertmann, U., 2003. *The iron oxides: structure, properties, reactions, occurrences, and uses.* Wiley-VCH.
- Dai, C., Liu, J., Hu, Y., 2018. Impurity-bearing ferrihydrite nanoparticle precipitation/deposition on quartz and corundum. *Environ. Sci. Nano* 5, 141–149. doi:10.1039/C7EN00835J
- Dar, M.I., Shivashankar, S.A., 2014. Single crystalline magnetite, maghemite, and hematite nanoparticles with rich coercivity. *RSC Adv.* 4, 4105–4113. doi:10.1039/C3RA45457F
- Dixit, S., Hering, J.G., 2003. Comparison of arsenic(V) and arsenic(III) sorption onto iron oxide minerals: Implications for arsenic mobility. *Environ. Sci. Technol.* 37, 4182–4189. doi:10.1021/es030309t
- Du, J., Jing, C., Duan, J., Zhang, Y., Hu, S., 2014. Removal of arsenate with hydrous ferric oxide coprecipitation: Effect of humic acid. *J. Environ. Sci. (China)* 26, 240–247. doi:10.1016/S1001-0742(13)60437-4
- Elser, J.J., Bracken, M.E.S., Cleland, E.E., Gruner, D.S., Harpole, W.S., Hillebrand, H., Ngai, J.T., Seabloom, E.W., Shurin, J.B., Smith, J.E., 2007. Global analysis of nitrogen and phosphorus limitation of primary producers in freshwater, marine and terrestrial ecosystems. *Ecol. Lett.* 10, 1135–1142. doi:10.1111/j.1461-0248.2007.01113.x
- Farquhar, M.L., Charnock, J.M., Livens, F.R., Vaughan, D.J., 2002. Mechanisms of arsenic uptake from aqueous solution by interaction with goethite, lepidocrocite, mackinawite, and pyrite: An X-ray absorption spectroscopy study. *Environ. Sci. Technol.* 36, 1757–1762. doi:10.1021/es010216g
- Fendorf, S., Eick, M.J., Grossl, P., Sparks, D.L., 1997. Arsenate and chromate retention mechanisms on goethite. 1. Surface structure. *Environ. Sci. Technol.* 31, 315–320. doi:10.1021/es950653t
- Frau, F., Addari, D., Atzei, D., Biddau, R., 2010. Influence of Major Anions on As ( V )

- Adsorption by Synthetic 2-line Ferrihydrite . Kinetic Investigation and XPS Study of the Competitive Effect of Bicarbonate. *Water, Air, & Soil Pollut.* 205, 25–41. doi:10.1007/s11270-009-0054-4
- Gao, Y., Mucci, A., 2001. Acid base reactions, phosphate and arsenate complexation, and their competitive adsorption at the surface of goethite in 0.7 M NaCl solution. *Geochim. Cosmochim. Acta* 65, 2361–2378. doi:10.1016/S0016-7037(01)00589-0
- Goh, K.H., Lim, T.T., 2010. Influences of co-existing species on the sorption of toxic oxyanions from aqueous solution by nanocrystalline Mg/Al layered double hydroxide. *J. Hazard. Mater.* 180, 401–408. doi:10.1016/j.jhazmat.2010.04.045
- Han, J., Ro, H.-M., 2018. Identification of Bernalite Transformation and Tridentate Arsenate Complex at Nano-goethite under Effects of Drying, pH and Surface Loading. *Sci. Rep.* 8, 8369. doi:10.1038/s41598-018-26808-4
- Hongshao, Z., Stanforth, R., 2001. Competitive Adsorption of Phosphate and Arsenate on Goethite. *Environ. Sci. Technol.* 35, 4753–4757.
- Jain, A., Loeppert, R.H., 2000. Effect of competing anions on the adsorption of arsenate and arsenite by ferrihydrite. *J. Environ. Qual.* 29, 1422–1430. doi:10.2134/jeq2000.00472425002900050008x
- Jain, C., Ali, I., 2000. Arsenic: occurrence, toxicity and speciation techniques. *Water Res.* 34, 4304–4312.
- Jia, Y., Demopoulos, G.P., 2008. Coprecipitation of arsenate with iron(III) in aqueous sulfate media: Effect of time, lime as base and co-ions on arsenic retention. *Water Res.* 42, 661–668. doi:10.1016/j.watres.2007.08.017
- Khoe, G.H., Robins, R.G., 1988. The complexation of iron(III) with sulphate, phosphate, or arsenate ion in sodium nitrate medium at 25 °C. *J. Chem. Soc. Dalt. Trans.* 2015–2021. doi:10.1039/DT9880002015
- Kim, S.S., Min, J.H., Lee, J.K., Baik, M.H., Choi, J.W., Shin, H.S., 2012. Effects of pH and anions on the sorption of selenium ions onto magnetite. *J. Environ. Radioact.* 104, 1–6. doi:10.1016/j.jenvrad.2011.09.013
- Kubicki, J., Paul, K., Kabalan, L., Zhu, Q., 2012. ATR-FTIR and Density Functional Theory Study of the Structures, Energetics, and Vibrational Spectra of Phosphate Adsorbed onto Goethite. *Langmuir* 28, 14573–14587.
- Kubicki, J.D.J., Kwon, K.D., Paul, K.W., Sparks, D.L., 2007. Surface complex structures modelled with quantum chemical calculations: Carbonate, phosphate, sulphate, arsenate and arsenite. *Eur. J. Soil Sci.* 58, 932–944. doi:10.1111/j.1365-2389.2007.00931.x
- Kuzin, A. V., Gorichev, I.G., Lainer, Y.A., 2013. Stimulating Effect of Phosphate Ions on the Dissolution Kinetics of Iron Oxides in an Acidic Medium 2013, 652–657. doi:10.1134/S0036029513090073
- Kwon, J.S., Yun, S.T., Lee, J.H., Kim, S.O., Jo, H.Y., 2010. Removal of divalent heavy metals (Cd, Cu, Pb, and Zn) and arsenic(III) from aqueous solutions using scoria: Kinetics and equilibria of sorption. *J. Hazard. Mater.* 174, 307–313. doi:10.1016/j.jhazmat.2009.09.052
- Leermakers, M., Baeyens, W., De Gieter, M., Smedts, B., Meert, C., De Bisschop, H.C., Morabito, R., Quevauviller, P., 2006. Toxic arsenic compounds in environmental samples: Speciation and validation. *TrAC - Trends Anal. Chem.* 25, 1–10. doi:10.1016/j.trac.2005.06.004
- Li, F., Geng, D., Cao, Q., 2015. Adsorption of As(V) on aluminum-, iron-, and manganese-(oxyhydr)oxides: equilibrium and kinetics. *Desalin. Water Treat.* 56, 1829–1838. doi:10.1080/19443994.2014.954146

- Liu, C.H., Chuang, Y.H., Chen, T.Y., Tian, Y., Li, H., Wang, M.K., Zhang, W., 2015. Mechanism of Arsenic Adsorption on Magnetite Nanoparticles from Water: Thermodynamic and Spectroscopic Studies. *Environ. Sci. Technol.* 49, 7726–7734. doi:10.1021/acs.est.5b00381
- Liu, X., Li, J., Huang, Y., Wang, X., Zhang, X., Wang, X., 2017. Adsorption, Aggregation, and Deposition Behaviors of Carbon Dots on Minerals. *Environ. Sci. Technol.* 51, 6156–6164. doi:10.1021/acs.est.6b06558
- Loring, J.S., Sandström, M.H., Norén, K., Persson, P., 2009. Rethinking arsenate coordination at the surface of goethite. *Chem. - A Eur. J.* 15, 5063–5072. doi:10.1002/chem.200900284
- Lu, P., Zhu, C., 2010. Arsenic Eh–pH diagrams at 25°C and 1 bar. *Environ. Earth Sci.* 62, 1673–1683. doi:10.1007/s12665-010-0652-x
- Luengo, C., Brigante, M., Avena, M., 2007. Adsorption kinetics of phosphate and arsenate on goethite. A comparative study. *J. Colloid Interface Sci.* 311, 354–360. doi:10.1016/j.jcis.2007.03.027
- Mahmood, T., Din, S.U., Naeem, A., Tasleem, S., Alum, A., Mustafa, S., 2014. Kinetics, equilibrium and thermodynamics studies of arsenate adsorption from aqueous solutions onto iron hydroxide. *J. Ind. Eng. Chem.* 20, 3234–3242. doi:10.1016/j.jiec.2013.12.004
- Manning, B.A., Goldberg, S., 1996. Modeling Competitive Adsorption of Arsenate with Phosphate and Molybdate on Oxide Minerals. *Soil Sci. Soc. Am. J.* 60, 121. doi:10.2136/sssaj1996.03615995006000010020x
- Masscheleyn, P.P.H., Delaune, R.D., Patrick, W.H., 1991. Effect of redox potential and pH on arsenic speciation and solubility in a contaminated soil. *Environ. Sci. Technol.* 25, 1414–1419. doi:10.1021/es00020a008
- Michael Bolanz, R., Blöss, U., Ackermann, S., Ciobotaru, V., Rössler, P., Tarcea, N., Popp, J., Majzlan, J., 2013. The effect of antimonate, arsenate, and phosphate on the transformation of ferrihydrite to goethite, hematite, ferrioxhyte, and tripuyite. *Clays Clay Miner.* 61, 11–25. doi:10.1346/CCMN.2013.0610102
- Neupane, G., Donahoe, R.J., Arai, Y., 2014. Kinetics of competitive adsorption/desorption of arsenate and phosphate at the ferrihydrite-water interface. *Chem. Geol.* 368, 31–38. doi:10.1016/j.chemgeo.2013.12.020
- Paige, C.R., Snodgrass, W.J., Nicholson, R. V., Schärer, J.M., 1997. An arsenate effect on ferrihydrite dissolution kinetics under acidic oxic conditions. *Water Res.* 31, 2370–2382. doi:10.1016/S0043-1354(97)00107-3
- Panias, D., Taxiarchou, M., Paspaliaris, I., Kontopoulos, a., 1996. Mechanisms of dissolution of iron oxides in aqueous oxalic acid solutions. *Hydrometallurgy* 42, 257–265. doi:10.1016/0304-386X(95)00104-O
- Puls, R.W., Powell, R.M., Clark, D., Eldred, C.J., 1991. Effects of pH, solid/solution ratio, ionic strength, and organic adds 423–430.
- Roberts, L.C., Hug, S.J., Ruettimann, T., Billah, M., Khan, A.W., Rahman, M.T., 2004. Arsenic Removal with Iron(II) and Iron(III) in Waters with High Silicate and Phosphate Concentrations. *Environ. Sci. Technol.* 38, 307–315. doi:10.1021/es0343205
- Ruiz-Baltazar, A., Esparza, R., Rosas, G., Pérez, R., 2015. Effect of the Surfactant on the Growth and Oxidation of Iron Nanoparticles. *J. Nanomater.* 2015. doi:10.1155/2015/240948
- Scheckel, K.G., Chaney, R.L., Basta, N.T., Ryan, J.A., 2009. Chapter 1 Advances in Assessing Bioavailability of Metal(Loid)s in Contaminated Soils. *Adv. Agron.* 104, 1–



# **CHAPTER 6. CHARACTERIZING PREFERENTIAL ADSORPTION OF PHOSPHATE ON BINARY SORBENTS OF GOETHITE AND MAGHEMITE SURFACE USING *in situ* ATR-FTIR AND FE-SEM/EDS**

## **List of contents**

<b>CHAPTER 6. CHARACTERIZING PREFERENTIAL ADSORPTION OF PHOSPHATE ON BINARY SORBENTS OF GOETHITE AND MAGHEMITE SURFACE USING <i>in situ</i> ATR-FTIR AND FE-SEM/EDS</b>	<b>6-1</b>
List of contents .....	6-1
Abstract .....	6-2
6.1. Introduction .....	6-3
6.2. Material and methods .....	6-5
6.2.1. Physicochemical characterization .....	6-5
6.2.2. Adsorption isotherm .....	6-5
6.2.3. <i>in situ</i> ATR-FTIR setup .....	6-11
6.2.4. Identification of sorbent concentration .....	6-12
6.2.5. Adsorption kinetics in single and binary sorbents .....	6-16
6.2.6. Drying effect in single and binary sorbents .....	6-17
6.3. Result and discussion .....	6-19
6.3.1. Physicochemical characteristics and adsorption isotherm .....	6-19
6.3.2. Identification of sorbent thickness and morphology .....	6-20
6.3.3. Kinetic studies on single and binary sorbents .....	6-28
6.3.4. Drying effect in single and binary sorbents with precipitates .....	6-39
6.4. Conclusion .....	6-41
References .....	6-47

## Abstract

Recent developments in analytics using infrared spectroscopy enabled the identification of the adsorption mechanism at the interface, but it is applicable only for simple systems. In this study, I developed an experimental procedure to measure preferential adsorption of phosphate on the binary sorbents of goethite and maghemite before and after dehydration using batch experiment, *in-situ* attenuated total reflection-Fourier transform infrared spectroscopy (ATR-FTIR) and field emission scanning electron microscopy (FE-SEM) with energy dispersive X-ray spectroscopy (EDS) (FE-SEM/EDS). Maximum adsorption capacity for phosphate of goethite at pH 4 was about 1.2 times as high as that of maghemite. I observed the uniform layer in maghemite and heterogeneous layer with aggregates (up to 6  $\mu\text{m}$ ) in goethite, and confirmed no significant change in the layers during experiment. I also observed the spectral evolution at the interface, and calculated the fraction of phosphate complex on goethite and maghemite using multiple linear regressions (MLR) as -0.68 and 0.57, respectively, clearly showing the phosphate desorption from goethite and subsequent adsorption onto maghemite. I also calculated the fraction of the precipitate (1.2) and the complex in goethite (0.25) and maghemite (0.91) to describe the dehydration effect using MLR, and FE-SEM/EDS. The amount of phosphate adsorbed on goethite and maghemite was 0.59 and 0.83  $\mu\text{mol mg}^{-1}$ , respectively. I observed that phosphate adsorbed preferentially on maghemite over goethite, and therefore believe that this procedure would be applicable for more complex systems in the future to simulate the real natural reactions.

## Keywords

Binary sorbent, *in situ* ATR-FTIR, Goethite, Maghemite, Preferential adsorption, Phosphate

## 6.1. Introduction

Phosphorus is one of the essential elements in the soil environment and is a key element for the growth of terrestrial organisms in most environments. In the past, phosphorus acted as a limiting factor for cultivation; however, recent developments in fertilization have caused over-fertilization in most agricultural regions to maximize agricultural productivity(Elser et al., 2007). As a consequence, the excess phosphorus has leached out into the water system, leading to eutrophication, creating serious health and environmental problems worldwide(Barberis et al., 1995; Elser et al., 2007). Therefore, it is essential to understand how the phosphorus interacts with soil components and what critical factor governs the structural configuration of phosphorus to retain the phosphorus in the soil environment(Kubicki et al., 2007).

Numerous studies have been conducted to identify the sorption mechanisms of phosphate (oxyanion of phosphorus) on the individual soil components or soil mixtures(Atkinson et al., 1974; Elzinga et al., 2012; Elzinga and Sparks, 2007; Kubicki et al., 2012; Parikh et al., 2014; Tofan-Lazar and Al-Abadleh, 2012; Zheng et al., 2012). Among the various technical and experimental schemes, *in-situ* attenuated total reflection-Fourier transform infrared spectroscopy (ATR-FTIR) showed interesting results for interpreting the adsorption mechanism of phosphate by utilizing the evanescent wave from the total reflection at the interface between the ATR crystal and the singly formed metal (hydr)oxide in the aqueous phase. The single major problem for the data interpretation from ATR-FTIR has been the complex overlapped peaks from the various vibrations of the molecular structures; however, recent developments in computational chemistry have enabled us to separate the overlapped peaks and have led us to identify the structural configuration of the complex between oxyanions and metal (hydr)oxides(Acelas et al., 2013;

Kubicki et al., 2012, 2007).

The technologies that have been developed was not satisfactory for interpreting the sorption mechanism in the real environment because the *in situ* ATR-FTIR technique with computational chemistry is available only for a simple system, for example, one or two solutes on a single sorbent. Many studies have identified the structural configuration of phosphate (oxyanion form of phosphorus) by changing environmental conditions (pH, ionic strength and surface loading)(Arai and Sparks, 2001; Elzinga and Sparks, 2007; Waiman et al., 2013), and a few studies have already conducted the competitive adsorption of several oxyanions onto a single metal (hydr)oxide(Carabante and Grahn, 2010; Lindegren and Persson, 2009; Rahnemaie et al., 2007; Waiman et al., 2013). However, I could not find any articles employing dual or multiple sorbents in *in-situ* ATR-FTIR that could interpret the preferential adsorption of oxyanions onto the target sorbents.

For that reason, I employed phosphate as a target solute, and I selected the goethite and maghemite as binary sorbents, which showed significantly different spectra in our preliminary experiment using a single solute with a single sorbent. The main idea came from the experiment conducted by Tofan-Lazar and Al-Abadleh (2012)(Tofan-Lazar and Al-Abadleh, 2012), which showed significantly different spectra of phosphate on the goethite and hematite. Previous studies also identified the spectral change by the surface loading(Abdala et al., 2015; Daou et al., 2007; Kubicki et al., 2007); I employed only the high surface loading condition ( $0.67 \text{ mmol g}^{-1}$ ) from the preliminary experiment, which showed no significant changes in the spectrum to demonstrate the preferential adsorption on the binary sorbents using *in-situ* ATR-FTIR. In this study, I developed a simple procedure to characterize preferential adsorption using *in-situ* ATR-FTIR on the binary sorbents, tried to semi-quantify preferential adsorption of phosphate between two sorbents, and identified

the dehydration effect to characterize preferential adsorption of phosphate on the binary sorbents of goethite and maghemite.

## **6.2. Materials and Methods**

### **6.2.1. Physicochemical characterization**

A rod-shaped nanogoethite (Cat. No. US3162) was purchased from US Research Nanomaterials (USA), and sphere-shaped nanomaghemite (Cat. No. 544884) was purchased from Sigma-Aldrich (USA). For the characterization of the crystal structure, I employed X-ray diffraction (XRD) using D8 Advance (Bruker, Germany) with Cu K $\alpha$  radiation from 5 to 90°. The XRD spectrum was compared to previous data from the American mineralogist crystal structure database (AMCSD)(Downs and Hall-Wallace, 2003). The point of net zero charge (PNZC) was measured using the drift method(Yang et al., 2004), and the pH was potentiometrically measured using Orion 5 Star (Thermo, USA) in 1:200 (W/V). A Brunauer-Emmett-Teller (BET) isotherm with N<sub>2</sub> gas was applied to measure surface area (SA) using an ASAP 2010 (Micromeritics, USA) at 77 K. I measured high-resolution transmission electron microscopy (HR-TEM) for morphology and elemental concentration characterization. All characteristics of nanosorbents are summarized in Table 7-1, and the XRD diffractogram and HR-TEM image are illustrated in Fig. 6-1 and 6-2, respectively.

### **6.2.2. Adsorption isotherm**

THE phosphate adsorption isotherm was measured by varying the pH (4 and 7) and surface loading (0, 0.11, 1.1, 5.5 and 11 mM). Fifty milliliters of phosphate solution at different concentrations were mixed with 0.25 g of dried

**Table 6-1** Physicochemical characteristics of goethite and maghemite.

Iron Oxide	Formula	Manufacturer (Catalog #)	Shape	Crystal Structure	pH	EC	PZC	Measured SA ( $\text{m}^2 \text{g}^{-1}$ )	Calculated SA ( $\text{m}^2 \text{g}^{-1}$ )	Cell Volume ( $\text{nm}^3$ )	Proposed Size (nm)	Measured Size (nm)
Goethite	FeOOH	US-Nano (US3162)	Rod	isometric	5.7	0.13	5.7	84.0	113.1	0.1386	50x10	50.3x10.8 ( $n=151$ )
Maghemite	Fe <sub>2.67</sub> O <sub>4</sub>	Sigma-Aldrich (544884)	Spherical	isometric	5.1	0.14	4.7	35.6	23.0	0.5825	30	53.7 ( $n=116$ )

*pH* proton concentration, *EC* electric conductivity ( $\mu\text{S cm}^{-1}$ ), *PZC* point of zero charge, *SA* surface area ( $\text{m}^2 \text{g}^{-1}$ )

*pH* and *EC* were measured at 1:200 (g:mL).

*PZC* and *SA* were measured by the drift method and N<sub>2</sub>-BET method at 77K, respectively.

**Fig. 6-1** X-ray diffraction pattern of goethite and maghemite. All peaks are indexed to the goethite and maghemite phase. The red bars indicate the reference position (red bar) from the American mineralogist crystal structure database.

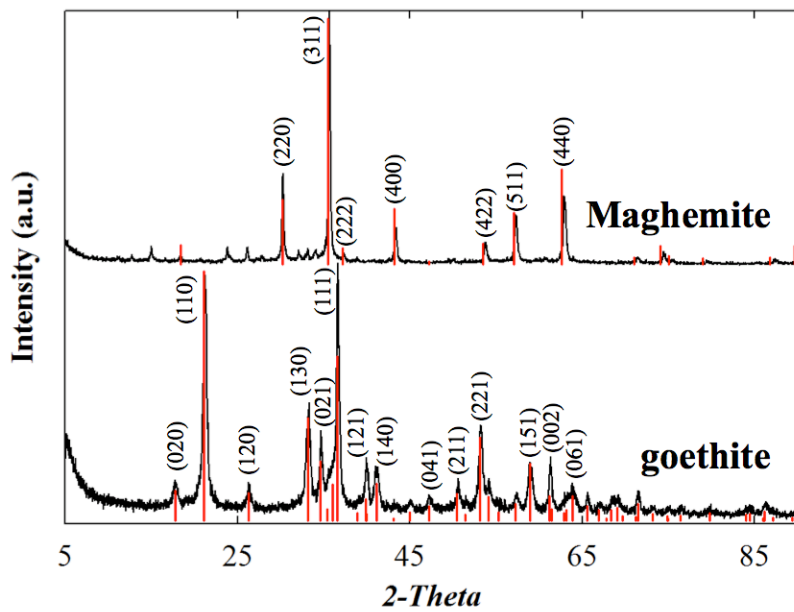
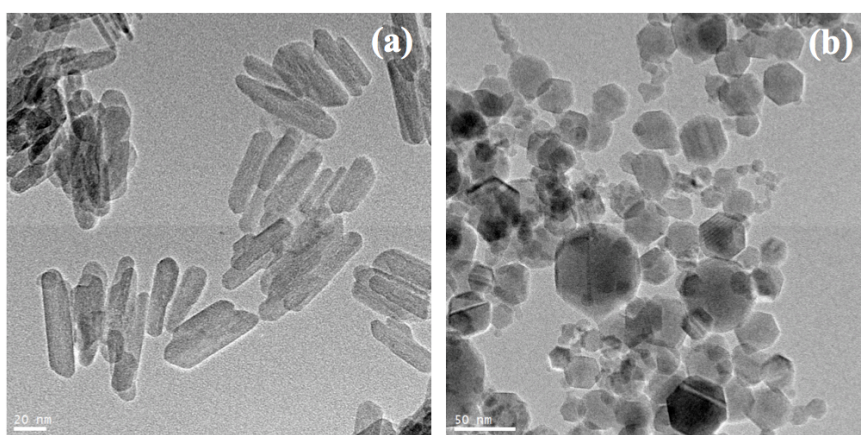


**Fig. 6-2** HR-TEM image of nanosized goethite (a) and maghemite (b).



goethite or maghemite in a 50 mL conical tube. All solutions contained 0.1 M NaCl to maintain the ionic strength, and the mixtures were agitated for 48 h using a vertical shaker (Daehan, Korea) at 200 rpm. The pH was readjusted with 0.1 M HCl or NaOH at 12 h intervals; then, the mixtures were centrifuged at 4,200 RCF for 1 h, and the supernatant was filtered with a 200 nm PTFE syringe filter (Advantec, Japan). The supernatant was acidified with a drop of 10 M HCl solution, and inductively coupled plasma-optical emission spectrometry (ICAP-7200, Thermo, USA) was used to measure the aqueous phosphate concentration. The adsorbed phosphate was calculated by subtracting the initial concentration from the aqueous concentration. The Langmuir isotherm was employed for the evaluation of the sorption characteristics of iron (hydr)oxides. The Langmuir model is expressed as follows:

$$Q_{eq} = (Q_{max} \cdot K_L \cdot C_{eq}) / (1 + K_L \cdot C_{eq}) \quad \text{(Eq. 6-1)}$$

where  $Q_{eq}$  and  $C_{eq}$  are the equilibrium concentrations of phosphate on the adsorbed ( $\text{mmol g}^{-1}$ ) and solution (mM), respectively, while  $Q_{max}$  and  $K_L$  are the maximum adsorption capacity ( $\text{mmol g}^{-1}$ ) and Langmuir constant ( $\text{L mmol}^{-1}$ ), respectively. The isotherm fitting was conducted with the dynamic fit function in Sigmaplot 10 (Systat, USA), and I constrained  $0 < Q_{max} < 100$  and  $0 < K_L < 1,000$  and employed 1,000 fits with 2,000 iterations.

### 6.2.3. *in situ* ATR-FTIR measurement setup

The goethite or maghemite was dispersed in the distilled water at  $1 \text{ g L}^{-1}$ , and 0.75 mL of dispersions of goethite and maghemite were placed on the ZnSe ATR crystal ( $77 \times 8 \times 2 \text{ mm}$  and  $45^\circ$  cut edges, Piketech, USA) side by side to form binary sorbent layers. The ATR plate was placed under room temperature (controlled to  $25 \pm 2 \text{ }^\circ\text{C}$ ) and dried at least 24 h before the experiment. A P solution

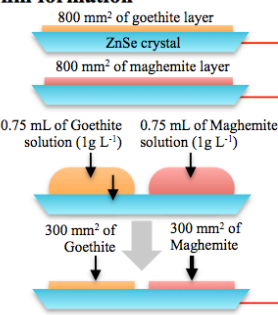
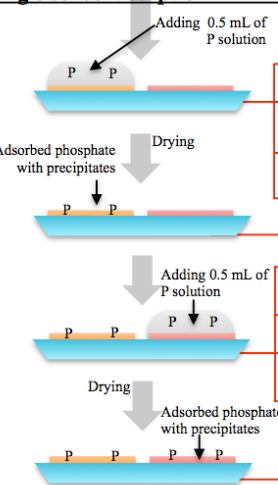
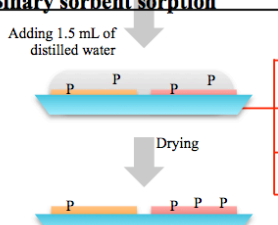
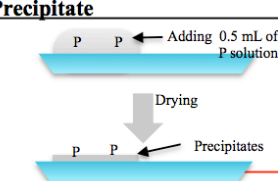
containing 1 mM NaH<sub>2</sub>PO<sub>4</sub> and 10 mM NaCl was prepared, and the pH of the P solution was adjusted to 4.0 with 0.1 M HCl or NaOH solution. The P adsorption kinetics at the interface and the spectra of dried samples were measured. The experimental scheme is illustrated in Fig. 6-3 for better description. Two layers on the single ZnSe crystal was prepared, and only goethite layer was reacted with 0.5 mL of P solution. The spectral changes on the single goethite layer were measured to identify the adsorption kinetics and the dehydration effect of phosphates. After dehydration of the goethite layer, additional 0.5 mL of P solution was added to the single maghemite layer to measure the corresponding spectral changes. After dehydration of the single maghemite, 1.5 mL of distilled water was added to soak goethite and maghemite layers together to measure the adsorption kinetics and the dehydration effect on the binary sorbents. There is an approximately 9 mm gap between the two sorbents. Thus, 1.5 mL of DW was added instead of 1 mL to make the bridge between the sorbents and to extend the reaction time. All spectra were collected by IR tracer-100 (Shimadzu, Japan) equipped with Deuterated TriGlycine Sulfate detector. Sixty-four scans were co-added at a resolution of 4 cm<sup>-1</sup> under atmospheric conditions. Happ-Genzel apodization was employed, and the aperture was set to 3. The time interval between each of the spectra was approximately 96 sec. All spectra were collected by IR solution software (Shimadzu, Japan), and spectral processing was conducted using Essential FTIR software (Operant LLC, USA). All analytical chemicals were purchased from Sigma-Aldrich (USA) at a high purity grade.

#### 6.2.4. Identification of sorbent concentration

It is important to know the sorbent concentration for an adsorption experiment, and the concentration could be obtained easily in the traditional

**Fig. 6-3** Schematic diagram of experimental setup, spectral measurement and data processing for characterizing the preferential adsorption using *in situ* ATR-FTIR in the binary adsorbents.

# Experiment procedure for characterizing preferential adsorption

in situ ATR-FTIR setup	Spectra measurement	Data processing
<p><b>Film formation</b></p> 	<p><math>A_{(Gt),\lambda,t=dried}</math></p> <p><math>A_{(Mh),\lambda,t=dried}</math></p> <p><b>FTIR condition</b></p> <ul style="list-style-type: none"> <li>- Splitter: KBr with Ge coating</li> <li>- Windows: NaCl</li> <li>- Detector: DTGS</li> <li>- Range: 4000-650 <math>cm^{-1}</math></li> <li>- Scan mode: Absorbance</li> <li>- Mirror speed: 2 mm/s</li> <li>- Accumulations: 64 scans</li> <li>- Aperture size: 3</li> <li>- Resolution: 4 <math>cm^{-1}</math></li> <li>- Apodization: Happ-Gezel</li> </ul> <p><math>A_{(Gt+Mh),\lambda,t=dried}</math></p>	<p><b>Sorbent concentration using MLR</b></p> $A_{(Gt+Mh),\lambda,t=dried} = f_{Gt} \cdot A_{Gt,\lambda,t=dried} + f_{Mh} \cdot A_{Mh,\lambda,t=dried} \quad (1)$ <p>The <math>A_{Gt,\lambda,t=dried}</math> and <math>A_{Mh,\lambda,t=dried}</math> are the absorbance of goethite and maghemite covered whole ZnSe crystal individually (800 <math>mm^2</math>) while <math>A_{(Gt+Mh),\lambda,t=dried}</math> is the absorbance of sum of goethite and maghemite covered approximately 300 <math>mm^2</math> each. Based on the eq. (1), we can calculate the sorbent concentration (<math>f_{Gt}</math> and <math>f_{Mh}</math>) in the evanescent wave path.</p>
<p><b>Single sorbent sorption</b></p> 	<p><math>A_{((P+Gt)+Mh),\lambda,t=0}</math></p> <p><math>A_{((P+Gt)+Mh),\lambda,t=initial}</math></p> <p><math>A_{((P+Gt)+Mh),\lambda,t=x}</math></p> <p><math>A_{((P+Gt)+Mh),\lambda,t=final}</math></p> <p><math>A_{((P/Gt)+Mh),\lambda,t=dried}</math></p> <p><math>A_{((P/Gt)+(P+Mh)),\lambda,t=0}</math></p> <p><math>A_{((P/Gt)+(P+Mh)),\lambda,t=initial}</math></p> <p><math>A_{((P/Gt)+(P+Mh)),\lambda,t=x}</math></p> <p><math>A_{((P/Gt)+(P+Mh)),\lambda,t=final}</math></p> <p><math>A_{((P/Gt)+(P/Mh)),\lambda,t=dried}</math></p>	<p><b>Adsorption kinetics in single goethite</b></p> $A_{(P-Gt),\lambda,t=x} = A_{((P+Gt)+Mh),\lambda,t=x} - A_{((P+Gt)+Mh),\lambda,t=initial} \quad (2)$ <p>The <math>A_{(P-Gt),\lambda,t=x}</math> is the subtracted absorbance of phosphate complex on the goethite without the absorbance of the goethite.</p>
<p><b>Binary sorbent sorption</b></p> 	<p><math>A_{(DW+(P/Gt)+(P/Mh)),\lambda,t=0}</math></p> <p><math>A_{(DW+(P/Gt)+(P/Mh)),\lambda,t=initial}</math></p> <p><math>A_{(DW+(P/Gt)+(P/Mh)),\lambda,t=0}</math></p> <p><math>A_{(DW+(P/Gt)+(P/Mh)),\lambda,t=final}</math></p> <p><math>A_{(P/(Gt+Mh)),\lambda,t=dried}</math></p>	<p><b>Adsorption kinetics in single Maghemite</b></p> $A_{(P-Mh),\lambda,t=x} = A_{((P/Gt)+(P+Mh)),\lambda,t=x} - A_{((P/Gt)+(P+Mh)),\lambda,t=initial} \quad (3)$ <p>The <math>A_{(P-Mh),\lambda,t=x}</math> is the subtracted absorbance of phosphate complex on the maghemite without the absorbance of the goethite.</p>
<p><b>Precipitate</b></p> 	<p><math>A_{P,\lambda,t=dried}</math></p>	<p><b>Adsorption kinetics in binary sorbents</b></p> $A_{(P-(Gt+Mh)),\lambda,t=x} = A_{(DW+(P/Gt)+(P+Mh)),\lambda,t=x} - A_{(DW+(P/Gt)+(P+Mh)),\lambda,t=initial} \quad (4)$ <p>The <math>A_{(P-(Gt+Mh)),\lambda,t=x}</math> is the subtracted absorbance of phosphate complex on the binary goethite and maghemite without the absorbance of the goethite and maghemite. We calculated the individual fraction using MLR analysis in eq (5),</p> $A_{(P-(Gt+Mh)),\lambda,t=x} = f_{Gt} \cdot A_{(P-Gt),\lambda,t=x} + f_{Mh} \cdot A_{(P-Mh),\lambda,t=x} \quad (5)$
		<p><b>Drying effect in single and binary sorbents</b></p> $A_{(P/Gt),\lambda,t=dried} = A_{((P/Gt)+Mh),\lambda,t=dried} - A_{(Gt+Mh),\lambda,t=dried} \quad (6)$ $A_{(P/Mh),\lambda,t=dried} = A_{((P/Gt)+(P/Mh)),\lambda,t=dried} - A_{((P/Gt)+Mh),\lambda,t=dried} \quad (7)$ $A_{(P/(Gt+Mh)),\lambda,t=dried} = A_{((P/(Gt+Mh)),\lambda,t=dried)} - A_{(Gt+Mh),\lambda,t=dried} \quad (8)$ <p>The <math>A_{(P/Gt),\lambda,t=dried}</math>, <math>A_{(P/Mh),\lambda,t=dried}</math> and <math>A_{(P/(Gt+Mh)),\lambda,t=dried}</math> are the subtracted absorbance of phosphate complex and precipitate on the maghemite without the absorbance of the goethite. We calculated the individual fraction using MLR analysis in eq. (9),</p> $A_{(P/(Gt+Mh)),\lambda,t=dried} = f_{(P/Gt),\lambda,t=dried} \cdot A_{(P/Gt),\lambda,t=dried} + f_{(P/Mh),\lambda,t=dried} \cdot A_{(P/Mh),\lambda,t=dried} + f_{P,\lambda,t=dried} \cdot A_{P,\lambda,t=dried} \quad (9)$
		<p><b>Description on the abbreviations</b></p> <p><math>A</math> absorbance; <math>f</math> fraction <math>MLR</math> multiple linear regression; <math>P</math> phosphate; <math>Gt</math> goethite; <math>Mh</math> maghemite; <math>DW</math> distilled water; <math>\lambda</math> range of wavenumber.</p> <p>The first subscript indicates phosphate loading condition or isolated spectra; <math>(P+Gt)</math> phosphate solution on the goethite; <math>(P/Gt)</math> adsorbed phosphate and precipitate on the goethite under dried condition; only; <math>(DW+(P/Gt))</math> distilled water on the adsorbed phosphate and precipitate; <math>(P-Gt)</math> isolated spectra of adsorbed phosphate complex on the goethite; <math>(P/Mh)</math> isolated spectra of adsorbed phosphate and precipitate.</p> <p>The 2<sup>nd</sup> and 3<sup>rd</sup> subscripts indicate range of wavenumber and time; <math>t=0</math> start time, <math>t=initial</math> initial time at no fluctuation on the water bands, <math>t=final</math> final time before decrease of the water bands, <math>t=dried</math> time after complete drying.</p>

adsorption experiment. However, it is extremely difficult to know the sorbent concentration passed through the evanescent wave in the *in-situ* ATR-FTIR measurement. Because only 8 mm of distance was allocated to each evanescent wave from total reflection, and the diameter of infrared light is determined by the FTIR instrumental conditions such as aperture size and alignment. The aperture size can easily be controlled, but the alignment is extremely hard to control and easily shifted by little perturbation. Thus, it is very difficult to maintain the constant condition of sorbent concentration. For that reason, the sorbent concentration was calculated using MLR, and the thickness and atomic composition were confirmed using a field emission scanning electron microscope (FE-SEM, SIGMA, Carl Zeiss, Germany) equipped with energy dispersive spectroscopy (EDS). For the calibration between the layer volume in the evanescent wave and absorbance, spectra of single goethite layer or a maghemite layer was measured, which is single-covered over the whole ZnSe surface (approximately 530 nm<sup>2</sup>) with 1.2 mL of dispersion to calculate relative sorbent concentration in the evanescent wave with ZnSe crystal background. Multiple linear regression (MLR) analysis was applied to calculate the individual fraction of goethite and maghemite from the binary sorbents. The MLR is simply expressed as:

$$A_{(Gt+Mm),\lambda,t=dried} = A_{Gt,\lambda,t=dried} \cdot f_{Gt} + A_{Mm,\lambda,t=dried} \cdot f_{Mm} \quad \text{(Eq. 6-2)}$$

where  $A_{Gt,\lambda}$ ,  $A_{Mm,\lambda}$  and  $A_{(Gt+Mm),\lambda}$  are the absorbances of a single goethite, single maghemite and binary goethite and maghemite at the wavelength ( $\lambda$ ) while  $f_{Gt}$  and  $f_{Mm}$  are the fraction of goethite and maghemite layer in the binary system, respectively. Based on eq. (6-2), the individual absorbance of the goethite and maghemite layers was identified under the path range of the evanescent wave in the experiment, and the absorbance easily converted to sorbent concentration using the calibration mentioned above.

### 6.2.5. Adsorption kinetics in single and binary sorbents

The phosphate adsorption kinetics was measured in single goethite by adding 0.5 mL of the P solution to the single goethite with time-series measurement of the ATR-FTIR spectra. The adsorbed phosphate on the single goethite at time  $x$  ( $A_{(P\sim Gt),\lambda,t=x}$ ) was calculated using the following eq. (6-3);

$$A_{(P\sim Gt),\lambda,t=x} = A_{((P+Gt)+Mh),\lambda,t=x} - A_{((P+Gt)+Mh),\lambda,t=initial} \quad (\text{Eq. 6-3})$$

The  $A_{((P+Gt)+Mh),\lambda,t=x}$  and  $A_{((P+Gt)+Mh),\lambda,t=initial}$  are the overlapped ATR-FTIR spectra of the P solution on the single goethite with the dried absorbance of single maghemite at time  $x$  and initial time, respectively. The subscript of  $(P\sim Gt)$  and  $((P+Gt)+Mh)$  indicate the spectrum of phosphate complex on the single goethite and overlapped spectrum of P solution and two single sorbents, respectively. The subscript of  $t=initial$  was used instead of  $t=0$  because the water molecule could not immediately saturate the pore space of the sorbent after adding the P solution. It needed time for the saturation, and I defined the  $t=initial$  as no more increase of water peaks in ATR-FTIR spectra while the  $t=final$  was the last absorbance before starting the decrease of water peaks in ATR-FTIR spectra because of evaporation of the water molecules in the path of the evanescent wave. I also defined the  $t=dried$  as no more decrease of water peaks in the spectra because of the complete drying, and I discussed the spectra with  $t=dried$  below the section. After completely drying the phosphate adsorbed single goethite, the spectrum of the adsorbed phosphate on the single maghemite ( $A_{(P\sim Mh),\lambda,t=x}$ ) was calculated using the following eq. (6-4):

$$A_{(P\sim Mh),\lambda,t=x} = A_{((P/Gt)+(P+Mh)),\lambda,t=x} - A_{((P/Gt)+(P+Mh)),\lambda,t=initial} \quad (\text{Eq. 6-4})$$

The  $A_{((P/Gt)+(P+Mh)),\lambda,t=x}$  and  $A_{((P/Gt)+(P+Mh)),\lambda,t=initial}$  are the overlapped spectra of the P solution on the single maghemite with the dried and phosphate-adsorbed single goethite at time  $x$  and initially, respectively. The subscript of  $(P/Gt)$  indicates the

spectrum of the dried and phosphate-adsorbed single goethite. Based on the proposed procedure, the spectral evolution of the phosphate complex in the single goethite and single maghemite was obtained, sequentially.

The phosphate adsorption kinetics was also measured by adding 1.5 mL of the distilled water (DW) to the binary goethite and maghemite. In this experiment, phosphate-adsorbed goethite and maghemite was used, and I connected the two sorbents with the water bridge to cause desorption and dissolution of adsorbed and precipitated phosphate. Finally, the preferential adsorption was happened over the two sorbents. The spectrum of adsorbed phosphate on the binary sorbents at time  $x$  ( $A_{(P\sim(Gt+Mh)),\lambda,t=x}$ ) was calculated following eq. (6-5):

$$A_{(P\sim(Gt+Mh)),\lambda,t=x} = A_{(DW+(\frac{P}{Gt})+(\frac{P}{Mh})),\lambda,t=x} - A_{(DW+(P/Gt)+(P/Mh)),\lambda,t=initial} \quad (\text{Eq. 6-5})$$

The  $A_{(DW+(P/Gt)+(P/Mh)),\lambda,t=x}$  and  $A_{(DW+(P/Gt)+(P/Mh)),\lambda,t=initial}$  are the overlapped spectra of the DW on the phosphate-adsorbed goethite and maghemite at time  $x$  and initially, respectively. For the separation of individual spectra, I applied MLR analysis with 2 parameters according to the following eq. (6-6):

$$A_{(P\sim(Gt+Mm)),\lambda,t=final} = A_{(P\sim Gt),\lambda,t=final} \cdot f_{(P\sim Gt),t=final} + A_{(P\sim Mm),\lambda,t=final} \cdot f_{(P\sim Mm),t=final} \quad (\text{Eq. 6-6})$$

where  $A_{(P\sim(Gt+Mm)),\lambda,t=final}$ ,  $A_{(P\sim Gt),\lambda,t=final}$  and  $A_{(P\sim Mm),\lambda,t=final}$  are the absorbance of the adsorbed phosphate before starting the decrease of the water bands in the binary sorbent, single goethite and single maghemite, respectively. The  $f_{(P\sim Gt),t=final}$  and  $f_{(P\sim Mm),t=final}$  are the fraction of the two adsorbed phosphates in the single goethite and maghemite, respectively.

#### 6.2.6. Drying effect in single and binary sorbents

The spectra of the dried binary sorbents without phosphate ( $A_{(Gt+Mm),\lambda}$ ) was masured above, and I also measured the dried and phosphate-adsorbed spectra on the

single goethite ( $A_{((P/Gt)+Mh),\lambda,t=dried}$ ), single maghemite ( $A_{((P/Gt)+(P/Mh)),\lambda,t=dried}$ ) and binary sorbents ( $A_{(P/(Gt+Mh)),\lambda,t=dried}$ ) after measuring the kinetic studies. I dried the sorbent at least for 2 h after the disappearance of the water bands in the ATR-FTIR spectra. I separated the phosphate complex absorbance from the overlapped spectra with the phosphate complex and sorbents by following eq. (6-7), (6-8) and (6-9) for acquiring the absorbance of only the phosphate complex on the single goethite ( $A_{(P|Gt),\lambda,t=dried}$ ), single maghemite ( $A_{(P|Mh),\lambda,t=dried}$ ) and binary sorbents ( $A_{(P|(Gt+Mh)),\lambda,t=dried}$ ), respectively;

$$A_{(P|Gt),\lambda,t=dried} = A_{((P/Gt)+Mh),\lambda,t=dried} - A_{(Gt+Mh),\lambda} \quad \text{(Eq. 6-7)}$$

$$A_{(P|Mh),\lambda,t=dried} = A_{((P/Gt)+(P/Mh)),\lambda,t=dried} - A_{((P/Gt)+Mh),\lambda,t=dried} \quad \text{(Eq. 6-8)}$$

$$A_{(P|(Gt+Mh)),\lambda,t=dried} = A_{(P/(Gt+Mh)),\lambda,t=dried} - A_{(Gt+Mh),\lambda} \quad \text{(Eq. 6-9)}$$

I also dried 0.5 mL of the P solution without the sorbent on the ZnSe crystal, and the spectra was measured to identify the absorbance of phosphate precipitate ( $A_{P,\lambda,t=dried}$ ). I tried to semi-quantify the fraction of the phosphate precipitate ( $f_{(P),\lambda,t=dried}$ ), phosphate complex on the single goethite ( $f_{(P|Gt),\lambda,t=dried}$ ) and phosphate complex on single maghemite ( $f_{(P|Mh),\lambda,t=dried}$ ) using MLR analysis with 3 parameters following eq. (6-10).

$$A_{(P|(Gt+Mm)),\lambda,t=dried} = A_{(P|Gt),\lambda,t=dried} \cdot f_{(P|Gt),\lambda,t=dried} + A_{(P|Mm),\lambda,t=dried} \cdot f_{(P|Mm),\lambda,t=dried} + A_{(P),\lambda,t=dried} \cdot f_{(P),\lambda,t=dried} \quad \text{(Eq. 6-10)}$$

The MLR analysis was conducted with the dynamic fit function in Sigmaplot 10 (Systat, USA), and I constrained  $0 < f$  for eq. (2) and (10), but I did not constrain the  $f$  in eq. (6) because of absorbance decrease by the phosphate desorption. 1,000 fits with 2,000 iterations were employed. The predicted value and residuals of fitting were presented in the figures below.

### 6.3. Results and Discussion

#### 6.3.1. Physicochemical characteristics and adsorption isotherm

The physicochemical characteristics of the goethite and maghemite were summarized in Table 6-1. The goethite and maghemite were identified as rod- and spherical-shaped nanoparticles with 50.3x10.8 and 50.7 nm sizes using HR-TEM, respectively. The EC, pH and PZC were measured as 0.13  $\mu\text{S cm}^{-1}$ , 5.7 and 5.7 for goethite and 0.14  $\mu\text{S cm}^{-1}$ , 5.1 and 4.7 for goethite, respectively. I measured the SA as 84.0 and 35.6  $\text{m}^2 \text{g}^{-1}$  for goethite and maghemite, and I also calculated the theoretical surface area based on the measured size using HR-TEM and cell volume from the literature (Multani, 1990; Yang et al., 2006). The results were 113.1 and 23.0  $\text{m}^2 \text{g}^{-1}$  for goethite and maghemite, respectively. I assumed the rectangular and spherical shape for the calculation, and I used the average size of the nanoparticles, but it was difficult to correlate the measured SA and calculated SA. However, I compared the trends, and opposite pattern in the measured SA and calculated SA was found. The calculated SA was higher than the measured SA in the goethite, but *vice versa* in the maghemite. Based on the FE-SEM/EDS and HR-TEM observations, more densely aggregated structure in the goethite than in the maghemite was found, and the rod-shaped goethite was placed side by side, which possibly decreased the available surface area by blocking adsorption of the  $\text{N}_2$  sorbate during the BET measurement. However, the spherical shape of the maghemite minimized the decrease in the surface area by contacting each other. Thus, the measured SA showed higher than calculated SA. The XRD (Fig. 6-1) and HR-TEM (Fig. 6-2) clearly confirmed the structure of the nanoparticles as the goethite and maghemite based on the AMCSD.

The  $Q_{max}$  of goethite and maghemite were calculated as 0.352 and 0.296

mmol g<sup>-1</sup> for pH 4 while 0.333 and 0.227 mmol g<sup>-1</sup> for pH 7, respectively. The  $K_L$  values of goethite and maghemite were calculated as 8.93 and 2.13 L site<sup>-1</sup> for pH 4 while 5.39 and 1.56 L site<sup>-1</sup> for pH 7, respectively (Fig. 6-4). The goethite showed higher  $Q_{max}$  than the maghemite, and the similar pattern was observed in  $K_L$ . In the previous literature, several studies already reported the adsorption capacity of the goethite (Boukemara et al., 2016; Gao and Mucci, 2001; Geelhoed et al., 1997; Manning and Goldberg, 1996), but no study was found for the maghemite. I also failed to find the adsorption characteristics with other oxyanions in the maghemite. Our result for the goethite showed results similar to previous studies (Fig. 6-5) (Boukemara et al., 2016; Gao and Mucci, 2001; Geelhoed et al., 1997; Manning and Goldberg, 1996), and I could not identify the difference in  $Q_{max}$  and  $K_L$  based on the previous studies. I presume that the reason for the difference in the  $Q_{max}$  between the goethite and maghemite could be attributed not only to the difference in the binding affinity on the surface but also to the difference in the aggregation of nanoparticles *via* the phosphate as the bridge (Dickson et al., 2017). For that reason, I briefly evaluated the sedimentation by the phosphate concentration (0, 0.5 mM and 5 mM), and I observed the phosphate concentration effect on the acceleration of the sedimentation on the maghemite, but no significant effect was observed on the goethite because the aggregates in the goethite were immediately settled in all phosphate concentrations (Fig. 6-6), clearly indicating that the aggregates of goethite were formed during the synthesis of goethite. The sedimentation result corresponds to the observation in the FE-SEM, below.

### 6.3.2. Identification of sorbent thickness and morphology

Based on the FE-SEM observations, I confirmed the maghemite layer as a relatively uniform thickness on the ZnSe crystal while I observed the few  $\mu\text{m}$ -

**Fig. 6-4** Langmuir adsorption isotherm of phosphate (0, 0.11, 1.1, 5.5 and 11 mM initial concentration) on the goethite (square) and maghemite (circle) plotted with adsorbed phosphate ( $\text{mmol g}^{-1}$ ) at pH 4 (red) and 7 (black) after 48 h of incubation.  $Q_{max}$ ,  $K_L$  and  $adj. R^2$  are maximum adsorption capacity ( $\text{mmol g}^{-1}$ ), Langmuir coefficient ( $\text{L mmol}^{-1}$ ) and adjusted coefficient of determination, respectively. Error bars indicate the standard deviation of three replicates.

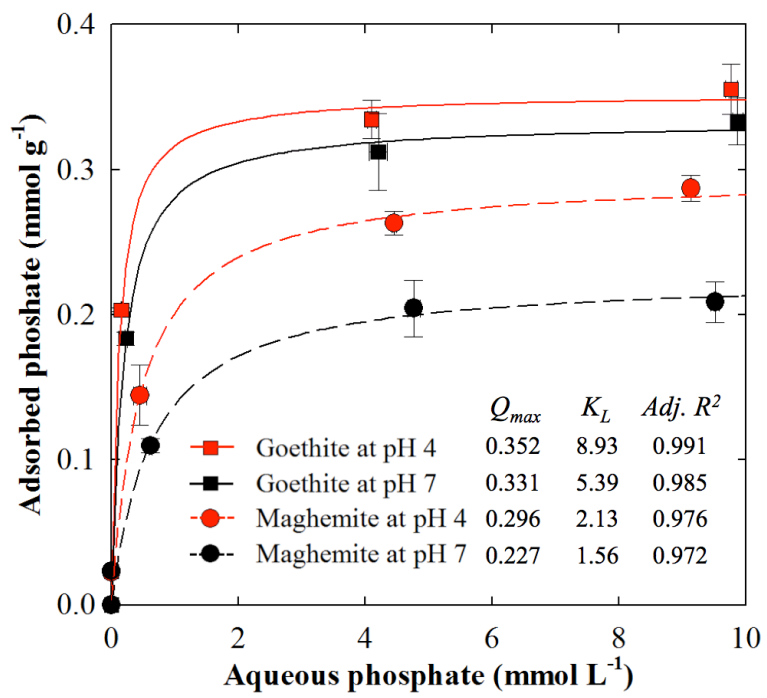


**Fig. 6-5** Scatter plot between the surface loading (molecule  $\text{nm}^{-2}$ ) and surface density (molecule  $\text{nm}^{-2}$ ) on the goethite from the previous literature (triangle, diamond, hexagon and circle) and this study (rectangle) at pH 4 (black) and 7 (white). The axis was log-scaled for better understanding.

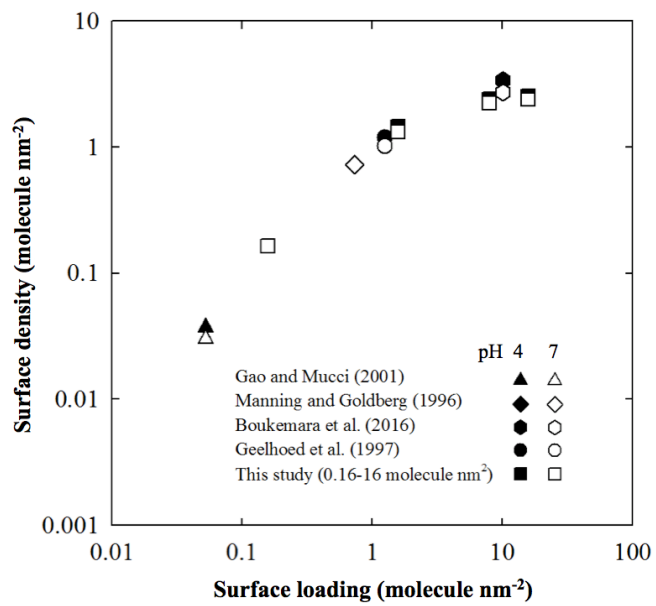
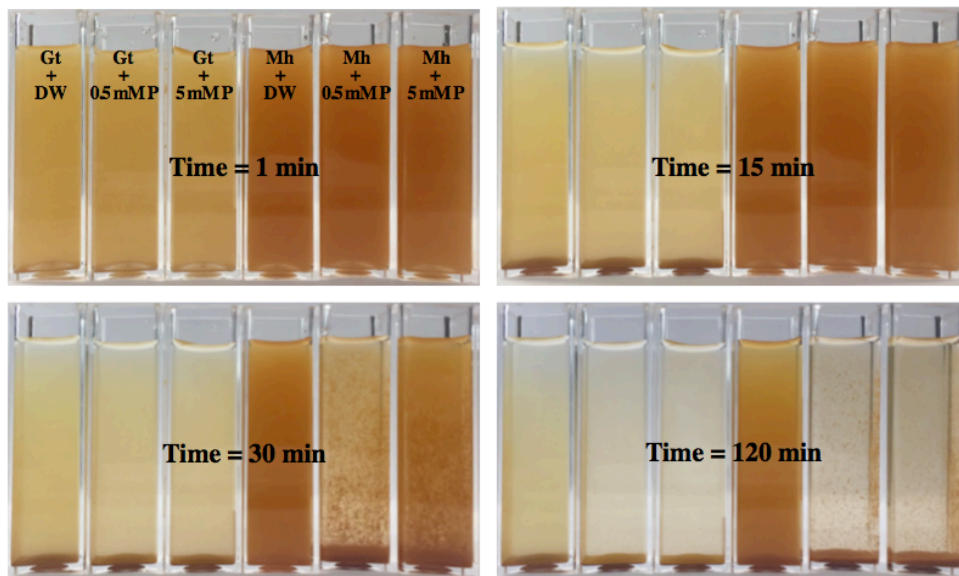


**Fig. 6-6** Sedimentation photographs of nanosized goethite (Gt) and maghemite (Mh) at different phosphate concentrations (0, 0.5 and 5 mM) after standing for 1, 15, 30 and 120 min. DW is the abbreviation of distilled water.



sized aggregates in the goethite layer, which appeared less uniform in the thickness. The layer thickness of goethite and maghemite were approximately 1.5 and 1.1  $\mu\text{m}$ , respectively. The aggregates in the goethite layer were observed up to 6  $\mu\text{m}$  as a diameter. The high magnification in FE-SEM and HR-TEM clearly confirmed that the  $\mu\text{m}$ -sized particle was the aggregate of goethite nanorods (Fig. 6-2 and 6-7). I found that the decrease in the pH of the goethite dispersion below pH 2 led to a dramatic decrease of the aggregates, but the pH was only decrease to 4 to prevent damage to the ZnSe crystal and to control the pH near 4, which was our target pH condition for the experiment.

The area of goethite and maghemite layers was calculated as 250 and 234  $\text{mm}^2$ . The MLR analysis was employed using eq. (3) and the spectra of the goethite and the maghemite layers covered approximately 484  $\text{mm}^2$  to identify the fraction of goethite and maghemite, and the  $f_{gt}$  and  $f_{Mh}$  were 0.39 and 0.50, respectively. The fractions should be near the 0.42 (=0.5 mL/1.2 mL) because equal amount of dispersion was introduced, but I assumed that the layer formation caused the difference in the fraction. In addition, there was a time difference between the measurements, and the optic system could be fluctuating because of the alignment and beam condition over time. I understood that the fractions were reasonable. Furthermore, I also tried to identify the  $f_{gt}$  and  $f_{Mh}$  at the end of the experiment to check the stability of the sorbent in the path of the evanescent wave, but there was an increase in the background absorbance. The background was increased during the experimental period, and I confirmed that the phosphate and NaCl precipitate increased the background level (Fig. 6-8). For that reason, I could not quantify the  $f_{Gt}$  and  $f_{Mh}$  at the end of experiment using MLR analysis because of the phosphate and precipitate peaks in the 1300-900  $\text{cm}^{-1}$  region; thus, I tried to measure the integrated absorbance at a specific region (840-760  $\text{cm}^{-1}$  for goethite and 750-680  $\text{cm}^{-1}$  for

maghemite) with linear background correction. The average, standard deviation and coefficient of variation of  $IA_{840-760}$  calculated from three dried samples ( $A_{((P/Gt)+Mh),\lambda,t=dried}$ ,  $A_{((P/Gt)+(P/Mh)),\lambda,t=dried}$  and  $A_{(P/(Gt+Mh)),\lambda,t=dried}$ ) were 9.07, 0.13 and 1.46 % while  $IA_{750-680}$  was 3.94, 0.089 and 2.26 %, respectively. Based on the result, I concluded that there was no significant change in the iron oxide layers over time in this experiment.

### 6.3.3. Kinetic studies on single sorbent and binary sorbents

The time-course patterns of the ATR-FTIR spectra at the interface between the iron (hydr)oxides and aqueous phase with 1 mM phosphate solution before and after dehydration (evaporation) of all water molecules from the iron (hydr)oxide surface were measured. In the interfacial measurement, I could not reach the equilibrium state because the concentration of aqueous phosphate continuously increased because of the evaporation of the solution. I chose not to prevent the evaporation by employing a closed system reactor because the objective of this study was to demonstrate the idea of easily measuring the preferential adsorption on binary sorbents. For that reason, I should keep in mind that the interfacial measurement was under the non-equilibrium conditions by continuously increasing the phosphate concentration and evaporation of water from the solution.

The spectral evolution was illustrated by the time increase in the single sorbent and binary sorbents in Fig. 6-9. For better comparison of the spectra, I chose to collect a certain time in the spectra from the successive measurements. In Fig. 6-9, I only chose the spectra without the change in the absorbance of water peaks, because the evaporation was allowed in the experiment. Thus, there would be the different volumes of water at the marginal and center areas. In addition, the difference in the absorbance of water led to the significant alteration in the

**Fig. 6-7** Micro-scale image of the goethite surface (a) and maghemite surface (b) on the ZnSe crystal, 20-degree tilted image of goethite layer (c) and maghemite surface (d) on ZnSe crystal by SE2 mode under 25 kV using FE-SEM, and nanoscale image of the goethite (e) and maghemite film (f) by InLens mode under 2 kV.

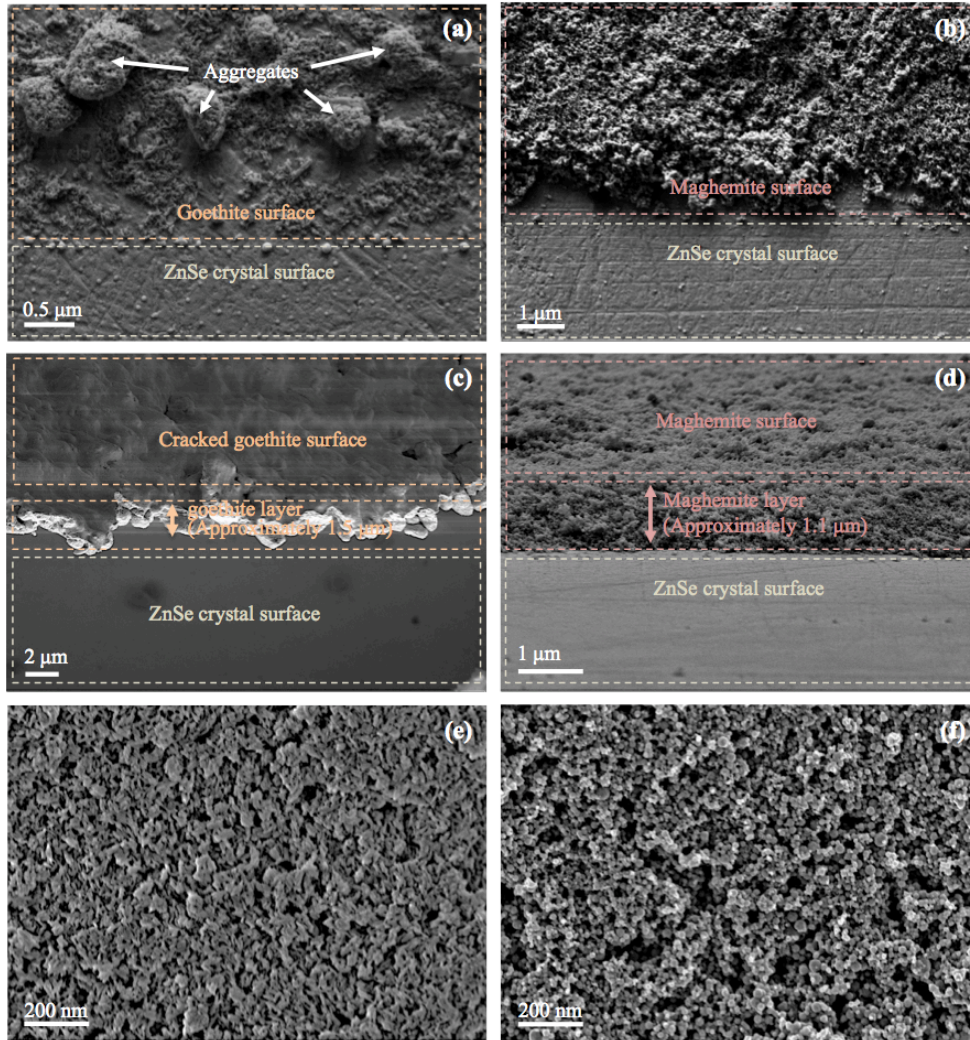


**Fig. 6-8** Stitched image of FE-SEM at 100 x magnification using SE2 mode (a), mapping image of FE-SEM-EDS at 30,000 x magnification at dark spot (b) and crystal structure (c). The right side is the marginal part of the maghemite layer, and the left side is the direction to the center part of layer. The red and blue boxes in (a) indicate the location of the mapping image (b) and (c), respectively.

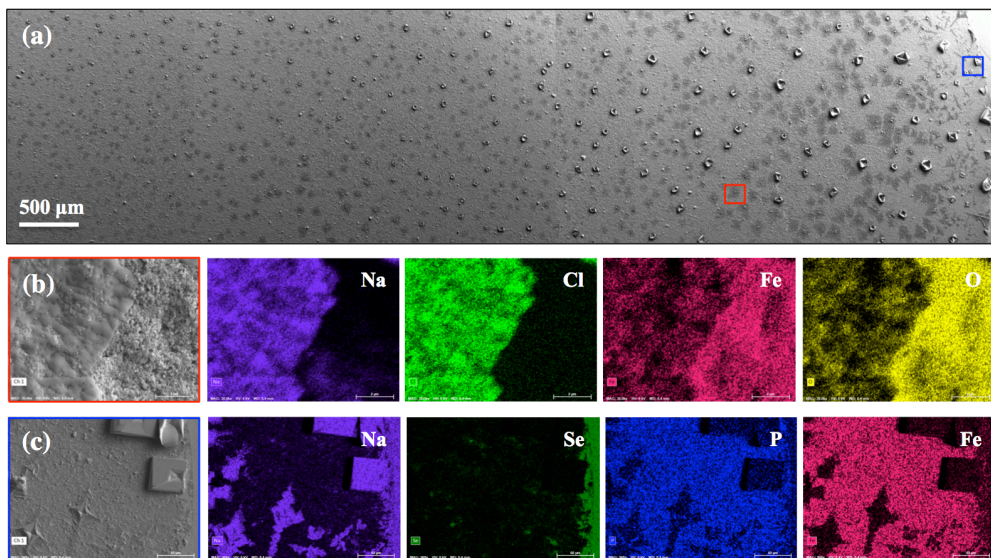
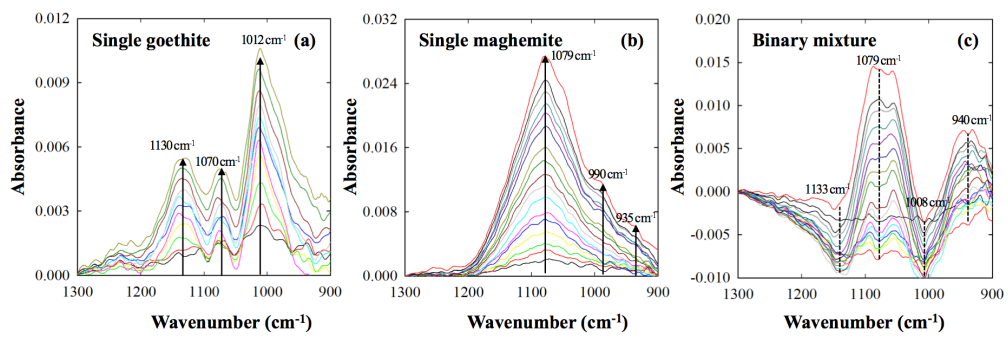


**Fig. 6-9** Evolution of time series ATR-FTIR spectra of 1 mM phosphate on the single goethite (a), single maghemite (b) and binary mixture (c) at different times up to 3 h after phosphate addition. The spectrum was calculated by subtracting the spectra at each time from the initial spectra after water saturation, and we employed only the spectra, which maintained the absorbance of the water molecule. The time for constant absorbance of the water molecule was 48, 74 and 96 min for single goethite, single maghemite and binary sorbent, respectively. The arrow line indicates the sequential increase of absorbance over time while the dotted line means the fluctuation in the absorbance over time.



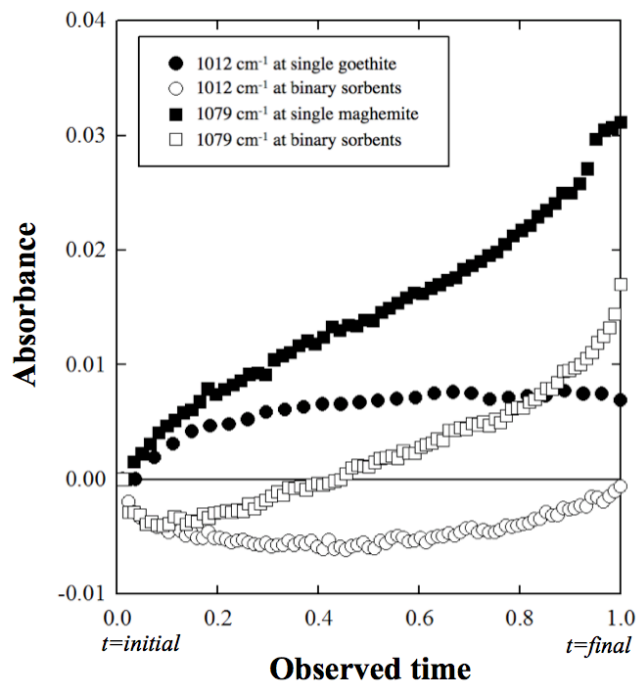
background of the ATR-FTIR spectrum, and it was complicated to isolate a meaningful signal under the different background conditions. For that reason, I defined the time without fluctuation in the water peak as the observed time of the kinetic study, and I also defined the initial ( $t=initial$ ) and final time ( $t=final$ ) as the start and end with no fluctuation of the water peak in the spectrum over time. In the result, the observed time of the kinetic study ( $t=final - t=initial$ ) was 48, 74 and 96 min for single goethite, single maghemite and binary sorbents. I understood that the binary sorbents would take a longer time in decreasing the water because 0.5 mL was added for single goethite or maghemite while 1.5 mL for the binary mixture was added to make a water bridge between the two sorbents and to give a longer time for the preferential adsorption to occur. However, I did not expect 1.54 times higher observed time for the kinetic study of maghemite over the goethite. Based on the FE-SEM observations, I identified that the porous structure in maghemite would prevent the evaporation of the water molecule by decreasing the contact area of the water with the atmosphere.

Three peaks in the single goethite or maghemite were identified, and I observed the increase of peaks at 1130, 1070 and 1012  $cm^{-1}$  with a time increase in the goethite while peaks at 1079, 990 and 935  $cm^{-1}$  were increased in the maghemite (Fig. 6-9a and 6-9b). The peaks at 1012 and 1079  $cm^{-1}$  were highest in the goethite and maghemite, and the absorbance at 1079  $cm^{-1}$  of maghemite was 2.4 times higher than the absorbance at 1012  $cm^{-1}$  of goethite. The difference was calculated in  $IA$  at 1300 to 900  $cm^{-1}$  from initial to final time, and the  $IA_{Gt,1300-900}$  and  $IA_{Mg,1300-900}$  of the single goethite and maghemite was 0.777 and 3.809, respectively. It is impossible to compare the absorbance or  $IA$  directly, because of the difference in molar absorptivity of the complex and the area of the sorbent, but if I presumed that there would no significant difference in the molar absorptivity, the maghemite had more

inner-sphere complex than the goethite. The absorbance from the outer-sphere complex or phosphate ion in the solution was not considered because we could not detect significant signal using 1 mM P solution (data not shown). Thus, I considered that the absorbance was caused mainly by the inner-sphere complex of phosphate. In the adsorption isotherm, the goethite showed 1.19 times higher  $Q_{max}$  than the maghemite, and two results from the isotherm and ATR-FTIR showed the possibility of a opposite adsorption pattern.

In the binary sorbents experiment, it showed a more complicated spectrum than the single sorbent experiment (Fig. 6-9c). The similar peaks with the single sorbent were found, but only gradual increase in the single sorbent was found while the fluctuation in the absorbance with time increase in the binary sorbents was observed. The gradual increase was illustrated in the single sorbent and the fluctuation in the binary sorbents in Fig. 6-10 for the comparison. I observed different pattern in the spectral evolution in the single sorbent because the goethite showed a saturated curve while the maghemite showed a linear curve. In addition, there was no peak shifting in the single sorbent (Fig. 6-9a and 6-9b), which indicated that a single adsorption mechanism or several adsorption mechanisms at an equivalent ratio were involved in the adsorption. In the binary sorbents, I found the decrease of absorbance initially in 1012 and 1079  $\text{cm}^{-1}$ , and it gradually increased over time. The peaks found in the goethite of binary sorbents decreased slightly, then increased over the time, and the peaks found in the maghemite of the binary sorbents were quickly decreased and dramatically increased over the time. Based on these results, I presumed that the phosphate adsorbed onto the maghemite more preferentially adsorbed than the goethite, and I tried to quantify using MLR analysis. Two parameters were set, which are the spectra from the single goethite and the single maghemite to calculate the fraction of desorption from the goethite and

**Fig. 6-10** Absorbance over time at  $1012\text{ cm}^{-1}$  in the single goethite (black circle),  $1012\text{ cm}^{-1}$  in the binary sorbents (white circle),  $1079\text{ cm}^{-1}$  in the single maghemite (black rectangle) and  $1079\text{ cm}^{-1}$  in the binary sorbents (white rectangle). The absorbance was calculated by subtracting the absorbance at each time from the initial absorbance after water saturation from  $t=\text{initial}$  to  $t=\text{final}$ , which is the observed time without the change in the water peak in the spectra.



adsorption on the maghemite. As a result, the  $f_{P/Gt,1300-880,t=48min}$  and  $f_{P/Mm,1300-880,t=96min}$  were -0.68 and 0.57, and the values clearly indicated the desorption from the goethite and adsorption onto the maghemite. I presumed the reason for the relatively poor prediction (adjusted  $r^2=0.64$ ) was because the adsorption spectrum was employed for estimating desorption and adsorption. In addition, there was the possibility of spectral shifting by changing the type of inner-sphere complex, but I found that the peaks in the binary sorbent experiment were highly correlated with the single sorbent experiment. Based on the results, it was reasonable to explain that the spectral evolution was caused by the preferential sorption of phosphate occurring on the maghemite surface with desorption from the goethite in the binary sorbent experiment compared with a single sorbent experiment.

#### 6.3.4. Drying effect in single sorbent and binary sorbents

Three ATR-FTIR spectra after drying the single goethite or maghemite with phosphate adsorption, binary sorbents with phosphate adsorption, and phosphate precipitate on the ZnSe crystal without sorbent were measured (Fig. 6-11). The single goethite or maghemite without phosphate adsorption was also measured (Fig. 6-12). The reason for measuring phosphate precipitate was that the evaporation would lead the precipitation from both outer-sphere complex and aqueous phosphate, and the binary sorbents would yield more or less precipitate than the single sorbent experiment. I calculated  $A_{(P|Gt),\lambda,t=dried}$ ,  $A_{(P|Mh),\lambda,t=dried}$  and  $A_{(P|(Gt+Mh)),\lambda,t=dried}$  according to eq. (6-7), (6-8) and (6-9), respectively. In Fig. 6-11, I illustrated the  $A_{(P|Gt),\lambda,t=dried}$ ,  $A_{(P|Mh),\lambda,t=dried}$  and  $A_{(P|(Gt+Mh)),\lambda,t=dried}$  from the measurement, and the predicted value and residuals using MLR analysis was listed (eq. (6-10)), and the adjusted  $r^2$  was 0.988. The  $A_{(P|Gt),\lambda,t=dried}$  and  $A_{(P|Mh),\lambda,t=dried}$  were the overlapped absorbance from the inner-sphere complex and precipitate (sum of the outer-sphere and aqueous

phosphate). Thus, it was impossible to separate the individual fraction of the inner-sphere complex and precipitate, but it could quantify the increase or decrease of the inner-sphere complex. In the MLR analysis, there should be two prerequisites: 1) there was no spectral change from the single sorbent to binary sorbents except the effect of the precipitate; 2) the outer-sphere complex and aqueous phosphate had the same spectrum by the precipitation. The MLR analysis was performed according to Eq. (6-10), and the  $f_{(P|Gt),\lambda,t=dried}$ ,  $f_{(P|Mh),\lambda,t=dried}$  and  $f_{(P),\lambda,t=dried}$  were 0.25, 0.91 and 1.20, respectively. I found a dramatic increase in the  $f_{(P),\lambda,t=dried}$  and dramatic decrease in the  $f_{(P|Gt),\lambda,t=dried}$  while the  $f_{(P|Mh),\lambda,t=dried}$  showed no significant change compared with the others. If there was no preferential adsorption and additional precipitation, the  $f_{(P|Gt),\lambda,t=dried}$  and  $f_{(P|Mh),\lambda,t=dried}$  should be close to 1 while  $f_{(P),\lambda,t=dried}$  should be close to 0. However, I did a single goethite and maghemite experiment in the area of 250 and 234 mm<sup>2</sup> while the total area of ZnSe was 616 mm<sup>2</sup>. Therefore, there was approximately 86 mm<sup>2</sup> for ZnSe surface where the DW was overlaid for making a bridge between the two sorbents, and there was 46 mm<sup>2</sup> as a marginal space where no DW and sorbent was overlaid. In the ZnSe surface overlaid with DW, there was the possibility of the precipitation from the desorbed and dissolved phosphate on the ZnSe surface between the two sorbents. I also examined the water movement to the two sorbents by the drying, because the small gradient on the crystal led to more P solution on the maghemite, and it caused the greater phosphate loading. However, I observed that an approximately equal amount of water was moved to the two sorbents after splitting the water bridge.

Based on these results, I inferred that the phosphate on the goethite dramatically decreased while the phosphate on the maghemite was stable, but I could not separate the fraction of precipitate for both sorbents and the ZnSe crystal. To solve the problem, I employed FE-SEM analysis equipped with EDS. The P/Fe

atomic ratio of the binary sorbent experiment by FE-SEM/EDS was 0.0521 on the goethite and 0.0656 on the maghemite. It was layered each 0.75 mg of each sorbent, and the Fe concentration of the goethite (FeOOH) and maghemite (Fe<sub>2.67</sub>O<sub>4</sub>) was 1.125 and 1.253 mmol g<sup>-1</sup>. Thus, the adsorbed phosphate was 0.44 and 0.62 μmol for the 0.75 mg of goethite and maghemite, respectively. I could not detect the precipitate on the ZnSe crystal, and it was presumed that the solubility of sodium phosphate (118 g L<sup>-1</sup>) was higher than the experimental conditions (0.156 g L<sup>-1</sup>), and if we considered the drying effect, the charged phosphate was precipitated at the sorbent surface, where the water molecules were last retained. In addition, I found no significant difference in the P/Fe atomic ratio between the margin and center of the layers in all experiments (data not shown). However, the gradient distribution of NaCl precipitate was found, and the concentration and size of the NaCl precipitate was higher at the marginal part of the layer, and it gradually decreased at the center (Fig. 6-8). As a result, the adsorbed phosphate on the maghemite was 1.4 times higher than on the goethite, and a similar result with the ATR-FTIR experiment was observed. In addition, a total of 1 μmol of phosphate was introduced, and there was a total of 1.06 μmol from the FE-SEM/EDS analysis, and the recovery was 106 %, which was a satisfactory result considering the relatively high error of the FE-SEM/EDS measurement.

#### **6.4. Conclusions**

In this study, I demonstrated how to measure the preferential adsorption of phosphate on the binary goethite and maghemite surface. I developed the experimental procedure to measure the preferential adsorption using *in situ* ATR-FTIR, and I measured the spectral evolution to identify the phosphate adsorption on the single sorbent, and binary sorbents with the drying effect on the preferential

adsorption. Based on the kinetic study at the interface, and MLR analysis with FE-SEM/EDS in the dried samples, I confirmed that the water bridge between two sorbents led to phosphate desorption from the goethite and adsorption on the maghemite. As the result, the phosphate preferentially adsorbed on the maghemite rather than the goethite, and I clearly observed the spectral difference of the phosphate complex between the interface and dried measurement, and it implied that the phosphate complex would be different under the dried condition.

In the real environment, a soil is the mixture of uncountable components, and various chemicals interact with the numerous surfaces of the soil components. It is easy to examine the total concentration of target chemical in a soil, but it is difficult to analyze the target chemical adsorption at the specific surface among the soil components at the interface, and it is also difficult to understand the adsorption mechanism when the various surfaces are available for the adsorption. The experimental procedure proposed in this study would enable us to observe the preferential adsorption on the multi iron (hydr)oxide sorbents, and it showed the actual preferential adsorption at the interface and in real time. There were numerous limitations and shortages in the experimental procedure. For example, the pH, equilibrium state and surface loading are known as the critical factors for governing the complexation at the interface, but such factor was not fully addressed. If I designed the reaction with an ATR crystal, it would reveal the effect of such factors, but I only concentrated on demonstrating the concept of measuring preferential adsorption using *in situ* ATR-FTIR. In the future, we will address such factors for better understanding of the adsorption mechanism, and we will increase the complexity of the experimental setup for more precise simulation of the natural reaction in the environment.

**Fig. 6-11** The ATR-FTIR spectra of kinetic study (a) and dried samples (b). The spectra used in multiple linear regressions (MLR) to calculate the fraction of individual components. The red, blue and black solid line indicate phosphate spectra on the goethite, phosphate spectra on the maghemite and phosphate spectra on the binary sorbents of goethite and maghemite, respectively. The grey solid line indicates the precipitate of 1 mM phosphate solution with 10 mM NaCl without sorbent. The predicted values (red dotted line) and residual (gray box) were calculated with MLR (Eq. (3)). The residual in (a) was shifted -0.01 for better illustration.

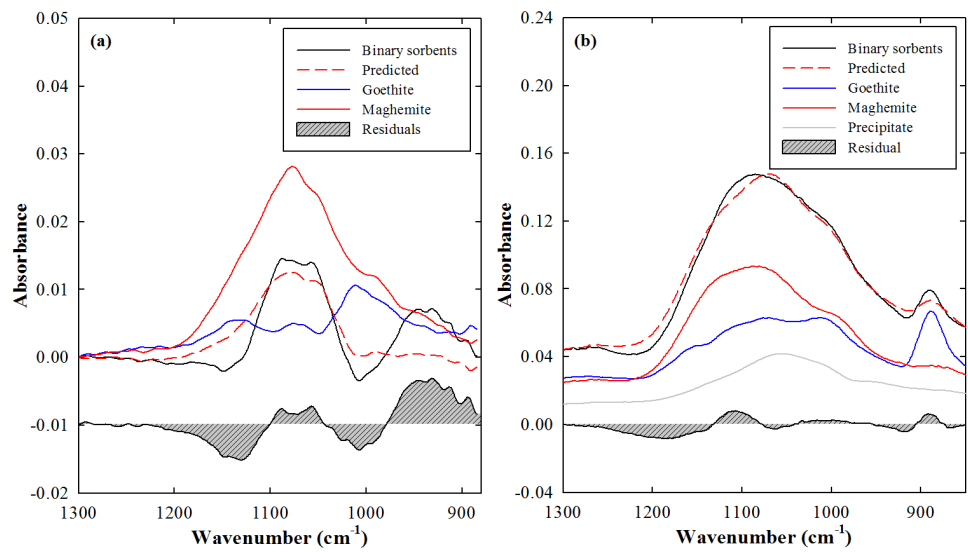
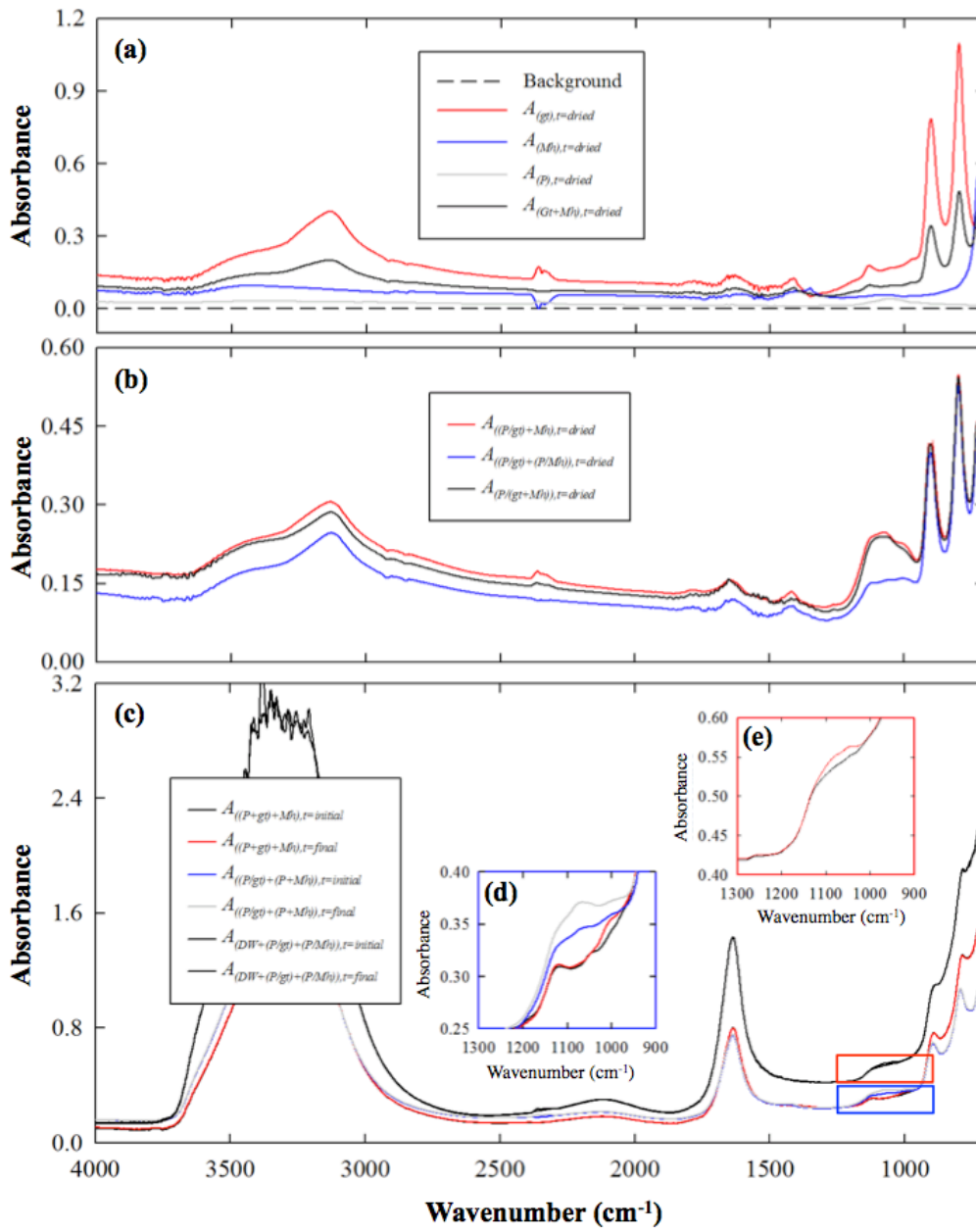


**Fig. 6-12** Measured spectra of background, phosphate precipitate, dried single sorbent and binary sorbents (a), phosphate adsorbed and dried single goethite, single maghemite and binary sorbents (b), and kinetic studies from the initial and final single goethite, single maghemite and binary sorbents (c). The small graphs in (c) are the enlargement of single sorbent (d) and binary sorbent experiment (e) from the kinetic studies for better illustration



## References

- Abdala, D.B., Northrup, P.A., Arai, Y., Sparks, D.L., 2015. Surface loading effects on orthophosphate surface complexation at the goethite/water interface as examined by extended X-ray Absorption Fine Structure (EXAFS) spectroscopy. *J. Colloid Interface Sci.* 437, 297–303. doi:10.1016/j.jcis.2014.09.057
- Acelas, N.Y., Mejia, S.M., Mondragón, F., Flórez, E., 2013. Density functional theory characterization of phosphate and sulfate adsorption on Fe-(hydr)oxide: Reactivity, pH effect, estimation of Gibbs free energies, and topological analysis of hydrogen bonds. *Comput. Theor. Chem.* 1005, 16–24. doi:10.1016/j.comptc.2012.11.002
- Arai, Y., Sparks, D.L., 2001. ATR–FTIR Spectroscopic Investigation on Phosphate Adsorption Mechanisms at the Ferrihydrite–Water Interface. *J. Colloid Interface Sci.* 241, 317–326. doi:10.1006/jcis.2001.7773
- Atkinson, R.J., Parfitt, R.L., Smart, R.S.C., 1974. Infra-red study of phosphate adsorption on goethite. *J. Chem. Soc. Faraday Trans. 1 Phys. Chem. Condens. Phases* 70, 1472. doi:10.1039/f19747001472
- Barberis, E., Ajmone Marsan, F., Scalenghe, R., Lammers, A., Schwertmann, U., Edwards, A.C., Maguire, R., Wilson, M.J., Delgado, A., Torrent, J., 1995. European soils overfertilized with phosphorus: Part 1. Basic properties. *Fertil. Res.* 45, 199–207. doi:10.1007/BF00748590
- Boukema, L., Boukhalfa, C., Reinert, L., Duclaux, L., 2016. Characterization of phosphate adsorption on goethite macroscopic and spectroscopic analyses. *J. Mater. Environ. Sci.* 7, 2541–2550.
- Carabante, I., Grahn, M., 2010. In situ ATR–FTIR studies on the competitive adsorption of arsenate and phosphate on ferrihydrite. *J. Colloid Interface Sci.* 351, 523–531. doi:10.1016/j.jcis.2010.07.064
- Daou, T.J., Grenche, J.M., Thomas, F., Derory, a, Bernhardt, P., Legar, P., Pourroy, G., Legare, P., 2007. Phosphate Adsorption Properties of Magnetite-Based Nanoparticles Phosphate Adsorption Properties of Magnetite-Based Nanoparticles 19, 4494–4505. doi:10.1021/cm071046v
- Dickson, D., Liu, G., Cai, Y., 2017. Adsorption kinetics and isotherms of arsenite and arsenate on hematite nanoparticles and aggregates. *J. Environ. Manage.* 186, 261–267. doi:10.1016/j.jenvman.2016.07.068
- Downs, R., Hall-Wallace, M., 2003. The American Mineralogist crystal structure database. *Am. Mineral.* 88, 247–250.
- Elser, J.J., Bracken, M.E.S., Cleland, E.E., Gruner, D.S., Harpole, W.S., Hillebrand, H., Ngai, J.T., Seabloom, E.W., Shurin, J.B., Smith, J.E., 2007. Global analysis of nitrogen and phosphorus limitation of primary producers in freshwater, marine and terrestrial ecosystems. *Ecol. Lett.* 10, 1135–1142. doi:10.1111/j.1461-0248.2007.01113.x
- Elzinga, E.J., Huang, J.-H., Chorover, J., Kretschmar, R., 2012. ATR-FTIR spectroscopy study of the influence of pH and contact time on the adhesion of

- Shewanella putrefaciens bacterial cells to the surface of hematite. *Environ. Sci. Technol.* 46, 12848–55. doi:10.1021/es303318y
- Elzinga, E.J., Sparks, D.L., 2007. Phosphate adsorption onto hematite: An in situ ATR-FTIR investigation of the effects of pH and loading level on the mode of phosphate surface complexation. *J. Colloid Interface Sci.* 308, 53–70. doi:10.1016/j.jcis.2006.12.061
- Gao, Y., Mucci, A., 2001. Acid base reactions, phosphate and arsenate complexation, and their competitive adsorption at the surface of goethite in 0.7 M NaCl solution. *Geochim. Cosmochim. Acta* 65, 2361–2378. doi:10.1016/S0016-7037(01)00589-0
- Geelhoed, J.S., Hiemstra, T., Van Riemsdijk, W.H., 1997. Phosphate and sulfate adsorption on goethite: Single anion and competitive adsorption. *Geochim. Cosmochim. Acta* 61, 2389–2396. doi:10.1016/S0016-7037(97)00096-3
- Kubicki, J., Paul, K., Kabalan, L., Zhu, Q., 2012. ATR-FTIR and Density Functional Theory Study of the Structures, Energetics, and Vibrational Spectra of Phosphate Adsorbed onto Goethite. *Langmuir* 28, 14573–14587.
- Kubicki, J.D.J., Kwon, K.D., Paul, K.W., Sparks, D.L., 2007. Surface complex structures modelled with quantum chemical calculations: Carbonate, phosphate, sulphate, arsenate and arsenite. *Eur. J. Soil Sci.* 58, 932–944. doi:10.1111/j.1365-2389.2007.00931.x
- Lindgren, M., Persson, P., 2009. Competitive adsorption between phosphate and carboxylic acids: Quantitative effects and molecular mechanisms. *Eur. J. Soil Sci.* 60, 982–993. doi:10.1111/j.1365-2389.2009.01171.x
- Manning, B.A., Goldberg, S., 1996. Modeling Competitive Adsorption of Arsenate with Phosphate and Molybdate on Oxide Minerals. *Soil Sci. Soc. Am. J.* 60, 121. doi:10.2136/sssaj1996.03615995006000010020x
- Multani, M.S., 1990. *Physics of clusters and nanophase materials*. 2. Gordon and Breach.
- Parikh, S.J., Mukome, F.N.D., Zhang, X., 2014. ATR-FTIR spectroscopic evidence for biomolecular phosphorus and carboxyl groups facilitating bacterial adhesion to iron oxides. *Colloids Surf., B* 119, 38–46. doi:10.1016/j.colsurfb.2014.04.022
- Rahnemaie, R., Hiemstra, T., van Riemsdijk, W.H., 2007. Carbonate adsorption on goethite in competition with phosphate. *J. Colloid Interface Sci.* 315, 415–425. doi:10.1016/j.jcis.2007.07.017
- Tofan-Lazar, J., Al-Abadleh, H., 2012. Kinetic ATR-FTIR Studies on Phosphate Adsorption on Iron (Oxyhydr)oxides in the Absence and Presence of Surface Arsenic: Molecular-Level Insights into the Ligand Exchange Mechanism. *J. Phys. Chem. A* 116, 10143–10149.
- Waiman, C. V., Avena, M.J., Regazzoni, A.E., Zanini, G.P., 2013. A real time in situ ATR-FTIR spectroscopic study of glyphosate desorption from goethite as induced by phosphate adsorption: Effect of surface coverage. *J. Colloid Interface Sci.* 394, 485–489. doi:10.1016/j.jcis.2012.12.063

- Yang, H., Lu, R., Downs, R.T., Costin, G., 2006. Goethite,  $\alpha$ -FeO(OH), from single-crystal data. *Acta Crystallogr. Sect. E Struct. Reports Online* 62, i250–i252. doi:10.1107/S1600536806047258
- Yang, Y., Chun, Y., Sheng, G., Huang, M., 2004. pH-Dependence of Pesticide Adsorption by Wheat-Residue-Derived Black Carbon. *Langmuir* 20, 6736–6741. doi:10.1021/la049363t
- Zheng, T.T., Sun, Z.X., Yang, X.F., Holmgren, A., 2012. Sorption of phosphate onto mesoporous  $\gamma$ -alumina studied with in-situ ATR-FTIR spectroscopy. *Chem. Cent. J.* 6, 1–10. doi:10.1186/1752-153X-6-26

(This page intentionally left blank)

## CHAPTER 7. SUMMARY AND CONCLUSION

### 7.1. Summary

In the literature review, the importance of mutual interactions was explained for controlling the bioavailability of oxyanions in the rhizosphere with the examples from the previous studies. The transformation of iron (hydr)oxides during the adsorption experiment were identified, and the oxyanions, pH, and time control the transformation directly while the exudation from the plant also affects the transformation indirectly. For the structural configuration, the inner-sphere bidentate complex was predominant for arsenate, arsenite, phosphate, and silicate; the monodentate and bidentate complexes were abundant in carbonate, chromate, selenite, and selenate whereas only a monodentate complex was observed in sulfate. The competing ions, pH and surface loading significantly affected the structural configuration of oxyanions, and a higher surface loading with a lower sorption site decreased the dentation in arsenate. For competitive sorption, the *CSR*, *RSP*, and *CE* were used for a quantitative comparison. A similar pattern between the selectivity sequence using the *RSP* and previous literature was found, and the *CE* between arsenate and arsenite was increased by the surface loading increment. The organic acid competed with the oxyanions at low pH, and it also affected the iron (hydr)oxides. The pH and surface loading were the most significant factors for controlling competitive sorption. Based on these observations, I concluded that the complex with higher dentation would dominate the sorption sites during competitive sorption but the increase of competition or decrease of sorption site reduces the dentation of complex.

In the experimental procedure, advantage and limitation in computational chemistry, infrared and X-ray spectroscopy were summarized to identify and understand the rhizospheric interactions among organic acids, oxyanions, and metal oxides. Since organic acids and metal oxides determine dynamics of oxyanions in the soil environment, the knowledge of fundamental mechanisms is a prerequisite for understanding the interactions at soil-water interface. The ATR-FTIR is a powerful tool to measure the interfacial reactions, but the ATR-FTIR measurements are abstruse in certain conditions because the optical characteristics for measurements are variable depending on the experimental setup. Besides, spectral overlapping is a primary obstacle to the analysis of the interfacial reaction; thus, it is essential to detect and deconvolute bands for the significant signal interpretation. The fundamental principles for spectrum processing and band identification methods were described with an example of aqueous phosphate speciation for ATR-FTIR and sodium arsenate for XAS. But, the spectrum processing and computational chemistry improved interpretation and spectral deconvolution of overlapped spectra in a relatively simple system, but it was still unsatisfactory for the problems in a more complex system like nature. Based on the literature review and experimental procedure, the structural configuration and the interfacial measurement were conducted as follows.

The structural configuration of oxyanions on the iron (hydr)oxide determines its leachability and bioavailability in the soil environment. It is important to understand how the stability of iron hydroxide and structural configuration of arsenate complexes varies in response to changes in environmental conditions. Therefore, the effects of drying, pH and surface loadings were investigated on the stability of goethite and structural configuration of arsenate through batch experiments and TEM and XAS measurements with DFT calculation.

As a result, we observed no significant transformation of goethite under the most conditions, but TEM analysis confirmed a partial formation of bernalite in the presence of arsenate at pH 10, and the bernalite showed 2.18 times higher arsenate sorption than the goethite. Linear combination fitting of EXAFS spectrum with DFT calculations revealed that tridentate and bidentate complexes were dominant under low surface loading and pH in the sedimented samples, while monodentate complexes were abundant under high surface loading and pH. The transition of structural configuration was clearly observed with the perturbation in the arsenate concentration, surface loading, and pH condition.

The arsenate and phosphate have similar properties because of their electrochemical structures, but their environmental impacts are unique. Numerous chemicals co-exist in the soil environment at various concentrations, and their abundance and competition determine the bioavailability and leachability. The effects of pH and surface loading on the competitive adsorption between arsenate and phosphate were evaluated on four synthetic iron (hydr)oxides by employing the Langmuir isotherm and developed equations, and I assessed the stability and transformation of the iron (hydr)oxides. As a result, various adsorption patterns were observed in the single and mixture treatments by controlling the oxyanion, pH, surface loading and type of iron (hydr)oxides, and I employed  $CSR$  and  $CE$  equations, which are the equation used in the literature review. As a result, the arsenate was preferentially adsorbed at a low pH, while phosphate was the opposite. The  $CE_{As(V),P(V)}$  was close to zero at a low surface density (no competition), and it sequentially changed to negative and positive values with the increasing surface density, because of the sequential development of the promotive and competitive effects. The transformation in goethite was identified at a high pH with the presence of both arsenate and phosphate, except that no transformation was observed upon

the addition of oxyanion and with the pH change. However, the stability of the iron (hydr)oxides decreased with a low pH and with the presence of phosphate or arsenate or both. The hematite showed a significant promotive effect regardless of the pH condition.

Recent developments in analytics using infrared spectroscopy enabled the identification of the adsorption mechanism at the interface, but it is applicable only for simple systems. An experimental procedure was developed to measure preferential adsorption of phosphate on the binary sorbents of goethite and maghemite before and after dehydration using batch experiment, *in-situ* ATR-FTIR, and FE-SEM/EDS. The  $Q_{max}$  for phosphate of goethite at pH 4 was about 1.2 times as high as that of maghemite. I observed the uniform layer in maghemite and heterogeneous layer with aggregates (up to 6  $\mu\text{m}$ ) in goethite and confirmed no significant change in the layers during the experiment. The spectral evolution at the interface was observed, and the fraction of phosphate complex on goethite and maghemite was calculated using multiple linear regressions (MLR) as -0.68 and 0.57, respectively, clearly showing the phosphate desorption from goethite and subsequent adsorption onto maghemite. The fraction of the precipitate (1.2) and the complex in goethite (0.25) and maghemite (0.91) was also computed to describe the dehydration effect using MLR. The amount of phosphate adsorbed on goethite and maghemite was 0.59 and 0.83  $\mu\text{mol mg}^{-1}$ , respectively *via* FE-SEM-EDS. The preferential adsorption of the phosphate on maghemite over goethite was clearly observed.

## 7.2. Conclusion

The most of scientific researches have employed top-down, bottom-up, or both approaches to expand our scientific knowledge, but I believe that the top-down approaches were predominant for the last centuries in the field of soil science, because of the heterogeneity of soil and the lack of sufficient analytical technique. Recent development in the nano-science has enabled us to observe the chemical structure in an atomic level, and it has informed us another level of knowledge to understand the chemical reactions in nature. The soil scientists and geologists have succeeded to identify the most significant factors dominating the chemical reactions from the heterogeneous soil, but it has not clearly explained the detailed mechanisms or the explained mechanisms were not applicable in other cases. On the other hands, the scientists in catalyst and material have tried to understand the individual chemical reactions on monologue materials, and they have shown the significant improvement of our understanding, but the extrapolation from the result in monologue media to predict the chemical reactions in the heterogeneous media was also challenging. The modern analytical technique and theoretical chemistry have provided us to challenge such problems, and they have made a great advance to reduce the knowledge gaps between the top-down and bottom-up approaches. I have tried to reduce the knowledge gaps by the bottom-up approach, and only iron (hydr)oxides were employed in this study, but further investigation on a more heterogeneous model soil with background knowledge on the monologue media would eliminate the gaps in the future.

### 7.2.1. Study background

As an undergraduate student, biology was my major, and ecology

specifically the plant-environment interaction was my favorite field of study. For that reason, I choose to study further in the field of phytoremediation. As a graduate student in the ecological and environmental engineering, I had tried to reveal the eco-toxicological effect of heavy-metal polluted soil on the seedling growth, and the heavy metal stabilization study was conducted using iron-containing byproduct in the abandoned mine areas. Based on the studies, I had gotten the interesting results, but my interpretation was ambiguous. I could not isolate the effect of individual heavy-metal in both eco-toxicological and stabilization studies, but I found a significant reciprocal correlation between the bioavailable fraction of arsenic and phosphorus by sequential extraction procedure.

Interestingly, the arsenic uptake in the cultivation area and the soil near the drainage system was significantly lower than the uncultivated area, which the phosphorus fertilizer was not applied. From the studies, I found who, when, what, and where cause the phenomenon, but I could not understand why and how the phenomenon happens. I did the literature review and found several studies reporting the competitive sorption of arsenic and phosphorus, but the result was differed case by case especially in the studies employing natural soils. But, I found few interesting studies employing ATR-FTIR and EXAFS to identify the structural configuration of arsenic and phosphorus on monologue media, and it showed the possibility to explain the study result, but it was not applicable for the study, because it was impossible to use the ATR-FTIR and EXAFS at that time. When I was planning to acquire a doctorate, I designed a study by employing the bottom-up approach for the model soil with the ATR-FTIR and EXAFS techniques, but I have only focused on the iron (hydr)oxides with two oxyanions in this dissertation, because there are plenty of missing information or opposite results in the similar experimental conditions.

### 7.2.1. Stability of nanoparticles and its colloidal transport

Based on this study and previous literature, the transformation of iron (hydr)oxides was confirmed, the minor perturbation in the environmental condition would lead to significant different result of the transformation. The pH, redox, dehydration, presence, and concentration of ions, temperature, pressure and atmospheric condition are complexly inter-connected, and the transformation of iron(hydr)oxides was determined upon the conditions. The topotactic transformation requires massive energies or excessive perturbation in the conditions, such as forest fire and subsidence, while the reconstructive transformation occurs in the most of soil environment with water contents. During the reconstructive transformation, the oxyanions work as both protector and destroyer of Iron-nanoparticles, and the oxyanions would be the part of iron (hydr)oxides itself by coprecipitation. The environmental conditions started the transformation of iron (hydr)oxides, but the transformation also alters the environmental conditions too.

The complexly inter-connected mechanisms determine the stability and transport of nanoparticles and oxyanions together, but the most of previous studies could not fully address such effect. In this study and previous research found only two days were required for the transformation in the moderate conditions, the majority of adsorption studies using oxyanion and iron (hydr)oxides has not addressed such transformation effect. In addition, the filter size for measuring the concentration in the most studies was not able to filter the nanoparticles, which indicates that the possibility of underestimation during the isotherm studies. In this result, the bernalite was transformed from the goethite at pH 10 with arsenate, and the diameter was approximately 27.3 nm as average, which was not filtered by the commercial filters. The centrifugation was also applied to separate the aqueous ions and bernalite, but the bernalite was still found in the solution after filtration and

centrifugation. The inner-sphere complex on the bernalite surface changes the electrochemical properties of bernalite, and it might increase the colloidal stability of bernalite.

The paddy field is the typical land use scheme in Asia countries, the transformation of iron (hydr)oxides is easily observed by the cultivation and seasonal variation. As mentioned above, not only the crystal structure but also the morphology can be easily changed, and it could lead dramatic flux of oxyanions from soil to water system. Recent eutrophication accompanying the increase of phosphorus level causes severe threats to the ecosystem, and the possibility of transformation has been identified, but its contribution has not fully estimated yet. However, the colloidal mobilization and combination with soil erosion by flooding or intensified rainfall would accelerate the eutrophication in the water system, and it would yield severe disasters to humans eventually. This study would help to reduce such mobilization by controlling the environmental conditions with a better understanding of the oxyanion dynamics.

#### 7.2.2. Proton concentration effect

The proton concentration has known as the most important factor governing the chemical reactions and transformations of oxyanions in the soil environment. It controls the electrochemical characteristics of the surface, and it is also connected to the colloidal stability of iron (hydr)oxides by changing the net surface charge, and the reactivity of oxyanions by the protonation or deprotonation. The proton is known as the strongest competitor among the cations, and it easily replaces the cations from the iron (hydr)oxide surface or it binds with the oxygen of iron (hydr)oxides, and change to a positive charge of the surface. The positively charged surface attracts the aqueous oxyanions, and the formation of OS and IS

complexes would be increased. For that reason, the adsorption capacity would be increased; the repulsive force between the colloidal nanoparticles decreased with the pH decrease at the PNZC, and the repulsive force would be increased by the increase of positively charged surface.

The proton concentration has effects on the dissolution rate of iron (hydr)oxides and structural configuration of arsenate on the goethite surface. More aqueous iron was detected at the low pH condition than the high pH, and the presence of reducing agents such as oxalate, ascorbate, and antimonate also decreased the dissolution rate. By increasing pH condition, the adsorption capacity and fraction of TB and BB complex were dramatically decreased. It clearly implies the pH effect on the structural configuration. Based on recent observations, the transition of structural configuration has reported, and the pH and surface loading causes similar result together.

#### 7.2.3. Surface loading effect

The abundance of individual components such as oxyanions, cations, phyllosilicate, metal (hydr)oxides and organic matters have extremely differed in nature, and there are additional variations in the time, organism, space, and season. As a result, their concentration determines the pathways of chemical reactions, and the ratio between the limited sorption sites of sorbent and available sorbates showed interesting results. Based on the isotherm studies, the increase of surface loading elevates the adsorbed oxyanions on the iron (hydr)oxide surface, and the EXAFS study with the DFT calculation revealed that the transition from TB and BB to MM complex was the reason for the elevated arsenate concentration in the goethite surface. The surface loading showed a similar result with the proton concentration, which deduced the fraction of available sorption site, but the increase of surface

loading leads the increase available sorbate; thus, the similar result was observed.

As I discussed in chapter 5, the surface loading effect showed significant change on the competitive sorption of arsenate and phosphate, and there is no competition at low surface loading condition, but the competition (expressed as *CE*) was dramatically increased at a certain point. Two reasons for the phenomenon could be estimated; first, the arsenate and phosphate might have slightly different sorption affinity on the sorption site; second, the increased surface loading eventually decreases the thickness of the diffuse double layer; thus, the coagulation between nanoparticle would be formed.

#### 7.2.4. Dehydration effect

The ATR-FTIR and EXAFS studies clearly confirmed the significant difference of the structural configuration between the wet and dried samples. As discussed above, the previous studies mainly employed the dried samples for the analysis, and it has caused severe problems to interpret the bioavailable fraction, which is surface specific complex and a minor portion from the total concentration. Based on the EXAFS study, the aqueous arsenate and OS complex was transitioned to the arsenate precipitates, and the IS complex was not identified except the BB complex. The ATR-FTIR spectra of arsenate precipitate, dried and wet sample clearly demonstrated the transition of the complex by the dehydration process.

Not only the structural configuration of surface complex but also the crystal structure of iron (hydr)oxides is determined by the level of dehydration. During the dehydration process, the concentration of solute is increased, and it causes the precipitation as unknown composition, and it also has a similar effect with the surface loading before the complete dehydration. In addition, the coagulation between nanoparticles would be accelerated during the dehydration,

and the complexly connected interactions between environmental conditions control the behavior of oxyanions in the soil environment.

#### 7.2.5. Competitive adsorption and preferential adsorption

If the sorption site is a monologue and constant, the sorption of oxyanions is determined by the competition by individual oxyanion. The surface loading is the competition between the single species, but it could not be observable in nature. As described in chapter 5, the oxyanions have different sorption characteristics, and the perturbation in the environmental conditions would influence the sorption characteristics. More arsenate was adsorbed than the phosphate at low pH condition, but the more phosphate was abundant at high pH conditions, and the crystal structures of iron (hydr)oxides showed slightly different sorption characteristics too.

On the other hand, the preferential adsorption is more related to the affinities of certain oxyanions on the multi-sorption sites, and this study described how to easily measure the preferential adsorption using the ATR-FTIR technique with an example of phosphate complexation. Based on the observation, the unexpected result was concluded, the isotherm result showed that the goethite showed more maximum sorption capacity, but the ATR-FTIR and SEM-EDS results indicated that more phosphate was adsorbed on the maghemite, not to the goethite. Based on the result, the adsorption behaviors of oxyanions in the complex mixtures is not linearly correlated with the adsorption behaviors of oxyanions in the single sorbent system, and various environmental conditions determine the adsorption characteristics.

#### 7.2.6. Environmental implication and further prospect

The colloidal stability and mobilization is the most important factor to

estimate the behaviors of oxyanions in the soil environment, and understanding such behavior is critical to reducing the environmental problems caused by the oxyanions. As repeatedly mentioned above, the environmental conditions are complexly connected, and it is almost impossible to understand the behaviors completely. However, recent development in the signal processing, theoretical chemistry, and analytical technique enable us to reduce the knowledge gaps.

In this study, I presented only parts of the whole experiment results, which the data was analyzed and submitted to the journals; thus, I still have various data sets and plans for further experiments to reveal the mystery of bioavailability and leachability. For example, the transition of phosphate was also observed by changing pH and surface loading using ATR-FTIR with DFT calculation, which is similar with chapter 4, and the effect of the presence of organic acids on the structural configuration was studied too. The structural configuration of arsenate using ATR-FTIR and EXAFS has also measured in four iron (hydr)oxides with changing the pH and surface loading. In addition, the preferential sorption of arsenate was conducted, even the bi-solutes of arsenate and phosphate on bi-sorbents of goethite and maghemite were performed, and these data wait for the interpretation in near future. I believe that the bottom-up approach from simplest system to the more complex system would eventually explain the adsorption characteristics of all types of soils, and the environmental problems would be diminished by controlling the bioavailability and leachability in the future, and I will do my best to make it happen.

## ABSTRACT IN KOREAN

산화음이온은 유기체의 중요한 구성 성분이며, 산화음이온, 유기산, 그리고 금속 (수)산화물들 간의 상호 작용은 토양 및 수질 환경에서 산화음이온의 생물유효도와 용출도를 결정한다. 결합 구조와 경쟁 그리고 선호 흡착은 산화음이온의 거동을 결정하지만, 다양한 환경 조건의 변화에 따라 이들이 어떻게 산화음이온의 거동에 영향을 미치는지에 대한 연구는 아직 부족한 실정이다. 이 연구에서는, 나노 입자 크기의 철 (수)산화물의 변형과 산화음이온의 결합 구조, 경쟁적 흡착 그리고 선호 흡착을 리뷰하였다. 또한, 수소이온 농도와 표면 부하를 변화시키면서 산화음이온의 결합구조를 연구하였고, 이중-흡착물 혹은 이중-흡착제 계를 설치하여 경쟁적 흡착이나 선호 흡착을 연구하였다. 그 결과, 범밀도함수이론을 이용한 계산과 X선 흡수 광원 미세구조 분광 분석은 낮은 수소이온농도와 표면 부하 조건에서 침철석 표면에서 비산염의 삼중 결합 구조를 형성하는 것을 확인하였고, 높은 pH와 표면 부하 조건에서는 단일 및 이중결합 구조를 형성하는 되는 것과 동시에 침철석의 bernalite로의 변형도 관찰하였다. 배치실험을 통한 랭뮤어 흡착등온식은 네개의 철 수산화물 표면에서 비산염이 낮은 수소이온농도 조건일 때 더 많이 경쟁적으로 흡착하고, 반대로 높은 수소이온농도 조건일때는 인산염이 더 많이 흡착하는 것을 확인하였다. 이중-흡착물 계에서 표면 부하를 증가시킬수록 촉진 효과와 경쟁 효과가 순차적으로 나타나는 것을 확인하였다. 이중-흡착제 실험에서는 감쇄전반사-적외선 분광법과 주사전자현미경-에너지분산 분광법을 이용하여 인산염이

침철석보다 마그네사이트 표면에 더 선호 흡착을 하는 것을 처음 실험적으로 확인하였다. 이러한 연구를 통하여 흡착에 유효한 표면의 형태나, 경쟁 이온의 농도, 시료의 상, 표면 부하 그리고 수소이온농도 등이 산화음이온의 결합 구조와 경쟁 그리고 선호 흡착에만 영향을 끼치는 것이 아니라, 철 (수)산화물의 변형에도 영향을 미치며, 이렇게 상호 연계되어 있는 기작들이 토양 환경에서 산화음이온의 거동을 결정하는 것을 확인할 수 있었다. 본 연구를 통하여 나는 간단한 계로 부터 조금 더 복잡한 계로의 연구, 즉 상향식 연구 방법이 모든 토양 형태에서 산화음이온의 거동을 설명하고, 이러한 이해를 통하여 생물유효도와 용출도를 조절함으로써 우리가 직면하고 있는 다양한 환경문제를 해결할 수 있을 것이라 판단한다.

**중심어:** X선 흡수 광연 미세구조 분광학, 감쇄전반사-적외선 분광학, 경쟁적 흡착, 선호 흡착, 산화음이온, 철 (수)산화물

**학번:** 2014-31235

(This page intentionally left blank)

# LIST OF PUBLICATIONS

## Published articles

- Han, J.**, Ro, H., 2018. Identification of Bernalite Transformation and Tridentate Arsenate Complex at Nano-goethite under Drying, pH and Surface Loading. *Sci. Rep.* 1–10. doi:10.1038/s41598-018-26808-4 (SCI, IF=4.85)
- Han, J.**, Ro, H.-M., Cho, K.H., Kim, K.-W., 2016. Fluxes of nutrients and trace metals across the sediment-water interface controlled by sediment-capping agents: bentonite and sand. *Environ. Monit. Assess.* 188, 566. doi:10.1007/s10661-016-5583-x (SCIE, IF=1.71)
- Han, J.**, Kim, J., Kim, M., Moon, D.H., Sung, J.-S., Hyun, S., 2014. Chemical Extractability of As and Pb from Soils Across Long-term Abandoned Metallic Mine Sites in Korea and Their Phytoavailability Assessed by *Brassica juncea*. *Environ. Sci. Pollut. Res. Int.* 22, 1270–8. doi:10.1007/s11356-014-3441-3 (SCI, IF=2.74)
- Han, J.**, Ro, H., 2017. Reviews in Infrared Spectroscopy and Computational Chemistry to Reveal Rhizospheric Interactions among Organic Acids, Oxyanions and Metal oxides: Fundamental Principles and Spectrum Processing. *J. Korean Soc. Environ. Eng.* 39, 426–439. (KCI)
- Lee, S., **Han, J.**, Ro, H., 2018. Interpreting the pH-dependent mechanism of simazine sorption to *Miscanthus* biochar produced at different pyrolysis temperatures for its application to soil 35, 1–9. doi:10.1007/s11814-018-0054-4 (SCI, IF=2.01)
- Kim, M., **Han, J.**, Hyun, S., 2013. Anion exchange of organic carboxylate by soils responsible for positive Km-*fc* relationship from methanol mixture. *Chemosphere* 93, 133–9. doi:10.1016/j.chemosphere.2013.05.005 (SCI, IF=4.12)
- Ro, H.M., Kim, P.G., Park, J.S., Yun, S.I., **Han, J.**, 2018. Nitrogen removal through N cycling from sediments in a constructed coastal marsh as assessed by <sup>15</sup>N-isotope dilution. *Mar. Pollut. Bull.* 129, 275–283. doi:10.1016/j.marpolbul.2018.02.037 (SCI, IF=3.34)

## Accepted or in progress articles

- Han, J.**, Ro, H., 2018. Review in Structural Configuration and Competitive Sorption of Oxyanions and Organic acids on Iron (Hydr)oxide Surfaces Geoderma (Under major revision) (SCI, IF=4.16)
- Han, J.**, Ro, H., 2018. Interpreting Competitive Adsorption of Arsenate and Phosphate on Synthetic Nano-iron (hydr)oxides: Effects of pH and Surface Loading *Env. Sci. Pol. Res.* (Under major revision) (SCI, IF=2.8)
- Han, J.**, Ro, H., 2018. Characterizing Preferential Adsorption of Phosphate on Binary Sorbents of Goethite and Maghemite Surface using in situ ATR-FTIR and FE-SEM/EDS Geoderma (Submitted) (SCI, IF=4.71)

## Patents

- Hyun S., Kim, Y.S., Han J., 2016, 식물 독성 평가용 식물 생장 용기 및 이를 이용한 식물독성 평가 방법 (특허번호:10-2016-012856)

## ACKNOWLEDGEMENT

2002년 대학 생활을 시작하고, 2018년 졸업을 준비하는 오늘까지 정말 많은 시련과 고난이 저를 찾아왔던 것 같습니다. 힘든 과정 중에서도 오늘 이렇게 작은 결실을 볼 수 있었던 것은 하늘에서 언제나 저를 지켜봐 주시고 응원해주시는 부모님, 무엇보다 바꿀 수 없는 내 가족, 항상 나를 걱정해주고 쓰러지지 않도록 지지해준 친구들 그리고 공부와 연구의 재미를 알게 해 주신 교수님들과 연구실 선배님들의 덕분이라 생각합니다.

특히 본 논문을 완성하기까지 많은 조언과 지도를 해주신 노희명 교수님께 감사의 말씀을 드립니다. 부족한 저를 보듬어주시고 많은 관심을 가져주셔서 지금의 제가 있는 것 같습니다. 그리고 바쁘신 가운데 논문심사 및 논문에 대해서 많은 조언을 해주신 김정한 교수님, 배의영 교수님, Yoshio Takahashi 교수님 그리고 김민희 박사님께도 감사를 드립니다. 또한 많은 가르침과 연구에 조언을 주신 김수연 교수님, 최양도 교수님, 오기봉 교수님, 이상기 교수님, 김민균 교수님 그리고 신찬석 교수님께도 감사의 인사를 드리고 싶습니다. 그리고 처음 연구라는 것을 너무 재미있게 가르쳐주셨던 고려대학교 임수길 교수님과 현승훈 교수님, 그리고 다양한 연구 경험을 하게 해주신 광주과학기술원 김경웅 교수님께도 감사드립니다.

4년이란 시간 동안 연구실에서 시간 대부분을 함께 지내면서 공부와 연구에 많은 도움과 동기부여가 되어준 서연, 지숙, 명석, 윤미, 재원, 미혜 그리고 종서 형님께 고마움을 전하고 싶습니다. 저를 이끌어주시고 조언을 아끼시지 않는 이군택 박사님, 이상모 박사님, 윤석인 박사님 그리고 남영준 선배님께도 감사한 마음을 전합니다. 그리고 삶과 연구에 많은 도움을 주셨던 고려대학교 민희 누나, 용성 형님, 승모 형님, 영록 형님,

주희, 원재, 민석, 찬양 그리고 권민에게도 고맙다는 말을 하고 싶습니다. 특히 아무것도 모르던 저를 가르치고 또 가르쳐서 오늘날에 연구자 한준호를 만들어주신 민희 누나에게 정말 감사드리고 싶습니다. 또한 광주과기원에서 나노 연구에 대해 많은 것들을 알려주신 이병태 박사님, 김현아 박사님, 김기락 박사님, 이상호 박사님, 계산화학을 알려준 동경대 Masato Tanaka 박사님, 아제르바이잔 과제를 함께 하면서 많은 도움을 주시는 Garib Mammadov 교수님, Zaman Mammadov 교수님과 Elton Mammadov 교수님께도 감사드립니다.

어려울 때 항상 내 옆에서 묵묵히 서 있어 주었던 상호, 나랑 많이 닮은 친구 성욱, 그리고 항상 존경스럽고 넓은 가슴을 가진 용현, 나의 삶의 활력소이자 나침반인 성진, 장가를 보내야 하는 민수, 누구보다 부러운 친구 동욱, 언제나 멋지고 강한 친구인 근철, 꿈을 쫓아가는 성민, 항상 관심이 가는 태현, 항상 나에 안부를 묻는 준원 형님, 여러분 덕분에 제가 이 자리에서 이렇게 서 있을 수 있습니다. 정말 고맙고 감사합니다.

힘든 시간을 함께 이겨온 장한 동생이자 인생의 친구인 재호와 행복한 웃음을 짓게 만들어주는 은혜, 그런 저희를 부모님처럼 항상 지켜봐 주시고 챙겨주셨던 선종근 이모부님과 박숙자 이모님, 그리고 박향점 이모님과 외할머님께 정말 감사합니다. 하늘에서 언제나 저를 응원해주시고, 바르게 살 수 있도록 끝은 정신을 선물해주신 아버지와 어머니, 사랑하고 많이 보고 싶습니다. 박사과정 4년 동안 옆에서 항상 저를 지켜줬던 아내이자 동료인 이서연에게 정말 감사하다고 이해해줘서 고맙다고 말하고 싶습니다. 항상 당신이 말한 것처럼 당신은 나에게 복덩이네요. 앞으로도 복덩이를 애지중지하며 살겠습니다. 그리고 장인어른 장모님, 이런 복덩이를 제게 주셔서 감사합니다. 마지막으로, 오늘날 저를 있게 만들어 주신 모든 분께 감사의 마음을 전합니다.

(This page intentionally left blank)